Title
Classification and characterization of topological insulators and superconductors

Author
Mong, Roger

Publication Date
2012

Classification and characterization of topological insulators and superconductors

by

Roger Mong

A dissertation submitted in partial satisfaction of the
requirements for the degree of
Doctor of Philosophy

in

Physics

in the

Graduate Division
of the
University of California, Berkeley

Committee in charge:
Professor Joel E. Moore, Chair
Professor Dung-Hai Lee
Professor Michael Hutchings

Spring 2012

The dissertation of Roger Mong,
titled Classification and characterization of topological insulators and superconductors,
is approved:

Chair Date

Date

Date

University of California, Berkeley

Spring 2012

Classification and characterization of topological insulators and superconductors

Abstract

Classification and characterization of topological insulators and superconductors

by

Roger Mong
Doctor of Philosophy in Physics

University of California, Berkeley

Professor Joel E. Moore, Chair

Topological insulators (TIs) are a new class of materials which, until recently, have been overlooked despite decades of study in band insulators. Like semiconductors and ordinary insulators, TIs have a bulk gap, but feature robust surfaces excitations which are protected from disorder and interactions which do not close the bulk gap. TIs are distinguished from ordinary insulators not by the symmetries they possess (or break), but by topological invariants characterizing their bulk band structures. These two pictures, the existence of gapless surface modes, and the nontrivial topology of the bulk states, yield two contrasting approaches to the study of TIs. At the heart of the subject, they are connected by the bulk-boundary correspondence, relating bulk and surface degrees of freedom. In this work, we study both aspects of topological insulators, at the same time providing an illumination to their mysterious connection.

First, we present a systematic approach to the classification of bulk states of systems with inversion-like symmetries, deriving a complete set of topological invariants for such ensembles. We find that the topological invariants in all dimensions may be computed algebraically via exact sequences. In particular, systems with spatial inversion symmetries in one-, two-, and three-dimensions can be classified by, respectively, 2, 5, and 11 integer invariants. The values of these integers are related to physical observables such as polarization, Hall conductivity, and magnetoelectric coupling. We also find that, for systems with "antiferromagnetic symmetry," there is a $\mathbb{Z}_2$ classification in three-dimensions, and hence a class of "antiferromagnetic topological insulators" (AFTIs) which are distinguished from ordinary antiferromagnets. From the perspective of the bulk, AFTI exhibits the quantized magnetoelectric effect, whereas on the surface, gapless one-dimensional chiral modes emerge at step-defects.

Next, we study how the surface spectrum can be computed from bulk quantities. Specifically, we present an analytic prescription for computing the edge dispersion $E(k)$ of a tight-binding Dirac Hamiltonian terminated at an abrupt crystalline edge, based on the bulk Hamiltonian. The result is presented as a geometric formula, relating the existence of surface states as well as their energy dispersion to properties of the bulk Hamiltonian. We

further prove the bulk-boundary correspondence for this specific class of systems, connecting the Chern number and the chiral edge modes for quantum Hall systems given in terms of Dirac Hamiltonians. In similar spirit, we examine the existence of Majorana zero modes in superconducting doped-TIs. We find that Majorana zero modes indeed appear but only if the doped Fermi energy is below a critical chemical potential. The critical doping is associated with a topological phase transition of vortex lines, which supports gapless excitations spanning their length. For weak pairing, the critical point is dependent on the non-abelian Berry phase of the bulk Fermi surface.

Finally, we investigate the transport properties on the surfaces of TIs. While the surfaces of "strong topological insulators" – TIs with an odd number of Dirac cones in their surface spectrum – have been well studied in literature, studies of their counterpart "weak topological insulators" (WTIs) are meager, with conflicting claims. Because WTIs have an even number of Dirac cones in their surface spectrum, they are thought to be unstable to disorder, which leads to an insulating surface. Here we argue that the presence of disorder alone will not localize the surface states, rather, presence of a time-reversal symmetric mass term is required for localization. Through numerical simulations, we show that in the absence of the mass term the surface always flow to a stable metallic phase and the conductivity obeys a one-parameter scaling relation, just as in the case of a strong topological insulator surface. With the inclusion of the mass, the transport properties of the surface of a weak topological insulator follow a two-parameter scaling form, reminiscent of the quantum Hall phase transition.

To my parents,

Contents

Acknowledgments **vi**

List of Acronyms **viii**

Preface **ix**

I Introduction 1

1 Brief introduction to topological insulators **2**
- 1.1 Quantum Hall effect 4
  - 1.1.1 Landau levels and band theory 5
  - 1.1.2 Berry phase, Chern integer, and topology 6
  - 1.1.3 Gapless chiral edge modes 9
- 1.2 Quantum spin Hall effect 10
  - 1.2.1 $\mathbb{Z}_2$ classification and edge states 11
- 1.3 Topological insulators in 3D 13
  - 1.3.1 Strong topological insulators (STI) 15
  - 1.3.2 Weak topological insulators (WTI) 17
- 1.4 Topological superconductors 18
  - 1.4.1 Symmetries, Altland-Zirnbauer classification 18
  - 1.4.2 Realizing topological superconductors 23
- 1.5 Applications and outlook 24

2 Overview of thesis **26**

II Classification of Band Insulators **28**

Notation and conventions **29**

3 Topology of Hamiltonian spaces 31
- 3.1 Topological classification of band structures 33
- 3.2 Classification with Brillouin zone symmetries 40

4 Inversion symmetric insulators 47
- 4.1 Summary of results 50
- 4.2 Classifying inversion symmetric insulators 57
  - 4.2.1 Outline of the argument 59
  - 4.2.2 Topology of the space of Hamiltonians 61
  - 4.2.3 Hamiltonians, classifying spaces and homotopy groups 62
  - 4.2.4 Relative homotopy groups and exact sequences 63
  - 4.2.5 One-dimension 65
  - 4.2.6 Two-dimensions 67
  - 4.2.7 Going to higher dimensions 71
- 4.3 Physical properties and the parities 74
  - 4.3.1 A coarser classification: grouping phases with identical responses . . . 75
  - 4.3.2 Constraint on parities in gapped materials 78
  - 4.3.3 Polarization and Hall conductivity 81
  - 4.3.4 Magnetoelectric response 84
- 4.4 Parities and the entanglement spectrum 85
- 4.5 Conclusions 92

5 Antiferromagnetic topological insulators 94
- 5.1 $\mathbb{Z}_2$ topological invariant 95
  - 5.1.1 Relation to the time-reversal invariant topological insulator 97
  - 5.1.2 Magnetoelectric effect and the Chern-Simons integral 98
  - 5.1.3 Invariance to choice of unit cell 99
- 5.2 Construction of effective Hamiltonian models 101
  - 5.2.1 Construction from strong topological insulators 101
  - 5.2.2 Construction from magnetically induced spin-orbit coupling 102
- 5.3 Surface band structure 104
- 5.4 Surfaces with half-integer quantum Hall effect 107
- 5.5 Conclusions and possible physical realizations 110

III Edge Spectrum and the Bulk-Boundary Correspondence 112

6 Computing the edge spectrum in Dirac Hamiltonians 113
- 6.1 Characterization of the nearest-layer Hamiltonian 114
- 6.2 Edge state theorem 115
  - 6.2.1 Edge state energy 116
  - 6.2.2 Discussion 118

6.3 Proof by Green's functions . . . 118
  6.3.1 Bulk Green's function . . . 119
  6.3.2 Green's function of the open system . . . 121
  6.3.3 Existence and spectrum of edge modes . . . 122
  6.3.4 Constraints on $\mathbf{h}_{\|}$ and E^2 . . . 122
  6.3.5 Sign of the energy . . . 125
6.4 Proof by transfer matrices . . . 125
  6.4.1 Relation between left-right boundaries . . . 126
  6.4.2 Algebraic relation between λ_a, λ_b and E . . . 127
  6.4.3 Introducing functions L, $\bar{L}$ . . . 128
  6.4.4 Edge state energy . . . 128
  6.4.5 Existence of edge states . . . 129
  6.4.6 Sign of edge state energy . . . 130
  6.4.7 Effective surface Hamiltonian . . . 131
6.5 Bulk Chern number and chiral edge correspondence . . . 131
  6.5.1 Discussion . . . 134
6.6 Applications of Theorem 1 . . . 134
  6.6.1 Example: graphene . . . 134
  6.6.2 Example: $p + ip$ superconductor (lattice model) . . . 135
  6.6.3 Example: 3D topological insulator . . . 136
6.7 Continuum Hamiltonians quadratic in momentum . . . 138
  6.7.1 Discussion . . . 139
  6.7.2 Example: $p + ip$ superconductor (continuum model) . . . 139
  6.7.3 Proof for continuum Hamiltonians . . . 140
6.8 Outlook . . . 142

7 Majorana fermions at the ends of superconductor vortices in doped topological insulators 143
7.1 A vortex in superconducting topological insulators . . . 144
7.2 Vortex phase transition in models and numerical results . . . 146
  7.2.1 Lattice model . . . 146
  7.2.2 Continuum model . . . 148
7.3 General Fermi surface Berry phase condition . . . 149
  7.3.1 Summary of the argument and results . . . 149
  7.3.2 Bogoliubov-de Gennes Hamiltonian . . . 150
  7.3.3 Pairing potential . . . 151
  7.3.4 Projecting to the low energy states . . . 153
  7.3.5 Explicit solution with rotational symmetry . . . 154
  7.3.6 General solution without rotational symmetry . . . 156
  7.3.7 Vortex bound states . . . 159
7.4 Candidate materials . . . 160
  7.4.1 $Cu_xBi_2Se_3$ with s-wave pairing . . . 160

7.4.2 p-doped $TlBiTe_2$, p-doped Bi_2Te_3 and $Pd_xBi_2Te_3$ 162
7.4.3 Majorana zero modes from trivial insulators 162

IV Surface Transport 164

8 Quantum transport on the surface of weak topological insulators 165
8.1 Hamiltonian and disorder structure 166
8.1.1 Chirality of the Dirac cones 168
8.1.2 Constructing the mass for an arbitrary even number of Dirac cones . 168
8.2 Quantum spin Hall-metal-insulator transition 169
8.2.1 Numerical data 171
8.2.2 Conditions for localization 174
8.3 Two-parameter scaling 174
8.3.1 Possible realizations 176

Bibliography 178

Acknowledgments

First and foremost, my parents have been a tremendous source of support for me through my years in graduate school. Their unwavering support have given me strength to succumb the challenges that I have faced in my life. Without their love and kindness I would not be where I am today; to you I dedicate this thesis.

I owe many thanks to the people at Berkeley whom I've met in my journey through graduate school. They are what I would miss most – not the classes, not the food, not the endless stream of protests, counter-protests, counter-counter-protests, and parody-protests on Sproul plaza – but the individuals who made Berkeley such a memorable experience for me.

I acknowledge my collaborators Jens Bárðarson, Andrew Essin, Pouyan Ghaemi, Pavan Hosur, Joel Moore, Vasudha Shivamoggi, Ari Turner, Ashvin Vishwanath, Frank Yi Zhang, and Mike Zaletel. They have given me the honor to work and learn from them, to share with them one of the greatest pride and joy of being a researcher. Many of my ideas would not have come to fruition without their hard work.

I would like to thank my fellow physicists, Gil Young Cho, Tarun Grover, Jonas Kjäll, Dung-Hai Lee, Sid Parameswaran, Frank Pollmann, Shinsei Ryu, along with my collaborators, for the many wonderful discussions I shared them. They have taught me, challenged me, and inspired me to become a better physicist. I would often come to them with questions – sometimes because I'm too lazy to search for the references – and yet they take the time to patch up gaps of my knowledge. For those whom I have not yet collaborated with, I hope one day that may change.

I am indebted to the Berkeley Physics support staff, for their ability to keep the department running smoothly, to allow us to focus on what we love most. In particular, Anne, Claudia, and Donna have provided endless advice and help to guide me through my years at graduate school; Kathy for always having to hunt me down so that I can get paid (on time).

I would also like to thank my thesis committee, Joel E. Moore, Dung-Hai Lee, and Michael Hutchings. Coincidentally, I have took a number of classes from each member of the committee. They have shown me how much there is to learn, and I have greatly benefited from their experience; I yearn to be a great teacher just as they are.

I have enjoyed the company of my friends, far too numerous to be listed individually. They have shown me a life outside of physics, taught me ways to enjoy life, and provided me with much distraction from my Ph.D.

Finally, my deep gratitude to my Ph.D. advisor Joel Moore, for his commitment and dedication – not just to my work – but also to my career; for providing a direction to my research; for his deep insight on the problems that I struggle with; for his advices on navigating academia; for his hard work at securing financial support to my study; for rejecting many of my bad ideas; for his patience with me after numerous abandoned projects; and for his faith in my abilities. It has been a great privilege to be a student of his; I owe him for the immense ways he has shaped my career thus far, and the career that lies ahead.

List of Acronyms

1D, 2D, ...	one-dimension, two-dimension, ...
AFTI	antiferromagnetic topological insulator
ARPES	angle-resolved photoemission spectroscopy
BdG	Bogoliubov-de Gennes
BZ	Brillouin zone
CS	Chern-Simons
EBZ	effective Brillouin zone
FCC	face-centered cubic
FS	Fermi surface
MZM	Majorana zero mode
QH(E)	quantum Hall (effect)
QSH(E)	quantum spin Hall (effect)
SC	superconductor
STI	strong topological insulator
STM	scanning tunneling microscopy
TI	topological insulator
TRIM/TRIMs	time-reversal invariant momentum/momenta
TRS	time-reversal symmetry/symmetric
TKNN	Thouless, Kohmoto, Nightingale and den Nijs
VPT	vortex phase transition
WTI	weak topological insulator

Preface

Electrical insulators prevents the flow of electricity, thermal insulators impedes the flow of heat, so obviously *topological* insulators are materials which stops the flow of topology.

Imagine a partition dividing two regions. On one side there are a lot of topology, while the other side is devoid of topology. If the partition is made of a *topological superconductor*, then over time the topology will leak through and it'll get everywhere resulting in a giant topological mess. However, should the partition be a *topological insulator*, then the topologies remain safely on one side and everything is good.

This thesis is story of two cities. Two cities locked in a conflict for which there may be no victor. The city of topological insulator seeks contain and trap the most ancient and dangerous source of topology. The city of topological superconductors seeks to unleash and wield such power, to enrich all with the essence of topology. Neither will yield, neither will waver, neither will rest until judgment has passed and its enemies vanquished. This is a war for their future, a war for the fate of spacetime, a war with consequences that will reverberate for eons to come. This is a *topological war*.

Part I

Introduction

Chapter 1

Brief introduction to topological insulators

Recently a new class of materials have emerged, which are insulating in the bulk, but support gapless boundary conducting modes. These "topological insulators"[1] were predicted [1–5] to exist and subsequently confirmed experimentally in HgTe quantum wells and thermoelectric materials $\mathrm{Bi_2Se_3}$ and $\mathrm{Bi_2Te_3}$ [6–9]. The peculiar thing about the edges/surfaces of these materials is that they are robust to interaction and disorder, as long as the extended states in the bulk are gapped. In particular, the conducting boundary exhibits *antilocalization* behavior, in contrast to many one-dimensional (1D) and two-dimensional (2D) materials [10–12].

The history of topological insulators (TIs) began in the 80s with the quantum Hall effect (QHE), with the famous experiment by von Klitzing *et al.* [13] on 2D electron gases. Contrary to the classical Hall effect, in which the Hall conductance $\sigma^{xy} = j_x/E_y$ is proportional to the applied magnetic field $\mathbf{B}$, von Klitzing found σ^{xy} plateaus as a function of $\mathbf{B}$. In addition, he found that the conductivity was exactly quantized:

$$\sigma^{xy} = \nu \frac{e^2}{h} \tag{1.1}$$

where ν is an integer e is the electron charge and h is Planck's constant. It was through the works of Thouless *et al.* [14] along with Simon [15] that linked the Hall conductivity to the *topology* of Bloch wavefunctions, they showed that σ^{xy} is quantized provided the bulk gap exists. The quantum Hall effect may be regarded as the first topological insulator, with the Hall conductivity being a topological response function of the system. One may perturb a quantum Hall system – but as long as the material remains insulating, σ^{xy} is invariant under adiabatic changes to the system.

The discovery of QHE led to the birth of *topological phases*,[2] where phases of matter are not distinguished by broken symmetries as according to the Landau paradigm [17, 18], but

---

[1] The term "topological insulator" was coined by Joel E. Moore in Ref. [1].

[2] Topological phases does not necessarily imply topological order as defined by Wen [16]. Unfortunately,

are instead differentiated by *topological invariants.* Here the topological invariant is $\nu \in \mathbb{Z}$.[3] Now the answer to following question is evident: what are the possible insulating phases that cannot be deformed in to one another by a continuous change in the system? Simply, there is one class for every integer ν. For most insulators (*e.g.* silicon, vacuum) this invariant is zero, while each QH plateau belongs to a different class.

The QHE breaks time-reversal symmetry, from the fact that the Hall conductance σ^{xy} is odd under time-reversal symmetry (TRS); this symmetry breaking is due to the external magnetic field. What happens if we constrain ourselves to two-dimensional materials which does not break time-reversal? Evidently we cannot have the quantum Hall effect, but we can still apply the idea of a topological classification. In recent years Kane and Mele showed that within the set of time-reversal symmetric insulators, there are two subclasses which are adiabatically disconnected [3, 19]. Every TRS insulator belongs to the "even" subclass or the "odd" subclass, and we say that there is a $\mathbb{Z}_2 = \mathbb{Z}/2\mathbb{Z}$ classification among 2D TRS insulators. The even subclass is referred to as "topologically-trivial" (or ordinary) insulators, and the odd subclass as "topological insulators," or the quantum spin Hall (QSH) insulators. While many materials (including the vacuum) are in the even subclass, HgTe quantum wells are shown to be in the odd subclass [6]. From an experimental perspective, the restriction to time-reversal symmetric systems has a tradeoff: while this eliminates magnetic materials from the classification, the strong magnetic fields required to sustain the QHE are no longer needed.

The topological classification can be extended to 3D time-reversal invariant insulators [1, 4, 5]. Tens of compounds have been confirmed as topological insulators, including Bi_2Se_3 and Bi_2Te_3 [8, 9]. These two are particularly notable in that their band gaps are over 1000 K, allowing their special properties to be experimentally accessible at room-temperature. Common to all these types of topological insulators are conducting edge states. For example, the QHE admits chiral edge modes, fermionic modes that only propagate in single direction along the edge [20]. These edge modes are one of the physical manifestations of these otherwise abstract topological classification. In this thesis we explore many of these ideas in details, tackling the interplay between bulk topological invariants and surface excitations, and their phenomenology.

The purpose of this chapter is to serve as an introduction and a brief review to the theoretical concepts and phenomenology of topological insulators and topological superconductors. There are a number of excellent topical reviews covering the field in much greater depth than permitted here, the reader is encouraged to consult to Refs. [21–26] for a much more comprehensive review of the subject.

---

the use of "topological order" within the condensed matter community has been rather inconsistent, with conflicting definitions. In this text, we give a self-consistent definition of "topological phases" without reference to topological order.

[3] $\mathbb{Z}$ denotes the set of integers.

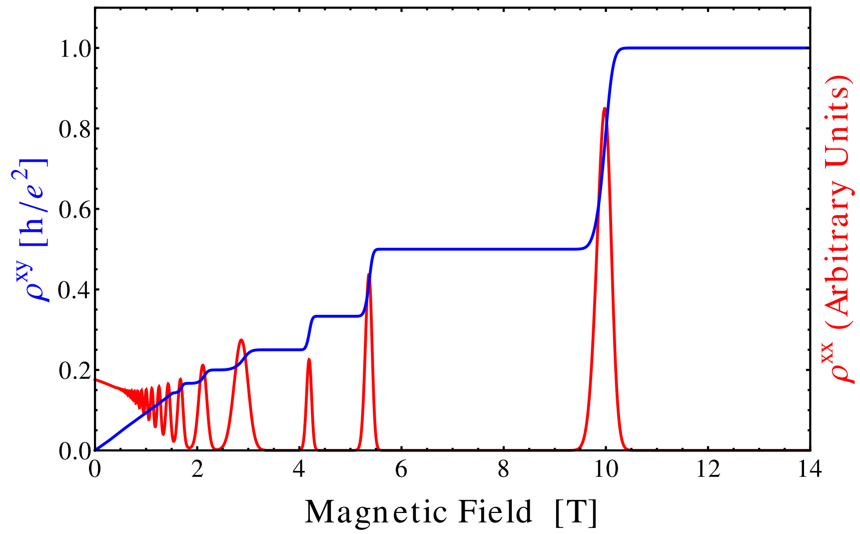

Figure 1.1: The quantum Hall effect.

The figure shows typical data for the integer QHE. The diagonal ρ^{xx} (blue) and Hall ρ^{xy} (red) resistivity plotted as a function of applied magnetic field. ρ^{xy} plateaus at $\frac{h}{\nu e^2}$ and ρ^{xx} is zero in a quantum Hall phase. During the transition from one quantum Hall state to another, ρ^{xx} is non-zero signaling a insulator-metal-insulator transition.

1.1 Quantum Hall effect

Consider the Hall experiment on a sample in the xy-plane, with a fixed magnetic field B_z in the z-direction. In the linear response regime, the relationship between the electric field $\mathbf{E}$ and current $\mathbf{j}$ can be captured by the resistivity/conductivity tensor:

$$\mathbf{j} = \sigma \mathbf{E}, \ \sigma = \begin{bmatrix} \sigma^{xx} & \sigma^{xy} \\ \sigma^{yx} & \sigma^{yy} \end{bmatrix}, \qquad \mathbf{E} = \rho \mathbf{j}, \ \rho = \begin{bmatrix} \rho^{xx} & \rho^{xy} \\ \rho^{yx} & \rho^{yy} \end{bmatrix}. \tag{1.2}$$

The matrices are related $\sigma\rho = 1$. From isotropy, we can argue that $\sigma^{xx} = \sigma^{yy}$ and $\sigma^{yx} = -\sigma^{xy}$. (Likewise for the resistivity) In the classical Hall experiment, the Hall resistivity is proportional to the magnetic field:

$$\rho^{xy} = B_z R_H = -B_z/ne \qquad \text{(classical formula)}, \tag{1.3}$$

where n is the electron density and e is the elementary charge [27].

In 1980, von Klitzing measured the Hall resistivity on 2D electron gas (MOSFET inversion layer) [13]. What he discovered was that the ρ^{xy} was not proportional to B_z, but has plateaus at quantized values

$$\rho^{xy} = -\frac{h}{\nu e^2} \qquad \text{(quantum Hall effect)}, \tag{1.4}$$

where ν is an integer. In addition, the diagonal resistivity ρ^{xx} vanishes at these plateaus (Fig. 1.1). Today, measurements have confirmed that ν is an integer to one part in a billion, this "exact quantization" in various materials points to the inadequacy of the classical theory and suggests that a new physical phenomenon is at work [28].

When $\rho^{xx} = 0$, then σ^{xx} is also zero and the Hall conductivity/resistivity[4] are related by $\sigma^{xy}\rho^{xy} = -1$ and hence $\sigma^{xy} = \nu e^2/h$. While it may seem paradoxical that both σ^{xx} and ρ^{xx} vanish, this is consistent considering the matrix relations $\sigma\rho = 1$. The vanishing conductivity $\sigma^{xx} = 0$ means that quantum Hall system is an insulator parallel to the electric field, while the vanishing resistivity $\rho^{xx} = 0$ means that there is no voltage drop parallel to the current. In this section, we will introduce basic concepts of topology in quantum Hall states.

1.1.1 Landau levels and band theory

Using basic quantum mechanics, it is easy to show that the energies of an electron in a magnetic field quantizes in to Landau levels $(n + \frac{1}{2})\hbar\omega$ where $\omega = \frac{eB}{m}$ is the cyclotron frequency. The magnetic length is defined $l_B = (\frac{\hbar}{m\omega})^{1/2}$, one can think of $\sqrt{2}l_B$ as the "classical radius" of the electron orbit. The Landau energy levels are highly degenerate, and the number of states per level can be approximated as follows:

$$N_L = \text{number of states} \approx \frac{\text{Area of sample}}{\text{Area of an electron}} \approx \frac{A}{2\pi l_B^2} = \frac{\Phi}{\Phi_0}\,. \tag{1.5}$$

$\Phi_0 = h/e$ is the flux quanta and $\Phi = AB$ is the magnetic flux through the sample.[5] If the Fermi level lies between Landau levels, there will be some integer number (N) of completely filled bands, hence NN_L number of electrons. In the simplest treatment, equation (1.3) gives the quantized $\rho^{xy} = -h/Ne^2$ that we are looking for. Here each Landau level contributes one unit (e^2/h) of conductance and σ^{xy} measures the number of filled bands.

While the above picture is simple, it fails to explain why the quantum Hall effect is universal – that is, the exact quantization is unaffected by the material geometry, impurities and electron interactions. Laughlin provided an elegant argument based on the principle of gauge invariance, and later Thouless, Kohmoto, Nightingale, and den Nijs (TKNN) along with Avron, Seiler, and Simon showed the relationship between the Hall conductivity and Bloch wavefunctions [14, 29].

In a periodic potential (*i.e.*, crystal), the single-electron wavefunctions satisfying Schrödinger's equation

$$H\psi^\mu_{\mathbf{k}}(\mathbf{r}) = E^\mu_{\mathbf{k}}\psi^\mu_{\mathbf{k}}(\mathbf{r}) \tag{1.6}$$

---

[4] In 2D, the Hall conductance and conductivity are the same; independent of material geometry. The same applies for resistance/resistivity.

[5] This approach to compute the degeneracy $N_L = \Phi/\Phi_0$ is meant to be intuitive rather than rigorous. A fully quantum mechanic treatment yield the same result.

can be decomposed as product of a plane wave and a periodic function [27, 30]:

$$\psi^\mu_{\mathbf{k}}(\mathbf{r}) = \exp(i\mathbf{k}\cdot\mathbf{r})u^\mu_{\mathbf{k}}(\mathbf{r})\,, \tag{1.7}$$

where μ is the band index, and $\mathbf{k}$ is the wavevector. The "Bloch function" $u^\mu_{\mathbf{k}}(\mathbf{r})$ has the same periodicity as the lattice, and hence we can think of the Bloch function living in a unit cell. The Bloch functions $u^\mu_{\mathbf{k}}$ along with the energies $E^\mu_{\mathbf{k}}$ determine the electronic spectrum of the material. The discrete translational symmetry of the lattice means that we may restrict $\mathbf{k}$ to a particular Brillouin zone (BZ), the periodicity of the BZ makes it topologically a torus.

The Hall conductivity for a 2D system may be written in terms of the Bloch functions [14]:

$$\nu = \frac{h}{e^2}\sigma^{xy} = \sum_{\mu\text{ occ.}} \oint_{\text{BZ}} \frac{i}{2\pi}\big(\langle\partial_{k_x}u^\mu_{\mathbf{k}}|\partial_{k_y}u^\mu_{\mathbf{k}}\rangle - \langle\partial_{k_y}u^\mu_{\mathbf{k}}|\partial_{k_x}u^\mu_{\mathbf{k}}\rangle\big)\,dk_x\,dk_y\,, \tag{1.8}$$

where the sum is over all occupied bands, and the integral is performed over the entire Brillouin zone (BZ). While the expression (1.8) looks complicated, we can infer a fair amount of information from it. First note that the expression only depends on the Bloch functions, but not the energy, the only role of the energy is to distinguish between the occupied and unoccupied bands. Second, the integral always evaluates to an integer over the Brillouin zone (to be explained later), so ν must be an integer as long as there are no partially filled bands [29]. Further, because ν is an integer, it must be a constant under continuous changes to the system, as long as the number of occupied bands remains fixed (gapped insulator).

1.1.2 Berry phase, Chern integer, and topology

The preceding explanation related the Hall conductance to the Bloch functions in an algebraic manner, but did not provide an explanation for why ν must be an integer. In this section we paint a geometric picture for the mysterious looking expression (1.8), but first we must define the concept of Berry[6] phase [32]. The Berry connection ($\mathcal{A}$) and Berry phase (ϕ) are defined as follows:

$$\mathcal{A}(\mathbf{k}) = \sum_{\mu\text{ occ.}} \langle u^\mu_{\mathbf{k}}|i\nabla_{\mathbf{k}}|u^\mu_{\mathbf{k}}\rangle\,, \tag{1.9}$$

$$\phi = \oint_\gamma \mathcal{A}\cdot d\mathbf{k}\,. \tag{1.10}$$

$\mathcal{A}$ is a vector defined in terms of the Bloch functions, and ϕ is the connection integrated over some loop γ. It is important to note that $\mathcal{A}$ is gauge dependent, and possibly multi-valued. What we mean is that there are more than one choice of Bloch functions $u^\mu_{\mathbf{k}}$ which satisfy Bloch's theorem (1.6) due to the phase ambiguity in quantum mechanics, and a different

---

[6] Also called the Pancharatnam phase, for Pancharatnam's study of phase shifts as the polarization of light is changed [31].

gauge choice gives a different connection $\mathcal{A}$. In addition, it is not always possible to find a set of Bloch functions which are continuous in the entire BZ, hence $\mathcal{A}$ can only be defined locally. More precisely, under the gauge transformation

$$u_{\mathbf{k}} \to e^{i\theta(\mathbf{k})} u_{\mathbf{k}} \,, \tag{1.11}$$

the Berry connection also changes:

$$\mathcal{A} \to \mathcal{A} - \nabla_{\mathbf{k}} \theta \,. \tag{1.12}$$

However, the Berry phase

$$\phi \to \phi - \theta \Big|_{\text{start}}^{\text{end}} \tag{1.13}$$

will only change by some integer multiple of 2π. The reason for this is that $\theta(\mathbf{k})$ may not be single-valued, but $e^{i\theta}$ must be such for the transformation (1.11) to be meaningful. Hence, $e^{i\phi}$ is a gauge invariant quantity depending on the loop γ. The form of $\mathcal{A}$ resembles that of the electromagnetic vector potential, and we can define another quantity called the Berry curvature:

$$\mathcal{F}(\mathbf{k}) = \nabla_{\mathbf{k}} \times \mathcal{A} \,, \tag{1.14}$$

such that equation (1.8) reads:

$$\nu = \frac{1}{2\pi} \oint_{\text{BZ}} \mathcal{F} \, d^2 k \,. \tag{1.15}$$

Notice that $\mathcal{A}$ is analogous to the vector potential $\mathbf{A}$ while $\mathcal{F}$ is analogous to magnetic field $\mathbf{B}$, this comparison makes it easy to see that $\mathcal{F}$ is indeed gauge invariant. The analogy is no accident, in fact, the equations of motions for a wave packet are [33]:

$$\dot{\mathbf{k}} = -\frac{e}{\hbar}\mathbf{E} - \frac{e}{\hbar}\dot{\mathbf{r}} \times \mathbf{B} \,, \tag{1.16a}$$

$$\dot{\mathbf{r}} = \frac{1}{\hbar}\nabla_{\mathbf{k}} E_{\mathbf{k}}^{\mu} - \dot{\mathbf{k}} \times \mathcal{F} \,, \tag{1.16b}$$

where $\mathbf{r}$ and $\mathbf{k}$ measure the average position and momentum of the wave packet, the dot implies time-derivative: $\dot{\mathbf{k}} = d\mathbf{k}/dt$. The first equation is simply the Lorentz force on an electron, but notice in the second equation there is an "anomalous velocity" term $\dot{\mathbf{k}} \times \mathcal{F}$. One can argue that the term makes the two equation more symmetric, and that the curvature $\mathcal{F}$ deflects an electron moving in k-space in the same way that the magnetic field deflects a particle in real space.

In 1931, Dirac showed that the existence of a magnetic monopole leads to the quantization of electric charge (and vice versa), the magnetic flux through a closed (boundaryless, *e.g.* a sphere or torus) surface must be multiples of the quantum flux $\Phi_0 = h/e$, in order for the

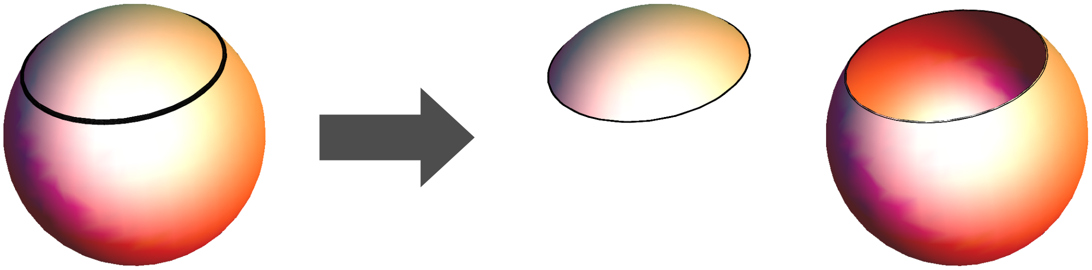

Figure 1.2: A loop γ on a sphere.

The loop divides the surface into two complementary areas, the boundary of each being γ. (These two areas have opposite orientation) The magnetic flux Φ through the two areas (accounting for orientation) differs by multiples of h/e. So the total flux of the sphere is quantized in units of the flux quanta h/e. This argument extends to any closed 2D (orientable) surface.

quantum mechanical theory to be self-consistent: $\Phi = n\Phi_0$ [34]. Dirac's argument was as follows: Consider an electron confined to a closed two-dimensional surface penetrated by a magnetic field. The Aharonov-Bohm phase for a closed loop γ is defined as $\phi = \frac{e}{\hbar}\oint_\gamma \mathbf{A}\cdot d\mathbf{r} = \frac{e}{\hbar}\iint \mathbf{B}\cdot d\mathbf{S}$, proportional to the magnetic flux through the area enclosed by the loop; however, there are two areas which share a common boundary γ, and the two areas are complement to each other. The Aharonov-Bohm phase for both areas must be compatible, which means they must differ by integer multiple of 2π; therefore, the net magnetic flux through the entire surface must be integer multiples of the flux quantum $\Phi_0 = h/e$, and so the magnetic charge inside the surface must be quantized (Gauss' law).

Extending our analogy between magnetism and Berry curvature, we apply the same argument. The Brillouin zone is a torus due to periodicity in reciprocal space, which is our closed surface. Just as the magnetic flux Φ is quantized, the Berry flux $2\pi\nu = \iint \mathcal{F}\, d^2k$ for the entire BZ must also be an integer multiple of 2π. The fact that ν must be an integer was demonstrated by TKNN, who at the time were unaware of the mathematical work by Chern in the classification of complex vector bundles. When the relationship between these two seeming different ideas were established, ν came to be known as the TKNN/Chern number [15, 29].[7]

We have argued that Φ and σ^{xy} were quantized based on purely geometric grounds. In the magnetic monopole case, it is only possible to change the number of flux quanta through the closed surface by passing a monopole in on out of its interior; however, the moment that the monopole passes through the surface, the surface vector potential and magnetic field are no longer continuously defined, leading to a singularity. Similarly for the quantum Hall system, it is possible to change the Hall conductivity by passing a "TKNN monopole" through the BZ, but doing so requires a singularity in the Berry connection and Bloch

---

[7] More accurately, the TKNN integer corresponds to the first Chern class.

Electromagnetism	**Bloch functions**
Vector potential $\mathbf{A}$	Berry connection $\mathcal{A} = \langle u_{\mathbf{k}} \vert i\nabla_{\mathbf{k}} \vert u_{\mathbf{k}} \rangle$
Aharonov-Bohm phase $\phi = \frac{e}{\hbar}\oint \mathbf{A} \cdot d\mathbf{r}$	Berry phase $\phi = \oint \mathcal{A} \cdot d\mathbf{k}$
Magnetic field $\mathbf{B} = \nabla \times \mathbf{A}$	Berry curvature $\mathcal{F} = \nabla_{\mathbf{k}} \times \mathcal{A}$
Lorentz force $\dot{\mathbf{r}} \times \mathbf{B}$	Anomalous velocity $\dot{\mathbf{k}} \times \mathcal{F}$
Quantized magnetic flux $\Phi = n\frac{h}{e}$	Quantized Hall conductivity $\sigma^{xy} = \nu\frac{e^2}{h}$
Magnetic monopole charge	TKNN/Chern number

Table 1.1: Comparison between the electromagnetic vector potential and Berry connection.

The Berry connection of Bloch states are in many ways analogous to the vector potential in electromagnetism. The same ideas that give rise to a quantized Dirac monopole charge also gives the quantum Hall effect.

functions. This can only happen when the valence and conduction bands intersect, leading to a metal-insulator transition. This can be seen in the quantum Hall experiment by peaks in the diagonal resistance ρ^{xx} in Fig. 1.1.

We now return to the question first posed in the introduction: What are the classes of band insulators that cannot be continuously deformed to one another, while maintaining a gapped system? From the geometric argument in this section, it is clear that quantum Hall systems with different TKNN/Chern number form subclasses of insulators which are disconnected from one another. We call this a $\mathbb{Z}$ classification, since each insulator is represented by an integer $\nu \in \mathbb{Z}$. It has been shown that this classification is *exhaustive* within the framework of 2D non-interacting electrons,[8] which is to say that the Hall conductance completely describes the topology of band insulators [29, 35].

1.1.3 Gapless chiral edge modes

In the previous sections, we have ignored an apparently flagrant paradox. If the quantum Hall systems are insulators, then how do they conduct the Hall current? The answer lies at the boundary: The quantum Hall system has gapless edge states, these edge states are conducting and form a persistent current around the boundary of the material [20].

The edge states are chiral, meaning the current has a preferred direction, behaving like perfect 1D quantum wires. These wires are "topologically protected;" as long as the bulk electronic gap exists, the edge states are perfectly conducting even in the presence of impurities and defects. This result is surprising due to the tendency for electron states to localize in one-dimension, in fact, any small amount of disorder in an 1D metal drives the system to an insulator [10, 12]. Intuitively one can understand the (anti)localization behavior by the following traffic analogy. Imagining a single wire (road) with left and right propagating

---

[8] The fractional quantum Hall effect requires electron-electron interaction and does not fit under the TKNN classification.

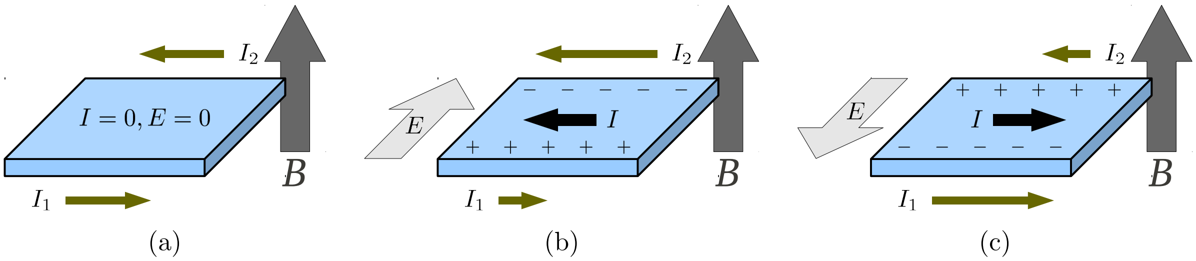

Figure 1.3: The edge of a quantum Hall system.

A chiral current runs around the edge of a quantum Hall system. In these figures, the net current results from the difference between the current on the top and bottom edges.

modes (traffic in both direction). In absence of electron interactions (passing) or impurity scattering (road obstacles) the electrons (cars) travel smoothly in both directions exhibiting metallic behavior; however, any small amount of interaction or impurities will allow the electrons to backscatter (forcing cars onto oncoming traffic), causing the electrons to localize (traffic jam). In a quantum Hall system, the left and right propagating modes are spatially separated on opposite edges of the material, making backscattering impossible.

The relation between the bulk spectrum and the edge spectrum is generally referred to as the “bulk-boundary correspondence,” which states that a gapless excitation must exist at the interface between two different topological classes of materials [20, 36, 37]. A heuristic way to understand the correspondence is as follows. Consider a domain wall between two bulk insulators with differing topological invariants ν_L and ν_R. Since the value of the invariant cannot change for finite energy gap, the bulk gap must closes at the interface. Midgap excitations can thus exist, but they are confined to the interface by the bulk gap in the other regions. In this particular case, the boundary of the quantum Hall is an interface between the system and vacuum (having $\sigma^{xy} = 0$). The difference in Chern number $\nu_{\mathrm{QH}} - \nu_{\mathrm{vacuum}} = \nu_{\mathrm{QH}}$ gives the number of chiral edge modes [38–41].

1.2 Quantum spin Hall effect

In the quantum Hall experiment, time-reversal is explicitly broken by the external magnetic field, which picks out a particular edge chirality and determines the sign of the Chern number ν. The Hall conductivity $\sigma^{xy} = j_x/E_y$ is odd under time-reversal, as the current $\mathbf{j}$ is odd under time-reversal but the electric field $\mathbf{E}$ is even. Hence, none of the topological classes $\nu \neq 0$ can be realized while maintaining time-reversal symmetry.

In 2005, Kane and Mele proposed the quantum spin Hall insulator - which is constructed by taking two copies of quantum Hall systems with opposite Chern number and spin [2]. Time-reversal flips both spin and the Chern number, mapping one quantum Hall layer to the

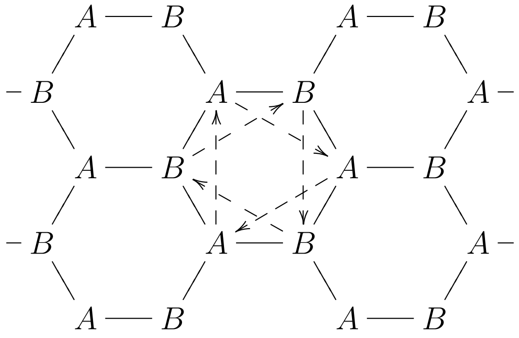

Figure 1.4: A lattice model of the quantum spin Hall insulator.

Kane and Mele's quantum spin Hall model on a honeycomb lattice from Ref. [2]. The model consists of a hopping term between nearest-neighbor with coefficient t. Next-nearest-neighbor hopping along dashed arrows are of the form $i\lambda_{\text{SO}}\sigma^z$ which is spin dependent, where λ_{SO} is the spin-orbit coupling. (Hopping against dashed arrow is $-i\lambda_{\text{SO}}\sigma^z$, such that the Hamiltonian is hermitian.)

other, such that time-reversal is preserved for the system as a whole. Their explicit model was constructed with a tight-binding model on a honeycomb lattice (Fig. 1.4), based on prior work by Haldane [42]. Spin-orbit coupling of the form $\nabla V(\mathbf{r}) \times \dot{\mathbf{r}} \cdot \boldsymbol{\sigma}$ plays the role of the magnetic field in the quantum Hall effect, deflecting opposite spins in opposite directions. (Here $\boldsymbol{\sigma} = (\sigma^x, \sigma^y, \sigma^z)$ are the Pauli matrices.) This causes the spin up electrons to behave as if they were under an out-of-plane magnetic field, and the spin down electrons in an in-plane field. Finally, the spin-orbit coupling also opens a gap in the electronic spectrum, since the nearest-neighbor hopping alone leads to a gapless conductor (*i.e.*, graphene).

Conceptually, this construction of the spin Hall insulator is simply two copies of quantum Hall such that total Chern number vanishes, and one might expect that we can classify all such systems by the Chern number of one of the layers $\nu_\uparrow = -\nu_\downarrow \in \mathbb{Z}$. However, the absence of interaction between the spin layers is not only unrealistic, but uninteresting from a theoretical point of view. When there are interaction between the two spins, the individual quantum Hall layers are not well-defined, and there is no longer a $\mathbb{Z}$ topological classification of the system. The question remains: Are there subclasses of time-reversal invariant insulators which are topologically distinct from one another?

1.2.1 $\mathbb{Z}_2$ classification and edge states

In another remarkable paper, Kane and Mele showed that even in the presence of spin mixing (*e.g.* Rashba effect), a topological distinction still remains between the "even" insulators and "odd" insulators [3]. What this means is that one can deform all the even subclasses (consisting of quantum Hall pairs $\nu_\uparrow = +2n$ and $\nu_\downarrow = -2n$) to one another, but these are topologically distinct from the odd subclasses. The authors then proceeded to show that their quantum spin Hall model (Fig. 1.4) belongs to the odd subclass. We call this a $\mathbb{Z}_2$ classification, where $\mathbb{Z}_2 = \mathbb{Z}/2\mathbb{Z}$ is a group of order two,[9] every time-reversal symmetric insulator is characterized by ν being even or odd (as opposed to an integer).[10] The even subclass (which includes the vacuum) is commonly referred to as the "ordinary insulator" or the "topologically trivial insulator" and the odd subclass is called the "2D topological insulator" or sometimes the "quantum spin Hall insulator [1]." While these names could be confusing and possibly misleading, they have been popularized and are widely used in literature.

Formally, the $\mathbb{Z}_2$ invariant can be formulated in terms of the band structure, specifically the Bloch functions $u^{\mu}_{\mathbf{k}}$, similar to the construction of $\mathbb{Z}$ invariant for the quantum Hall effect. In other words, for any time-reversal invariant band structure, there is an associated element of $\mathbb{Z}_2$ (*i.e.*, even or odd) which describes the topology of the Bloch functions. This invariant may be computed directly from the Bloch functions [3], from an integral of the Berry connection and curvature [1, 19], or in the presence of crystal inversion symmetry by counting the number of band inversions [43]. The last technique is particular useful as many materials have a spatial inversion, thus simplifying the calculations and also helping physicists identify new potential topological insulators.

The 2D topological insulators also have gapless edge modes by the bulk-boundary correspondence. The edge spectrum consists of opposite spins moving in opposite directions, consistent with the picture painted earlier in this section. (For example, the spin up and spin down electrons deflected in opposite directions due to spin-orbit interactions.) The two edge bands are time-reversal conjugates of one another, known as Kramers pair. It turns out that it is impossible for backscattering within a Kramers pair with a time-reversal invariant potential, which guarantees the stability of the topological insulator boundary spectrum as long as there are an odd number of Kramers pairs [44–46]. On the other hand, magnetic impurities (breaking time-reversal) would allow backscattering, thereby opening a mobility gap at the material edge. We see that the topological insulator is only stable within the constraints given by time-reversal symmetry, Fig. 1.5 shows a schematic phase diagram of how TRS fits in to the classification of 2D band insulators.

Kane & Mele originally suggested that the quantum spin Hall insulator could be realized in graphene, but it soon became clear that the spin-orbit coupling λ_{SO} in carbon was much too small for the desired effect. Since spin-orbit is a relativistic effect, heavy elements generate much larger spin-orbit coupling and are required for the realization of topological insulators. Bernevig *et al.* [47] suggested a possible realization of 2D topological insulator involving HgTe sandwiched between CdTe layers to create a 2D quantum well, which was soon confirmed by König *et al.* [6] in an experiment. With a six-terminal transport probe, they measured the

---

[9] The group structure of $\mathbb{Z}_2 = \{\text{even}, \text{odd}\}$ tells us what happens when we combine different insulators. For example, two topological insulators (odd) combine in to an ordinary insulator (odd + odd = even), but the combination of an ordinary and topological insulator gives a topological insulator (even + odd = odd).

[10] We also note that, in contrast to the QH case, the spin Hall conductivity is not quantized in QSH insulators. The $\mathbb{Z}_2$ invariant ν does not correspond to a linear response function.

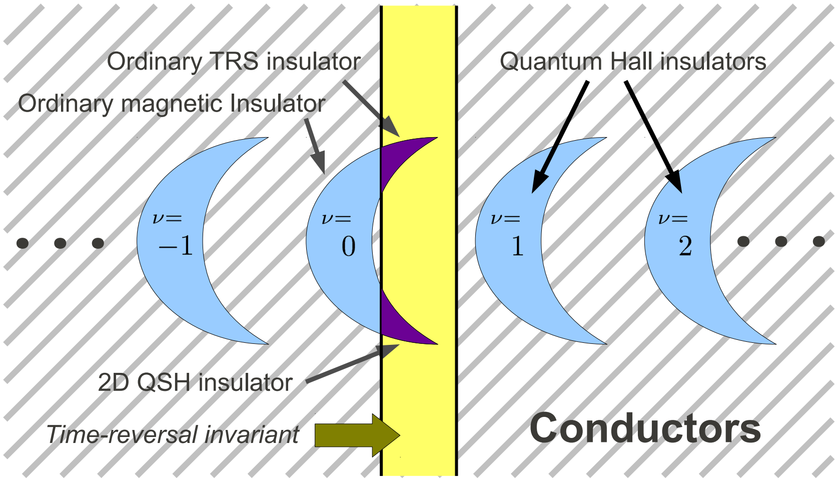

Figure 1.5: A schematic phase diagram for 2D materials.

The crescent-shaped regions represents insulating phases, while the surrounding regions (with diagonal stripes) are metallic. Each crescent region represents either a trivial or quantum Hall phase (characterized by ν), and are all disconnected from one another. The strip in the middle represents the subset which are time-reversal invariant. Within this strip, there are two insulating phases, the "ordinary insulator" and "2D topological insulator" ($\mathbb{Z}_2$ classification). Notice that these two regions are disconnected within the strip, but may be connected via $\nu = 0$ phase by breaking time-reversal symmetry; the $\mathbb{Z}_2$ topological invariant is only protected within the time-reversal symmetric class.

quantized conductance e^2/h for each edge of the system, thereby confirming the helical edge natural of the QSH insulator. The details of the experiments are presented in Refs. [6, 48].

1.3 Topological insulators in 3D

The quantum Hall and the quantum spin Hall effect are fundamentally two-dimensional, and it is natural to ask, are there three-dimensional generalizations of the topological insulator?

As shown by Refs. [1, 4, 5], there are four $\mathbb{Z}_2$ invariants associated with the Bloch functions inside the 3D Brillouin zone for TRS band insulators. The BZ is a 3-torus (3D box with periodic boundary conditions), which we can parametrize by three momentum coordinates $-\pi < k_1, k_2, k_3 \le \pi$. Time-reversal is an antiunitary operator, flipping the sign of the momentum: $\mathbf{k} \to -\mathbf{k}$. Notice that there are special values of k_1 which are invariant under time-reversal, namely 0 and π, since the periodicity of reciprocal space makes π and $-\pi$ equivalent in the BZ. Hence time-reversal takes a point $\mathbf{k} = (\pi, k_2, k_3)$ to $(\pi, -k_2, -k_3)$, mapping the plane $k_1 = \pi$ to itself. We can see that the 2D plane $k_1 = \pi$ has the same properties as the BZ of a 2D system respecting time-reversal. The same argument shows

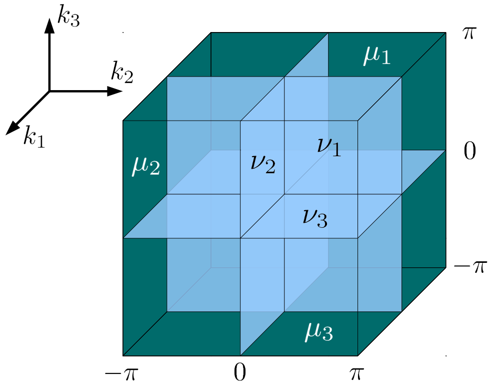

Figure 1.6: The 3D Brillouin zone.

Shown in the figure are six planes in the Brillouin zone (BZ) which are time-reversal invariant. Associated with each plane is a $\mathbb{Z}_2$ topological invariant. The three light blue planes corresponds to $k_1 = 0$, $k_2 = 0$, $k_3 = 0$, which gives the invariants ν_1, ν_2, ν_3. The three dark green planes corresponds to $k_1 = \pi$, $k_2 = \pi$, $k_3 = \pi$, which gives the invariants μ_1, μ_2, μ_3.

that $k_1 = 0$, $k_2 = 0$ or π, and $k_3 = 0$ or π planes are also time-reversal symmetric.[11] Each of these six planes has an associated $\mathbb{Z}_2$ invariant – we denote ν_i and μ_i $(i = 1, 2, 3)$ to be the topological invariants corresponding to $k_i = 0$ planes and $k_i = \pi$ planes respectively (see Fig. 1.6).

The six invariants ν_i, μ_i are computed from the bulk 3D band structure, however these quantities are not independent. The variables satisfy $\nu_1 + \mu_1 = \nu_2 + \mu_2 = \nu_3 + \mu_3$, giving us only four independent topological invariants. Defining $\nu_0 \equiv \nu_1 + \mu_1$, the four $\mathbb{Z}_2$ invariants ν_0, ν_1, ν_2, ν_3 provide a complete classification of the three-dimensional TRS insulators. Each of these quantities may be even or odd, giving us a total of 16 distinct classes.

- When all four invariants are even, then we have a “topologically-trivial insulator” or “ordinary insulator.” (*e.g.* vacuum)
- If at least one of ν_1, ν_2, ν_3 is odd while ν_0 is even, then we have a “weak topological insulator” (WTI), to be explained shortly. For this reason ν_1, ν_2, ν_3 are called *weak topological invariants.*
- Finally when ν_0 is odd, we have a “strong topological insulator,” (STI) or sometimes simply “topological insulator.” ν_0 is referred to as the *strong topological invariant.*

---

[11] There are more planes within the BZ that are time-reversal images of themselves. It can be shown that all these planes can be obtained by combining the six planes defined here in addition to a TRS deformation of planes. The important point here is that we can always write the $\mathbb{Z}_2$ invariant of any plane as some linear combination of the invariants ν_i, μ_i for the six planes, hence the six planes alone is sufficient for a topological classification.

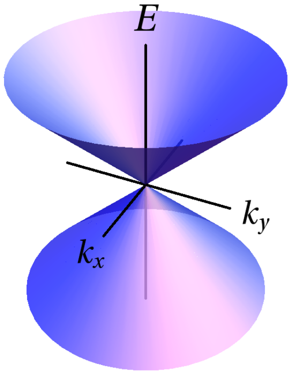

Figure 1.7: Dirac cone dispersion at the surface of strong topological insulators.

The surfaces of topological insulators consist of an odd number of Dirac cone with dispersion $E = \pm\hbar v|\mathbf{k}|$, where v is the "Dirac velocity." Near the Dirac point, the density of states is linear in the bias voltage $|E|$. The effective Hamiltonian is of the form $H = \hbar v(k_y\sigma^x - k_x\sigma^y)$, which guarantees spin-momentum locking in the cone. (In this simple model, the spin and momentum are always in the xy-plane, but perpendicular to each other.)

1.3.1 Strong topological insulators (STI)

The strong topological insulator has no analogy with the 2D quantum (spin) Hall effect, unlike the weak case. From the bulk-boundary correspondence, we expect gapless surface modes, these 2D modes are robust to disorder. The surface spectrum looks like a massless Dirac cone, where the energy is linear in momentum. The (2D) Dirac Hamiltonian for a massless particle is of the form

$$H_{\text{surface}} = \hbar v(k_y\sigma^x - k_x\sigma^y)\,, \tag{1.17}$$

where σ^α ($\alpha = x, y, z$) are the Pauli matrices, v is the "Dirac velocity," giving a linear energy-momentum dispersion (see Fig. 1.7). The spin degrees of freedom are coupled to momentum, which is sometimes referred to as spin-texture. Dirac cones dispersion also exist in graphene, but while graphene has four (including spin) Dirac cones in the BZ, strong topological insulators have an *odd* number of Dirac cones on the surface. The odd number and the absence of backscattering[12] protects the gapless spectrum in the presence of disorder [49–53].

How do we find these interesting materials? It turns out that almost all insulators are trivial, it is rather rare for a material to be a topological insulator. The mathematical formulation of the strong topological insulator was given earlier, but that gives little insight in to the physics driving a system to a topological state.

---

[12] While backscattering is forbidden by TRS, side-scattering is still permitted, allowing current dissipation. Hence the conductivity on the surface of a STI is not quantized unlike the edge of a QSH insulator.

A topological insulating phase requires some sort of *band inversion* at various points of the Brillouin zone [43, 47]. An example is if the valence band has s character at certain points (say Γ) but p character at other points (say X, L in a face-centered-cubic system), while the conduction band character has s and p reversed at these BZ points. This means that the s orbitals is below the Fermi energy at one BZ point, but above the Fermi energy at other BZ points. (In between these BZ points, the s and p orbitals are not energy eigenstates, in fact, this is required for the material to have a bulk gap.) The band inversion is be driven by spin-orbit coupling,[13] for which the effect is strongest in heavy elements. At the same time, the material must have a small enough band gap such that spin-orbit coupling is strong enough to modify the orbital energies, inverting the bands. Typically, a compound's band structure is computed (*e.g.* via density functional theory) with and without spin-orbit coupling to detect band inversions. Should the material exhibits an odd number of such inversions, it becomes a STI candidate to be confirmed by experiments. Coincidentally, these are the same characteristics shared by good thermoelectric materials; heavy elements reduces thermal conductivity from phonons and a small band gap gives a large Seebeck and electrical conductivity. For these reasons, one tends to look in similar classes of materials for both topological insulators and efficient thermoelectric materials.

The first (3D) topological insulator found was $\mathrm{Bi}_{1-x}\mathrm{Sb}_x$. It was predicted to be topologically insulating and later confirmed by angle-resolved photoemission spectroscopy (ARPES) experiments [7, 43]. Hsieh *et al.* [7] were able to see both the bulk and surface band structure, confirming a bulk gap and showing five Dirac cones on the surface. ARPES is a powerful technique in mapping the energy spectrum of materials. An incident photon causes electron to be ejected from the sample, and by controlling the incident energy and measuring the electrons momentum, one can map out the energy-momentum dispersion. One can further resolve the spin of the electron to map out the spin-texture of the Dirac cone [54–56].

Shortly after, $\mathrm{Bi}_2\mathrm{Te}_3$, $\mathrm{Bi}_2\mathrm{Se}_3$ and $\mathrm{Sb}_2\mathrm{Te}_3$ were predicted and confirmed to be topological insulators by similar experiments [8, 9, 57, 58]. These materials have been extensively studied in the past as they are widely used in thermoelectric applications.[14] The compounds are "simpler" in the sense that the elements are in stoichiometric ratios (in contrast to $\mathrm{Bi}_{1-x}\mathrm{Sb}_x$), and their surfaces has only one Dirac cone. Sometimes called the "hydrogen atom" of topological insulators,[15] these materials are much simpler from a theoretical point of view, and yet capture all of the theory. In addition, these materials have a large bulk band gap (300 meV in $\mathrm{Bi}_2\mathrm{Se}_3$), making their topological properties accessible at room temperature, and increasing their potential applications [22].

Similar to the quantum Hall effect, topological insulators can be characterized by a

---

[13] Without spin-orbit coupling, band inversion always occurs in pairs (spin degeneracy) at any given momentum in the BZ. Only an odd number of band inversions can drive the system to a TI.

[14] Even before the theoretical work on 3D topological insulators, $\mathrm{Bi}_2\mathrm{Te}_3$ and $\mathrm{Bi}_2\mathrm{Se}_3$ were known to possess surface states (*e.g.* Ref. [59]) with linear density of states. However, their significance were not realized at the time.

[15] The analogy first appeared in Ref. [8].

quantized response function, in this case the magnetoelectric polarizability [60, 61]

$$\alpha = \frac{\partial \mathbf{P}}{\partial \mathbf{B}} = n\frac{e^2}{2h}\,, \tag{1.18}$$

a measure of the electric polarization in response to an external magnetic field. By the Onsager reciprocal relation, the magnetoelectric coupling can also be written as $\frac{\partial \mathbf{M}}{\partial \mathbf{E}}$; the magnetization response to an applied electric field. For topological insulators, n is an odd integer, while for ordinary (time-reversal symmetric) insulators n is even (similar to ν_0). The constant $\frac{e^2}{h}$ is ubiquitous in condensed matter physics: contact conductance in 1D, Hall conductivity in 2D. Experiments for this quantized magnetoelectric response is underway and will complement photoemission experiments in the study of topological insulators.

1.3.2 Weak topological insulators (WTI)

For weak topological insulators, the invariant ν_0 vanishes and $\nu_1 = \mu_1$, etc. We can construct the reciprocal lattice vector $\mathbf{G}_\nu = \nu_1\mathbf{G}_1 + \nu_2\mathbf{G}_2 + \nu_3\mathbf{G}_3$, where $\mathbf{G}_i$ are the primitive reciprocal lattice vectors of the Brillouin zone [4]. Since one of the ν_i is nonzero, $\mathbf{G}_\nu \neq 0$ has a preferred spatial direction, hence WTIs are intrinsically anisotropic. They may be constructed by stacking 2D quantum spin Hall layers which are weakly coupled to each other (so to not close the bulk gap). The resulting surface spectrum always has an *even* number of Dirac cones – zero, two, or four are the most common. It is worth noting, that for any weak topological insulator, there always exist some surface which consists of two Dirac cones (to contrast ordinary insulators).

These weak topological insulators are only different from the trivial insulator in terms of the band structure, and hence their surface spectrums may be gapped out with appropriate surface perturbation. In particular, WTI are unstable to a period-doubling perturbations and its surface states do not enjoy the same level of protection from impurities or disorder the way STI do. From a topological classification point of view, WTIs are indistinguishable from ordinary insulators if one doubles the primitive unit cell, making it possible to deform a WTI to a trivial band insulator adiabatically without closing the bulk gap. For these reasons, WTIs are often overshadowed by their strong cousins.

While WTIs are only technically defined in the clean limit with a fixed lattice unit cell – a condition that can never be truly realized in experiments – there are a number of effects which should still be observable in the presence of disorder. For example, a line lattice dislocation in the bulk will support a gapless 1D helical mode running along the defect [62, 63]. In addition, the surface states are predicted to be stable even with disorder [64, 65], a somewhat counterintuitive statement given that lattice translational symmetry is a required to define a WTI. In Chap. 8, we examine the stability of the surfaces of WTIs in much greater depth.

Unfortunately, there are currently no candidate materials for WTIs. Since there is no fundamental reason why WTI does not exists in nature, the absence of candidates may be due to the lack of interest in the search for WTIs.[16]

---

[16] Na_2IrO_3 has been suggested as a potential WTI [66], however, experiments seems to suggests that the

1.4 Topological superconductors

A similar classification also applies to superconductors. At first glance, superconductors are closer to metals than insulators. However, (non-nodal) superconductors have a *quasiparticle* gap much like how insulators have an electronic gap. Just as insulators have zero electrical conductivity, superconductors have zero thermal conductivity.[17] While electrons and holes in band insulators can be described by hopping models and band Hamiltonians, superconductors and their quasiparticles can be characterized by a Bogoliubov-de Gennes Hamiltonian, which we explain in the next section.

From this perspective we can ask: when can we deform one gapped superconductor to another? Are there classes of superconductors which are not adiabatically connected to a simple conventional superconductor? The latter question we answer in the affirmative – they are called *topological superconductors*.

1.4.1 Symmetries, Altland-Zirnbauer classification

To understand the Bogoliubov-de Gennes Hamiltonian, we start by briefly reviewing the formalism of band insulators. In the cases discussed earlier (*e.g.*, QHE, QSHE, TI), the effective Hamiltonian of the system can be captured by band theory, that is, we can write down a Hamiltonian consisting of only electron hopping terms to model such systems. Imagine a lattice, with electronic degrees of freedom at every site. Every site can be filled or empty, and electrons are allowed to hop between such sites. The many body Hamiltonian $\mathcal{H}$ can be written as

$$\mathcal{H} = \sum_{\mathbf{r},\alpha,\mathbf{r}',\alpha'} t^{\mathbf{r}',\alpha'}_{\mathbf{r},\alpha} c^{\dagger}_{\mathbf{r}\alpha} c_{\mathbf{r}'\alpha'} \,, \tag{1.19}$$

where $\mathbf{r}$ and $\mathbf{r}'$ denotes the locations of the electronic orbitals, and α, α' denote all local degrees of freedom (such as orbital and spin) in a unit cell. $t^{\mathbf{r}',\alpha'}_{\mathbf{r},\alpha}$ are the hoppings amplitudes from one site/orbital to another, they must satisfy $t^{\mathbf{r},\alpha}_{\mathbf{r}',\alpha'} = \big(t^{\mathbf{r}',\alpha'}_{\mathbf{r},\alpha}\big)^*$ for $\mathcal{H}$ to be hermitian. The presence of translational symmetry, allows the Hamiltonian to be decomposed by momentum sectors

$$\mathcal{H} = \sum_{\mathbf{k}} \sum_{\alpha,\alpha'} c^{\dagger}_{\alpha,\mathbf{k}} \left(H^{\alpha'}_{\alpha}\right)_{\mathbf{k}} c_{\alpha',\mathbf{k}} \,. \tag{1.20}$$

The destruction (creation) operators momentum space are the (inverse) Fourier transforms of their counterparts $c_{\mathbf{r}\alpha}$ ($c^{\dagger}_{\mathbf{r}\alpha}$) in position space, and $(H^{\alpha'}_{\alpha})_{\mathbf{k}}$ is the Fourier transform of t, *i.e.*, $t^{\mathbf{r}',\alpha'}_{\mathbf{r},\alpha} = \frac{1}{N_f} \sum_{\mathbf{k}} (H^{\alpha'}_{\alpha})_{\mathbf{k}} e^{i\mathbf{k}\cdot(\mathbf{r}-\mathbf{r}')}$, where N_f = (number of sites × N_B), with N_B being the number of degrees of freedom per unit cell. $H_{\mathbf{k}}$ is an $N_B \times N_B$ square matrix, it is the

---

material develops magnetic order spontaneously, breaking time-reversal [67, 68].

[17] More, precisely, the electronic contribution to the thermal conductivity is zero, phonons in the materials may still carry heat current.

eigenvalues and eigenvectors of this matrix which gives the band energies $E_{\mathbf{k}}$ and Bloch functions $u_{\mathbf{k}}$ in Eq. (1.7). Written in matrix notation, Eq. (1.21) becomes

$$\mathcal{H} = \sum_{\mathbf{k}} \mathbf{c}_{\mathbf{k}}^{\dagger} \, H_{\mathbf{k}} \, \mathbf{c}_{\mathbf{k}} \,, \tag{1.21}$$

where now we've written the destruction operator $\mathbf{c}_{\mathbf{k}}$ is a column vector $(c_{1,\mathbf{k}}, \dots, c_{N_B,\mathbf{k}})^T$ (and $\mathbf{c}_{\mathbf{k}}^{\dagger}$ is row vector).

$H_{\mathbf{k}}$ captures all the information about the band model. The classification of band insulators amounts to asking which classes of $H_{\mathbf{k}}$ can and cannot be deformed to one another. Phrased another way, we examine the parameter space of all hermitian functions $H_{\mathbf{k}}$ with a gap, the topological invariants simply labels the components of this parameter space, where separate components are disconnected and hence cannot be adiabatically deformed to one another. (This is formulated more precisely in Chap. 3.)

How does symmetries fit in to this picture? The presence of a symmetry restricts the class of possible Hamiltonian to a subspace.

$$H_{-\mathbf{k}} = \Theta H_{\mathbf{k}} \Theta^{-1} \,, \tag{1.22}$$

where Θ is the time-reversal operator. Time-reversal is an antiunitary operator which reverses the spin of an electron: $\Theta|{\uparrow}\rangle = |{\downarrow}\rangle$, but also $\Theta|{\downarrow}\rangle = -|{\uparrow}\rangle$. The negative sign is important, a reflection of the algebra $\Theta^2 = -1$ for spin-1/2 particles. This minus sign have profound implications, the Kramers degeneracy theorem [69], stability of the QSH edge, weak antilocalization [70, 71] are among the physical consequences. By convention, we write $\Theta = -i\sigma^y\mathcal{K}$ with $\mathcal{K}$ the complex conjugation operator,[18] Eq. (1.22) can also be written as

$$H_{-\mathbf{k}} = \sigma^y H_{\mathbf{k}}^{*} \sigma^y \,. \tag{1.23}$$

This restriction can eliminate possible components of the Hamiltonian phase space, here time-reversal symmetry forbids phases with nonzero Chern number, restricting the space to $\nu = 0$. At the same time, the symmetry restriction may break a single phase into multiple components, here there are two time-reversal components within the $\nu = 0$ phase. (Figure 1.5 illustrates both these scenarios.)

We digress for a moment to address: Why is spin-orbit coupling important? TRS systems without spin-orbit coupling must have full electronic spin rotation invariance, the reason is that terms which differentiate between the spins involve the spin operators σ^α, and these are forbidden by time-reversal.[19] Spin rotation symmetry implies that the system is invariant under a global rotation of the electron spin, independent of the physical orientation of the system, which we abbreviate as $SU(2)$ symmetry.

---

[18] The Pauli matrix $\sigma^y = \left[\begin{smallmatrix} & -i \\ i & \end{smallmatrix}\right]$. Generally, $\Theta\big(a|{\uparrow}\rangle + b|{\downarrow}\rangle\big) = -b^*|{\uparrow}\rangle + a^*|{\downarrow}\rangle$. The $-i$ in $-i\sigma^y\mathcal{K}$ is not necessary, but is merely convention – even without the factor, $\Theta^2 = -1$ holds.

[19] Under time-reversal, $\sigma^\alpha \to -\sigma^\alpha$, so the spin operators cannot exist by themselves in TRS systems. On the other hand, time-reversal also flips the momentum, so spin-orbit combinations like $\mathbf{k} \cdot \boldsymbol{\sigma}$ are allowed.

The combination of TRS and $SU(2)$ symmetry imposes additional constraints of $H_{\mathbf{k}}$. With $SU(2)$ symmetry, the spin-up and spin-down subsystem must be identical and decoupled from one another. Time-reversal thus takes a state $|\mathbf{k}\uparrow\rangle$ to $|-\mathbf{k}\downarrow\rangle$, which is equivalent to $|-\mathbf{k}\uparrow\rangle$. Ignoring the spin index, the Hamiltonian satisfies

$$H_{-\mathbf{k}} = H^*_{\mathbf{k}}\,. \tag{1.24}$$

One can think that Eq. (1.22) still holds, but now the effective time-reversal operator is simply $\Theta = \mathcal{K}$. Notice now that $\Theta^2 = +1$, since we can treat our TRS and $SU(2)$ invariant Hamiltonian as two copies of some spinless fermionic system. The positive sign leads to *weak localization* [72, 73] and a completely different topological classification.

Superconductors and Bogoliubov-de Gennes Hamiltonian

To model a superconductor, we add in an effective electron-electron interaction term of the form $\sum_{\mathbf{k},\mathbf{k}'} V_{\mathbf{k},\mathbf{k}'} c^\dagger_{\mathbf{k}} c^\dagger_{-\mathbf{k}} c_{\mathbf{k}'} c_{-\mathbf{k}'}$, taking a pair of electrons from $\pm\mathbf{k}'$ to $\pm\mathbf{k}$. Let us for simplicity, assume a single orbital (with spin-up and down) and conventional s-wave superconductivity for the moment, our pairing term becomes $\sum V_{\mathbf{k},\mathbf{k}'} c^\dagger_{\mathbf{k}\uparrow} c^\dagger_{-\mathbf{k}\downarrow} c_{\mathbf{k}'\uparrow} c_{-\mathbf{k}'\downarrow}$ [74]. In the self-consistent mean field treatment, we let $\Delta_{\mathbf{k}} = \sum_{\mathbf{k}'} V_{\mathbf{k},\mathbf{k}'} \langle c_{\mathbf{k}'\uparrow} c_{-\mathbf{k}'\downarrow}\rangle$, treating it as a static quantity only as a function of $\mathbf{k}$. The pairing term is approximated by

$$\sum_{\mathbf{k}} \Delta_{\mathbf{k}} c^\dagger_{\mathbf{k}\uparrow} c^\dagger_{-\mathbf{k}\downarrow} + \Delta^*_{\mathbf{k}} c_{-\mathbf{k}\downarrow} c_{\mathbf{k}\uparrow}\,. \tag{1.25}$$

We have the Bogoliubov-de Gennes (BdG) Hamiltonian [75],

$$\begin{aligned} \mathcal{H} &= \frac{1}{2}\sum_{\mathbf{k}} \left(c^\dagger_{\mathbf{k}\uparrow}\; c^\dagger_{\mathbf{k}\downarrow}\; c_{-\mathbf{k}\uparrow}\; c_{-\mathbf{k}\downarrow} \right) \begin{bmatrix} H_{\mathbf{k}} & i\Delta_{\mathbf{k}}\sigma^y \\ -i\Delta^*_{\mathbf{k}}\sigma^y & -H^T_{-\mathbf{k}} \end{bmatrix} \begin{pmatrix} c_{\mathbf{k}\uparrow} \\ c_{\mathbf{k}\downarrow} \\ c^\dagger_{-\mathbf{k}\uparrow} \\ c^\dagger_{-\mathbf{k}\downarrow} \end{pmatrix} && (1.26) \\ &= \frac{1}{2}\sum_{\mathbf{k}} \Psi^\dagger_{\mathbf{k}}\, H^{\mathrm{BdG}}_{\mathbf{k}}\, \Psi_{\mathbf{k}}\,. && (1.27) \end{aligned}$$

This equation packs a lot of information regarding the Hamiltonian.

- Here $H^{\mathrm{BdG}}_{\mathbf{k}}$ is a 4×4 matrix, with Ψ being a four component vector.
- $H_{\mathbf{k}}$ is a 2×2 matrix describing the Hamiltonian of the original two band metal. It sits in the upper left corner of $H^{\mathrm{BdG}}_{\mathbf{k}}$ coupling $c^\dagger_{\mathbf{k}}$ and $c_{\mathbf{k}}$ just as in the Hamiltonian (1.21).
- $H_{-\mathbf{k}}$ sits in the lower right corner, coupling $c_{-\mathbf{k}}$ to $c^\dagger_{-\mathbf{k}}$. However, notice that the destruction operators are in the row vector on the *left* of the matrix, while the creation operators are on the right. The transpose takes care of the swapped row/column vectors, and the negative sign is from the exchange of c and $c^\dagger$.
- That means that for every term in the summation $\sum_{\mathbf{k}}$, both pieces $H_{\mathbf{k}}$ and $H_{-\mathbf{k}}$ are added to the sum. The factor of $\frac{1}{2}$ remedies the double counting that results.

- The $\Delta_{\mathbf{k}}$ and $\Delta^*_{\mathbf{k}}$ terms introduce mean field pairing into the Hamiltonian. The factor $i\sigma^y = \left[\begin{smallmatrix} & 1 \\ -1 & \end{smallmatrix}\right]$ is a 2×2 matrix which ensures spin-singlet pairing. (That is, pairing spin-up with spin-down consistent with Fermi statistics.)

Similar to $H_{\mathbf{k}}$ in Eq. (1.21), The eigenvectors and eigenvalues of $H^{\mathrm{BdG}}_{\mathbf{k}}$ tells us what the quasiparticles are and their energies. The difference here is that $\Psi^\dagger_{\mathbf{k}}$ contains both $c^\dagger_{\mathbf{k}}$ and $c_{-\mathbf{k}}$, meaning that quasiparticle excitations are superpositions of electrons and holes. The possibility of mixing particles with $+e$ and $-e$ charge together is allowed in a condensate of charge $2e$ Cooper pairs.

Each term $H^{\mathrm{BdG}}_{\mathbf{k}}$ captures the electron motion at both wavevector $\mathbf{k}$ and $-\mathbf{k}$, making $H^{\mathrm{BdG}}_{-\mathbf{k}}$ redundant. In fact, we can map H^{BdG} at $\mathbf{k}$ to that at $-\mathbf{k}$. First, notice we can take $\Psi^\dagger_{\mathbf{k}}$ to $\Psi^T_{-\mathbf{k}}$ (as a row vector) by swapping the first two with the last two elements, which we can write as $\Psi_{-\mathbf{k}} = (\Psi^\dagger_{\mathbf{k}}\tau^x)^T$. Here τ^x is a matrix which swaps the elements, defined as

$$\tau^x = \begin{bmatrix} & & 1 & \\ & & & 1 \\ 1 & & & \\ & 1 & & \end{bmatrix}. \tag{1.28}$$

We equate the terms $\Psi^\dagger_{\mathbf{k}}\, H^{\mathrm{BdG}}_{\mathbf{k}}\, \Psi_{\mathbf{k}} = \Psi^\dagger_{-\mathbf{k}}\, H^{\mathrm{BdG}}_{-\mathbf{k}}\, \Psi_{-\mathbf{k}}$. Skipping over the algebraic details, the matrices are related by the following equation,

$$H^{\mathrm{BdG}}_{-\mathbf{k}} = -\tau^x \big(H^{\mathrm{BdG}}_{\mathbf{k}}\big)^* \tau^x \,. \tag{1.29}$$

In words: Take the four 2×2 subblocks of $H^{\mathrm{BdG}}_{\mathbf{k}}$ in Eq. (1.26), swap each of them to the opposite quadrant, take the complex conjugate, multiply by -1, to get $H^{\mathrm{BdG}}_{-\mathbf{k}}$. This form is reminiscent of Eqs. (1.23) and (1.24), namely it places a constraint for the Hamiltonian at opposite momenta $\mathbf{k}$ and $-\mathbf{k}$. From this perspective, we can view BdG Hamiltonians as possessing a new type of symmetry – called *particle-hole* symmetry – for every quasiparticle excitation at energy E and wavevector $\mathbf{k}$, there also exists one at $-E$ and $-\mathbf{k}$. However, we note that the particle-hole symmetry is really an artifact of the way we create our BdG Hamiltonian; by doubling the system and coupling operators at momenta $\mathbf{k}$ and $-\mathbf{k}$ together. Hence, the BdG Hamiltonian modeling our superconductor gives twice the degree of freedom than it truly has, in particular, creating a quasiparticle at $(E, \mathbf{k})$ is exactly the same as removing one at $(-E, -\mathbf{k})$. Nevertheless, $H^{\mathbf{BdG}}$ proves to be useful in classifying superconductors.

More generally, superconductors (conventional or otherwise) can always be characterized by a BdG Hamiltonian of the form in Eq. (1.27), with a particle-hole symmetry

$$H_{-\mathbf{k}} = -\mathcal{C} H_{\mathbf{k}} \mathcal{C}^{-1} \,. \tag{1.30}$$

$\mathcal{C}$ is called either the *particle-hole operator* or the *charge-conjugation operator*. (In the single-orbital s-wave case, $\mathcal{C} = \tau^x \mathcal{K}$.) This allows us to view superconductors as band insulators with extra symmetries, and we can ask the same question as before: what classes of BdG Hamiltonians can and cannot be deformed to one another, while maintaining a gap?

	TRS	Spin-conserved	AZ name	Topological invariants		
				1D	2D	3D
Standard	No	Either	A		$\mathbb{Z}$	
	Yes	No	AII		$\mathbb{Z}_2$	$\mathbb{Z}_2$
	Yes	Yes	AI			
Chiral	No	Either	AIII	$\mathbb{Z}$		$\mathbb{Z}$
	Yes	No	CII	$\mathbb{Z}$		$\mathbb{Z}_2$
	Yes	Yes	BDI	$\mathbb{Z}$		
Bogoliubov-de Gennes	No	No	D	$\mathbb{Z}_2$	$\mathbb{Z}$	
	Yes	No	DIII	$\mathbb{Z}_2$	$\mathbb{Z}_2$	$\mathbb{Z}$
	No	Yes	C		$\mathbb{Z}$	
	Yes	Yes	CI			$\mathbb{Z}$

Table 1.2: List of symmetry classes and their topological invariants up to 3D

The table here reproduces the results from Ref. [77]. The “AZ name” is the designation given by Altland and Zirnbauer [76] for the corresponding disordered ensemble. The list of symmetries is complete among systems without any spatial (*e.g.* crystalline and inversion) symmetries.

Table 1.2 lists the possible symmetry classes by combining various combinations of symmetries, as well as the topological invariants that exists up to three-dimensions. Each row corresponds to a symmetry class – an ensemble of Hamiltonians satisfying certain symmetries and relations. The “AZ name” refers to the designation given by Altland and Zirnbauer [76], and while the labels are completely unilluminating as to the symmetries involved and how they could be physically realized, these names are used widely when discussing topological superconductors. The symmetry classes can be grouped in to three categories. The “standard” classes consist of the band Hamiltonians discussed earlier, with AII and AI corresponding to the constraints (1.23) and (1.24) respectively. The “chiral” classes can be realized in a hopping model with sublattice symmetry, that is, the system breaks in to two sublattices, called ‘A’ and ‘B,’ we allow hopping between ‘A’ sites and ‘B’ sites, but forbid those between ‘A’s and those between ‘B’s. The BdG classes exists in context of superconductors discussed a moment ago.

This table, called the “periodic table of topological insulators and superconductors,” was first put together by Schnyder, Ryu, Furusaki, and Ludwig [77], and independently by Kitaev [78]. These topological invariants are exhaustive, meaning that they describe all possible “strong” topological invariants in up to three-dimensions. $\mathbb{Z}$ denotes an integer invariant (*e.g.* in QH), $\mathbb{Z}_2$ denotes an even/odd type classification, and blank entries implies the lack of topological distinction among that symmetry class in the particular dimension.

An entry thus indicates the existence of a topological insulator or topological superconductor (TSC) in the corresponding class. A number of TIs/TSCs have been found experimentally, and there are candidate materials for a large number of these entries. Among those discussed earlier, the quantum Hall systems belong to the "A" class in 2D, the quantum spin Hall in HgTe wells belong to the "AII" class (also in 2D), and topological insulators (such as $\mathrm{Sb_2Te_3}$) belong to the 3D "AII" class. In the next section we discuss some of the properties of TSCs and their experimental status.

1.4.2 Realizing topological superconductors

Topological superconductors were actually conceived of before topological insulators. At the turn of the millennium, Read and Green [79] showed that the two-dimensional "$p+ip$" superconductor is in a nontrivial topological phase. A $p+ip$ superconductor, or more accurately p_x+ip_y superconductor, is one where the pairing term $\Delta_{\mathbf{k}}$ [as in Eq. (1.25)] is proportional to k_x+ik_y, (at least when $\mathbf{k}$ is small). Contrast to conventional (s-wave) pairing, where $\Delta_{\mathbf{k}}$ is constant coupling the spin in a singlet, in $p+ip$ pairing $\Delta_{\mathbf{k}}$ depends on k_x, k_y and couples like spins together.

The $p+ip$ superconductor breaks time-reversal symmetry; it belongs to the "D" class in Tab. 1.2, where 2D systems can be characterized by an integer. Similar to QH systems, Bogoliubov-de Gennes Hamiltonians in 2D can also be classified by their TKNN/Chern number. A $p+ip$ superconductor has a Chern number of 1, hence there is a single chiral mode which runs around its edge.[20]

Perhaps the most exciting part about these $p+ip$ superconductors are the Majorana fermion modes found pinned to the center of superconducting vortices. A Majorana fermion can be thought of as *half* a fermion which are their own antiparticles [80, 81].[21] These particles possess non-abelian statistics, which means that through braiding operations one can evolve from one degenerate ground state to another [82–84]. This is the idea behind a topological quantum computer, where information are stored by the Majorana fermions, and computation is performed by braiding operations [82, 83, 85, 86]. The degenerate ground states are stable in the sense that they cannot mix with one another via any local perturbations to the system, hence a topological quantum computer would be less susceptible to decoherence compared to other implementations of quantum computers.

Can such an exotic system be realized? Currently, $\mathrm{SrRu_2O_4}$ [87] is a candidate for $p+ip$ superconductors, although current experimental evidences are not completely clear. It is also suggested that the fractional quantum Hall at $\nu = 5/2$ could be a $p+ip$ 'superconductor,' not in terms of bare electrons, but constructed from pairing composite fermions [79].

While the use of Majorana fermions to construct a quantum computer seems far-fetched, Majorana fermions themselves have recently been observed in InSb wires in an experiment by Mourik *et al.* [88]. The experiment realizes a model by Kitaev [89]; a one-dimensional

---

[20] More precisely, a chiral Majorana mode around its edge.

[21] They arise naturally from the BdG Hamiltonian as states with zero energy.

topological superconducting wire with single Majorana modes on each end. (The model is an example of a nontrivial 1D system in the "D" class.) As the "Kitaev wire" is one of the simplest system to realize Majorana fermions, its implementation was the subject of a number of theoretical proposals [90–92]. The essential ingredients are: a superconductor, spin-orbit coupling, and time-reversal breaking. In the experiment, this is realized with InSb wires (for the spin-orbit effect), in proximity with NbTiN superconducting electrodes, immersed in a magnetic field (breaking time-reversal). Transport measurements show a zero-bias conductance peak, a signature that is characteristic of Majorana fermions.

Finally, we'd like to comment on time-reversal symmetric superconductors (class "DIII" in Tab. 1.2). $Cu_xBi_2Se_3$ is shown to be a superconductor and is currently a candidate to be a 3D topological superconductor [93–96]. If such is the case, then their surface would support "Dirac cones of Majorana fermions." (As opposed to Dirac cones of electrons for TIs.) The current difficulty lies in the ability to probe the superconducting surface states, and to distinguish the their signatures from those of TIs (as the parent compound Bi_2Se_3 is also a TI). Curiously, superfluid ^{3}He-B is also proposed to realize a 3D topological superconducting phase [97]. Here the electrons do not pair to become a superconductor, but the helium-3 atoms pair to become a superfluid.

1.5 Applications and outlook

The search for more topological insulating materials continues. For example, thallium based compounds such as $TlBiSe_2$ have been suggested to be a topological insulator [98–100] which have subsequently been experimentally verified [101–104]. Recent *ab-initio* calculations of various ternary compounds including half-Heusler alloys suggest new classes of semiconductors which are topological insulators, some which have been confirmed experimentally [105–108]. Much work has been focused on band structure calculations of semiconductors in a race to discover more topological insulators, this along with the competition to fabricate new materials and experimentally confirm their topological properties has led to myriad of new TI compounds [109–114]. This larger pool of materials will allow greater control over properties such as the bulk gap, chemical potential, lattice structure, surface Dirac velocity, superconductivity, *etc.* for various applications.

Much experiments have been based on surface-sensitive techniques such as ARPES and scanning tunneling microscopy (STM) [52, 115–117], as these directly probe surface states which are the key experimental signatures of a topological insulator. On the other hand, transport experiments are crucial to complement these results, and gives us information regarding the bulk region of these materials. For example, Peng *et al.* [118] used the Aharonov-Bohm interference to confirm the surface conduction in nanoribbons while other groups used Shubnikov-de Haas oscillations to probe their 2D surface properties [113, 119–123]. The main challenge in these transport experiments is the ability to tune the chemical potential to be in the bulk gap of the material as to maximize the contribution from surface electrons to conductance [9, 113, 121, 124, 125]. Currently many topological insulators samples are either

p-typed or n-typed and are not truly insulating, *i.e.*, the conduction channels are dominated by the bulk carriers. Improvements in materials fabrication and the ability to control the chemical potential are among the most difficult hurdles in the study of topological insulators. (Refer to Ref. [126] for a more comprehensive review of transport in TIs.)

There have also been interests in the fabrication of topological insulators nanostructures, particularly nanoribbons [118, 127, 128] and thin films [129–134] where nanoscale effects become important. For instance, in a thin film of TI, the opposite surfaces can be close enough to each other to allow interlayer electron hopping [130, 135–137], or Coulomb interactions between the surfaces [133, 134]. At the same time, these geometry optimizes the surface to volume ratio, a way to enhance surface contributions to transport. In light of the realization that topological insulators (namely Bi_2Te_3 and Bi_2Se_3) also tends to be good thermoelectric materials, our new theoretical understanding of TIs could help us further improve their thermoelectric efficiency [138–143]. Roughly, to have an efficient thermoelectric material one desires a large electrical conductivity, but a small thermal conductivity. These nano-geometries may improve thermoelectric performance in two ways. Spatial confinement of phonons tends to reduce their mobility, thereby reducing the overall thermal conductivity, At the same time, increasing surface-to-bulk ratio also increases the density of states (per volume) due to the surface excitations, potentially raising the overall electrical conductivity.

Perhaps the most promising direction for topological insulators are heterojunctions with conventional superconductors. The superconducting proximity effect opens a gap at the interface surface, which may host Majorana fermions [144]. The properties of these SC–TI junctions are in many ways similar to that of a $p + ip$ superconductor, where the Majorana fermions obey non-abelian statistics. There are a number of proposals to create Majorana fermions involving topological insulators, Refs. [145–147] to name a few. All these proposals involve similar ingredients: Take a topological insulator, put it in proximity with a superconductor, and break time-reversal symmetry. Refs. [148, 149] review various proposals of realizing Majorana fermions in SC–TI interfaces, and more generally, semiconductor systems.

The study of topological insulators and superconductors is a rapidly developing field in condensed matter physics and material science. This is an exciting time for both theorists and experimentalists, as many ideas are being tested, and many open questions remain. The potential applications such as thermoelectricity and topological quantum computing will further expand the breadth of this field.

Chapter 2

Overview of thesis

The thesis is divided in to three parts. In Part II, we study the bulk properties of topological insulators, specifically the topological invariants which distinguishes one class from another. We then discuss how these invariants could be observed physically. In Part III, we focus on the relationship between the bulk and surface properties, specifically in cases where the surface spectrum could be determined from geometric bulk properties alone. In Part IV, we analyze the transport properties of the surface of weak topological insulators.

Part II is further subdivided into three chapters.

- Chapter 3, "Topology of Hamiltonian spaces," presents a mathematical approach to the classification of band insulators. In any dimension, we devise a formalism and an algorithm to compute topological invariants for inversion-like symmetry classes. While the work is unpublished, some of the ideas presented have been published in Ref. [150], here in this thesis we give much more rigorous treatment of the subject and generalizes the method to many more symmetry classes.

- Chapter 4, "Inversion symmetric insulators," applies the classification scheme of the previous chapter to the inversion symmetry class. We show that with only inversion symmetry, 3D insulators are characterized by an integer invariant at each of the 8 time-reversal invariant momenta (TRIMs), as well as 3 Chern numbers, for a total of 11 integers. We also examine various properties associated with each topological invariants and distills physically observable quantities, such as frozen polarization and the magnetoelectric coupling. The work was completed in collaboration with Ari M. Turner, Yi Zhang, and Ashvin Vishwanath, published at Ref. [150].

- Chapter 5, "Antiferromagnetic topological insulators," classifies antiferromagnets preserving a combination of translation and time-reversal symmetry. We find that in 3D, a $\mathbb{Z}_2$ invariant exists distinguishing antiferromagnetic trivial insulators from antiferromagnetic topological insulators (AFTIs). This chapter uses some of the ideas presented earlier, but is largely focused on the physical implications and the potential realizations in experiments. The work was completed in collaboration with Andrew M. Essin, Joel E. Moore, published at Ref. [151].

Part III consists of two chapters.

- Chapter 6, “Computing the edge spectrum in Dirac Hamiltonians,” presents a geometric prescription for computing edge state energies of Dirac Hamiltonians. The prescription applies even when the edge states are not topologically protected, such as in the case of graphene. However, when applied to topological insulators, we show that the edge modes are indeed robust, and proves the bulk-boundary correspondence for the case of Dirac Hamiltonians. The work was completed in collaboration with Vasudha Shivamoggi, published at Ref. [40].
- Chapter 7, “Majorana fermions at the ends of superconductor vortices in doped topological insulators,” examines when Majorana fermions can be found without the proximity effect. We argue that their existence is dependent not on the surface band structure of the parent compound, but on the bulk Fermi surface properties – another example of the subtle interplay between the bulk and the surface. Specifically, we demonstrate that the minigap spectrum within the vortex can be computed from the non-abelian Berry phase of the bulk Fermi surface, which in turn determines the critical doping level for which Majorana fermions can be localized. The work was completed in collaboration with Pavan Hosur, Pouyan Ghaemi, and Ashvin Vishwanath, published at Ref. [152].

Part IV has only one chapter.

- Chapter 8, “Quantum transport on the surface of weak topological insulators,” resolves the surface properties of WTIs with two Dirac cones. Unlike the STIs, the surface states may be gapped out with a TRS ‘mass’ term coupling the two Dirac cones. At the same time, WTIs require lattice translational symmetry to be distinguished from a trivial insulators, which raises the issue of disorder on the surfaces of WTIs. We find that the surface conductance flows to an insulator or a symplectic metal, governed by a competition between disorder and mass. The work was completed in collaboration with Jens H. Bárðarson and Joel E. Moore, published at Ref. [65].

Part II

Classification of Band Insulators

Notation and conventions for the following chapter

- S^n is an n-sphere. D^n is an n-disk. T^n in an n-torus.
  Note that $\partial D^n \cong S^{n-1}$, $T^n \cong \underbrace{S^1 \times \cdots \times S^1}_{n}$.
  Also, I is the unit interval $[0,1]$.
- A pointed space is a pair (X, x_0) where X is a topological space and $x_0 \in X$. Often we write X instead of the pair when the meaning is implied. Unless otherwise specified, maps between pointed spaces are basepoint preserving, as are homotopies between such maps. Formally, a pointed space is always required to define homotopy groups $\pi_n(X)$.
- ΩX is the space of loop in the pointed space (X, x_0); set of maps $f : I \to X, f(0) = f(1) = x_0$ along with a compact-open topology. The base point of ΩX is defined to be the constant loop at x_0.
- $\binom{n}{k}$ is a binomial coefficient, equals to $\dfrac{n!}{k!\,(n-k)!}$.
- As a group, 0 denotes the trivial group. (In tables, entries with 0 will be left blank.)
- $\mathbb{Z}_n$ denotes the cyclic group of order n. (Sometimes written as $\mathbb{Z}/n\mathbb{Z}$ literature.)
- Given two complex vectors $u, v \in \mathbb{C}^n$, the inner product is defined as $\langle u, v\rangle = \sum_\mu u_\mu^* v_\mu$.
- $\mathbb{1}_n$ denotes an $n \times n$ identity matrix. (Depending on the context, it is also used to denote the identity map/operator on a n-dimensional vector space.)
- A^T, A^*, $A^\dagger$ denotes the transpose, complex conjugation, and hermitian conjugate (or conjugate transpose) of the matrix A. If A is invariant under A^T, A^*, or $A^\dagger$, then A is respectively, symmetric, real, or hermitian.
- σ^x, σ^y, σ^z are the Pauli matrices. $\sigma^x = \left[\begin{smallmatrix} & 1 \\ 1 & \end{smallmatrix}\right]$, $\sigma^y = \left[\begin{smallmatrix} & -i \\ i & \end{smallmatrix}\right]$, $\sigma^z = \left[\begin{smallmatrix} 1 & \\ & -1 \end{smallmatrix}\right]$. $\boldsymbol{\sigma}$ is a vector of matrices: $(\sigma^x, \sigma^y, \sigma^z)$.

- $\mathcal{K}$ is the complex conjugation operator. Θ, $\mathcal{C}$, $\mathcal{S}$, Π are the time-reversal, charge-conjugation, sublattice, and inversion operators respectively.

- $\mathbb{H}$ is the set of quaternions of the form $a = a_0 + a_1\mathbf{i} + a_2\mathbf{j} + a_3\mathbf{k}$, with $\mathbf{ij} = \mathbf{k}$ and $\mathbf{i}^2 = \mathbf{j}^2 = \mathbf{k}^2 = -1$. The quaternion conjugation a^* is given by negating a_1, a_2, a_3. Often we will employ their 2×2 complex matrix representation $a = a_0\mathbb{1}_2 - i\mathbf{a} \cdot \boldsymbol{\sigma}$, such that quaternion multiplication is compatible with matrix multiplication. The quaternion conjugation becomes the conjugate transpose $a^\dagger$.

- $O(N)$, $SO(N)$, $U(N)$, $SU(N)$ are the orthogonal, special orthogonal, unitary, special unitary groups respectively. We will always represent an element of these groups by an $N \times N$ matrix.

- $Sp(N)$ is the compact symplectic group: set of $N \times N$ unitary matrix of quaternions. Alternatively defined as the set of $2N \times 2N$ matrices A such that $A^T J A = J$ and $A \in SU(2N)$, where J is the standard symplectic 2-form: $J = \left[\begin{smallmatrix} & \mathbb{1}_N \\ -\mathbb{1}_N & \end{smallmatrix}\right]$.

- $\mathrm{Gr}_k(\mathbb{F}^n)$ is the Grassmannian of a associative division algebra $\mathbb{F}$. (We will only use $\mathbb{R}$, $\mathbb{C}$ and $\mathbb{H}$ in this text.) That is, the space of all k-dimensional subspace of $\mathbb{F}^n$. The projective spaces are special cases of Grassmannians with $k = 1$, *e.g.*, $\mathbb{C}\mathrm{P}^n \cong \mathrm{Gr}_1(\mathbb{C}^{n+1})$.

- BG denotes the classifying space of group G. We are particularly interested in the classifying space of classical Lie groups, which can be thought of as the direct limit of Grassmannians, *e.g.*, $BSp(N) \sim \mathrm{Gr}_N(\mathbb{H}^\infty)$.

Chapter 3

Topology of Hamiltonian spaces

In this chapter, we approach the problem of classifying band insulators from a homotopy point of view. By providing formal definitions for physical concepts such as band structures and symmetries, we can pose the problem in a rigorous setting. This chapter is intended to be much more mathematical than the rest of this work, drawing on formal concepts from abstract algebra and algebraic topology.[1] Readers unfamiliar with some of the concepts or terminology may consult textbooks in algebraic topology.

We motivate this chapter with a puzzle, but first some definitions. A d-dimensional *band structure* is a matrix-valued function $H(\mathbf{k})$, where $\mathbf{k}$ is the momentum which lives in the Brillouin zone, topologically equivalent to a torus: $\mathbf{k} \in T^d$. Rephrased in another way, a band structure is a map from T^d to the set of $N_B \times N_B$ hermitian matrices. The *spectrum* of the band structure are the eigenvalues of $H(\mathbf{k})$, a set of N_B real numbers at every $\mathbf{k}$. The spectrum represents the excitation energies of the system, and system is called gapless if there is a zero eigenvalue in the Brillouin zone. On the other hand, if there are no zero eigenvalues anywhere, we say the system is gapped, and $H(\mathbf{k})$ describes a *band insulator*.

What are properties of band insulators? Let $H(\mathbf{k})$ be gapped, hence at every $\mathbf{k}$ the matrix has some number of positive and negative eigenvalues, call them M and N respectively, such that $M + N = N_B$. Of course, we are dealing with continuous maps,[2] hence M and N must be constant throughout the Brillouin zone. Physically, N is the number of filled bands (or filled orbitals), M is the number of empty bands, and N_B is the total number of bands. Moreover, any deformation of the band structure, as long as it remains gapped, cannot change M or N. We ask the general question.

> Given two band insulators $H(\mathbf{k})$ and $H'(\mathbf{k})$, can we adiabatically deform one to the other without breaking the gap? That is, is there a homotopy between the two maps?

---

[1] There will be no category theory, anywhere.

[2] $H(\mathbf{k})$ is actually the Fourier transform of the electron hopping amplitude in *real* space. The condition that $H(\mathbf{k})$ is a continuous function of $\mathbf{k}$ comes from the requirement that the hoppings are *local*, *i.e.*, they are exponentially decaying as a function of distance. The concept of locality is paramount in physics.

Clearly $H(\mathbf{k})$ and $H'(\mathbf{k})$ must share the same N, which physically amounts to counting the number of electrons per unit cell, a necessary, but not very interesting distinction. As it turns out, there are additional requirements for H and H' to be homotopic, the answer depending on the number of dimensions d. The set of $N_B \times N_B$ Hermitian matrices is $\mathbb{R}^{N_B^2}$, a retractable space that is of little interest in terms of homotopy. However, the constraint that there are no zero eigenvalues yield a subspace which is not topologically trivial (*i.e.*, not retractable). An algebraic topologist will immediately recognize the subspace is homotopic to a Grassmannian $\mathrm{Gr}_N(\mathbb{C}^{N+M}) = \frac{U(N+M)}{U(N)U(M)}$, and the problem related to the classifying vector bundles on tori, we will return to the latter point in a moment.

To rephrase the question, what are the homotopy classes of maps from T^d to $\mathrm{Gr}_N(\mathbb{C}^{N+M})$? In $d = 2$, and for $N, M \geq 1$ (so there are at least one filled and empty band), we get a class of maps characterized by an integer ν. This integer is related to $\pi_2(\mathrm{Gr}_N(\mathbb{C}^{N+M})) = \mathbb{Z}$.[3] The homotopy groups classifies maps from spheres to a pointed space, in this context $S^2 \to \mathrm{Gr}_N(\mathbb{C}^{N+M})$. But a torus T^2 and a sphere S^2 are not the same – here we are in a fortuitous situation where the Grassmannian is simply-connected, *i.e.*, its π_1 is trivial. A map $T^2 \to \mathrm{Gr}_N(\mathbb{C}^{N+M})$ may be deformed to $S^2 \to \mathrm{Gr}_N(\mathbb{C}^{N+M})$ by taking two 'perpendicular' loops in T^2 and contracting them to form a sphere. In any case, we have the following necessary (and sufficient) criteria in 2D: the maps H and H' must share the same N and ν to be homotopic. The ν here describes the "Chern number" of quantum Hall phases described in the introduction.

In 3D, the classification is more complicated. Looking at $\pi_3(\mathrm{Gr}_N(\mathbb{C}^{N+M}))$ is insufficient since the second homotopy group does not vanish. In the case when $N = M = 1$, the space becomes a sphere: $\mathrm{Gr}_1(\mathbb{C}^2) \approx S^2$. Based on the homotopy groups ($\pi_2(S^2) = \pi_3(S^2) = \mathbb{Z}$), one might may a naive guess that maps $T^3 \to S^2$ are classified by 4 integers invariant, 3 integers for each 2-cells in T^3, and the last one related to the Hopf invariant. Unfortunately, this is not the case,[4] as was shown by Pontryagin [153].

We can also add an additional constraint. We can restrict to systems with time-reversal symmetry, which puts the constraint that $H(-\mathbf{k}) = U_\Theta H(\mathbf{k})^* U_\Theta^{-1}$ (for some unitary matrix U_Θ with $U_\Theta U_\Theta^* = -\mathbb{1}_{M+N}$). What are the classification of band insulators with this additional symmetry constraint? Existing classes (from the case without the constraint) may be forbidden, while some classes may split in to disconnected pieces, creating a new classes. This is realized with the quantum spin Hall effect with the presence of time-reversal.

For such classification problems in general to be tractable, we make a few assumptions and simplifications. First, we let the number of empty bands M go to infinity, which effectively equates the problem with classifying vector bundles. Second, we consider only stably isomorphic vector bundles, reproducing the results from K-theory. With the inclusion of symmetries, the classification is in same spirit as equivariant K-theory.

---

[3] This integer is also the pullback of the cohomology $H^2(\mathrm{Gr}_N(\mathbb{C}^{N+M})) \to H^2(T^2)$, but we will defer this point until much later.

[4] The naive guess fails because of the nontrivial Whitehead product $\pi_2(S^2) \times \pi_2(S^2) \to \pi_3(S^2)$. Using cohomology also fails, as $H^3(S^2) = 0$ is unable to capture the Hopf map.

3.1 Topological classification of band structures

Definition 1. Let Z be a topological space. Z is an *H-group* if it satisfies the following.

1. There exists a composition map $\mu : Z \times Z \to Z$.
2. There exists a distinguished element – the "identity" – $e \in Z$ for which the maps $x \mapsto \mu(e, x)$ and $x \mapsto \mu(x, e)$ are both homotopic to the identity map.
3. μ is associative up to homotopy: The maps $A_1, A_2 : Z \times Z \times Z \to Z$ are homotopic to each other where $A_1(x, y, z) = \mu(\mu(x, y), z)$ and $A_2(x, y, z) = \mu(x, \mu(y, z))$.
4. There exists (right) inverses up to homotopy: For all $x \in Z, \exists x^{-1}$ such that $x \mapsto \mu(x, x^{-1})$ is deformable to the constant map $x \mapsto e$.

In addition, an H-group is *commutative* if it satisfies the following.

5. The maps $\mu, \mu' : Z \times Z \to Z$ are homotopic to each other, with $\mu'(x, y) = \mu(y, x)$.

Hence we can see that a (commutative) H-group, for the purposes of homotopy theory, is a (commutative) group. Note that the first two conditions alone defines an H-space. In a moment, we will give some examples of H-groups useful in the chapter.

H-groups are useful in situations where defining a strict group structure is impractical, but for the purposes of classifying maps, they can be treated as groups. The homotopy groups of H-spaces and H-groups have additional properties.

- The fundamental group $\pi_1(Z)$ of an H-space is abelian.
- The homotopy composition of $\pi_n(Z)$ is the same as the induced composition map $\mu_* : \pi_n(X) \times \pi_n(X) \to \pi_n(X)$.
- Properties of Z carries over to $\pi_0(Z)$. If Z is an H-space, H-group, or commutative H-group, then $\pi(Z)$ is a monoid, group, or commutative group respectively.

Example 2. Infinite Grassmannian.

Let $\mathrm{Gr}_n(\mathbb{C}^\infty)$ be the limit of the sequence

$$\mathrm{Gr}_n(\mathbb{C}^n) \subset \mathrm{Gr}_n(\mathbb{C}^{n+1}) \subset \mathrm{Gr}_n(\mathbb{C}^{n+2}) \subset \cdots . \tag{3.1}$$

($\mathrm{Gr}_n(\mathbb{C}^\infty)$ is homotopy equivalent to $BU(n)$.) We represent an element of $\mathrm{Gr}_n(\mathbb{C}^\infty)$ as an $m \times m$ idempotent[5] hermitian matrix P with trace equals to n. The inclusion map is performed by padding zeros to the bottom and right of the matrix.

We let M be the disjoint union of $\mathrm{Gr}_n(\mathbb{C}^\infty)$ for all integers $n \geq 0$. For $X, Y \in M$, define $\mu(a, b)$ as 'interlacing' the matrices where the elements $\mu(X, Y)_{2a-1,2b-1} = X_{a,b}$ and $\mu(X, Y)_{2a,2b} = Y_{a,b}$, and zero otherwise. (If a or b is larger than the size of the matrix, assume

---

[5] An idempotent matrix P satisfies $P^2 = P$.

the matrix element is zero.) Pictorially, the construction is as follows:

$$\mu(X,Y)_{a,b} = \begin{bmatrix} X_{11} & & X_{12} & & \cdots & \\ & Y_{11} & & Y_{12} & & \cdots \\ X_{21} & & X_{22} & & \cdots & \\ & Y_{21} & & Y_{22} & & \cdots \\ \vdots & & \vdots & & \ddots & \\ & \vdots & & \vdots & & \ddots \end{bmatrix}.$$

The size of $\mu(X,Y)$ would be $2m \times 2m$, where m is the dimension of the larger matrix. The identity element is the zero matrix in $\mathrm{Gr}_0(\mathbb{C}^\infty)$.

Define $G_{\mathbb{C}}$ to be the set of pairs (X,Y), where $X, Y \in M$, and with the identification $(X,Y) \sim (AX, AY)$ for any A. The identity is (e,e) (or (A,A)). Composition and inverse are defined as

$$\mu\big((A,B),(C,D)\big) = \big(\mu(A,C), \mu(B,D)\big)\,, \qquad (A,B)^{-1} = (B,A)\,. \tag{3.2}$$

Proposition. $G_{\mathbb{C}}$ is a commutative H-group.

Proof. This is relatively straightforward to show, albeit tedious.

- Commutativity. It suffices to show that M satisfies criteria 5 for an H-group. Let A, B be $m \times m$ matrices in M, then $C = \mu(A,B)$ and $C' = \mu(B,A)$ are $2m \times 2m$ matrices.[6] C and C' are related by a unitary transformation $C' = WCW^\dagger$ (with $WW^\dagger = \mathbb{1}_{2m}$), where $W_{2a,2a-1} = -W_{2a-1,2a} = 1$ for $1 \leq a \leq m$, and zero otherwise. In matrix form:

  $$W = \begin{bmatrix} & -1 & & & \\ 1 & & & & \\ & & & -1 & \\ & & 1 & & \\ & & & & \ddots \end{bmatrix}.$$

  We can see that conjugation by W simply swaps the even and odd rows. Since $W \in U(2m)$, which is a connected space, we can deform W to the identity $\mathbb{1}_{2m}$, which gives us the homotopy between C and C'.[7]

- Properties of identity. It suffices to show that M satisfies criteria 2 for an H-group. Let X be an $m \times m$ matrix in M, then $X' = \mu(e, X)$ is a $2m \times 2m$ matrix, related to the original matrix by $X'_{2a,2b} = X_{a,b}$. We construct a series of homotopies $W_{(n)}(t)$ where $W_{(n)}(0)$ is the identity matrix, and $W_{(n)}(1)$ swaps rows (and columns) n with

---

[6] If A and B have different sizes, one can pad the smaller one with zeros until they are of the same size.

[7] For example, we can use $W_2 = \left[\begin{smallmatrix} \cos\theta & -\sin\theta \\ \sin\theta & \cos\theta \end{smallmatrix}\right]$ where $\theta = \pi t/2$ for each 2×2 subblock of W. It is important to note that the homotopy does not depend on C or C'.

$2n$, similar to the case before. Applying the homotopies $W_{(1)}$, $W_{(2)}$, ... takes $\mu(e, X)$ back to X. We chain the homotopies together by performing the n^{th} one in the interval $[1/2^n, 1/2^{n-1}]$. Each point in M lies in some finite Grassmannian $\mathrm{Gr}_n(\mathbb{C}^{n+m})$ which is eventually stationary in the infinite chain of homotopies.

- Associativity. Let $A, B, C \in M$. $\mu(\mu(A, B), C)$ and $\mu(A, \mu(B, C)$ have the same elements, but with its rows (and columns) swapped. The rows with $a = 1, 2, 3, \ldots$ of the former corresponds to rows $1, 4, 2, 8, 3, 12, 5, \ldots$ in the latter matrix. We can construct W to be an appropriate permutation matrix that takes one form to the other.
- Inverse. For $(A, B) \in G_{\mathbb{C}}$. We have (AB, BA) is homotopic (by commutativity) to $(AB, AB) \sim e$. □

In this construction, (M, μ) satisfies the properties of a commutative monoid[8] up to homotopy. The group composition μ is very much similar to a direct sum ($\oplus$) applied on vector bundles. Physically, the matrix-valued function $P(\mathbf{k})$ captures a flattened band structure, where P is a projector on to the filled states. From this viewpoint, the composition $\mu(P, P')$ formalizes the concept of combining band structures.

Here we have define $G_{\mathbb{C}}$ to be the "Grothendieck group" of M, allowing inverses to be defined. In general, the Grothendieck group of a commutative monoid $(M, +)$ are formally pairs of elements $(x, y) \in M \times M$ with the identification $(z + x, z + y) \sim (x, y)$. Intuitively, (x, y) describes the object $x - y$. For example, the Grothendieck group for the nonzero integers under multiplication $(\mathbb{Z} - \{0\}, \times)$ gives the fractions $\mathbb{Q}$.

As it turns out, $G_{\mathbb{C}}$ is homotopy equivalent to "the classifying space" $\mathbb{Z} \times BU$. The integer $\mathbb{Z}$ can be interpreted as the quantity $(\operatorname{Tr} A - \operatorname{Tr} B)$ for the pair $A, B \in G_{\mathbb{C}}$, physically, it describes the number of filled bands.

Example 3. Unitary groups.

Let $\mathcal{S}_n$ be a $2n \times 2n$ matrix with $1, -1, 1, -1, \ldots$ along its diagonal, and zeros elsewhere. Let M_n be the set of $2n \times 2n$ hermitian matrices which *anticommutes* with $\mathcal{S}_n$ and squares to the identity,[9] that is,

$$M_n \equiv \left\{ X \in \mathbb{C}^{2n \times 2n} \,\middle|\, X^\dagger = X, X^2 = \mathbb{1}_{2n}, X\mathcal{S}_n + \mathcal{S}_n X = \mathbf{0} \right\}. \tag{3.3}$$

Define the inclusion may $M_n \to M_{n+1}$ by taking a matrix X by padding two rows of zeros below, two columns of zeros to the right, and the matrix $\left[\begin{smallmatrix} 0 & 1 \\ 1 & 0 \end{smallmatrix}\right]$ at the bottom right. Pictorially,

$$X \mapsto \begin{bmatrix} & & & 0 & 0 \\ & X & & \vdots & \vdots \\ & & & 0 & 0 \\ 0 & \cdots & 0 & 0 & 1 \\ 0 & \cdots & 0 & 1 & 0 \end{bmatrix}.$$

---

[8] A monoid is a group without the invertibility requirement.

[9] We note that M_n is homeomorphic to $U(n)$. Also, the entries of the matrix $X \in M_n$ has $X_{a,b} = 0$ if $a + b \equiv 0 \pmod 2$.

Let M be the limit of the sequence

$$M_0 \subset M_1 \subset \cdots \ . \tag{3.4}$$

Define the composition map μ in the same manner as in Ex. 2, but in blocks of twos. The picture is

$$\mu(X,Y) = \left[\begin{array}{cccccccccc}
X_{11} & X_{12} & & & X_{13} & X_{14} & & & \cdots & \\
X_{21} & X_{22} & & & X_{23} & X_{24} & & & & \\
& & Y_{11} & Y_{12} & & & Y_{13} & Y_{14} & & \cdots \\
& & Y_{21} & Y_{22} & & & Y_{23} & Y_{24} & & \\
X_{31} & X_{32} & & & X_{33} & X_{34} & & & \cdots & \\
X_{41} & X_{42} & & & X_{43} & X_{44} & & & & \\
& & Y_{31} & Y_{32} & & & Y_{33} & Y_{34} & & \cdots \\
& & Y_{41} & Y_{42} & & & Y_{43} & Y_{44} & & \\
\vdots & & & & \vdots & & & & \ddots & \\
& & \vdots & & & & \vdots & & & \ddots
\end{array}\right] . \tag{3.5}$$

The identity element is the matrix in M_0.

Once again, we define U as the set of pairs $(X, Y) \in M \times M$ with the identification $(X, Y) \sim (AX, AY)$. We also define composition and inverse the exact same way as in the previous example [see Eq. (3.2)].

The spaces $\mathbb{Z} \times BU$ and U have been well-studied in context of topological K-theory. The bundle $\mathbb{Z} \times EU \to \mathbb{Z} \times BU$ classifies complex vector bundle, up to stable isomorphism, in the same manner that $EU(n) \to BU(n)$ classifies n-dimensional vector bundles. Their homotopy groups are given in Tab. 3.1. For example, $\pi_n(\mathbb{Z} \times BU)$ are the stable homotopy groups π_n^s of the complex Grassmannians $[\mathrm{Gr}_N(\mathbb{C}^{N+M})]$.

Via similar constructions to Ex. 2 and Ex. 3, we can define a number of infinite symmetric spaces associated with KO-theory. For example, restricting Ex. 2 to real numbers, gives $G_{\mathbb{R}}$ which is homotopic to $\mathbb{Z} \times BO$. The quaternion analogue yields $G_{\mathbb{H}} \approx \mathbb{Z} \times BSp$ (*cf.* Ex. 19).

Example 4. Loop spaces.

Given a pointed space (X, x_0), the loop space ΩX is an H-group. Representing an element of ΩX as $f(x)$, we define the following.

- The identity is the loop $f(x) = x_0$.
- Composition of loops f, g is given by $\mu(f, g)(x) = \begin{cases} f(2x) & x \leq 1/2 \\ g(2x-1) & x \geq 1 \end{cases}$.
- Inverse of $f(x)$ is given by reversal of the loop: $f(1-x)$.

It is straightforward to show that ΩH satisfies the properties of an H-group.

Definition 5. Let d be a positive integer. Define the "Brillouin zone" BZ^d be a topological space $(\mathbb{R}/2\pi\mathbb{Z})^d$. $\mathbb{R}/2\pi\mathbb{Z}$ is the quotient space where points $x \sim x + 2\pi$ are identified.

	d	π_m stable for $m \leq \dots$	π_0^s	π_1^s	π_2^s	π_3^s	π_4^s	π_5^s	π_6^s	π_7^s
$U(N)$	N^2	$2N-1$		$\mathbb{Z}$		$\mathbb{Z}$		$\mathbb{Z}$		$\mathbb{Z}$
$\mathbb{Z} \times \mathrm{Gr}_N(\mathbb{C}^{M+N})$	$2MN$	$2M, 2N$	$\mathbb{Z}$		$\mathbb{Z}$		$\mathbb{Z}$		$\mathbb{Z}$	
$O(N)$	$\frac{N(N-1)}{2}$	$N-2$	$\mathbb{Z}_2$	$\mathbb{Z}_2$		$\mathbb{Z}$				$\mathbb{Z}$
$\mathbb{Z} \times \mathrm{Gr}_N(\mathbb{R}^{M+N})$	MN	$M-1, N-1$	$\mathbb{Z}$	$\mathbb{Z}_2$	$\mathbb{Z}_2$		$\mathbb{Z}$			
$\frac{U(N)}{O(N)}$	$\frac{N(N+1)}{2}$	$N-1$		$\mathbb{Z}$	$\mathbb{Z}_2$	$\mathbb{Z}_2$		$\mathbb{Z}$		
$\frac{Sp(N)}{U(N)}$	$N(N+1)$	$2N$			$\mathbb{Z}$	$\mathbb{Z}_2$	$\mathbb{Z}_2$		$\mathbb{Z}$	
$Sp(N)$	$N(2N+1)$	$4N+1$				$\mathbb{Z}$	$\mathbb{Z}_2$	$\mathbb{Z}_2$		$\mathbb{Z}$
$\mathbb{Z} \times \mathrm{Gr}_N(\mathbb{H}^{M+N})$	$4MN$	$4M+2, 4N+2$	$\mathbb{Z}$				$\mathbb{Z}$	$\mathbb{Z}_2$	$\mathbb{Z}_2$	
$\frac{U(2N)}{Sp(N)}$	$N(2N-1)$	$4N-1$		$\mathbb{Z}$				$\mathbb{Z}$	$\mathbb{Z}_2$	$\mathbb{Z}_2$
$\frac{O(2N)}{U(N)}$	$N(N-1)$	$2N-2$	$\mathbb{Z}_2$		$\mathbb{Z}$				$\mathbb{Z}$	$\mathbb{Z}_2$

Table 3.1: Table of stable homotopy groups.

The first column denotes a series of topological spaces $X(N)$ (or $X(N,M)$) for various N (and M), the second column d denotes the dimensionality of the manifold. These sequences have stable homotopy groups, that is, for sufficiently large N (and M), the inclusion $X(N) \to X(N+1)$ (or $X(N,M) \to X(N,M+1)$) induces an isomorphism in π_m. Blank entries denote the trivial group. For the first two rows, Bott periodicity implies that the stable homotopy groups π_m is isomorphic to π_{m-2} for $m \geq 2$. For the latter rows, π_m is isomorphic to π_{m-8} (for $m \geq 8$).

We can use the coordinate system $\mathbf{k} = (k_1, \dots, k_d)$ to describe a point in BZ^d. It is understood that $\mathbf{k} \sim \mathbf{k} + 2\pi(n_1, \dots, n_d)$ for integers $n_1, \dots, n_d$. For consistency, we define BZ^0 to be a single point. Furthermore, we define the map $-\mathbf{1}_{\mathbf{k}} : BZ^d \to BZ^d$ be the map that takes $\mathbf{k} \mapsto -\mathbf{k}$. Note that this map has 2^d fixed points, where $k_a = 0$ or π for all a, these points are referred to as *time-reversal invariant momenta* (TRIMs).[10]

Definition 6. Let $\mathcal{H}_0$ be a commutative H-group. A d-dimensional *band structure* is a map $H : BZ^d \to \mathcal{H}_0$.

Here $\mathcal{H}_0$ is thought of as the space of 0D Hamiltonians. It is convenient to talk about the set of all band structures as a topological space. (In the text to follow, we will standard

---

[10] For some reason we don't call them "inversion invariant momenta." The first use of the term "TRIM" may have been Ref. [4].

notation ab to denote group composition $\mu(a,b)$. For a series of compositions, we will use the convention of left-to-right, *e.g.*, $abcd = ((ab)c)d$.)

Definition 7. Define $\mathcal{H}_d$ as the set of all d-dimensional band structures, with compact-open topology. Group composition is defined in a pointwise manner: given $H, H' \in \mathcal{H}_d$, $HH'(\mathbf{k}) = H(\mathbf{k})H'(\mathbf{k})$.

With this definition, the classification of d-dimensional band insulators is equivalent to finding discrete pieces of $\mathcal{H}_d$, or $\pi_0(\mathcal{H}_d)$. Note that $\mathcal{H}_d$ being an H-group endows π_0 with a group structure.

Theorem 8. $\mathcal{H}_d$ is homotopic to the Cartesian product

$$\mathcal{H}_0 \times (\Omega\mathcal{H}_0)^d \times (\Omega^2\mathcal{H}_0)^{\binom{d}{2}} \times \cdots \times (\Omega^d\mathcal{H}_0) \,.$$

(Here $\binom{d}{n}$ is a binomial coefficient, and Ω is the loop space functor.) Taking π_0 of both sides gives us the following relation.

$$\pi_0(\mathcal{H}_d) \cong \pi_0(\mathcal{H}_0) \times \pi_1(\mathcal{H}_0)^d \times \pi_2(\mathcal{H}_0)^{\binom{d}{2}} \times \cdots \times \pi_d(\mathcal{H}_0) \,. \tag{3.6}$$

The factors $\binom{d}{n}$ arises from the cellular decomposition of a d-torus: if we construct a T^d by taking a d-cube I^d and identifying opposite $(n-1)$-faces together, then there are exactly $\binom{d}{n}$ n-cells. Physically, we can interpret $\pi_d(\mathcal{H}_d)$ as the "strong" topological index, and the remaining ones as "weak" indices which are constructed from lower dimensional objects.

Before we prove the theorem, it is useful to define $\tilde{\mathcal{H}}_d$.

Definition 9. Denote v_0 as the identity element of $\mathcal{H}_0$. Define $\tilde{\mathcal{H}}_0$ to be $\mathcal{H}_0$. For $d > 0$, define $\tilde{\mathcal{H}}_d$ to be the sub-H-group of $\mathcal{H}_d$ such that $H(\mathbf{k}) = v_0$ whenever *any one* of the components of $\mathbf{k}$ is zero. Define the basepoint $v_d \in \tilde{\mathcal{H}}_d$ as the constant map to v_0.

It is straightforward to see that $\tilde{\mathcal{H}}_d$ is equivalent to the set of maps $I^d \to \mathcal{H}_0$ with the restriction that ∂I^d must map to v_0. The following statement is trivial.

Proposition 10. $\tilde{\mathcal{H}}_d$ is isomorphic $\Omega^d\mathcal{H}_0$.

Proof of Theorem 8. Consider the cellular decomposition of BZ^d where there is a cell for each subset of the coordinates $\{k_1, k_2, \ldots, k_d\}$, and for each subset of coordinates $c = \{k_{c_1}, k_{c_2}, \ldots, k_{c_n}\}$, the n-cell e_c lives in the plane where $k_i = 0$ for each k_i not in c. (*I.e.*, e_c is completely described by the coordinates c, and contains the origin $(0, \ldots, 0)$.) Hence there is a 0-cell corresponding to the empty set $\{\}$, $\binom{d}{n}$ n-cells corresponding to the sets with n coordinates, for a total of 2^d cells. Denote the n-skeleton (union of all m-cells with $m \leq n$) as A^n. We define the 'boundary' of the n-cell e_c as its intersection with A^{n-1}.[11]

---

[11] Technically the cells as defined here have no actual boundaries, because $0 \sim 2\pi$ by construction of BZ^d.

Let $H(\mathbf{k})$ be an element of $\mathcal{H}_d$. We decompose $H(\mathbf{k})$ as a product of $h_c(\mathbf{k}) \in \mathcal{H}_d$, one for each cell e_c, as follows.[12]

$$H \sim \left(h_{\{\}}\right)\left(h_{k_1} h_{k_2} \cdots h_{k_d}\right)\left(h_{k_1,k_2} h_{k_1,k_3} \cdots h_{k_{d-1},k_d}\right) \cdots \left(h_{k_1,k_2,\dots,k_d}\right) . \tag{3.7}$$

The first term corresponds to the 0-cell, terms in the second set of parentheses corresponds to 1-cells, *etc.* Within each set of parentheses we place the terms in lexicological order. We also impose the constraints:

1. For each cell e_c, $h_c(\mathbf{k})$ is independent of the coordinates k_i which are not in c.
2. $h_c(\mathbf{k})$ restricted to the 'boundary' of e_c is v_0 (identity of $\mathcal{H}_0$).

For example, $h_{\{\}}(\mathbf{k})$ is a constant map, $h_{k_1}(\mathbf{k})$ is a function of k_1 only, with $h_{k_1}(0, k_2, \dots) = v_0$, *etc.* This construction yields the property, that for each n-cell e_c, the restriction $h_c|_{e_c}$ completely determines h_c on the entire BZ^d. However, restricting h_c to e_c gives an element of $\tilde{\mathcal{H}}_n$, and so Eq. (3.7) provides the map

$$\tilde{\mathcal{H}}_0 \times \tilde{\mathcal{H}}_1^d \times \tilde{\mathcal{H}}_2^{\binom{d}{2}} \times \cdots \times \tilde{\mathcal{H}}_d \xrightarrow{\phi} \mathcal{H}_n . \tag{3.8}$$

We now argue that decomposition (3.7) is always possible, constructing a map $\mathcal{H}_n$ to the product of $\tilde{\mathcal{H}}_n$'s. Let $H_{(n)}(\mathbf{k})$ be a partial product of Eq. (3.7), where we only keep the first $(n+1)$ parentheses. First, we let $h_{\{\}}(\mathbf{k}) = H_{(0)}(\mathbf{k}) = H(0, \dots, 0)$, and then proceed inductively on the skeletons A^n.

Suppose that, in restricting to the $(n-1)$-skeleton, $H_{(n-1)}|_{A^{n-1}}$ is homotopic to $H|_{A^{n-1}}$. For each n-cell e_c, we let $h_c|_{e_c}$ be homotopy equivalent to $H_{(n-1)}^{-1}|_{e_c} H|_{e_c}$, where the restriction to the 'boundary' of e_c is v_0. This defines h_c (up to homotopy) over all of BZ^d, and guarantees that the partial product $H_{(n)}|_{A^n}$ is homotopic to $H|_{A^n}$. Repeating this process, h_c is well-defined for all cells, which gives us the map

$$\mathcal{H}_d \xrightarrow{\psi} \tilde{\mathcal{H}}_0 \times \tilde{\mathcal{H}}_1^d \times \tilde{\mathcal{H}}_2^{\binom{d}{2}} \cdots \times \tilde{\mathcal{H}}_d . \tag{3.9}$$

The compositions $\phi\psi$ takes $H(\mathbf{k})$ and returns $H_*(\mathbf{k})$ which is homotopic to it (and similarly for $\psi\phi$ acting on $h_c(\mathbf{k})$'s). This establishes an isomorphism between π_0 of each side of (3.9) above, and hence proves Eq. (3.6). To proof the stronger statement in the theorem, we can show that $\phi\psi$ and $\psi\phi$ induces an automorphism on all homotopy groups as follows. Take $H(x, \mathbf{k})$ as a map $S^m \to \mathcal{H}_d$, where $x \in S^m$. Repeat the existing argument, replacing e_c and A^n with $S^m \times e_c$ and $S^m \times A^n$ respectively. This shows that homotopy classes of maps $S^m \to \mathcal{H}_d$ are equivalent to that of $S^m \to \tilde{\mathcal{H}}_0 \times \cdots \times \tilde{\mathcal{H}}_d$ for all m, and the desired result follows from the Hurewicz Theorem. □

With Thm. 8, we can compute the topological invariants for two symmetry classes. Table 3.2 gives some possible symmetry classes and their invariants. The table is by no means exhaustive, but captures some likely symmetries found in physical systems. (At least those without too much fine tuning.) Of the classes listed, their Hamiltonian space $\mathcal{H}_0$ determines all the topological invariants in all dimensions.

---

[12] Note that $h_c(\mathbf{k})$ lives on the entire BZ^d, not just on e_c.

Symmetry class	Symmetries present	$\mathcal{H}_0$	$\pi_d(\mathcal{H}_0)$			
			π_0	π_1	π_2	π_3
Unitary (A)	$\varnothing$ (None)	$\mathbb{Z} \times BU$	$\mathbb{Z}$		$\mathbb{Z}$	
Chiral (AIII)	$\mathcal{S}$	U		$\mathbb{Z}$		$\mathbb{Z}$
Inversion · TR	$\Pi\Theta_{-1}$	$\mathbb{Z} \times BSp$	$\mathbb{Z}$			
Inversion · TR	$\Pi\Theta_{+1}$	$\mathbb{Z} \times BO$	$\mathbb{Z}$	$\mathbb{Z}_2$	$\mathbb{Z}_2$	

Table 3.2: Topological invariants for symmetry classes without BZ symmetries.

The first two rows belong in the Altland-Zirnbauer classification [76], while the latter rows required lattice symmetries (*i.e.*, inversion). The operators $\mathcal{S}$, Π, Θ are the sublattice, inversion, and time-reversal symmetries respectively. (*E.g.*, $\Pi\Theta_{-1}$ denotes that the combination of inversion and time-reversal (squaring to -1) is present, but not separately. This might be applicable to certain types of magnetic materials with zero net-magnetization.) The column π_0, π_1, *etc.* gives the strong topological invariants found in 0-, 1-, *etc.* dimensions. (Blank entries denote the trivial group.)

3.2 Classification with Brillouin zone symmetries

We now turn our attention to band structures with additional constraints. These constraints are 'nonlocal' in the sense that they impose constraints between Hs at different points $\mathbf{k}$ and $-\mathbf{k}$.

Definition 11. Let $\mathcal{H}_0$ be a commutative H-group and $\mathcal{T} : \mathcal{H}_0 \to \mathcal{H}_0$ be an automorphism with $\mathcal{T}^2 = \mathbf{1}_{\mathcal{H}_0}$ is the identity. A d-dimensional *band structure respecting* $\mathcal{T}$ is a map $H : BZ^d \to \mathcal{H}_0$, such that

$$H(-\mathbf{k}) = \mathcal{T} H(\mathbf{k})\,. \tag{3.10}$$

Definition 12. Given the H-group $\mathcal{H}_0$ and the map $\mathcal{T}$, define $\mathcal{I}_d$ for $d > 0$ as the set of all d-dimensional band structures respecting $\mathcal{T}$, with compact-open topology. Composition is defined in a pointwise manner: given $H, H' \in \mathcal{H}_d$, $HH'(\mathbf{k}) = H(\mathbf{k})H'(\mathbf{k})$. Define $\mathcal{I}_0$ as the sub-H-group of $\mathcal{H}_0$ which is invariant under $\mathcal{T}$.

Our goal is to be able to say for each $(\mathcal{H}_0, \mathcal{T})$, what band structures can and cannot be deformed to one another, *i.e.*, compute $\pi_0(\mathcal{I}_d)$. Similar to the case without $\mathcal{T}$, we define $\tilde{\mathcal{I}}_d$ as a subset of the spaces $\mathcal{I}_d$. Again, they describe maps from S^d to $\mathcal{H}_0$ (subject to symmetry $\mathcal{T}$) rather than from BZ^d. The separation into "strong" and "weak" topological indices also carries over to the case with Brillouin zone symmetries, the precise meaning of this is made clear in Thm. 14.

Definition 13. Define $\tilde{\mathcal{I}}_d$ to be the intersection of $\tilde{\mathcal{H}}_d$ and $\mathcal{I}_d$ for all $d \geq 0$. Define $i^d : \tilde{\mathcal{I}}_d \to \tilde{\mathcal{H}}_d$ as the inclusion map.

Hence we have $\tilde{\mathcal{I}}_0 = \mathcal{I}_0$. For $d > 0$, an element $H \in \tilde{\mathcal{I}}_d$ satisfies $H(\mathbf{k}) = v_0$ whenever any component of $\mathbf{k}$ is zero, in addition to (3.10). Similar to before, $\tilde{\mathcal{I}}_d$ may be thought of as maps $(2\pi I)^d \to \mathcal{H}_0$ subject to constraints $\partial(2\pi I)^d \mapsto v_0$ and $H\big((2\pi, 2\pi, \ldots, 2\pi) - \mathbf{k}\big) = \mathcal{T} H(\mathbf{k})$.

Theorem 14. $\mathcal{I}_d$ is homotopic to the Cartesian product

$$\tilde{\mathcal{I}}_0 \times \tilde{\mathcal{I}}_1^d \times \tilde{\mathcal{I}}_2^{\binom{d}{2}} \times \cdots \times \tilde{\mathcal{I}}_d \,.$$

In addition, the following is a group isomorphism.

$$\pi_0(\mathcal{I}_d) \cong \pi_0(\tilde{\mathcal{I}}_0) \times \pi_0(\tilde{\mathcal{I}}_1)^d \times \pi_0(\tilde{\mathcal{I}}_2)^{\binom{d}{2}} \times \cdots \times \pi_0(\tilde{\mathcal{I}}_d) \,. \tag{3.11}$$

The proof is identical to that of Thm. 8, with the addition check that each term in the decomposition (3.7) respects (3.10).[13]

Theorem 15. $\pi_n(\tilde{\mathcal{I}}_d)$ is isomorphic to the relative homotopy group $\pi_{n+1}(\tilde{\mathcal{H}}_{d-1}, \tilde{\mathcal{I}}_{d-1})$.

Proof. Let $A, B \subset X$. Denote $\mathfrak{P}(X, A, B)$ as the space of paths in X from A to B, that is,

$$\mathfrak{P}(X, A, B) \equiv \{f : I \to X \mid f(0) \in A, f(1) \in B\} \,. \tag{3.12}$$

An element $H(\mathbf{k}) \in \tilde{\mathcal{I}}_d$ can be characterized as a path in $\tilde{\mathcal{H}}_{d-1}$.

$$f_t(k_2, \ldots, k_d) = H(\pi t, k_2, \ldots, k_d) \,,$$

for $t \in I$. It suffices to only describe H for half the Brillouin zone $k_1 \in [0, \pi]$ as the other half is related by $\mathcal{T}$. At $t = 0$, $f_0(k_2, \ldots) = v_0$. At $t = 1$, $f_1(k_2, \ldots) = H(\pi, k_2, \ldots, k_d) = \mathcal{T} H(\pi, -k_2, \ldots, -k_d)$. Hence, $\tilde{\mathcal{I}}_d$ is homeomorphic to $\mathfrak{P}(\tilde{\mathcal{H}}_{d-1}, v_{d-1}, \tilde{\mathcal{I}}_{d-1})$ as a topological space.

Consider a map $f : (I^n, \partial I^n) \to (\tilde{\mathcal{I}}_d, v_d)$. Seeing that elements of $\tilde{\mathcal{I}}_d$ can be represented as paths $I \to \tilde{\mathcal{H}}_{d-1}$, f can be recast as a map $I^n \times I \to \tilde{\mathcal{H}}_{d-1}$ subject to the following constraints.

- $\partial I^n \times I$ maps to v_{d-1}.
- $I^n \times \{0\}$ maps to v_{d-1}.
- $I^n \times \{1\}$ maps to $\tilde{\mathcal{I}}_{d-1}$.

The set of f is then equivalent to maps $(I^{n+1}, \partial I^{n+1}, J^n) \to (\tilde{\mathcal{H}}_{d-1}, \tilde{\mathcal{I}}_{d-1}, v_{d-1})$, where J^n is the closure of $\partial I^{n+1} - I^n \times \{1\}$. Therefore, the homotopy classes $\pi_n(\tilde{\mathcal{I}}_d)$ and $\pi_{n+1}(\tilde{\mathcal{H}}_{d-1}, \tilde{\mathcal{I}}_{d-1})$ are equivalent. □

---

[13] Note that in the proof of Thm. 8, the cells e_c and their 'boundaries' are invariant under $-\mathbf{1}_k : \mathbf{k} \mapsto -\mathbf{k}$.

With this equivalence, we have the long exact sequence. (Refer to Sec. 4.2.4 for a detailed explanation of this exact sequence.)

$$\cdots \longrightarrow \pi_{n+1}(\tilde{\mathcal{I}}_d) \xrightarrow{i^d_*} \pi_{n+1}(\tilde{\mathcal{H}}_d) \xrightarrow{j^d_*} \pi_n(\tilde{\mathcal{I}}_{d+1}) \xrightarrow{\partial_*} \pi_n(\tilde{\mathcal{I}}_d) \xrightarrow{i^d_*} \pi_n(\tilde{\mathcal{H}}_d) \longrightarrow \cdots \,. \tag{3.13}$$

Here $j^d : \Omega\tilde{\mathcal{H}}^d \to \tilde{\mathcal{I}}_{d+1}$, a map which takes a loop in $\tilde{\mathcal{H}}_d$ to a path in $\tilde{\mathcal{I}}_{d+1} \simeq \mathfrak{P}(\tilde{\mathcal{H}}_d, v_d, \tilde{\mathcal{I}}_d)$ in a straightforward manner. j^d_* is the induced map from $\pi_{n+1}(\tilde{\mathcal{H}}_d) = \pi_n(\tilde{\mathcal{H}}_{d+1})$ to $\pi_n(\tilde{\mathcal{I}}_{d+1})$. The boundary map $\partial : \tilde{\mathcal{I}}_{d+1} \to \tilde{\mathcal{I}}_d$ takes a path and gives the endpoint at $t = 1$, with ∂_* the induced map for the homotopy groups.

Definition 16. Define the map $\mathcal{T}^d : \tilde{\mathcal{H}}_d \to \tilde{\mathcal{H}}_d$ as $\mathcal{T}^d : H(\mathbf{k}) \mapsto \mathcal{T}H(-\mathbf{k})$.

$\mathcal{T}^0$ is simply $\mathcal{T}$ restricted to $\tilde{\mathcal{H}}_0$, while $\tilde{\mathcal{I}}_d$ is the subgroup of $\tilde{\mathcal{H}}_d$ invariant under $\mathcal{T}^d$. $\mathcal{T}^d$ induces an automorphism in the homotopy groups $\pi_n(\tilde{\mathcal{H}}_d)$. We have the following diagram.[14]

$$\begin{tikzcd}
\pi_{n+1}(\tilde{\mathcal{H}}_d) \arrow[r, "\cong"] \arrow[d, "-\mathcal{T}^d_*"'] & \pi_n(\tilde{\mathcal{H}}_{d+1}) \arrow[d, "\mathcal{T}^{d+1}_*"] \\
\pi_{n+1}(\tilde{\mathcal{H}}_d) \arrow[r, "\cong"] & \pi_n(\tilde{\mathcal{H}}_{d+1})
\end{tikzcd} \tag{3.14}$$

The isomorphism between $\pi_{n+1}(\tilde{\mathcal{H}}_d)$ and $\pi_n(\tilde{\mathcal{H}}_{d+1})$ is induced by identifying maps $(I^n \times I) \to \tilde{\mathcal{H}}_d$ with $I^n \to (I \to \tilde{\mathcal{H}}_d)$.

Proposition 17. The diagram (3.14) is commutative.

Proof. Let $f : I^{n+1} \to \tilde{\mathcal{H}}_d$ and $f' : I^n \to \tilde{\mathcal{H}}_{d+1}$. Represent f and f' as a function

$$f(x_1, \ldots, x_{n+1}; k_1, \ldots, k_d) \in \mathcal{H}_0 \,,$$
$$f'(x_1, \ldots, x_n; k_1, \ldots, k_{d+1}) \in \mathcal{H}_0 \,.$$

Both functions takes in $n + d + 1$ parameters, with a different location of the semicolon. Application of $\mathcal{T}^d$ on f flips d variables, while application of $\mathcal{T}^{d+1}$ flips $d+1$ variables, hence the two induced maps on the homotopy groups are related by a negation. $\square$

Proposition 18. The following diagram commutes

$$\begin{tikzcd}
\Omega\tilde{\mathcal{H}}_d \arrow[r, "j^d"] \arrow[dr, "\mathbf{1}_{\tilde{\mathcal{H}}} \circ (\mathcal{T}^d)^{-1}"'] & \tilde{\mathcal{I}}_{d+1} \arrow[d, "i^{d+1}"] \\
& \tilde{\mathcal{H}}_{d+1}
\end{tikzcd} \tag{3.15}$$

---

[14] The homotopy groups $\pi_{n+1}(\tilde{\mathcal{H}}_d)$ and $\pi_n(\tilde{\mathcal{H}}_{d+1})$ are both abelian. $-\mathcal{T}^d_*$ means applying $\mathcal{T}^d_*$ followed by taking the group inverse.

The unconventional use of symbols require an explanation. $\mathbf{1}_{\tilde{\mathcal{H}}}$ and $\mathcal{T}^d$ denotes maps in the space $\tilde{\mathcal{H}}_d$, and is applied pointwise to $\Omega\tilde{\mathcal{H}}_d$. The composition $\circ$ and inverse $()^{-1}$ is applied as loops, as defined in Ex. 4.

Proof. We represent an element of $\tilde{\mathcal{I}}_{d+1}$ as a path in $\mathfrak{P}(\tilde{\mathcal{H}}_d, v_d, \tilde{\mathcal{I}}_d)$, it is important to note that this representation only captures half of the Brillouin zone, with the other half related by $\mathcal{T}^d$. Elements of $\Omega\tilde{\mathcal{H}}_d$, $\tilde{\mathcal{I}}_{d+1}$, and $\tilde{\mathcal{H}}_{d+1}$ are of the form:

$$f(x; k_1, \ldots, k_n) \xmapsto{j^d} g(t; k_1, \ldots, k_n) \xmapsto{i^{d+1}} h(k_1, \ldots, k_{n+1}) \quad .$$

(Each function as written produces an element of $\mathcal{H}_0$.) The map j^d does not alter the function, but simply relabels x as t. The map $i^{d+1} : g \mapsto h$ takes two copies of the path g to form a loop h:

$$h(k_1, k_2, \ldots, k_{n+1}) = \begin{cases} g(\frac{k_1}{\pi}; k_2, \ldots, k_{n+1}) & k \in [0, \pi] \\ \mathcal{T}g(2 - \frac{k_1}{\pi}; -k_2, \ldots, -k_{n+1}) & k \in [\pi, 2\pi] \end{cases} ,$$

the expression for the second case may be written as $\mathcal{T}^d g(2 - \frac{k_1}{\pi})$. In words: $i^{d+1} \circ j^d$ takes a loop f and gives $f(x)$ glued to $\mathcal{T}^d f(x)$ running backwards. □

The induced maps of diagram (3.15) gives the simple expression:

$$i^{d+1}_* \circ j^d_* = 1 - \mathcal{T}^d_* \tag{3.16}$$

Equations (3.14) and (3.16) gives us a prescription to compute $\mathcal{T}^{d+1}_*$ and i^{d+1}_* recursively. We can chain all the exact sequences (3.13) together to get the following "staircase" diagram.

$$\begin{tikzcd}
\ddots & \vdots \arrow[d] & \vdots & \vdots \arrow[d] & \vdots & \vdots \arrow[d] & \vdots \\
\cdots \arrow[r] & \pi_2(\tilde{\mathcal{I}}_1) \arrow[r, "i^1_*"] \arrow[d, "\partial_*"] & \pi_2(\tilde{\mathcal{H}}_1) \arrow[r, "j^1_*"] & \pi_1(\tilde{\mathcal{I}}_2) \arrow[r, "i^2_*"] \arrow[d, "\partial_*"] & \pi_1(\tilde{\mathcal{H}}_2) \arrow[r, "j^2_*"] & \pi_0(\tilde{\mathcal{I}}_3) \arrow[r, "i^3_*"] \arrow[d, "\partial_*"] & \pi_0(\tilde{\mathcal{H}}_3) \\
 & \pi_2(\tilde{\mathcal{I}}_0) \arrow[r, "i^0_*"] & \pi_2(\tilde{\mathcal{H}}_0) \arrow[r, "j^0_*"] & \pi_1(\tilde{\mathcal{I}}_1) \arrow[r, "i^1_*"] \arrow[d, "\partial_*"] & \pi_1(\tilde{\mathcal{H}}_1) \arrow[r, "j^1_*"] & \pi_0(\tilde{\mathcal{I}}_2) \arrow[r, "i^2_*"] \arrow[d, "\partial_*"] & \pi_0(\tilde{\mathcal{H}}_2) \\
 & & & \pi_1(\tilde{\mathcal{I}}_0) \arrow[r, "i^0_*"] & \pi_1(\tilde{\mathcal{H}}_0) \arrow[r, "j^0_*"] & \pi_0(\tilde{\mathcal{I}}_1) \arrow[r, "i^1_*"] \arrow[d, "\partial_*"] & \pi_0(\tilde{\mathcal{H}}_1) \\
 & & & & & \pi_0(\tilde{\mathcal{I}}_0) \arrow[r, "i^0_*"] & \pi_0(\tilde{\mathcal{H}}_0)
\end{tikzcd} \tag{3.17}$$

Starting from any $\pi_n(\tilde{\mathcal{I}}_d)$, traversing right two units, then moving down one unit, and repeating in the staircase manner gives the exact sequence (3.13). Note that the diagram is trivially commutative, as $j_* i_* = 0$.

Example 19. Classifying systems with time-reversal symmetry (symplectic class AII).

As an example, we look at the symmetry class where the only symmetry present is time-reversal Θ_- satisfying $\Theta_-^2 = -1$ (and translation symmetry). The band Hamiltonian satisfies[15]

$$H(-\mathbf{k}) = \sigma^y H(\mathbf{k})^* \sigma^y \,. \tag{3.18}$$

This constraints the relationship of H at time-reversal conjugate points, but not at any particular momentum. If there are $2N$ filled bands and $2M$ empty bands, then $H(\mathbf{k})$ must be a Hermitian $2(N+M) \times 2(N+M)$ matrix, with $2N$ negative eigenvalues. This space is homotopy equivalent to $\mathrm{Gr}_{2N}(\mathbb{C}^{2N+2M})$.

At the TRIM (fixed points of $-\mathbf{1_k}$ map), $H(\mathbf{k})$ must itself satisfy $H(\mathbf{k}) = \sigma^y H(\mathbf{k})^* \sigma^y$, *i.e.*, the matrix itself time-reversal symmetric. This constraints what normally is a $2(N+M) \times 2(M+N)$ complex hermitian matrix to a $(M+N) \times (M+N)$ quaternion hermitian matrix.[16] The space of such matrices is homotopy equivalent to $\mathrm{Gr}_N(\mathbb{H}^{M+N})$. Applying a similar construction as in Ex. 2, we have $\tilde{\mathcal{H}}_0 = \mathcal{H}_0 \approx \mathbb{Z} \times BU$, and $\tilde{\mathcal{I}}_0 = \mathcal{I}_0 \approx \mathbb{Z} \times BSp$.

From Tab. 3.1, the homotopy groups $(\pi_0, \pi_1, \dots)$ of $\mathbb{Z} \times BU$ are $(\mathbb{Z}, 0, \mathbb{Z}, 0, \dots)$, and $(\mathbb{Z}, 0, 0, 0, \mathbb{Z}, \dots)$ for $\mathbb{Z} \times BSp$. We examine the following maps.

- $i^0_{(0)} : \pi_0(\tilde{\mathcal{I}}_0)(= \mathbb{Z}) \to \pi_0(\tilde{\mathcal{H}}_0)(= \mathbb{Z})$ is given by $x \mapsto 2x$. Heuristically, this is because every "matrix element" of $\mathrm{Gr}(\mathbb{H})$ is a 2×2 matrix in $\mathrm{Gr}(\mathbb{C})$. Physically, this is a statement that states always appear in Kramers doublet.

- $\mathcal{T}^0_{(2)} : \pi_2(\tilde{\mathcal{H}}_0)(= \mathbb{Z}) \to \pi_2(\tilde{\mathcal{H}}_0)(= \mathbb{Z})$ is given by $x \mapsto -x$. Physically, this says that time-reversal negates the Chern number / Hall conductivity.

We can proceed to classify time-reversal symmetric insulators in up to three-dimensions. The staircase diagram (3.17) is as follows.

$$\begin{tikzcd}
\cdots \arrow[r] & 0 \arrow[r, "j^0_{(2)}"] & \pi_2(\tilde{\mathcal{I}}_1) \arrow[r, "i^1_{(2)}"] \arrow[d, "\partial_*"] & 0 \arrow[r, "j^1_{(1)}"] & \pi_1(\tilde{\mathcal{I}}_2) \arrow[r, "i^2_{(1)}"] \arrow[d, "\partial_*"] & 0 \arrow[r, "j^2_{(0)}"] & \pi_0(\tilde{\mathcal{I}}_3) \arrow[r, "i^3_{(0)}"] \arrow[d, "\partial_*"] & 0 \\
 & & \begin{matrix}\pi_2(\tilde{\mathcal{I}}_0)\\ 0\end{matrix} \arrow[r, "i^0_{(2)}"] & \begin{matrix}\pi_2(\tilde{\mathcal{H}}_0)\\ \mathbb{Z}\end{matrix} \arrow[r, "j^0_{(1)}"] \arrow[rr, bend right, "\times 2"'] & \pi_1(\tilde{\mathcal{I}}_1) \arrow[r, "i^1_{(1)}"] \arrow[d, "\partial_*"] & \begin{matrix}\pi_1(\tilde{\mathcal{H}}_1)\\ \mathbb{Z}\end{matrix} \arrow[r, "j^1_{(0)}"] \arrow[rr, bend right, "\times 0"'] & \pi_0(\tilde{\mathcal{I}}_2) \arrow[r, "i^2_{(0)}"] \arrow[d, "\partial_*"] & \begin{matrix}\pi_0(\tilde{\mathcal{H}}_2)\\ \mathbb{Z}\end{matrix} \\
 & & & & \begin{matrix}\pi_1(\tilde{\mathcal{I}}_0)\\ 0\end{matrix} \arrow[r, "i^0_{(1)}"] & 0 \arrow[r, "j^0_{(0)}"] & \pi_0(\tilde{\mathcal{I}}_1) \arrow[r, "i^1_{(0)}"] \arrow[d, "\partial_*"] & 0 \\
 & & & & & & \begin{matrix}\pi_0(\tilde{\mathcal{I}}_0)\\ \mathbb{Z}\end{matrix} \arrow[r, "i^0_{(0)}", "\times 2"'] & \begin{matrix}\pi_0(\tilde{\mathcal{H}}_0)\\ \mathbb{Z}\end{matrix}
\end{tikzcd}$$

---

[15] Here σ^y is shorthand for $\mathbb{1}_{M+N} \otimes \sigma^y$, where $H(\mathbf{k})$ is a square matrix of size $2(M \times N)$.

[16] Quaternions (in their 2×2 matrix representation) can be defined as the set of complex matrices A satisfying $A = \sigma^y A^* \sigma^y$.

We can algebraically deduce π_0 of $\tilde{\mathcal{I}}_1$, $\tilde{\mathcal{I}}_2$, and $\tilde{\mathcal{I}}_3$ as follows.

1. $\pi_0(\tilde{\mathcal{I}}_1) = 0$, from exactness with the sequence $(\tilde{\mathcal{I}}_0, \tilde{\mathcal{H}}_0, \tilde{\mathcal{I}}_1)$.
2. $\pi_1(\tilde{\mathcal{I}}_1) = \mathbb{Z}$, also from exactness with the sequence $(\tilde{\mathcal{I}}_0, \tilde{\mathcal{H}}_0, \tilde{\mathcal{I}}_1)$, with $j^0_{(1)} : \pi_2(\tilde{\mathcal{H}}_0) \to \pi_1(\tilde{\mathcal{I}}_1)$ being an isomorphism.
3. The map $i^1_{(1)} j^0_{(1)} : \pi_2(\tilde{\mathcal{H}}_0) \to \pi_1(\tilde{\mathcal{H}}_1)$ (left curved arrow) is the same as $1 - \mathcal{T}^0_{(2)}$ mapping x to $2x$.
4. Hence, the map $i^1_{(1)} : \pi_1(\tilde{\mathcal{I}}_1) \to \pi_1(\tilde{\mathcal{H}}_1)$ also takes $x \mapsto 2x$.
5. The cokernel of $i^1_{(1)}$ is $\mathbb{Z}_2$, so $\pi_0(\tilde{\mathcal{I}}_2) = \mathbb{Z}_2$ from exactness.
6. Since $i^2_{(0)} : \pi_0(\tilde{\mathcal{I}}_2) \to \pi_0(\tilde{\mathcal{H}}_2)$ is zero, $\pi_0(\tilde{\mathcal{I}}_3) = \mathbb{Z}_2$ from exactness.

To conclude, the classes of 3D time-reversal symmetric insulators are

$$\begin{aligned}\pi_0(\mathcal{I}_3) &= \pi_0(\tilde{\mathcal{I}}_0) \oplus \pi_0(\tilde{\mathcal{I}}_1)^3 \oplus \pi_0(\tilde{\mathcal{I}}_2)^3 \oplus \pi_0(\tilde{\mathcal{I}}_3) \\ &= \mathbb{Z} \oplus \mathbb{Z}_2^3 \oplus \mathbb{Z}_2\,.\end{aligned}$$

The $\mathbb{Z}$ labels the number of filled pairs of bands, a physical invariant, although not a particularly significant one. $\mathbb{Z}_2^3$ are the three "weak" indices, while the last $\mathbb{Z}_2$ is the strong index.

Table 3.3 gives a number of topological invariants for eight of the Altland-Zirnbauer classes, while Tab. 3.4 lists a few non-standard symmetry classes.

Symmetry class	Symmetries present	$\mathcal{H}_0$	$\mathcal{I}_0$	$\pi_0(\tilde{\mathcal{I}}_d)$			
				$\tilde{\mathcal{I}}_0$	$\tilde{\mathcal{I}}_1$	$\tilde{\mathcal{I}}_2$	$\tilde{\mathcal{I}}_3$
(D)	$\mathcal{C}_{+1}$	$\mathbb{Z} \times BU$	O/U	$\mathbb{Z}_2$	$\mathbb{Z}_2$	$\mathbb{Z}$	
Chiral orthogonal (BDI)	$\mathcal{C}_{+1}, \Theta_{+1}, \mathcal{S}$	U	O	$\mathbb{Z}_2$	$\mathbb{Z}$		
Orthogonal (AI)	Θ_{+1}	$\mathbb{Z} \times BU$	$\mathbb{Z} \times BO$	$\mathbb{Z}$			
(CI)	$\mathcal{C}_{-1}, \Theta_{+1}, \mathcal{S}$	U	U/O				$\mathbb{Z}$
(C)	$\mathcal{C}_{-1}$	$\mathbb{Z} \times BU$	Sp/U			$\mathbb{Z}$	
Chiral symplectic (CII)	$\mathcal{C}_{-1}, \Theta_{-1}, \mathcal{S}$	U	Sp		$\mathbb{Z}$		$\mathbb{Z}_2$
Symplectic (AII)	Θ_{-1}	$\mathbb{Z} \times BU$	$\mathbb{Z} \times BSp$	$\mathbb{Z}$		$\mathbb{Z}_2$	$\mathbb{Z}_2$
(DIII)	$\mathcal{C}_{+1}, \Theta_{-1}, \mathcal{S}$	U	U/Sp		$\mathbb{Z}_2$	$\mathbb{Z}_2$	$\mathbb{Z}$

Table 3.3: Topological invariants for the Altland-Zirnbauer classes.

The symmetries Θ, $\mathcal{C}$, $\mathcal{S}$ are time-reversal, particle-hole, and sublattice symmetries respectively. The symmetry classes gives the names of the corresponding disorder ensembles, as appeared in Ref. [76]; they are Cartan's labels of the symmetric spaces associated with the disorder ensemble having the desired symmetries [154]. This (and the first two rows of Tab. 3.2) reproduces the results from Refs. [77, 78].

Symmetries present	$\mathcal{H}_0$	$\mathcal{I}_0$	$\pi_0(\tilde{\mathcal{I}}_d)$			
			$\tilde{\mathcal{I}}_0$	$\tilde{\mathcal{I}}_1$	$\tilde{\mathcal{I}}_2$	$\tilde{\mathcal{I}}_3$
Π	$\mathbb{Z} \times BU$	$(\mathbb{Z} \times BU)^2$	$\mathbb{Z}^2$	$\mathbb{Z}$	$\mathbb{Z}^2$	$\mathbb{Z}$
Π, Θ_{-1}	$\mathbb{Z} \times BSp$	$(\mathbb{Z} \times BSp)^2$	$\mathbb{Z}^2$	$\mathbb{Z}$	$\mathbb{Z}$	$\mathbb{Z}$

Table 3.4: Topological invariants for non-Altland-Zirnbauer classes.

In addition to the symmetries described in the previous table (Tab. 3.3), Π refers to spatial inversion symmetry. Unlike Tab. 3.3, this list contains symmetry classes which contain some sort of spatial symmetries, *i.e*, inversion. This list is by no mean exhaustive.

Chapter 4

Inversion symmetric insulators

In addition to there protected surface states, topological insulators also have a magnetoelectric response [60, 61] in which (*e.g.*) an applied electric field induces a magnetization $\mathbf{M} = \theta\frac{e^2}{2\pi h}\mathbf{E}$ for the magnetoelectric coupling quantized at $\theta = \pi$. The magnetoelectric response may be observed only if there is a gap on the surface as well as in the bulk, so the "chiral" surface states must be eliminated by breaking time-reversal symmetry. In principle, coating the surface with a magnetic material and getting the Fermi energy into the band gap would allow the magnetoelectric to be measured.

If the material were spontaneously magnetically ordered, one would be able to observe the magnetoelectric effect without treating the surface first. However, materials that break time-reversal symmetry in the bulk tend to have a small value of θ, a couple of percent [155]. The origin of the large θ in a topological insulator is related to the time-reversal symmetry, surprisingly: symmetries usually force quantities to vanish, but the time-reversal invariance of the insulator keeps θ large. The allowed values of θ are quantized because time-reversal takes $\theta \to -\theta$. This seems to rule out a nonzero θ, but since θ is defined only modulo 2π, both 0 and π are compatible with the TRS.[1]

In this chapter, we will look at magnetically ordered materials (so that the surface states are gapped) but which have some spatial symmetry group in place of time-reversal, in order to keep θ large. One might expect a whole variety of phases as one varies the symmetry group, perhaps displaying effects besides θ, but since there are 230 space groups altogether, we will focus here on a single simple one. This is the symmetry group with just inversion ($\mathbf{r} \to -\mathbf{r}$), a symmetry that is commonly realized in magnetic insulators. For example, all Bravais lattices are inversion symmetric.

Now, inversion transforms θ the same way as time-reversal does, so θ will have two possible values in this case also, 0 and π. Since θ is quantized, there should be a simple rule for determining its value, and in fact we show that the formula of Fu and Kane [43]

---

[1] In an experiment, the magnetoelectric effect could combine with a 2D Hall effect on the surface effectively causing θ to jump between $\pm\pi$ in different parts of the sample. Thus, the bulk magnetization may average out. In reflectivity measurements on the surface [156] the cancellation does not occur, and one can also correct for the effects of the dielectric constant in the material.

(originally derived when both TRS *and* inversion symmetry are present) generalizes to the case with magnetic order, where time-reversal is absent.

Rather than focusing solely on the magnetoelectric effect, we will study a more general question: Which phenomena in topological insulators can be determined by studying just the symmetry properties of Bloch states at special momenta? When inversion is the only symmetry, Bloch states at TRIMs can be classified by their *inversion parities*, which generalize the notion of the sign ±1 picked up by an orbital wavefunction of a molecule when it is inverted. In an infinitely-large insulator, inversion parities are defined for the Bloch states at special momenta, those that are left invariant under the inversion $\boldsymbol{\kappa} \to -\boldsymbol{\kappa}$ (*i.e.*, the TRIMs). In molecules, parity eigenvalues lead mainly to microscopic effects, such as selection rules for transitions. In bulk, though, phenomena on a large scale can be determined by just these parities, as Fu and Kane's result exemplifies.

When inversion symmetry alone is present, the number of odd states at each of the eight TRIMs can be anything at all (since time-reversal is broken, the states do not have to come in pairs). What are the phenomena associated with these parity patterns, which are permitted after the breaking of time-reversal symmetry? We find the following phenomena: first, if the total number of odd states *at all TRIMs* is an *odd* integer, then the material is *not insulating.* Second, if the material is insulating and the number of odd states at some *individual* TRIMs is odd, then the material has either *electrostatic polarization* or *bulk quantized Hall conductivity.* Third, if the material is insulating, and the *total* number of odd states is *twice an odd integer* then the material must have a magnetoelectric effect of $\theta = \pi$. It is natural that unpaired odd states at TRIMs indicate either a quantum Hall effect or electrostatic polarization, since these phenomena (like the odd states) are ruled out by time reversal symmetry.

Of these phenomena, the non-insulating behavior and the magnetoelectric effect imply interesting experimental possibilities. If the product of all the TRIM parities is -1, as for the parity assignment in Fig. 4.1a, then the material cannot be an insulator (as just mentioned). Such a material is likely to be a "Weyl Semimetal," one of the two classes of semimetal introduced in Ref. [157]. For such parities, the dispersions for the filled and empty bands with the minimum overlap between them have two touching points. These points are called Weyl points. Such materials have thermodynamic and conductivity properties related to their vanishing density of states. Furthermore, they should have interesting quantized responses, corresponding to the "chiral anomalies" of field theory, as pointed out by Volovik [158]. Weyl points cannot occur in a material with both time-reversal and inversion symmetry: then energy levels come in Kramers pairs, so the product of the parities is always $+1$.

The formula for θ helps in the search for materials with a large magnetoelectric effect. It shows that a magnetic material may have a magnetoelectric response, but not have protected surface states, as we had hoped. Furthermore, the formula for θ suggests that the magnetoelectric effect can occur in materials with essentially no spin-orbit coupling, but which have nonplanar magnetic order. In these materials, nontrivial band topology can be induced by Berry's phases in the hopping amplitudes due to the magnetic order, rather than to the spin orbit coupling (which was required in the TRS case).

For an investigation of whether these properties might occur in particular materials, see Ref. [159]. This article studies whether the magnetoelectric effect and Weyl metal behavior can be present in magnetically ordered iridates, and finds that the Weyl metal behavior seems to be more likely.

We will begin (see Sec. 4.1) with a brief summary of our results, explaining the various conductivity and response properties that are constrained by the inversion symmetry of a band structure. After this, we present the derivation of these results systematically. The goal is to try to find *all* the response properties that are determined by symmetry properties, given inversion symmetry. There are three steps. We begin (see Sec. 4.2) by classifying all the phases with inversion symmetry, similar to how the phases with the different Altland and Zirnbauer symmetry groups have been classified before [77, 78]. Next (see Sec. 4.3.1), we identify which of these phases have a chance of having robust dynamical responses. Last (see Sec. 4.3), we determine what the responses are.

The outcome is that all insulators in three-dimensions are parametrized by three Chern numbers and a set of inversion parities. Chern numbers, which describe topological properties of the Bloch states as a function of momentum, were already present in the absence of inversion symmetry. The Chern number has three integer components (whereas in two-dimensions, it is a single integer, in three, it is a reciprocal lattice vector). The inversion parities can be encapsulated in eight integers describing the number of odd states at each of the TRIMs.

The second step, in Sec. 4.3.1, is a preliminary study to determine which of these phases corresponding to these integers have the potential to have interesting quantized responses. This section organizes the problem: it simplifies a mess of infinitely many phases down to 16. This uses a process of elimination: we first identify the quantum numbers of dull "frozen insulators;" the remaining insulators are the interesting ones.

Section 4.3 contains the last step and the outcome: it determines the quantized responses in the interesting phases and how they are related to the inversion parities. It derives the condition that ensures a material is non-insulating and the criterion for an insulator to be magnetoelectric as well as some relations between the parities, Hall conductivity, and polarization.

This procedure implies that these are the only response properties, even though there are infinitely many different ways of assigning inversion parities. Infinitely many of these phases have no response, because they can be realized in ionic crystals in which each electron is tightly bound to a single atom. After ionic portions of a band structure are separated out, only finitely many phases remain.

At the end, we give an alternative approach based on entanglement. In particular, we will see why the relationships between inversion parities and responses usually depend on the numbers of odd states modulo 2 or 4. The entanglement spectrum of a material is a set of quantities that can be derived from the ground state wavefunction. It consists of a set of modes that behave like physical surface modes, although they can be determined (at least in principle) without perturbing the system into an excited state, and they can give a signature that a material is in a topological phase [160–165]. Section 4.4 gives a formula for the number of entanglement modes in an inversion symmetric insulator in terms of the inversion parities. This result is then used to rederive some of the electromagnetic properties in a simple fashion and to understand why all these relations depend on the parities modulo 4.

The present chapter addresses some questions left open in earlier work in which we participated. Reference [164] discusses the entanglement spectrum of inversion symmetric insulators, without presenting the exact relation to TRIM parities. The discussion here provides the basis for the investigation in Ref. [159] which studied the electronic structure of a specific material (yttrium iridate) using the constraint on the total number of odd states and expressions for θ in terms of the TRIM parities.

The formula derived here for the magnetoelectric effect depends on the inversion parities in the same way as Fu and Kane's formula, but it applies to a wider class of materials, including materials that can't even be adiabatically connected to any material with time-reversal symmetry. The first prediction – that a material with an odd number of states is metallic – has an interesting corollary that has been noticed before. If time-reversal symmetry is broken, then continuous transitions between $\theta = 0$ and $\theta = \pi$ insulators cannot be found generically [166]. A metallic (or Weyl-metal) phase intervenes except possibly at isolated points.

4.1 Summary of results

Let us first define some conventions about the 3D crystal lattice. We will for simplicity assume that the lattice is cubic (although there is no symmetry required beyond inversion) and has a lattice spacing equal to one unit. All quantities will be written with respect to a coordinate system xyz that is aligned with the axes of the crystal. The primitive lattice vectors are $\mathbf{R}_i$ (*i.e.*, the unit vectors along the axes) and the reciprocal lattice vectors are $\mathbf{G}^i$ where $\mathbf{G}^i \cdot \mathbf{R}_j = 2\pi\delta^i_j$. We also define $\tilde{\mathbf{G}}$ to be $\frac{\mathbf{G}}{2\pi}$ to be a vector of integers $(\tilde{G}_x, \tilde{G}_y, \tilde{G}_z)$. If one wants to apply the results to a non-cubic crystal, it is straightforward to translate the results described here to any lattice, by interpreting the expressions in the appropriate coordinate system.[2]

To study insulators with inversion symmetry it is useful to look at inversion parities, as in the study of spectra of small molecules Such parities seem to describe static properties of wavefunctions, yet in a bulk material, they can determine how electrons move in response to a field. The point of this article is to understand such relationships. The numbers of occupied states with each parity provides integers that can be used to classify the phases (analogous

---

[2] If a quantity is described by a vector in real space (such as the electrical polarization) and we obtain a formula for its coordinates v^x, v^y, v^z, then the quantity should be obtained from $\mathbf{v} = v^x\mathbf{R}_1 + v^y\mathbf{R}_2 + v^z\mathbf{R}_3$. The coordinates of a quantity that is described by a vector $\mathbf{u}$ in reciprocal space determine the vector $\mathbf{u} = \frac{1}{2\pi}(u_x\mathbf{G}^1 + u_y\mathbf{G}^2 + u_z\mathbf{G}^3)$. Electrical polarization is a real space vector; 3D Hall conductivity and momentum are in reciprocal space. We also use upper and lower indices on the coordinates as a reminder of what basis to use.

to how "topological integers" are used to understand other types of phases, for example, the quantum Hall conductance in Hall insulators or the $\mathbb{Z}_2$ index for strong topological insulators). The main technical distinction between solids and molecules is that, in solids, the occupied states can be labeled by momentum $\mathbf{k}$ and the band index a. Let these states be given by $\psi_{a\mathbf{k}}(\mathbf{r}) = u_{a\mathbf{k}}(\mathbf{r})e^{i\mathbf{k}\cdot\mathbf{r}}$. States at the TRIMs (and only these) can be classified by parity under inversion. The TRIMs are the momenta given by

$$\boldsymbol{\kappa} = \frac{n_1}{2}\mathbf{G}^1 + \frac{n_2}{2}\mathbf{G}^2 + \frac{n_3}{2}\mathbf{G}^3 \tag{4.1}$$

where n_1, n_2, n_3 are integers. (Hence components of κ are integral multiples of π.) Such a momentum maps to itself under inversion symmetry modulo the reciprocal lattice, $-\boldsymbol{\kappa} \equiv \boldsymbol{\kappa}$. Hence the wavefunctions at $\boldsymbol{\kappa}$ must be invariant under inversion Π, and their parities can be defined:

$$\Pi\psi_{a\boldsymbol{\kappa}}(\mathbf{r}) = \eta_a(\boldsymbol{\kappa})\psi_{a\boldsymbol{\kappa}}(\mathbf{r}) \tag{4.2}$$

We now introduce a key quantity $n_o(\boldsymbol{\kappa})$ at every TRIM $\boldsymbol{\kappa}$. This is defined as the *number of states with odd parities* at that TRIM. Note, these cannot change without a phase transition (at least in a non-interacting system). Besides these 8 integers, the quantum Hall conductance gives three more invariant integers, since it is quantized:

$$\sigma_H = \frac{e^2}{2\pi h}\mathcal{G}_H \tag{4.3}$$

where $\tilde{\mathcal{G}}_H = \frac{\mathcal{G}_H}{2\pi}$ has integer components.[3] (Note that $\mathcal{G}_H$ is a reciprocal lattice vector according to the conventions defined above, and σ_H gives the Hall conductance per unit length.)

For inversion symmetric insulators, the Chern numbers and the n_o-counts of odd states give parameters that can be used to distinguish among phases. Furthermore, these 11 integers, together with the total number of occupied bands n, give a complete description of the set of phases – any two band structures with the same integers can be tuned into one another without a phase transition This scheme is derived in Sec. 4.2.

Certain physical properties of each phase can be predicted in terms of these integers. We will find all the basic observable quantities that can be expressed in terms of the n_o's.

Total parity constraint and metallic behavior

The first two relationships between physical properties and inversion parities can be written in terms of *net* parities:

$$\eta_{\boldsymbol{\kappa}} = (-1)^{n_o(\boldsymbol{\kappa})} = \prod_a \eta_a(\boldsymbol{\kappa}). \tag{4.4}$$

---

[3] For a general lattice system, $\tilde{\mathcal{G}}_H = (n_1, n_2, n_3)$ is a vector of integers where $n_\alpha = \frac{\mathcal{G}_H}{2\pi}\cdot\mathbf{R}_\alpha$ for $\alpha = 1, 2, 3$.

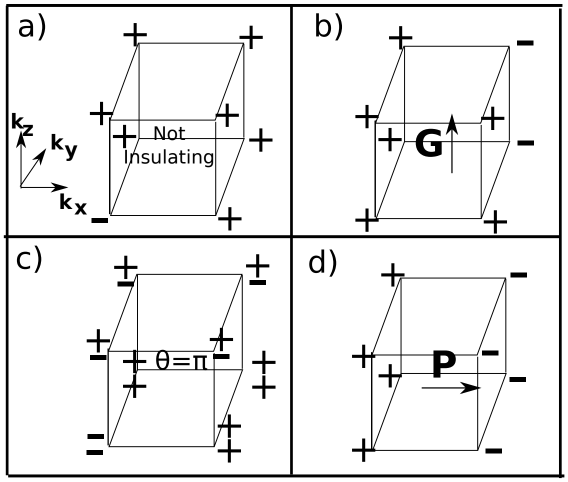

Figure 4.1: Determining properties of systems using parities.

The boxes represent an eighth of the Brillouin Zone; the TRIMs are at the corners. The signs represent the parities of the occupied states at the TRIMs. In (a) the parity constraint of even number of odd parity states is violated, hence it cannot be an insulator. In (b) the parities require a nonvanishing Hall conductance, with odd Chern number in the $k_x k_y$ planes. (c) Quantized magnetoelectric response $\theta = \pi$ determined from number of odd parity states being 2 (modulo 4). (d) A parity configuration corresponding to a frozen polarization.

For any insulator, one can show:

$$\prod_{\boldsymbol{\kappa}} \eta_{\boldsymbol{\kappa}} = 1. \tag{4.5}$$

That is, the total number of filled odd parity states must be even. This is shown in Sec. 4.3.2.

The contrapositive of this statement is the most interesting form of it: if, for some band structure, $\prod_{\boldsymbol{\kappa}} \eta_{\boldsymbol{\kappa}} = -1$, then the system must be gapless. For example, if a system has the parities in Fig. 4.1a, it must be metallic, because there are an odd number of odd occupied states. The gap must close at some momentum $\mathbf{k}$ in the Brillouin zone.

Materials with $\prod_{\boldsymbol{\kappa}} \eta_{\boldsymbol{\kappa}} = -1$ should be interesting. They will have Weyl points, three-dimensional points where the valence and conduction bands meet with a dispersion shaped like a cone. Under certain circumstances, the Fermi energy is expected to pass right through the cone points, so that the material is a semimetal with a density of states that is equal to zero.

Note that the right hand side in Eq. (4.5) differs from the index $(-1)^{\delta_0}$ used by Fu and Kane – their index is only the product of the parities of 'half' the occupied states; since they focused on systems with both time-reversal and inversion symmetry, the states always come in pairs due to the Kramers degeneracy theorem. The product in Eq. (4.5) is automatically equal to 1 when these symmetries are present, so it did not come up in that context. The result in Eq. (4.7), below, generalizes the strong index.

Quantum Hall effect

The net parities also determine the quantum Hall integers modulo 2. The z-component of $\mathcal{G}_H$, for example, satisfies

$$\exp\left[\tfrac{i}{2}\mathcal{G}_H \cdot \mathbf{R}_z\right] = \prod_{\boldsymbol{\kappa};\, \boldsymbol{\kappa}\cdot\mathbf{R}_z=0} \eta_{\boldsymbol{\kappa}} \,. \tag{4.6}$$

That is, whether the Hall conductivity σ_H along the z-direction is an even or odd multiple of $\frac{e^2}{h}$ can be determined by multiplying the η's around either of the squares parallel to the xy-plane. This result is derived in Sec. 4.3.3.

If a system has the parities shown in Fig. 4.1b the Hall conductivity cannot vanish. The component along the z-direction, $\mathcal{G}_H \cdot \mathbf{R}_z$, must be an odd multiple of 2π (per layer of the crystal).

Eqs. (4.5) and (4.6) also have a formal interpretation: they are constraints between the invariants of insulating phases. The 11 integers $\tilde{\mathcal{G}}_H$ and $n_o(\boldsymbol{\kappa})$ are not completely independent of one another, but have to satisfy these four relationships between their parities. Moreover, these are the only constraints – if the relationships are satisfied, the invariants can be realized in principle in some band structure.

Magnetoelectric effect

The magnetoelectric effect is related to the magnetoelectric polarizability α^i_j. An applied magnetic field induces a polarization, $P^i = \alpha^i_j B^j$. In the absence of the quantum Hall effect, α^i_j is well-defined. (Otherwise the polarization can be neutralized by a flow of charge in the surface states associated with the Hall effect.) The polarizability α^i_j is odd under inversion: Under inversion symmetry, $\mathbf{P}$ changes sign, while $\mathbf{B}$ does not.

If the crystal is inversion symmetric, it seems that α must vanish. However, α is ambiguous. An isotropic portion ($\frac{e^2}{h}\delta^i_j \times$ integer) is indeterminate because it can be mimicked by an integer quantum Hall coating on the surface. Thus α^i_j can be inversion symmetric if it is isotropic and has a quantized value: $\theta\frac{e^2}{2\pi h}\delta^i_j$, where θ is a multiple of π.

Earlier work has considered θ for the case of materials with TRS. In that context, the magnetoelectric effect (*i.e.*, $\theta = \pi$) and a nonzero strong index are two aspects of the same phenomenon [60, 61]. If the system also has inversion symmetry, the criterion under which these phenomena occur was found by Fu and Kane [43]. We find that essentially the same formula can be used to determine when $\theta = \pi$ even when the time-reversal symmetry is not present. This formula depends on the n_o parameters, and not just the $\eta_{\boldsymbol{\kappa}}$'s:

$$\frac{\theta}{\pi} \equiv \frac{1}{2}\sum_{\boldsymbol{\kappa}} n_o(\boldsymbol{\kappa}) \pmod 2. \tag{4.7}$$

According to Eq. (4.5), this is always an integer. This expression is proved in Sec. 4.3.4.

This result is somewhat more general than the results for materials with time-reversal as well as inversion symmetry, because the details of the band structure can be quite different in the presence of magnetism: when time-reversal is broken, there may be an odd number of occupied states at some of the TRIMs. Such band structures cannot even be adiabatically connected to the band structure of a material with time-reversal symmetry because of the Kramers degeneracy theorem, yet the magnetoelectric effect is still determined by Eq. (4.7).

One such band structure is illustrated in Fig. 4.1c; it is not adiabatically connected to any insulator with TRS because of the unpaired odd states at the TRIMs. Although the number of odd states at each individual TRIM in Fig. 4.1c is either even or odd, the total number of odd states is even [in accord with Eq. (4.5)] and is twice an odd number; hence $\theta = \pi$.

One may concoct examples of Hamiltonians on a cubic lattice with such patterns of parities. One constructs a hopping model where the local orbitals are labeled as being even-type orbitals $(s, d, \dots)$ or odd-type orbitals $(p, f, \dots)$. Electrons can hop between these orbitals. The hopping matrix elements can be chosen almost arbitrarily except that they must respect inversion symmetry, which constrains the relative signs of hopping in two opposite directions. If orbital a is centered around a point of inversion symmetry, $t_{a\to b} = \pm t_{a\to b'}$ where the orbitals b and b' are corresponding orbitals on sites displaced from orbital a in opposite directions. The sign depends on whether a and b have the same or opposite parities.

Frozen polarization

Finally, let us complete the discussion of physical properties that are constrained by the "net parities" $\eta_{\boldsymbol{\kappa}} = \pm 1$. Eq. (4.6) shows that they determine the Chern numbers modulo 2. This accounts for three of the eight independent bits of information contained in the parities. Note that any pattern of parities satisfying the constraint Eq. (4.5) can be factored into 7 basis patterns:

$$\eta(\boldsymbol{\kappa}) = \pm(-1)^{\frac{1}{\pi^2}\tilde{H}_x\kappa_y\kappa_z}(-1)^{\frac{1}{\pi^2}\tilde{H}_y\kappa_x\kappa_z}(-1)^{\frac{1}{\pi^2}\tilde{H}_z\kappa_x\kappa_y}(-1)^{\frac{2}{\pi}\tilde{\mathbf{P}}_e\cdot\boldsymbol{\kappa}}. \tag{4.8}$$

This factors into seven parts: the three factors depending on $\tilde{H}_i$, the three depending on $\tilde{\mathbf{P}}_e$ and the overall sign in front. (Note that the components of $\tilde{\mathbf{P}}_e$ are half-integers while those of $\tilde{\mathbf{H}}$ are integers. The factors of π are included to make the exponents into integers.) The pattern corresponding to $\tilde{H}_z = 1$ (and all other $\tilde{\mathbf{G}}$ and $\tilde{\mathbf{P}}_e$ variables set to 0) is just the same one shown in Fig. 4.1b. Hence $\tilde{\mathbf{H}}$ is just the (unitless integral) Hall conductivity modulo 2. The patterns of $\eta_{\boldsymbol{\kappa}}$ on the vertices of the cube corresponding to some $\tilde{\mathbf{P}}_e$ (with $\tilde{\mathbf{H}}$ set to zero) vary as a plane wave. The wavenumber, $\tilde{\mathbf{P}}_e$ turns out to determine the intrinsic polarization.

Intrinsic electrical polarization is a phenomenon found in ferroelectrics. When analyzed carefully [167], one finds that it is ambiguous like θ: the total polarization can be altered by charges on the surface, but an intrinsic part of it is determined by the bulk properties. The intrinsic portion is determined modulo a lattice vector times e. Inversion symmetry constrains the components to be integers or half-integers times e. Hence the polarization is determined by three bits, which are revealed in Eq. (4.8). $\mathbf{P}_e$ actually describes only the polarization of the electrons relative to the Bravais lattice; one also needs to include the compensating charges of the nuclei:

$$\mathbf{P} = e\tilde{\mathbf{P}}_e - e\sum_i Z_i \mathbf{r}_{Ni}, \tag{4.9}$$

where $\mathbf{r}_{Ni}$ is the position vector of the i^{th} nucleus, with charge $-Z_i e$. This result is derived in Sec. 4.3.3.

Consider the polarization of the crystal with the band structure illustrated in Fig. 4.1d; it is $\frac{e}{2}\mathbf{R}_1$ if the nuclei are all on the sites of the Bravais lattice. This quantity is called "intrinsic polarization," but it does not actually appear as a polarization all the time. When it is nonzero, it *could* lead to a ferroelectric moment, so that the crystal would have a surface charge of $\frac{1}{2}e$ per unit cell and a large electric field. The alternative possibilities are more likely: the translational symmetry of the surface may be spontaneously broken or the surface may be metallic (see Ref. [168]).

Other effects?

There are many combinations of parities an insulator could have and yet not display any of the phenomena described above. Such insulators cannot be characterized in any other macroscopic way either. They belong to distinct phases (there are gapless regions between them in a phase diagram), but these phases all behave in the same way. For example, if there are 4 odd states at $\boldsymbol{\kappa} = 0$, and 4 even states at all other TRIMs, then Eqs. (4.6), (4.7), and (4.8) give trivial Hall conductivity, θ, and polarization. This phase is definitely a distinct phase, separated by a phase transition, from the one where all states are even, so it may seem likely that some other property would distinguish the two phases. However, in Sec. 4.3.1 we show that no response property distinguishes this phase (or any insulating phase θ, the Hall coefficients, and the polarization vanish).

Parity constraints in general dimensions

The results in higher dimensions have a surprising feature: as the number of dimensions increases the sum of the n_o's must be divisible by larger and larger powers of 2 if the material is to be insulating.

Specifically, in $2s$-dimensions, the sum of the n_o's is a multiple of 2^{s-1}. This multiple is related to the $2s$-dimensional Chern number C_{2s} (defined as an integer):

$$\frac{1}{2^{s-1}} \sum_{\text{TRIM } \boldsymbol{\kappa}} n_o(\boldsymbol{\kappa}) \equiv C_{2s} \pmod{2}; \tag{4.10}$$

the quantum Hall conductance is the 2-dimensional special case.

In $2s+1$-dimensions, the sum of the n_o's is a multiple of 2^s and is related to the Chern-Simons integral

$$\frac{\theta_{2s+1}}{\pi} = \frac{1}{2^s} \sum_{\boldsymbol{\kappa}} n_o(\boldsymbol{\kappa}) \pmod 2. \tag{4.11}$$

where the polarization and magnetoelectric effect are the one- and three-dimensional versions.

Note that insulators with inversion symmetry are quite different from ones without any assumed symmetry: There is an insulator in $2s$-dimensions with a Chern number C_{2s} equal to 1 which has just s filled bands.[4] This insulator is not inversion symmetric, though. The simplest inversion symmetric insulator with the identical Chern number has a minimum of 2^s bands, exponentially more bands than are necessary without symmetry (see Sec. 4.2.7).

The entanglement spectrum

The entanglement spectrum (a concept used to study quantum fluctuations [169]) produces an alternative explanation for these results. Each of the phenomena is connected to a certain type of "entanglement surface state." These states may be counted using inversion symmetry. An insulator with inversion symmetry has a particle-hole symmetry Π_e in its entanglement spectrum $\epsilon_a(\mathbf{k})$ when it is cut on a plane through a center of inversion. This makes it very easy to determine qualitative properties of the Fermi arcs of the entanglement spectrum – it is possible to count (without topological arguments) the number of zero modes in the entanglement spectrum at the TRIMs $\boldsymbol{\kappa}_\perp$ along the surface. Let $\Delta N_e(\boldsymbol{\kappa}_\perp) = \operatorname{tr}_{\epsilon=0} \Pi_e$; that is, $\Delta N_e(\boldsymbol{\kappa}_\perp)$ is the number of even modes minus the number of odd modes with zero entanglement-energy at $\boldsymbol{\kappa}_\perp$.

The $\Delta N_e(\boldsymbol{\kappa})$ parameters can be expressed in terms of parities of the bulk states through $n_o(\boldsymbol{\kappa})$. (The parities of the bulk states are to be defined using an inversion center on the plane of the entanglement cut.) The quantity that appears is $\Delta N(\boldsymbol{\kappa}) = \operatorname{tr}_{E<0} \Pi$, or $n - 2n_o(\boldsymbol{\kappa})$:

$$\Delta N_e(\boldsymbol{\kappa}_\perp) = \frac{1}{2}\big(\Delta N(\boldsymbol{\kappa}_1) + \Delta N(\boldsymbol{\kappa}_2)\big), \tag{4.12}$$

where $\boldsymbol{\kappa}_1$ and $\boldsymbol{\kappa}_2$ are the two TRIMs that project to $\boldsymbol{\kappa}_\perp$. In words: the difference between the number of even and odd states on the "entanglement Fermi surface" at a TRIM is half the difference between the even and odd states in the bulk, at the corresponding TRIMs.

To illustrate an actual entanglement spectrum, we constructed a Hamiltonian with a cubic unit cell whose inversion parities suggest that $\theta = \pi$ and $\tilde{\mathcal{G}}_H \cdot \mathbf{R}_\alpha \equiv 0 \pmod 2$ for $\alpha = x, y, z$. The parities and the spectrum are shown in Fig. 4.2. The entanglement spectrum was calculated for a cut along the xy-plane. As expected, there is a Dirac point at $(0, 0)$,

---

[4] This follows from the relation between topological insulators and the homotopy groups of Grassmannian spaces $\mathrm{Gr}_s(\mathbb{C}^{2s})$; the essential fact is that the homotopy group $\pi_{2m}\big(\mathrm{Gr}_s(\mathbb{C}^{2s})\big) = \mathbb{Z}$ when s is sufficiently large.

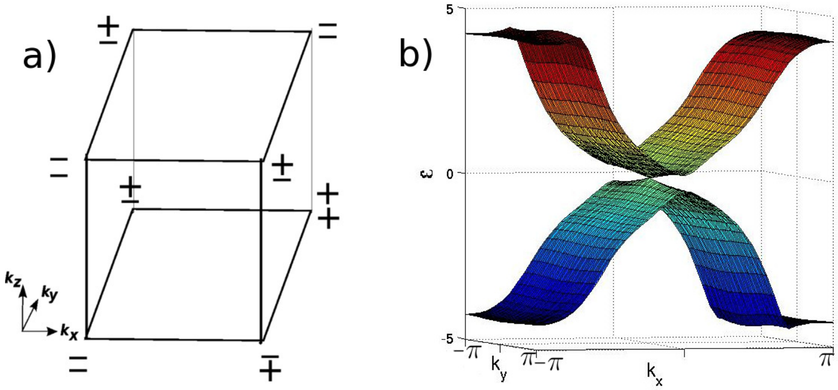

Figure 4.2: Entanglement spectrum of a hopping Hamiltonian.

(a) The parities at the TRIMs. (b) The entanglement modes on a cut parallel to the xy-plane. Note that there are two zero-modes at the TRIM $(0,0)$ and none at the other TRIMs, as expected from the parities.

although there are no physical surface states. The entanglement states reflect the nonzero θ, though physical states do not.

From the relation between the entanglement spectrum and the parities, one can give alternative derivations of the connections between electromagnetic properties and inversion parities. This formula also leads to a simple alternative derivation of Fu and Kane's formula for the indices of topological insulators. These indices count the *physical* surface states. The entanglement states are easy to count with the help of symmetry, and they can be continuously deformed into the physical spectrum.

4.2 Classifying inversion symmetric insulators

This section will show why the inversion parities and the Chern numbers give the full classification of non-interacting insulators with inversion symmetry. This result follows from the classification of Hamiltonians without any symmetry, because the space of inversion symmetric Hamiltonians and the space of all Hamiltonians are related. The Hamiltonians without symmetry are already classified by Chern numbers for each 2D cross-section of the Brillouin zone. The only additional parameters that appear when the Hamiltonians have to be inversion symmetric come from the classification of "zero-dimensional insulators" associated with the TRIMs. Like finite molecules, these states can be classified by inversion parities.

Consider the Hamiltonian $H(\mathbf{k})$ for the wavefunctions $\psi_{a\mathbf{k}}$. This Hamiltonian can be taken to be an $N \times N$ matrix by using a tight-binding model with N bands (n of which are filled). Since this Hamiltonian is inversion symmetric,

$$\Pi H(\mathbf{k})\Pi^{-1} = H(-\mathbf{k}), \tag{4.13}$$

where Π is the matrix describing how the orbitals within the unit cell transform under inversion.[5] Note that $\Pi^2 = 1$, or $\Pi^{-1} = \Pi$.

For non-interacting insulators, a phase transition occurs when the gap closes and states cross the Fermi energy, $\mu = 0$, say. Let us determine when two Hamiltonians are in the same phase – *i.e.*, can be connected without a phase transition. Topologically speaking, we wish to find criteria on the matrix fields $H(\mathbf{k})$ that can be used to determine whether they can be deformed into one another without any zero energy eigenvalues.

The only points in the Brillouin zones where the inversion symmetry constrains the Hamiltonian are the TRIMs, $\boldsymbol{\kappa}$. Each of these points can be interpreted as a 0D system, with a Hamiltonian $H(\boldsymbol{\kappa})$ that is invariant under Π, since Eq. (4.13) implies $\Pi H(\boldsymbol{\kappa})\Pi = H(\boldsymbol{\kappa})$. Let $n_o(\boldsymbol{\kappa})$ be the number of eigenvalues at negative energy which are odd under Π. As the Hamiltonian evolves, the states at this TRIM can mix together, but even states can mix only with even states and odd ones can mix only with odd ones, so the value of $n_o(\boldsymbol{\kappa})$ cannot change.

The second set of parameters characterizing the Hamiltonian are the Chern numbers $\tilde{\mathcal{G}}_H$ which are topological winding numbers that also turn out to describe the Hall conductivity [14, 29]. Because they are integers, they are also invariant.

We will now show that these integers give a complete classification of Hamiltonians with inversion symmetry. That is, if $H(\mathbf{k})$ and $H'(\mathbf{k})$ are two Hamiltonians both with n occupied states, N states total, N_o of which are odd, then they can be deformed into one another while preserving inversion symmetry if

$$\begin{aligned} n_o(\boldsymbol{\kappa}) &= n'_o(\boldsymbol{\kappa}) \quad \text{(for all TRIMs } \boldsymbol{\kappa}\text{)}, \\ \tilde{\mathcal{G}}_H &= \tilde{\mathcal{G}}'_H\,, \end{aligned} \tag{4.14}$$

at least if $N - n, n \geq 2$.

We do not usually consider the integers N and N_o to be important invariants – their values can be changed by adding even or odd orbitals with a very high energy. In continuous space, there are infinitely many available orbitals.

The assumption $N - n, n \geq 2$ is included because, when there are too few bands, there are some Hamiltonians that cannot be deformed into one another simply because there are not enough degrees of freedom.[6] For example, "Hopf insulators" are only nontrivial when restricted to two bands [170]. Our classification theorem does not capture these distinctions, but the distinctions are not related to any generic properties. If one adds sufficiently many trivial occupied and unoccupied bands to an insulator, any two insulators with the same invariants can be deformed into one another.

---

[5] There are technical problems when an orbital $|\alpha\rangle$ is at a half-lattice vector – choosing which copy of it belongs to the unit cell breaks inversion symmetry. The simplest solution is to slice the orbital into two parts that are images of each other under inversion, $|\alpha\rangle = \frac{1}{\sqrt{2}}(|\alpha_1\rangle \pm |\alpha_2\rangle)$. The opposite combination of these orbitals is then assigned a very large energy so that it has no effect.

[6] In a sequence such as $U(1)$, $U(2)$, *etc.*, the homotopy groups of the first few elements are irregular, but a pattern emerges farther into the sequence.

4.2.1 Outline of the argument

The result can be derived by relating a Hamiltonian in d-dimensions to one in $(d-1)$-dimensions, starting with $d = 3$. Let us take d to be arbitrary at first, so that we can describe the general procedure for reducing the number of dimensions. Let $\mathcal{H}_d$ be the space of general Hamiltonians in d-dimensions, while $\mathcal{I}_d$ is the subspace of Hamiltonians that have inversion symmetry. A generic Hamiltonian in $\mathcal{H}_d$ can be regarded as a closed loop in $\mathcal{H}_{d-1}$: Fixing the d^{th} component of $\mathbf{k}$ to have an arbitrary value k_d results in a $(d-1)$-dimensional Hamiltonian H_K, $H_K(k_1, k_2, \ldots, k_{d-1}) \equiv H(k_1, k_2, \ldots, k_{d-1}, K)$. As K varies, H_K traces out a closed loop in $\mathcal{H}_{d-1}$ because the Brillouin zone is periodic.

A Hamiltonian in $\mathcal{I}_d$ has an alternative representation, as just an arc in $\mathcal{H}_{d-1}$, half of the loop just described (from $k_d = 0$ to π). The rest of the loop is determined by the inversion symmetry. The end-points of this arc have to be on $\mathcal{I}_{d-1}$ because the inversion takes the $k_d = 0, \pi$ cross-sections to themselves.

Thus, classifying inversion symmetric Hamiltonians is equivalent to the problem of classifying which arcs can be deformed into one another, as illustrated in Fig. 4.3. That is, consider arcs γ_1, γ_2 in $\mathcal{H}_{d-1}$ connecting two points in the subspace $\mathcal{I}_{d-1}$. What conditions ensure that it is possible to move arc γ_1 to arc γ_2? This deformation is possible if we can first slide the end-points of γ_1 within $\mathcal{I}_{d-1}$ onto the end-points of γ_2 and then smoothly deform the curves connecting them. That is, two arcs are equivalent if their end-points are in the same component of $\mathcal{I}_{d-1}$ (like γ_1 and γ_2 in the figure) but do not have any hole in between them.

We can thus classify d-dimensional Hamiltonians by solving two problems: describing the different components of $\mathcal{I}_{d-1}$, and classifying the arcs connecting a pair of points in $\mathcal{H}_{d-1}$ up to homotopy.

Let us now consider $d = 3$. The first step (classifying the end-points) is analogous to the problem we are trying to solve, just in one-dimension less. (The components of $\mathcal{I}_2$ are just the different classes of 2-dimensional inversion symmetric Hamiltonians.) Let us suppose we know how to deform the two arcs γ_1, γ_2 so that their end-points are the same under the assumptions of Eq. (4.14).

We now have to slide the *interior* of arc 1 onto arc 2. Classifying arcs with fixed end-points in a given space is closely related to classifying closed loops. For example, consider the complex plane with a hole at the origin. Paths connecting a fixed pair of points are classified by $\int d\theta$ (where θ is the polar angle) just as closed loops are: the possible values of the integrals are separated by multiples of 2π (corresponding to the number of times the path encircles the origin) offset by the angle between the points. The *loops* in $\mathcal{H}_2$ can be classified by two winding numbers $\oint d\alpha(k_z)$ and $\oint d\beta(k_z)$, where α and β are angular variables around holes in $\mathcal{H}_2$. This is a restatement of the well-known fact that the Hamiltonians in $\mathcal{H}_3$ are classified by their Chern numbers. A loop corresponds to a three-dimensional Hamiltonian without any special symmetry. The two winding numbers equal the $\tilde{\mathcal{G}}_{Hx}$ and $\tilde{\mathcal{G}}_{Hy}$ Chern numbers of this Hamiltonian. The remaining Chern number is not important because it is determined by the base-point of the loop.

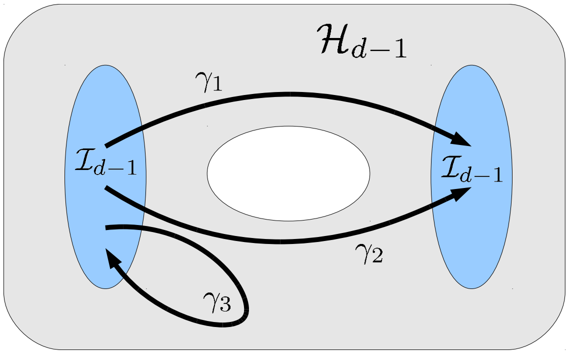

Figure 4.3: Schematic phase space of d-dimensional Hamiltonians.

We can representation of d-dimensional Hamiltonians by arcs and loops in the space of $(d-1)$-dimensional Hamiltonians. The gray region represents $\mathcal{H}_{d-1}$: each point corresponds to a generic $(d-1)$D Hamiltonian. The two ellipses on the side represent the components of $\mathcal{I}_{d-1}$, the Hamiltonians with inversion symmetry. Inversion-symmetric d-dimensional Hamiltonians (three of which are shown) are represented by arcs connecting points in $\mathcal{I}_{d-1}$. Two of these Hamiltonians are equivalent if the end-points are in the same component of $\mathcal{I}_{d-1}$ and have the same winding numbers around holes in the space (represented by the white ellipse). For example, γ_2 and γ_3 are not equivalent because their final end-points are in different components; γ_1 and γ_2 are not equivalent because $\gamma_1\gamma_2^{-1}$ winds around the hole.

Now it follows, by analogy with the example of arcs in the complex plane, that an *arc* connecting two fixed points in the space $\mathcal{H}_2$ can be classified by the change in α and β. The inversion symmetric Hamiltonians can therefore be classified by $\Delta\alpha = \int_0^\pi d\alpha(k_z)$ and $\Delta\beta = \int_0^\pi d\beta(k_z)$.

The Chern numbers $\tilde{\mathcal{G}}_{Hx}$ and $\tilde{\mathcal{G}}_{Hy}$ of the full Hamiltonian are given by $\oint_{-\pi}^{\pi} d\alpha(k_z)$, $\oint_{-\pi}^{\pi} d\beta(k_z)$; hence the "winding numbers" of the open arcs are half as big as the Chern numbers (by inversion symmetry). So if the Chern numbers of the Hamiltonians are equal, then the arcs have the same values of $\Delta\alpha$ and $\Delta\beta$ and so they are equivalent.

We now have to return to the problem of showing that the end-points can be slid to one another under the assumptions. This is the same as classifying inversion symmetric Hamiltonians in *two*-dimensions. This problem may be solved by studying arcs and loops in $\mathcal{H}_1$ reducing it by one more dimension. For two Hamiltonians in (k_x, k_y) space to be equivalent, the single winding number, $\tilde{\mathcal{G}}_{Hz}$, must be the same, and the one-dimensional boundary Hamiltonians must be equivalent.

Now we must classify inversion symmetric Hamiltonians in *one*-dimension, *i.e.*, arcs in $\mathcal{H}_0$. There are no 1D winding numbers in $\mathcal{H}_0$, so the problem reduces directly to classifying the zero-dimensional end-points.

Two *zero*-dimensional Hamiltonians (*i.e.*, matrices) are clearly equivalent if the numbers of even and odd occupied states are the same – just shift the energy eigenvalues so that the two Hamiltonians match. Hence the last condition is that the eight integers $n_o(\boldsymbol{\kappa})$ and the total number of occupied states n must match. The number of even and odd unoccupied states above the Fermi energy must also be the same, but as mentioned above, there are an infinite number of these in continuous space. The original Hamiltonian has bifurcated into eight 0D Hamiltonians since each step of passing from arcs to end-points doubles the number of Hamiltonians.

Hence, three-dimensional Hamiltonians are classified by $\tilde{\mathcal{G}}_{Hx}$, $\tilde{\mathcal{G}}_{Hy}$ and $\tilde{\mathcal{G}}_{Hz}$ together with the parities at the TRIMs.

4.2.2 Topology of the space of Hamiltonians

In this section we will show how to use systematic methods from topology to classify the insulators with inversion symmetry. The materials presented in this section should be accessible to readers with elementary knowledge of topology. We will employ various tools from Algebraic topology, readers may wish to consult Ref. [171] for an introduction of the subject. In the interest of pedagogy, some technical details are overlooked, a far more rigorous derivation is given in chapter 3.

In general we write a band insulator as $H(\mathbf{k})$, which we think of as a vector bundle on the Brillouin zone. The eigenvectors of $H(\mathbf{k})$ with energies below the chemical potential are the occupied states, defining a vector subspace of the entire Hilbert space at $\mathbf{k}$. For inversion symmetric insulators, there is an additional constraint on the Hamiltonian: $\mathcal{T}^0[H(\mathbf{k})] \equiv \Pi H(\mathbf{k})\Pi = H(-\mathbf{k})$, this relates the Hamiltonians at $\mathbf{k}$ and $-\mathbf{k}$.

The idea behind our method of classification, similar to the one used for time-reversal invariant topological insulators, is to look only at half the Brillouin zone.

For a Hamiltonian H in d-dimensions, one can construct a path

$$f_t(k_2, k_3, \dots) = H(k_1 = \pi t, k_2, k_3, \dots) \tag{4.15}$$

in the space of $(d-1)$-dimensional Hamiltonians, where the endpoints ($t = 0, 1$) are inversion symmetric. Thus the classification of d-dimensional Hamiltonians is equivalent to the classification of paths in $\mathfrak{P}(\mathcal{H}_{d-1}; \mathcal{I}_{d-1}, \mathcal{I}_{d-1})$, where $\mathcal{H}_d$ is the set of general d-dimensional Hamiltonians and $\mathcal{I}_d \subset \mathcal{H}_d$ is the subset which is inversion symmetric. The symbol $\mathfrak{P}(X; A, B)$ is defined to be:

$$\begin{aligned} \mathfrak{P}(X; A, B) &\equiv \text{Set of paths in } X \text{ from } A \text{ to } B \\ &= \{f : [0,1] \to X \mid f(0) \in A, f(1) \in B\}, \end{aligned} \tag{4.16}$$

where $A, B \subset X$. We want to divide up $\mathcal{I}_d$ into sets such that paths from different sets are not homotopic to each other. Heuristically, the classes of paths of $\mathfrak{P}(X; A, B)$ are given by the number of components of A, B which determines the set of possible endpoints, and the loop structure of X which determines the number of ways to travel from A to B. The classes of insulators in d-dimensions is very roughly given by:

$$\begin{aligned}&\text{Components of } \mathcal{I}_d \\ &\quad\sim \frac{\text{Loops in } \mathcal{H}_{d-1}}{\text{Loops in } \mathcal{I}_{d-1}} \times \left(\text{Components of } \mathcal{I}_{d-1}\right)^2 . \end{aligned} \tag{4.17}$$

This idea is made precise using algebraic topology, and is captured by an exact sequence below (4.19) (which explains the reason for the denominator here).

There is an addition structure in the classification of insulators, which comes from the fact that one can combine two insulators together using direct sums "$\oplus$". To simplify the classification, it is useful to also have a subtraction "$\ominus$" operation between insulators. This would give the topological invariants (*e.g.* $\mathbb{Z}$) a group structure.

The subtraction procedure is realized by considering an ordered pair of bands (H_1, H_2), which represents the 'difference' of the two Hamiltonians. Addition by H' is given by $(H_1 \oplus H', H_2)$ and subtraction is given by $(H_1, H_2 \oplus H')$. Imposing the equivalence relation $(H_1 \oplus H', H_2 \oplus H') \sim (H_1, H_2)$ makes the addition and subtraction processes cancel each other. Physically, we are interested in classifying difference of two topological insulators – this is analogous to studying domain walls between them whose properties are determined only by the difference in topological invariants. With this interpretation, it is possible to talk about a negative number of filled bands (whenever H_2 has more bands than H_1).

The construction above, called the *Grothendieck group*, has two interpretations. First, two insulators H_1, H_2 are deformable to one another when the topological invariants of the band structure (H_1, H_2) are all trivial. Second, the invariants classifying phases of H can be defined as the topological invariants of (H, vacuum).

4.2.3 Hamiltonians, classifying spaces and homotopy groups

Consider an $N_B \times N_B$ matrix H with n occupied states and $N_B - n$ empty states. Setting the chemical potential to be zero, H is a matrix with n negative eigenvalues and $N_B - n$ positive eigenvalues. In the topological classification of insulators, the energies are irrelevant so long as we can distinguish between occupied and unoccupied states, and hence we can deform the energies (eigenvalues) of all valence bands to -1 and the energies of conduction bands to $+1$. We can also assume there are an infinite number of conduction bands, and so we let $N_B \to \infty$. $\mathcal{H}_0$ is the set of such 0D Hamiltonians, and can be separated into discrete components based on the number of filled bands (which may be negative for *differences* of Hamiltonians). The space $\mathcal{H}_0$ is homeomorphic to $\mathbb{Z} \times BU$, where BU is the classifying space of the unitary groups.

At a TRIM, the Hamiltonian is inversion symmetric and commutes with the operator Π. The Hilbert space is divided into an even subspace and an odd subspace, based on the inversion eigenvalues. Hence the set of inversion symmetric (0D) Hamiltonians $\mathcal{I}_0$ is homeomorphic to $\mathcal{H}_0 \times \mathcal{H}_0$.[7]

---

[7] Because $\mathcal{H}_0$ is an infinite-dimensional space, we can have $\mathcal{H}_0 \times \mathcal{H}_0 \subset \mathcal{H}_0$.

Finally, we introduce the "vacuum" $v_0 \in \mathcal{I}_0 \subset \mathcal{H}_0$, which is a Hamiltonian with no filled bands. v_0 is a useful object in that it allows us to compare any Hamiltonian to it, and also acts as the basepoint when we compute the homotopy groups of $\mathcal{H}_0$, $\mathcal{I}_0$.

Given a topological space X and a basepoint within the space x_0, the *homotopy group* $\pi_s(X)$ is the set of equivalence classes of maps $f : (S^s, b_0) \to (X, x_0)$, where the basepoint $b_0 \in S^s$ and $f(b_0) = x_0$. For example, $\pi_0(X)$ gives the number of connected components of X, and $\pi_1(X)$ tells us which loops in X are equivalent and which loops are contractible.

The group structure of $\pi_s(X)$ is given by concatenation of maps. However, the group structure of the Hamiltonians has already been defined based on direct sums. Fortunately, the group composition defined based on the two methods (concatenation / direct sums) are equivalent.

The homotopy groups of $\mathcal{H}_d$ are known: $\pi_0(\mathcal{H}_0) = \mathbb{Z}$ because 0-dimensional Hamiltonians are classified by the number of filled bands n. $\pi_1(\mathcal{H}_0) = 0$ means that the loops in $\mathcal{H}_0$ are all contractible. $\pi_2(\mathcal{H}_0) = \mathbb{Z}$, because maps of the sphere are classified by the first Chern class (or the Chern number). This invariant gives rise to the integer quantum Hall effect. For higher dimension, $\pi_s(\mathcal{H}_0)$ is 0 when s is an odd integer, and $\mathbb{Z}$ when s is an even integer, corresponding to the $(s/2)^{\text{th}}$ Chern class. In this section, Chern numbers are taken to be integers rather than multiples of 2π.

The homotopy groups of $\mathcal{I}_0$ are simply the squares of the homotopy groups of $\mathcal{H}_0$. In particular, the set of components $\pi_0(\mathcal{I}_0) = \mathbb{Z}^2$ is labeled by two integers: (n, α), where n is the total number of valence 'bands' and $\alpha = n_o$ is the number of states which have odd inversion parity.

4.2.4 Relative homotopy groups and exact sequences

The homotopy groups $\pi_s(X)$ classifies components, loops, and maps from higher dimensional spheres to the space X. The *relative homotopy groups* $\pi_s(X, A)$ classify maps from paths, disks, *etc.* where the boundary must lie in some subspace. This is how topologists define "winding numbers" of open arcs, which were discussed in Sec. 4.2. Relative homotopy groups were applied much earlier by Refs. [172, 173] to an interesting problem within physics: classifying defects of ordered phases when the defects are stuck to the surface.

Given a space X a subspace $A \subset X$, and a basepoint $x_0 \in A$, the relative homotopy group $\pi_s(X, A)$ is the equivalence classes of maps $(D^s, \partial D^s, b_0) \to (X, A, x_0)$. The boundary of the disk $\partial D^s = S^{s-1}$ must map to A, and the basepoint $b_0 \in \partial D^s$ maps to x_0. The relative homotopy groups can be computed via the exact sequence

$$\pi_s(A) \xrightarrow{i_*} \pi_s(X) \xrightarrow{j_*} \pi_s(X, A) \xrightarrow{\partial} \pi_{s-1}(A) \xrightarrow{i_*} \pi_{s-1}(X) . \tag{4.18}$$

An *exact sequence* is a sequence of groups along with maps defined from one group to the next, each map preserving the group operations. In an exact sequence, the image of every map is the same as the kernel of the subsequent map.

In the one-dimensional case, the relative homotopy group $\pi_1(X,A)$ describes the set of possible paths in X from x_0 to A up to homotopy, that is, the classes of paths $\mathfrak{P}(X;x_0,A)$. The exact sequence becomes:

$$\pi_1(A) \xrightarrow{i_{(1)}} \pi_1(X) \xrightarrow{j_{(0)}} \pi_1(X,A) \xrightarrow{\partial} \pi_0(A) \xrightarrow{i_{(0)}} \pi_0(X)\,. \tag{4.19}$$

In the exact sequence above, the maps are defined as follows.

- $i : A \to X$ is the inclusion map which takes every point from A to itself interpreted as a point in X. The induced maps $i_{(s)} : \pi_s(A) \to \pi_s(X)$ take components/loops from one space to the other.
- j: All the loops in X start and end at x_0, and so they are also clearly paths in $\mathfrak{P}(X;x_0,A)$ seeing $x_0 \in A$. $j_{(0)}$ is the map that takes the equivalence classes of loops $\pi_1(X)$ to the equivalence classes of paths $\pi_1(X,A)$.
- $\partial : \pi_1(X,A) \to \pi_0(A)$ is a map that takes a path and selects its second endpoint to give a component of A. ∂ is called the boundary map, it takes a "1D object" to give a "0D object."

It appears that the maps i and j 'do nothing' to the objects (points, loops) they act on. However, each map gives the loop/path more freedom to move around. For example, $j_{(0)}$ takes a loop to a path where the endpoints no longer have to be the same, so it may map a nontrivial path to a trivial one.

The exact sequence captures the idea that the paths in $\mathfrak{P}(X;x_0,A)$ can be classified once one knows the properties of X and A, based on their end-points and how they wind. Suppose we are constructing a path in $\mathfrak{P}(X;x_0,A)$.

1. First, we pick the endpoint $x \in A$ of the path p. x can be in any component of A that is connected to x_0 within X and this is captured by the statement $\ker(i_{(0)}) = \mathrm{img}(\partial)$.
2. Given a choice of a path p from x_0 to x, we can construct all the other paths between the points. We can create any other path p' by concatenating a loop $l \in \pi_1(X)$ at the beginning of p. This is the exactness at $\pi_1(X,A)$.
3. However, the paths p and p' are only different (*i.e.*, not homotopic to each other) only if the loop l cannot be unwound within A, this is to say that $p \sim p'$ if l is homotopic to a loop in A. See Fig. 4.4. This idea is captured by the exactness at $\pi_1(X)$. Hence we think of l belonging to the quotient $\frac{\pi_1(X)}{i_{(1)}\pi_1(A)}$, and this group is called the *cokernel* of the map $i_{(1)}$.

We see that any path may be constructed by its endpoint x and a loop l.

$$p = j(l) + \partial^{-1}x\,. \tag{4.20}$$

The inverse boundary operator ∂^{-1} is not unique, but that does not affect the structure of the group $\pi_1(X,A)$ for the cases we are considering. The equivalence classes of x form

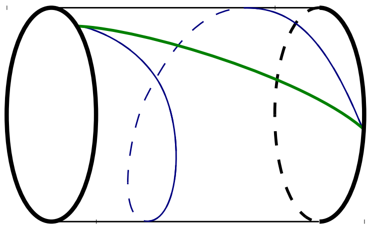

Figure 4.4: An illustration of the exact sequence.

> The cylinder here represents X and the two dark circles at the ends represent A. Paths in $\pi_1(X,A)$ can be enumerated by taking one path for each inequivalent end-point x and adding loops from $\pi_1(X)$ to the paths. This description is redundant for the topology shown in the figure. Consider the paths shown: they are p (green) and another path $p' = p + l$ (blue) obtained from it by adding l (black), which winds around the cylinder. The two paths are equivalent because they can be deformed into one another by bringing the right end-point around A. This happens because l can be smooshed into A.

$\ker(i_{(0)})$, while the equivalence classes of l make up $\operatorname{coker}(i_{(1)})$. The relative homotopy group is a semidirect product

$$\pi_1(X,A) = \operatorname{coker}(i_{(1)}) \rtimes \ker(i_{(0)})\,. \tag{4.21}$$

What this means is that $\operatorname{coker}(i_{(1)})$ is a normal subgroup of $\pi_1(X,A)$ and $\ker(i_{(0)})$ is the quotient of the two. For the purpose of classifying inversion symmetric insulators, we can treat the semidirect product as simply a product.[8]

4.2.5 One-dimension

In this section we examine the classification of 1D inversion symmetric Hamiltonians $H(k)$. Let $\mathcal{I}_1$ be the set of maps $H : S^1 \to \mathcal{H}_0$ such that $\mathcal{T}^0[H(k)] = H(-k)$. $\mathcal{I}_1$ is homeomorphic to the set of paths in $\mathcal{H}_0$ that start and end in $\mathcal{I}_0$ [*i.e.*, $\mathcal{I}_1 \approx \mathfrak{P}(\mathcal{H}_0; \mathcal{I}_0, \mathcal{I}_0)$], and we seek to classify all such paths – to compute $\pi_0(\mathcal{I}_1)$.

For a 1D band structure $H(k)$, we can 'factor' out $H(0)$ by letting $H'(k) = H(k) \ominus H(0)$ so that $H'(0) = v_0$. The decomposition $H(k) = H(0) \oplus H'(k)$ can be expressed as

$$\mathcal{I}_1 \approx \mathcal{I}_0 \times \tilde{\mathcal{I}}_1\,. \tag{4.22}$$

$H(0)$ is an element of $\mathcal{I}_0$ while $H'(k)$ is an element of $\tilde{\mathcal{I}}_1$, where $\tilde{\mathcal{I}}_1$ is the subset of $\mathcal{I}_1$ with a fixed basepoint ($H'(0) = v_0$). Hence the classification of $\mathcal{I}_1$ can be broken up in to two parts, the classification of $\mathcal{I}_0$ and that of $\tilde{\mathcal{I}}_1$. The former is understood already, $\pi_0(\mathcal{I}_0) = \mathbb{Z}^2$.

---

[8] This is because all the homotopy groups are free in the inversion symmetric case, *i.e.*, of the form $\mathbb{Z}^n$.

Notice that $\tilde{\mathcal{I}}_1$ is homeomorphic with the class of paths $\mathfrak{P}(\mathcal{H}_0; v_0, \mathcal{I}_0)$, whose components are described by the relative homotopy group $\pi_1(\mathcal{H}_0, \mathcal{I}_0)$. The relative homotopy group can be computed by the exact sequence (4.19). Using the fact that $\pi_0(\tilde{\mathcal{I}}_1) = \pi_1(\mathcal{H}_0, \mathcal{I}_0)$,

$$\begin{tikzcd} \pi_1(\mathcal{I}_0) \arrow[r, "i^0_{(1)}"] & \pi_1(\mathcal{H}_0) \arrow[r, "j^0_{(0)}"] & \pi_0(\tilde{\mathcal{I}}_1) \arrow[r, "\partial"] & \pi_0(\mathcal{I}_0) \arrow[r, "i^0_{(0)}"] & \pi_0(\mathcal{H}_0) \\ 0 & 0 & & \mathbb{Z}^2 & \mathbb{Z} \end{tikzcd} \; . \tag{4.23}$$

(The upper index 0 on the maps indicate that this is the exact sequence for paths from $\mathcal{H}_0$ to $\mathcal{I}_0$.) Since $\pi_1(\mathcal{H}_0) = 0$, we can ignore the left side of the exact sequence (cokernel of $i_{(1)}$ is zero). The integer $n \in \pi_0(\mathcal{H}_0) = \mathbb{Z}$ tells us how many filled bands there are, and $(n_o, n_e) \in \pi_0(\mathcal{I}_0) = \mathbb{Z}^2$ are the number of even-parity and odd-parity bands. The map $i_{(0)}$ is given by $n = n_o + n_e$, and so the kernel of the map is the subset where $n_o = -n_e$, isomorphic to $\mathbb{Z}$.[9] Hence $\pi_0(\tilde{\mathcal{I}}_1)$ is isomorphic to $\ker(i_{(0)}) = \mathbb{Z}$. This is to say that the set of paths $\mathfrak{P}(\mathcal{H}_0; v_0, \mathcal{I}_0)$ are solely classified by the endpoint. Since $\mathcal{I}_1 = \mathcal{I}_0 \times \tilde{\mathcal{I}}_1$, we have

$$\begin{aligned} \pi_0(\mathcal{I}_1) &= \pi_0(\mathcal{I}_0) \times \pi_0(\tilde{\mathcal{I}}_1) \\ &= \pi_0(\mathcal{I}_0) \times \pi_1(\mathcal{H}_0, \mathcal{I}_0) \\ &= \mathbb{Z}^2 \times \mathbb{Z} \, . \end{aligned} \tag{4.24}$$

The invariant $\pi_0(\mathcal{I}_1) = \mathbb{Z}^2$ corresponds to the number of total bands and odd-parity states at $k = 0$: $n, n_o(0)$. The invariant $\pi_0(\tilde{\mathcal{I}}_0) = \mathbb{Z}$ corresponds to the difference in number of odd bands at $k = \pi$ and $k = 0$: $\alpha_x = n_o(\pi) - n_o(0)$. Hence the parities at the two TRIMs completely classify all 1D inversion symmetric Hamiltonians.

A *generator* of a group is an element which gives the entire group by group addition and subtraction; for example, 1 is a generator of $\mathbb{Z}$. In our case, the generators are Hamiltonians which form a basis for all Hamiltonians, up to homotopy. Knowing the generators amounts to having a list of all the possible phases. Moreover, the indices for classifying phases can be found using the generators: each phase can be written as a sum of the generators, and the coefficients are a possible set of indices. The indices we have used up to now, n_o and the Chern number, are simple linear combinations of them.

The generators of $\pi_0(\mathcal{I}_0) = \mathbb{Z}^2$ are two Hamiltonians H^0_n and H^0_α, the first increases the total number of bands n, the second one fixes n but increases the number of odd-parity bands n_o. (Remember that we are classifying ways of *changing* one Hamiltonian to another Hamiltonian.) Explicitly:

$$H^0_n = \big[-1\big]_{(+)} \, . \tag{4.25}$$

$$H^0_\alpha = \big[-1\big]_{(-)} \ominus H^0_n \, . \tag{4.26}$$

where the subscript ($\pm$) labels the inversion eigenvalue(s) of the orbital(s). The first expression H^0_n adds an inert band to increase n; the second expression H^0_α adds an odd-parity

---

[9] The Hamiltonian we are classifying $[H'(k) = H(k) \ominus H(0)]$ is one of the generalized Hamiltonians defined above; that is why a number of bands n_e or n_o can be negative.

band but subtracts an even-parity one to increase n_o while maintaining n. The generator for $\pi_0(\tilde{\mathcal{I}}_1) = \mathbb{Z}$ is:

$$H^1_\alpha(k) = \begin{bmatrix} -\cos k & \sin k \\ \sin k & \cos k \end{bmatrix}_{(+-)} \ominus H^0_n \,. \tag{4.27}$$

The subscript $(+-)$ specifies the inversion operator $\Pi = \left[\begin{smallmatrix} +1 & \\ & -1 \end{smallmatrix}\right]$ for this Hamiltonian. When $k = 0$, the matrix becomes $\left[\begin{smallmatrix} -1 & \\ & 1 \end{smallmatrix}\right]_{(+-)}$ and the occupied band is even under inversion. Similarly, the matrix at $k = \pi$ is $\left[\begin{smallmatrix} 1 & \\ & -1 \end{smallmatrix}\right]_{(+-)}$ and there the occupied band is odd. Hence $\alpha_x = n_o(\pi) - n_0(0) = 1 - 0 = 1$ and $H^1_\alpha(k)$ is a generator of $\pi_0(\tilde{\mathcal{I}}_1)$.

Therefore, any 1D inversion symmetric Hamiltonian is homotopic to

$$H(k) = nH^0_n \oplus \alpha H^0_\alpha \oplus \alpha_x H^1_\alpha(k) \,. \tag{4.28}$$

4.2.6 Two-dimensions

We apply the same ideas used in 1D to classify inversion symmetric insulators in 2D. The inversion symmetric Hamiltonians (k_x, k_y) in 2D satisfy: $\mathcal{T}^0 H(k_x, k_y) = H(-k_x, -k_y)$. The set of 2D inversion symmetric Hamiltonians ($\mathcal{I}_2$) is equivalent to $\mathfrak{P}(\mathcal{H}_1; \mathcal{I}_1, \mathcal{I}_1)$, where $\mathcal{H}_1$ is the set of 1D band structures (loops in $\mathcal{H}_0$).

Just as in the 1D case where we decompose $H(k)$ into a 0D and 1D object: $H(k) = H(0) \oplus H'(k)$, we decompose the 2D Hamiltonian into 0D, 1D and 2D components. Let

$$H'(k_x, k_y) = H(k_x, k_y) \ominus H(0,0) \,, \tag{4.29a}$$

so that $H'(0,0) = v_0$. Now we define

$$H''(k_x, k_y) = H'(k_x, k_y) \ominus H'(0, k_y) \ominus H'(k_x, 0) \,, \tag{4.29b}$$

so that

$$H''(0, k_y) = H''(k_x, 0) = v_0 \,. \tag{4.29c}$$

$H(0,0)$ is an element of $\mathcal{I}_0$, and $H'(0, k_y)$ and $H'(k_x, 0)$ are elements of $\tilde{\mathcal{I}}_1$. We define $\tilde{\mathcal{I}}_2$ to be the set of inversion symmetric Hamiltonians satisfying (4.29c). With this procedure, we have decomposed $\mathcal{I}_2$ as

$$\mathcal{I}_2 \approx \tilde{\mathcal{I}}_0 \times \tilde{\mathcal{I}}_1^2 \times \tilde{\mathcal{I}}_2 \,, \tag{4.30}$$

where $\tilde{\mathcal{I}}_0 = \mathcal{I}_0$. Explicitly, the decomposition is:

$$H(k_x, k_y) = \underbrace{H(0,0)}_{\tilde{\mathcal{I}}_0} \oplus \underbrace{H'(0, k_y) \oplus H'(k_x, 0)}_{\tilde{\mathcal{I}}_1 \times \tilde{\mathcal{I}}_1} \oplus \underbrace{H''(k_x, k_y)}_{\tilde{\mathcal{I}}_2} \,. \tag{4.31}$$

Due to (4.29c), we can think of Hamiltonians in $\tilde{\mathcal{I}}_2$ as maps from the sphere (rather than the torus) to $\mathcal{H}_0$. The Hamiltonian is constant around the edges of the Brillouin zone (when we take the Brillouin zone to extend over the range $[0, 2\pi]$ for each coordinate), and so the edges may all be identified to a single point to give a sphere.

We now analyze the properties of Hamiltonians in $\tilde{\mathcal{I}}_2$. For each fixed k_x, the Hamiltonian $H''(k_y)|_{k_x}$ is a map from the 1D Brillouin zone (S^1) to $\tilde{\mathcal{H}}_0$ (where we've also defined $\tilde{\mathcal{H}}_0 = \mathcal{H}_0$). Denote the set of such maps as $\tilde{\mathcal{H}}_1$, the set of loops in $\tilde{\mathcal{H}}_0$ with basepoint v_0: $\tilde{\mathcal{H}}_1 = \mathfrak{P}(\tilde{\mathcal{H}}_0; v_0, v_0)$. $\tilde{\mathcal{H}}_1$ is called the *loop space* of $\tilde{\mathcal{H}}_0$ and is denoted by $\tilde{\mathcal{H}}_1 = \Omega\tilde{\mathcal{H}}_0$.

The Hamiltonian at $k_x = \pi$ is inversion symmetric, and so $H''(k_y)|_{k_x=\pi} \in \tilde{\mathcal{I}}_1$. At $k_x = 0$, the line $H''(k_y)|_{k_x} = v_0$ is a constant map - which we call v_1 (a line of v_0). Clearly v_1 is an element of $\tilde{\mathcal{I}}_1$, and acts as the basepoint when we compute the homotopy groups of $\tilde{\mathcal{I}}_1$, $\tilde{\mathcal{H}}_1$.

Having defined the spaces $\tilde{\mathcal{I}}_2$, $\tilde{\mathcal{H}}_1$ and basepoint v_1, we can see that $\tilde{\mathcal{I}}_2$ is homeomorphic to the set of paths in $\tilde{\mathcal{H}}_1$ with endpoints at v_1 and somewhere in $\tilde{\mathcal{I}}_1$: $\tilde{\mathcal{I}}_2 \approx \mathfrak{P}(\tilde{\mathcal{H}}_1; v_1, \tilde{\mathcal{I}}_1)$. The exact sequence which gives the equivalence classes of such paths is

$$\pi_1(\tilde{\mathcal{I}}_1) \xrightarrow{i^1_{(1)}} \pi_1(\tilde{\mathcal{H}}_1) \xrightarrow{j^1_{(0)}} \pi_0(\tilde{\mathcal{I}}_2) \xrightarrow{\partial} \pi_0(\tilde{\mathcal{I}}_1) \xrightarrow{i^1_{(0)}} \pi_0(\tilde{\mathcal{H}}_1)\,. \tag{4.32}$$

Elements of $\pi_1(\tilde{\mathcal{H}}_1)$ are two-dimensional Hamiltonians that equal v_0 along $k_x = 0 \sim 2\pi$ and $k_y = 0 \sim 2\pi$, which are equivalent to maps $S^2 \to \tilde{\mathcal{H}}_0$. Hence

$$\pi_1(\tilde{\mathcal{H}}_1) = \pi_2(\tilde{\mathcal{H}}_0) = \mathbb{Z} \qquad\qquad \text{(Chern number)}. \tag{4.33}$$

The map j^1, which essentially maps general two-dimensional Hamiltonians to inversion symmetric ones, is defined by

$$\begin{aligned}&(j^1H)(k_x, k_y)\\ &\quad= \begin{cases} H(2k_x, k_y) & 0 \le k_x \le \pi \\ \mathcal{T}^0 H(4\pi - 2k_x, 2\pi - k_y) & \pi \le k_x < 2\pi \end{cases}.\end{aligned} \tag{4.34}$$

It builds an inversion symmetric Hamiltonian out of two copies of a Hamiltonian with no special symmetries. The map $\partial : \tilde{\mathcal{I}}_2 \to \tilde{\mathcal{I}}_1$ is defined by

$$[\partial H](k) = H(k_x = \pi, k_y = k) \tag{4.35}$$

which takes a 2D Hamiltonian and picks out the 1D Hamiltonian at $k_x = \pi$.

The exact sequence, Eq. (4.32) would fairly easily determine $\pi_0(\tilde{\mathcal{I}}_2)$ if we only knew that $\pi_1(\tilde{\mathcal{I}}_1)$ were equal to 0, as turns out to be true. However, to see this, we will have to do a recursive calculation, using another exact sequence for $\pi_1(\tilde{\mathcal{I}}_1)$ which classifies loops of 1D inversion symmetric insulators (not to be confused with 2D insulators). As argued in Fig. 4.5 and proved in Thm. 15, the group $\pi_1(\tilde{\mathcal{I}}_1)$ is isomorphic to $\pi_2(\tilde{\mathcal{H}}_0, \tilde{\mathcal{I}}_0)$. We can compute $\pi_1(\tilde{\mathcal{I}}_1) = \pi_2(\tilde{\mathcal{H}}_0, \tilde{\mathcal{I}}_0)$ via the exact sequence (4.18).

$$\begin{array}{ccccccccc} \pi_2(\tilde{\mathcal{I}}_0) & \xrightarrow{i^0_{(2)}} & \pi_2(\tilde{\mathcal{H}}_0) & \xrightarrow{j^0_{(1)}} & \pi_1(\tilde{\mathcal{I}}_1) & \xrightarrow{\partial} & \pi_1(\tilde{\mathcal{I}}_0) & \xrightarrow{i^0_{(1)}} & \pi_1(\tilde{\mathcal{H}}_0) \\ \mathbb{Z}^2 & & \mathbb{Z} & & & & 0 & & 0 \end{array}\,. \tag{4.36}$$

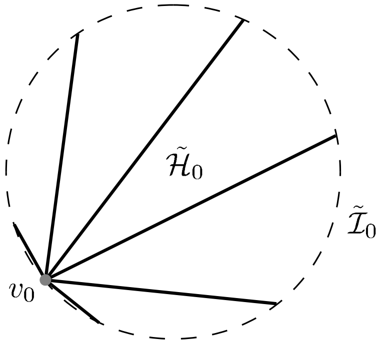

Figure 4.5: Isomorphism between $\pi_2(\tilde{\mathcal{H}}_0, \tilde{\mathcal{I}}_0)$ and $\pi_1(\tilde{\mathcal{I}}_1)$.

An element in $\tilde{\mathcal{I}}_1$ is a path from v_0 to an element of $\tilde{\mathcal{I}}_0$ (dark black lines). An element of $\pi_1(\tilde{\mathcal{I}}_1)$ is a family of such paths. The first path in the family must be v_1, a 'zero-length' constant path at v_0 (gray dot). The last path of the family must also be v_1, and so the paths must shrink back to v_0 at the end, because that is the base point for the homotopy groups. This family of paths traces out a disk D^2 which maps to $\tilde{\mathcal{H}}_0$, the endpoints of each path traces out a circle $S^1 = \partial D^2$ which maps to $\tilde{\mathcal{I}}_0$ (dashed circle). The basepoint of the circle maps to v_0, and hence every element of $\pi_1(\tilde{\mathcal{I}}_1)$ is also an element of $\pi_2(\tilde{\mathcal{H}}_0, \tilde{\mathcal{I}}_0)$ and vice-versa. This illustrates the isomorphism $\pi_2(\tilde{\mathcal{H}}_0, \tilde{\mathcal{I}}_0) = \pi_1(\tilde{\mathcal{I}}_1)$. The general case relating $\pi_{n+1}(\tilde{\mathcal{H}}_{d-1}, \tilde{\mathcal{I}}_{d-1})$ to $\pi_n(\tilde{\mathcal{I}}_d)$ is given by Thm. 15.

The first map $i^0_{(2)} : \pi_2(\tilde{\mathcal{I}}_0) \to \pi_2(\tilde{\mathcal{H}}_0)$ is given by $\beta = \beta_e + \beta_o$ (which means that the Chern numbers of the odd and even bands add to the total.) The image of $i^0_{(2)}$ is all of $i^0_{(2)}$, so its cokernel is trivial. Since on the right side the groups are also trivial ($\ker(i^0_{(1)}) = 0$), we have that $\pi_1(\tilde{\mathcal{I}}_1) = 0$.

We now return to the exact sequence (4.32) to compute the $\pi_0(\tilde{\mathcal{I}}_2)$.

$$\begin{array}{ccccccccc} \pi_1(\tilde{\mathcal{I}}_1) & \xrightarrow{i^1_{(1)}} & \pi_1(\tilde{\mathcal{H}}_1) & \xrightarrow{j^1_{(0)}} & \pi_0(\tilde{\mathcal{I}}_2) & \xrightarrow{\partial} & \pi_0(\tilde{\mathcal{I}}_1) & \xrightarrow{i^1_{(0)}} & \pi_0(\tilde{\mathcal{H}}_1) \\ 0 & & \mathbb{Z} & & & & \mathbb{Z} & & 0 \end{array} . \tag{4.37}$$

The exact sequence yields $\pi_0(\tilde{\mathcal{I}}_2) = \mathbb{Z} \times \mathbb{Z}$; the set of $H''(\mathbf{k})$ are classified by two integers $(\alpha_{xy}, \beta_{xy})$. The first integer α_{xy} coming from the map ∂ gives $n_o(\pi, \pi)$; the second integer β_{xy} is related to the Chern number of H''. The basis elements of $\pi_0(\tilde{I}_2)$ are found by taking the image of the generator in $\pi_1(\tilde{\mathcal{H}}_1)$ and one of the preimages of the generator element in $\pi_0(\tilde{I}_1)$, which we denote by $H^2_\beta(\mathbf{k})$ and $H^2_\alpha(\mathbf{k})$ respectively. Any Hamiltonian in $\tilde{\mathcal{I}}_2$, up to a homotopy, can be written as

$$H'' = \beta_{xy} H^2_\beta \oplus \alpha_{xy} H^2_\alpha . \tag{4.38}$$

The generator $H^2_\beta(\mathbf{k}) = j^1 H_{\text{chern}}(\mathbf{k})$ where H_{chern} is the generator of $\pi_1(\tilde{\mathcal{H}}_1) = \pi_2(\tilde{\mathcal{H}}_0)$, *i.e.*, a 2D band insulator with Chern number $+1$. $H^2_\alpha(\mathbf{k})$ is defined such that $(\partial H^2_\alpha)(k) = H^1_\alpha(\pi, k)$ is the 1D insulator (4.27).

Explicitly, the generator

$$H^2_\alpha(\mathbf{k}) = \frac{1}{1+x^2+y^2}\begin{bmatrix}1-x^2-y^2 & 2(y+ix) \\ 2(y-ix) & x^2+y^2-1\end{bmatrix}_{(+-)} \ominus H^0_n \,, \tag{4.39}$$

where $x = \cot\frac{k_x}{2}, y = \cot\frac{k_y}{2}$. When k_x or $k_y = 0$ (or 2π), then $x^2+y^2 \to \infty$ and $H^2_\alpha(\mathbf{k}) = \left[\begin{smallmatrix}-1 & \\ & 1\end{smallmatrix}\right]_{(+-)} \ominus [-1]_{(+)}$ so H^2_α is normalized properly, *i.e.*, $H^2_\alpha \in \tilde{\mathcal{I}}_2$. When $k_x = k_y = \pi$, it can be seen that $H^2_\alpha(\mathbf{k}) = \left[\begin{smallmatrix}1 & \\ & -1\end{smallmatrix}\right]_{(+-)} \ominus H^0_n$ and the filled band is odd under inversion. Note that the Hamiltonian has Chern number +1. Since $\alpha_{xy} = n_o(\pi,\pi)$ (and the other TRIMs have $n_o = 0$ because of the normalization), this is related to the constraint $\tilde{G} \equiv \sum_{\boldsymbol{\kappa}} n_o(\boldsymbol{\kappa}) \bmod 2$.

From the construction of j^1 (4.34), the other generator $H^2_\beta(\mathbf{k}) = j^1 H_{\text{chern}}(\mathbf{k})$ takes the form

$$H^2_\beta(k_x,k_y) = \begin{cases} H^2_\alpha(2k_x,k_y) & 0 \le k_x \le \pi \\ \Pi H^2_\alpha(-2k_x,-k_y)\Pi^{-1} & \pi \le k_x \le 2\pi \end{cases} . \tag{4.40}$$

The second half $k_x \in [\pi, 2\pi]$ is the inversion image of the first half $k_x \in [0,\pi]$, the function in second half simplifies as

$$\begin{aligned} &\Pi H^2_\alpha(-\mathbf{k})\Pi^{-1} \\ &= \frac{1}{1+x^2+y^2}\begin{bmatrix}1 & \\ & -1\end{bmatrix}\begin{bmatrix}1-x^2-y^2 & -2(y+ix) \\ -2(y-ix) & x^2+y^2-1\end{bmatrix}\begin{bmatrix}1 & \\ & -1\end{bmatrix}^{-1} \ominus [1]H^0_n[1]^{-1} \\ &= H^2_\alpha(\mathbf{k}) \,. \end{aligned} \tag{4.41}$$

This allows us to write

$$H^2_\beta(k_x,k_y) = H^2_\alpha(2k_x,k_y) \,. \tag{4.42}$$

Since 2D inversion does not flip the Chern number, each half has a Chern number of +1. Evidently, the Chern number of the entire Brillouin zone is given by

$$\tilde{\mathcal{G}}_H = \alpha_{xy} + 2\beta_{xy} \,, \tag{4.43}$$

since H^2_α, H^2_β has Chern number 1, 2 respectively.

The decomposition (4.30) gives us six $\mathbb{Z}$ invariants in 2D: two from $\tilde{\mathcal{I}}_0$, one from each of the two $\tilde{\mathcal{I}}_1$, and two more from $\tilde{\mathcal{I}}_2$. The six invariants $(n, \alpha, \alpha_x, \alpha_y, \alpha_{xy}, \beta_{xy})$ are related to the properties of the original Hamiltonian $H(k_x,k_y)$ as follows:

- n gives the number of filled bands, generated by (4.25).
- $\alpha = n_o(0,0)$ is the number of odd-parity states at $(k_x,k_y) = (0,0)$, generated by (4.26).
- $\alpha_x = n_o(\pi,0) - n_o(0,0)$ involves the difference between two parities, generated by (4.27) $(k \to k_x)$.

- $\alpha_y = n_o(0,\pi) - n_o(0,0)$ involves the difference between two parities, generated by (4.27) $(k \to k_y)$.
- $\alpha_{xy} = n_o(\pi,\pi) - n_o(\pi,0) - n_o(0,\pi) + n_o(0,0)$ involves the parities at all TRIMs, generated by (4.39).
- β_{xy} relates to the Chern number: $\tilde{\mathcal{G}}_H = 2\beta_{xy} + \alpha_{xy}$, generated by (4.42).

The rule for the Chern number's parity, Eq. (4.6), follows from the last constraint here.

4.2.7 Going to higher dimensions

In d-dimensions, we want to calculate $\pi_0(\tilde{\mathcal{I}}_d)$, the set of components of the space of inversion symmetric Hamiltonians. To calculate this in a larger dimension, we will need to know $\pi_s(\tilde{\mathcal{I}}_{d-s})$ in lower dimensions.

The relevant spaces are $\tilde{\mathcal{H}}_d$ and $\tilde{\mathcal{I}}_d$. The general Hamiltonian space $\tilde{\mathcal{H}}_d = \Omega\tilde{\mathcal{H}}_{d-1}$ is the space of loops of Hamiltonians in $\tilde{\mathcal{H}}_{d-1}$, which become trivial on $k_x = 0$ as well as on all the other boundaries $k_i = 0$ of the Brillouin zone. Their homotopy groups are given by $\pi_s(\tilde{\mathcal{H}}_d) = \pi_{s+d}(\tilde{\mathcal{H}}_0)$.

The homotopy groups of the subspace $\tilde{\mathcal{I}}_d \subset \tilde{\mathcal{H}}_d$ are harder to find. This space is homeomorphic to $\tilde{\mathcal{I}}_d \approx \mathfrak{P}(\tilde{\mathcal{H}}_{d-1}; v_{d-1}, \tilde{\mathcal{I}}_{d-1})$, since half of the Brillouin zone determines the Hamiltonian. The homotopy groups of $\tilde{\mathcal{I}}_d$ are therefore given by the relative homotopy groups $\pi_s(\tilde{\mathcal{I}}_d) \approx \pi_{s+1}(\tilde{\mathcal{H}}_{d-1}, \tilde{\mathcal{I}}_{d-1})$ (see Thm. 15). Via the relative homotopy exact sequence (4.18), one can relate $\pi_{s+1}(\tilde{\mathcal{H}}_{d-1}, \tilde{\mathcal{I}}_{d-1})$ to $\pi_s, \pi_{s+1}(\tilde{\mathcal{H}}_{d-1})$ and $\pi_s, \pi_{s+1}(\tilde{\mathcal{I}}_{d-1})$. The homotopy structure of $\tilde{\mathcal{I}}_d$ depends on that of $\tilde{\mathcal{I}}_{d-1}$. Iterating this process reduces the problem to that of the basic objects $\tilde{\mathcal{H}}_0$ and $\tilde{\mathcal{I}}_0$.

Specializing to 3D, we follow the same prescription as before to decompose Hamiltonians.

$$\mathcal{I}_3 \approx \tilde{\mathcal{I}}_0 \times \tilde{\mathcal{I}}_1^3 \times \tilde{\mathcal{I}}_2^3 \times \tilde{\mathcal{I}}_3 \,. \tag{4.44}$$

The homotopy group $\pi_0(\tilde{\mathcal{I}}_3) = \pi_1(\tilde{\mathcal{H}}_2, \tilde{\mathcal{I}}_2)$ can be computed from

$$\begin{tikzcd} \pi_1(\tilde{\mathcal{I}}_2) \arrow[r, "i^2_{(1)}"] & \substack{\pi_1(\tilde{\mathcal{H}}_2) \\ 0} \arrow[r, "j^2_{(0)}"] & \pi_0(\tilde{\mathcal{I}}_3) \arrow[r, "\partial"] & \substack{\pi_0(\tilde{\mathcal{I}}_2) \\ \mathbb{Z}^2} \arrow[r, "i^2_{(0)}"] & \substack{\pi_0(\tilde{\mathcal{H}}_2) \\ \mathbb{Z}} \end{tikzcd} \,. \tag{4.45}$$

We know that $\pi_0(\tilde{\mathcal{I}}_2) = \mathbb{Z}^2$ from the previous section and $\pi_0(\tilde{\mathcal{H}}_2) = \pi_2(\tilde{\mathcal{H}}_0) = \mathbb{Z}$ corresponds to the Chern number $\tilde{\mathcal{G}}_H$. In addition, the homotopy group $\pi_1(\tilde{\mathcal{H}}_2) = \pi_3(\tilde{\mathcal{H}}_0) = 0$ is trivial, so $\pi_1(\tilde{\mathcal{I}}_2)$ is irrelevant to the problem.

The map $i^2_{(0)} : \pi_0(\tilde{\mathcal{I}}_2) \to \pi_0(\tilde{\mathcal{H}}_2)$ is given by (4.43) which is surjective, hence $\mathrm{coker}(i^2_{(0)}) = \mathbb{Z}$. It follows that $\pi_0(\tilde{\mathcal{I}}_3) = \mathbb{Z}$; 3D insulators can be written as $\alpha_{xyz} H^3_\alpha$ where α_{xyz} is an integer and H^3_α is the generator. To relate α_{xyz} to band-structure properties (like n_o), we place the maps ∂ and i^2_* under further scrutiny. The relevant part of the exact sequence is:

$$\begin{tikzcd} 0 \arrow[r] & \substack{\pi_0(\tilde{\mathcal{I}}_3) \\ \mathbb{Z}[\alpha_{xyz}]} \arrow[r, "\partial"] & \substack{\pi_0(\tilde{\mathcal{I}}_2) \\ \mathbb{Z}^2[\alpha_{yz}, \beta_{yz}]} \arrow[r, "i^2_{(0)}"] & \substack{\pi_0(\tilde{\mathcal{H}}_2) \\ \mathbb{Z}[\tilde{G}]} \end{tikzcd} \,, \tag{4.46}$$

where the brackets show the names of the integers that are used to label the elements of the group. The map $i^2_{(0)}$ is given by $\tilde{G} = \alpha_{yz} + 2\beta_{yz}$. The kernel of the map is the set $(\alpha_{yz}, \beta_{yz}) = (2m, -m)$ for integers m. Since the kernel is isomorphic to $\pi_0(\tilde{\mathcal{I}}_3)$, we can define α_{xyz} to be m; hence ∂ is defined by $\partial\alpha_{xyz} = (\alpha_{yz}, \beta_{yz}) = (2\alpha_{xyz}, -\alpha_{xyz})$.

In terms of the band structure invariants, we have

$$\begin{aligned} 2\alpha_{xyz} &= \alpha_{yz}\big|_{k_x=\pi} \\ &= n_o(\pi,\pi,\pi) \, . \end{aligned}$$

Hence $n_o(\pi,\pi,\pi)$ is even. Note that all other n_o's are 0 because the Hamiltonian is normalized – adding back the lower-dimensional parts of the Hamiltonian that have been subtracted off does not change the parity of $\sum_{\boldsymbol{\kappa}} n_o(\boldsymbol{\kappa})$, so it remains even.

Explicitly, the generator H^3_α is

$$H^3_\alpha = \big[t_0\tau^z + \tau^x(\mathbf{t}\cdot\boldsymbol{\sigma})\big]_{(++--)} \ominus 2H^0_n \, , \tag{4.47}$$

where

$$(t_0, t_x, t_y, t_z) = \frac{(1 - x^2 - y^2 - z^2,\, 2y,\, 2z,\, 2x)}{1 + x^2 + y^2 + z^2} \, , \quad \text{with } x = \cot\tfrac{k_x}{2}, y = \cot\tfrac{k_y}{2}, z = \cot\tfrac{k_z}{2} \, .$$

At $k_x = k_y = k_z = \pi$, $(t_0, t_x, t_y, t_z) = (1, 0, 0, 0)$ and there are two filled bands with odd parity. At the plane $k_x = \pi$ the Hamiltonian reduces to two copies of (4.39), but with opposite Chern numbers so that the net Chern number is 0. One can think of the two subspaces of ∂H^3_α as H^2_α (Chern $+1$) and $H^2_\alpha \ominus H^2_\beta$ (Chern -1).

Therefore, there are 12 $\mathbb{Z}$ invariants in 3D, the eleven emphasized in the main part of the article together with the total number of occupied bands. They relate to the band structure invariants as follows:

- n is the number of filled bands.
- $\alpha = n_o(0,0,0)$.
- $\alpha_x = n_o(\pi,0,0) - n_o(0,0,0)$,
  $\alpha_y = n_o(0,\pi,0) - n_o(0,0,0)$,
  $\alpha_z = n_o(0,0,\pi) - n_o(0,0,0)$.
- $\alpha_{yz} = n_o(0,\pi,\pi) - \alpha_y - \alpha_z - \alpha$,
  $\alpha_{zx} = n_o(\pi,0,\pi) - \alpha_z - \alpha_x - \alpha$,
  $\alpha_{xy} = n_o(\pi,\pi,0) - \alpha_x - \alpha_y - \alpha$.
- $\beta_{yz} = \frac{1}{2}(\tilde{G}^{yz} - \alpha_{yz})$,
  $\beta_{zx} = \frac{1}{2}(\tilde{G}^{zx} - \alpha_{zx})$,
  $\beta_{xy} = \frac{1}{2}(\tilde{G}^{xy} - \alpha_{xy})$.
- $\alpha_{xyz} = \frac{1}{2}\big(n_o(\pi,\pi,\pi) - \sum\alpha_{\mu\nu} - \sum\alpha_\mu - \alpha\big)$.

The last equation explicitly written out as a function of $n_o(\boldsymbol{\kappa})$ is

$$\begin{aligned} 2\alpha_{xyz} = {} & n_o(\pi,\pi,\pi) \\ & - n_o(0,\pi,\pi) - n_o(\pi,0,\pi) - n_o(\pi,\pi,0) \\ & + n_o(\pi,0,0) + n_o(0,\pi,0) + n_o(0,0,\pi) \\ & - n_o(0,0,0)\,. \end{aligned}$$

From the formula, it is clear that the sum of parities of $n_o(\boldsymbol{\kappa})$ at the eight TRIMs is even, *i.e.*, Eq. (4.5).

In every higher dimension d, $\tilde{\mathcal{I}}_d$ has a $\mathbb{Z}$ invariant corresponding to the inversion parity $n_o(\pi,\dots,\pi)$ generated by H^d_α. For the even dimensions $d = 2s$, there is a second $\mathbb{Z}$ invariant corresponding to the s^{th} Chern class, generated by H^d_β. Hence $\pi_0(\tilde{\mathcal{I}}_{2s}) = \mathbb{Z}^2$ and $\pi_0(\tilde{\mathcal{I}}_{2s+1}) = \mathbb{Z}$.

The generator for the s^{th} Chern class is as follows. Let $\{\Gamma^1,\Gamma^2,\dots,\Gamma^{2s+1}\}$ be $2^s \times 2^s$ gamma matrices satisfying the Clifford algebra $\Gamma^i\Gamma^j+\Gamma^j\Gamma^i = 2\delta^{ij}$. First we warp the Brillouin zone to a sphere: $T^{2s}[k_1,\dots,k_{2s}] \to S^{2s}[\hat{\mathbf{n}}]$ by sending $\mathbf{k} = (\pi,\dots,\pi)$ to $\hat{\mathbf{n}} = (1,0,0,\dots)$ and all the planes bounding the Brillouin zone ($k_i = 0$) to $(-1,0,0,\dots)$. We choose the map so that it is inversion symmetric (*i.e.*, when $\mathbf{k} \to -\mathbf{k}$) all components of $\hat{\mathbf{n}}$ except the first switch sign. The Hamiltonian can be defined then as

$$H^{2s}_c(\mathbf{k}) = \hat{\mathbf{n}} \cdot \boldsymbol{\Gamma}\,, \tag{4.48}$$

where $\boldsymbol{\Gamma}$ is the $(2s+1)$-vector of gamma matrices. The generator (4.39) is an example of this construction for $d = 2s = 2$. The inversion matrix is given by the first gamma matrix: $\Pi = \Gamma^1$, and we can see that all the occupied states are odd at $\mathbf{k} = (\pi,\dots,\pi)$, so $n_o = 2^{s-1}$ there. At the other TRIMs, the occupied states have even inversion parity.

The s^{th} Chern number C_s may be computed by the formula:

$$C_s = \frac{1}{s!}\left(\frac{i}{2\pi}\right)^s \int \operatorname{Tr}[P(dP)^{2s}]\,, \tag{4.49}$$

where $P(\mathbf{k}) = \frac{1}{2}(1-H(\mathbf{k}))$ is the projector onto the filled states and d is the exterior derivative in the Brillouin zone. Evaluating the integral shows that $C_s = \pm 1$ for the Hamiltonian H^{2s}_c.

In $2s$-dimensions, Eq. (4.37) generalized to more dimensions, gives a preliminary way of choosing the generators: H^{2s}_β is the image under j of a generator of $\pi_0(\tilde{\mathcal{H}}_{2s})$ and H^{2s}_α is an arbitrary preimage under ∂^{-1} of the generator of $\pi_0(\tilde{\mathcal{I}})_{2s-1}$. Any Hamiltonian can be expanded as

$$H = \beta_{2s} H^{2s}_\beta \oplus \alpha_{2s} H^{2s}_\alpha\,. \tag{4.50}$$

H^{2s}_c can be used for the generator H^{2s}_α. To see this, we decompose H^{2s}_c in terms of the original pair of generators H^{2s}_α, H^{2s}_β. The s^{th} Chern number of H^{2s}_β is 2, since it is constructed using the map j which takes a general insulator to an inversion symmetric one by duplicating it in each half of the Brillouin zone [see Eq. (4.34)]. At all the TRIMs, $H_\beta^{2s}(\boldsymbol{\kappa}) = v_0$ and so n_o is zero. Using Eq. (4.50) for H_c^{2s} implies

$$C_s(H_c^{2s}) = 1 = 2\beta_{2s} + \alpha_{2s} C_s(H_\alpha^{2s}) \,, \tag{4.51a}$$

$$n_o(H_c^{2s}) = 2^{s-1} = 0 + \alpha_{2s} n_o(H_\alpha^{2s}) \,. \tag{4.51b}$$

The first expression requires α_{2s} to be odd, and the second requires it to be a factor of 2^{s-1}. Hence $\alpha_{2s} = \pm 1$ and we can use H_c^{2s} as the generator H_α^{2s}. Since every Hamiltonian can be expressed by Eq. (4.50), the number of odd inversion-parity states $n_o(\pi, \pi, \dots)$ is always a multiple of 2^{s-1}.

In terms of the general Hamiltonians in $\mathcal{I}_{2s}$, the total number of odd parity states at all the TRIMs must be a multiple of 2^{s-1}. Furthermore,

$$\frac{1}{2^{s-1}} \sum_{\text{TRIM } \mathbf{k}} n_o(\mathbf{k}) \equiv C_s \pmod 2 \qquad \text{in } 2s\text{-dimensions.} \tag{4.52}$$

In $(2s+1)$-dimensions, the Hamiltonians at $k_x = 0$ and π are both $2s$-dimensional inversion symmetric Hamiltonians, and they must have the same Chern number, so the constraint on the parities is

$$\sum_{\text{TRIM } \boldsymbol{\kappa}} n_o(\boldsymbol{\kappa}) \equiv 0 \pmod{2^s} \qquad \text{in } (2s+1)\text{-dimensions.} \tag{4.53}$$

This is related to the $(2s+1)$-dimensional Chern-Simons integral $\theta_{2s+1} \in [0, 2\pi)$ by

$$\frac{\theta_{2s+1}}{\pi} = \frac{1}{2^s} \sum_{\text{TRIM } \boldsymbol{\kappa}} n_o(\boldsymbol{\kappa}) \bmod 2 \,, \tag{4.54}$$

because we can evaluate θ by writing the Hamiltonian as the $k_x = \pi$ cross-section of a Hamiltonian in one more dimension, and then determining the Chern number of that Hamiltonian [60] using Eq. (4.52).

4.3 Physical properties and the parities

Now we will find the physical properties associated with the parities $n_o(\boldsymbol{\kappa})$ at the TRIMs. First we show that in the space of $\mathbb{Z}^8$ possible combinations of n_o's, we find that a subset of "frozen insulators,"[10] which can be constructed without electron hoppings. The frozen insulators do not yield any *dynamical* physical properties. Since combining two frozen insulator is still a frozen insulator, its parities n_o's form a subspace within $\mathbb{Z}^8$. As we show in the next section, the quotient of $\mathbb{Z}^8$ with that subspace is $\mathbb{Z}_2^3 \times \mathbb{Z}_4$. In other words, if we consider a courser classification of the parities where we do not distinguish frozen insulators from the vacuum, we only have $2^3 \times 4 = 32$ possible combinations.

---

[10] Or, as Ashvin calls them, *dead vegetables*.

In Sec. 4.3.2, we show that of the 32 parities combinations, only 16 of them can occur only in non-insulators; the next section shows that 14 of the remaining ones have a nonzero Hall conductivity, and the last section shows that the two remaining insulators can be distinguished by whether they have a magnetoelectric susceptibility or not.

4.3.1 A coarser classification: grouping phases with identical responses

So far, we have classified insulators by a set of integers without regards to their physical significance. We would now like to look for physical interpretations of the parities that classify the phases. One often uses parity symmetry to prove that a quantity vanishes, as in selection rules for certain types of transitions in a molecule. We will find that, in bulk systems, some sets of inversion parities imply the *non-vanishing* of a physical quantity. We would like to determine all such relationships.

We will search for sets of parities n_o's that ensure that a material has nontrivial responses by considering the opposite problem. That is, we will first find all the dull insulators, ones in which the electrons cannot move and therefore do not have any response: we call them frozen insulators. Then we will know by a process of elimination which materials have a chance of having an interesting response. We will find that many of the combinations of n_o's can occur in frozen insulators. Hence, even though the n_o quantum describe infinitely many phases, only finitely many of them have distinctive behavior. In the next section, we will determine the behavior for each of the phases with distinct properties.

To picture the different types of insulator, represent the n_o quantum numbers geometrically, as a vector in an eight-dimensional cubic lattice, which we write as $\vec{n}_o$.[11] Let us understand the crystal structure of this imaginary crystal. The vectors $\vec{n}_o$ for "frozen states" form a sublattice. One may imagine that there are two 'elements' A and B making up the compound, with the element A residing at the frozen insulator sublattice, and the other element residing at the remaining sites. The vectors of frozen states form a sublattice because the sum of two frozen vectors is also frozen: combining the orbitals of two materials together in the same volume of space (without any interactions between them) corresponds to adding their $\vec{n}_o$ vectors.

The frozen sublattice can then be characterized by some conditions similar to the description of a face-centered cubic (FCC) lattice. (For example, sodium ions in NaCl form an FCC, the sublattice of a cubic lattice consisting of the points whose coordinates sum to an even number.) For the crystal of $\vec{n}_o$ vectors, the frozen sublattice can be described as

---

[11] We denote vectors in this 8D space with a $\vec{}$ symbol, while physical (3D) vectors remain in **boldface**.

follows. First define

$$w_{xyz} = \sum_{\boldsymbol{\kappa}} n_o(\boldsymbol{\kappa}) \bmod 4\,, \tag{4.55a}$$

$$u_z = \sum_{\boldsymbol{\kappa}\perp\mathbf{R}_z} n_o(\boldsymbol{\kappa}) \bmod 2\,, \tag{4.55b}$$

and similarly for u_x and u_y. As we will show momentarily, the frozen site are ones where these remainders vanishes.

Returning back to our 3D system, we would like to identify the frozen crystals and their corresponding $\vec{n}_o$'s. Consider an ionic or frozen insulator with positive nuclei on the Bravais lattice and electrons fixed on certain sites, and with all hopping amplitudes equal to zero. The simplest example that is inversion symmetric involves a single electron per unit cell located at half of a Bravais lattice vector $\mathbf{d} = \frac{\mathbf{R}}{2}$ and its translates. When there are two electrons per unit cell, there is more freedom: they may be located at any point together with its inversion image. From these two cases all other insulators may be constructed.

The parities of the former insulator depend on $\boldsymbol{\kappa}$, and are found by transforming from the localized basis labeled by $\mathbf{R}$ to plane wave states labeled by $\mathbf{k}$, $|\mathbf{d}\rangle_{\mathbf{k}} = \sum_{\mathbf{R}} e^{i\mathbf{k}\cdot(\mathbf{R}+\mathbf{d})}|\mathbf{R}+\mathbf{d}\rangle$. Suppose that the orbital occupied by the electron is odd (for example). Then at a TRIM, the inversion eigenvalue is given by

$$\Pi|\boldsymbol{\kappa}\rangle_{\mathbf{d}} = -e^{2i\mathbf{d}\cdot\boldsymbol{\kappa}}|\boldsymbol{\kappa}\rangle_{\mathbf{d}}\,, \tag{4.56}$$

hence $n_o(\boldsymbol{\kappa})$ is one for each $\boldsymbol{\kappa}$ such that $\frac{2\mathbf{d}\cdot\boldsymbol{\kappa}}{\pi}$ is even. These eight vectors, (one corresponding to each $\mathbf{d}$,) which we call $\vec{f}_{\mathbf{d}}$, generate the set of $\vec{n}_o$ for frozen insulators. (The additional n_o's that come from frozen insulators with two electrons per unit cell just reproduce $\vec{f}_{\mathbf{d}=0}$. They have one odd and one even state at each TRIM.) Rewriting the above expression, the numbers of odd states at TRIMs are described by

$$\vec{f}_{\mathbf{d}}(\boldsymbol{\kappa}) = \Big(1 - \frac{\boldsymbol{\kappa}}{\pi}\cdot\mathbf{d}\Big) \bmod 2\,, \tag{4.57}$$

assuming the electrons to be in odd orbitals at $\mathbf{d}$. For each nonzero TRIM $\boldsymbol{\kappa}$, $\vec{f}_{\mathbf{d}}$ contains four zeros and four ones, and $\vec{f}_0(\boldsymbol{\kappa}) = 1$.

The goal is now to determine what vectors $\vec{n}_o$ are integer linear combinations of the $\vec{f}$'s. There is a coordinate system for $\mathbb{Z}^8$ where this is easy to solve. One has to find a set of basis vectors $\vec{v}_1, \ldots, \vec{v}_8$ for $\mathbb{Z}^8$, such that $n_1\vec{v}_1, n_2\vec{v}_2, \ldots, n_8\vec{v}_8$ is a basis for the frozen vectors $\vec{f}$ (where $n_1, \ldots n_8$ are certain integers). Then if a vector $\vec{n}_o$ is represented by $a_1\vec{v}_1 + \cdots + a_8\vec{v}_8$ in the new coordinate system, the criteria that it is a frozen vector are simple – a_i has to be a multiple of n_i. The classification theorem for finitely generated abelian groups describes an algorithm for finding such bases.

We find the following basis for the frozen crystals, $\vec{m}_0$, $\vec{m}_x$, $2\vec{m}_{xy}$, and $4\vec{m}_{xyz}$ and vectors symmetric with these. Here, $\vec{m}_0$ is the vector with ones at all corners of the cube, $\vec{m}_x$ is the

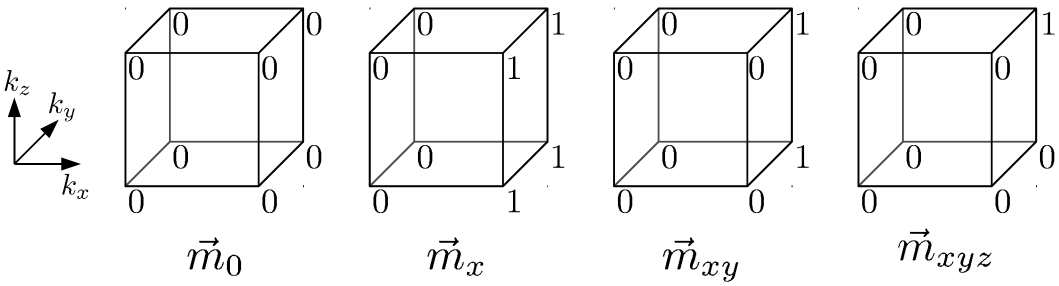

Figure 4.6: Representative examples of $\vec{n}_o$ basis.

The four cubes shows various $\vec{n}_o \in \mathbb{Z}^8$ which represents configurations n_o's at each TRIM. These four, along with their rotations $\vec{m}_y$, $\vec{m}_z$, $\vec{m}_{yz}$, $\vec{m}_{zx}$, form a basis for the set of all $\vec{n}_o$ vectors [see Eq. (4.58)]. The whole range of quantized behavior that can be found in insulators with inversion symmetry can be found with just linear combinations of the latter two $\vec{m}_{xyz}$ and $\vec{m}_{xy}$ (and the two rotations of $\vec{m}_{xy}$), because they form a basis for the unit cell of the 8-dimensional lattice of frozen and non-frozen $\vec{n}_o$ vectors.

vector with ones on the *face* of the cube defined by $\kappa_x = \pi$ (and zeros elsewhere), $\vec{m}_{xy}$ is the vector with ones on the *edge* defined by $\kappa_x = \kappa_y = \pi$, and $\vec{m}_{xyz}$ is the vector with a one at the *vertex* $\kappa_x = \kappa_y = \kappa_z = \pi$. The configurations of n_o's for each basis vector is shown in Fig. 4.6.

On the other hand, the vectors $\vec{m}_0$, $\vec{m}_i$, $\vec{m}_{ij}$ and $\vec{m}_{xyz}$ (without the factors of 2 and 4) span all combinations of 8 integers. Therefore any vector $\vec{n}_o$ can be decomposed as

$$\vec{n}_o = a_0\vec{m}_0 + \sum_i a_i\vec{m}_i + \sum_{i<j} a_{ij}\vec{m}_{ij} + a_{xyz}\vec{m}_{xyz}\,, \tag{4.58}$$

for integers a_0, a_i, *etc.* Hence, the quotient of $\mathbb{Z}^8$ by the subspace span by the $\vec{f}_{\mathbf{d}}$'s is $\mathbb{Z}_2^3 \times \mathbb{Z}_4$, generated by $\vec{m}_{xy}$, $\vec{m}_{zx}$, $\vec{m}_{yz}$ and $\vec{m}_{xyz}$. Since there are $2^3 \times 4$ possible combinations, this crystal has the chemical formula AB_{31}, that is, the unit cell contains 32 lattice points; one is frozen, and the other 31 can be represented in terms of four vectors (see Fig. 4.6):

$$\vec{n}_o = a_{xy}\vec{m}_{xy} + a_{xz}\vec{m}_{xz} + a_{yz}\vec{m}_{yz} + a_{xyz}\vec{m}_{xyz}\,, \tag{4.59}$$

where the a_{ij}'s are each 0 or 1 and a_{xyz} is 0, 1, 2 or 3.

To relate this with the definitions of w_{xyz} and u_α's from (4.55), we can check how these quantities depend on a's by computing w and u for Eq. (4.58). It is trivial to see that

$$w_{xyz} \equiv a_{xyz} + 2a_{yz} + 2a_{zx} + 2a_{xy} \pmod 4\,, \tag{4.60a}$$

$$u_x \equiv a_{yz} \pmod 2\,, \tag{4.60b}$$

$$u_y \equiv a_{zx} \pmod 2\,, \tag{4.60c}$$

$$u_z \equiv a_{xy} \pmod 2\,. \tag{4.60d}$$

This confirms our earlier assertion that w_{xyz} and u_α's alone characterizes all $\vec{n}_o$ modulo frozen crystals.

Compounds occupying equivalent positions in the $\vec{n}_o$ crystal (and with equal Chern numbers) have equivalent quantized response properties[12] as they differ by the addition of a frozen state. In the following sections, we will determine the properties of each of the different types of compound in the unit cell. Since the u_α's and w_{xyz} distinguish among the 32 sites in a unit cell, it will be these parameters that determine all the quantized response properties. (Note that materials corresponding to equivalent sites in this classifying crystal could have different *static* properties. Likely the only property of this type is that frozen insulators can have intrinsic electric polarization. Since polarization is defined modulo one-half of a Bravais lattice vector, there are still only a few combinations of the n_o-integers that have interpretations.)

To see in general that two materials (H and H') with the same Chern numbers whose $\vec{n}_o$ vectors differ by a vector in the frozen lattice have the same response whether the vector has negative or positive coefficients, write $\vec{n}_o - \vec{n}'_o = \sum_{\mathbf{d}} \vec{n}_{\mathbf{d}} \vec{f}_{\mathbf{d}}$. Define $\vec{f}_+$ to be the sum of just the terms in this sum with positive coefficients, and define $\vec{f}_-$ similarly as the sum of the terms with negative coefficients. Then $\vec{f}_\pm$ both are realized for ionic crystals. Furthermore, $\vec{n}_o + \vec{f}_- = \vec{n}'_o + \vec{f}_+$, so the materials obtained by combining the ionic crystals $\vec{f}_-$ and $\vec{f}_+$ with H and H' respectively belong to the same phase. Hence these materials and H and H' all have the same quantized response properties.

4.3.2 Constraint on parities in gapped materials

We will start by showing that if $w_{xyz} = \sum_{\boldsymbol{\kappa}} n_o(\boldsymbol{\kappa})$ is odd for a certain band structure, then this band structure is not an insulator [Eq. (4.5)]. This determines the basic behavior of a crystal with the $\vec{n}_o$ vector $\vec{m}_{xyz}$ (see Fig. 4.6), and more generally, any state with an odd multiple of $\vec{m}_{xyz}$ [see Eq. (4.59)].

There are two ways to see that w_{xyz} must be even in an insulator. For the first one, let us understand a more general question. Consider a Hamiltonian (not necessarily a gapped one) that is being altered. What happens when the parities of the occupied states at the TRIMs change? These parities can change if an even state at the TRIM below the Fermi energy and an odd state above the Fermi energy (or vice versa) pass through one another. Each time $n_o(\boldsymbol{\kappa})$ changes by 1 by means of such an interchange, a pair of Weyl points that are inversion images of each other appears or disappears. Weyl points are points in the Brillouin zone when the conduction and valence bands touch, hence when they are present, the material is not an insulator. Therefore, if the insulator starts out as a frozen insulator with all $n_o(\boldsymbol{\kappa}) = 0$, then the first change of $n_o(\boldsymbol{\kappa})$ makes the material non-insulating.

Furthermore, the material cannot become insulating again through a gaping out of the Weyl points, unless more n_o's change. A Weyl point is stable in isolation because it has

---

[12] Other properties, such as the dielectric constant, do not have to be the same of course.

a ‘chirality’ ±1 and the total chirality of Weyl points is conserved.[13] A pair of inversion symmetric Weyl points can either annihilate with a second pair or with one another. The latter cannot occur when the parities at the TRIMs are fixed, because by symmetry they would have to meet one another at a TRIM. Annihilating there would cause a change in the parities at it.

Now start from a trivial (*i.e.*, a frozen) Hamiltonian, with all electrons glued to the Bravais lattice; in this Hamiltonian, all the states at TRIMS are even. After an odd number of changes of $n_o(\boldsymbol{\kappa})$, there are an odd number of pairs of Weyl points, so the crystal is not insulating. Some of these may annihilate two pairs at a time, but one pair always remains. In general the number of pairs of Weyl points and the sum of the $n_o(\boldsymbol{\kappa})$'s are both even or both odd.

A material with a single pair of Weyl points (the simplest case that can occur with w_{xyz} odd) would be an example of a Weyl semimetal, and would have some unusual type of conductivity. Assuming the material is not doped, the Fermi energy would be forced to line up with the energy at the cone point, resulting in a density of states equal to zero. This is because the area of all electron-like Fermi surfaces has to cancel the area of the hole-like Fermi surfaces (due to the Luttinger theorem). Thus, if there is only one pair of Weyl points, the Fermi energy cannot move away from zero, since it would then intersect the cones in small Fermi spheres containing the same type of carrier. This phenomenon does not occur if time-reversal and inversion symmetry are both present, since a Weyl point is not invariant under the product of the symmetries (its chirality is reversed by them). Weyl points can also occur when $n_o(\boldsymbol{\kappa})$ is even [159], but in that case more symmetry would be necessary to pin the Fermi energy to them (since there would be additional pairs of Weyl points).

The stability of the Weyl points is explained in part by the basic result on degeneracies of eigenvalues, rather than by symmetry: in order to tune a Hamiltonian to a point where there is a degeneracy, three parameters are sufficient. Since $H(\mathbf{k})$ is a function of three momenta, these may be tuned to a point where there is a degeneracy, provided H is close enough to having a degeneracy in the first place.

Any set of parities $n_o(\boldsymbol{\kappa})$ satisfying $\prod_{\boldsymbol{\kappa}} \eta_{\boldsymbol{\kappa}} = 1$ can be realized in an insulator. There is never a direct phase transition (even with fine tuning) between two such phases when two or more $\eta_{\boldsymbol{\kappa}}$'s flip sign. When two modes cross at one TRIM in order to change the value of n_o there, Weyl points will form, and the system will be a semimetal. The Weyl points must then move to the second TRIM and reannihilate, so that the system becomes an insulator again, as illustrated in Fig. 4.7. There can be direct transitions where the value of n_o at a single TRIM changes by 2. However, such transitions are always fine-tuned, because two states above and below the Fermi energy have to switch places all at once.

The alternative argument for the presence of Weyl points when Eq. (4.5) is violated does not involve changing the Hamiltonian around and following its evolution. Instead, it is based on studying the Bloch states as a function of $\mathbf{k}$. Let us first suppose there is a single occupied

---

[13] In fact, Weyl points are Berry-flux monopoles in momentum space, so they have a conserved charge, see Ref. [97, Chap. 8, pp. 86–104].

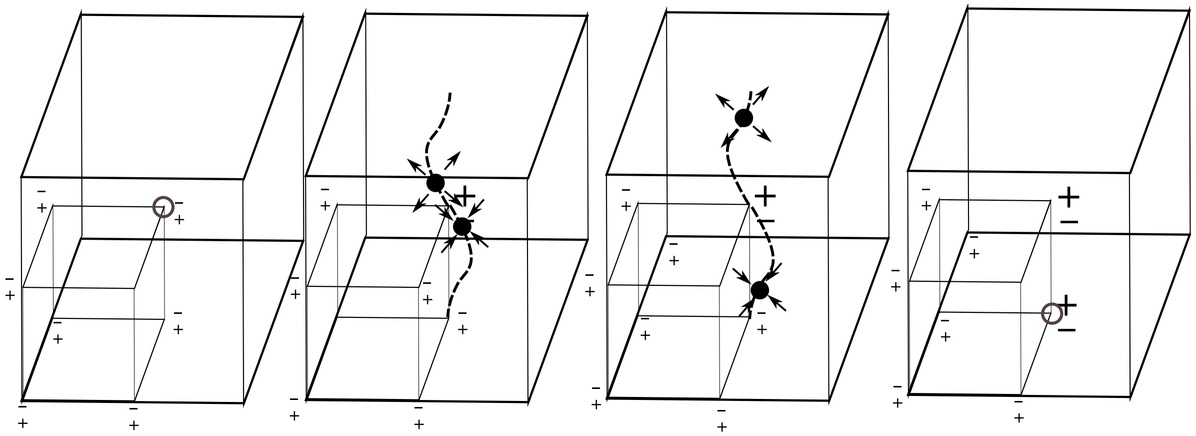

Figure 4.7: Changing the parities of bands at two TRIMs.

The figures represent the Brillouin zone of a system with two bands, one of which is filled. Initially, all the filled bands have parity +1, but the parities at two points are changed with the assistance of Weyl points which also act as monopoles in the Berry flux. A pair of monopoles forms at one TRIM and they move to another TRIM where they annihilate. In the process, the parities of the states at both TRIMs are reversed. The open circles indicate where the monopoles start out and disappear.

band $|\psi_{1\mathbf{k}}\rangle$. To determine whether the wavefunction is even or odd, let us take its overlap with an even orbital $|s\rangle$ centered on the origin, $s_1(\mathbf{k}) = \langle s|\psi_{1\mathbf{k}}\rangle$. Plot the solutions in the Brillouin zone to

$$s_1(\mathbf{k}) = 0\,. \tag{4.61}$$

This equation is a complex-valued, amounting to two equations in three variables, so its solutions are generically 1D curves. At a TRIM, $\psi_{1\boldsymbol{\kappa}}(\mathbf{r})$ is either even or odd. If it is odd, its overlap with $|s\rangle$ vanishes. Generically, if it is even, the overlap does not vanish. Hence, there is one curve through each TRIM at which $|\psi_{1\boldsymbol{\kappa}}\rangle$ is odd. But since the curves are inversion symmetric, they must pass through an even number of TRIMs (see Fig. 4.8). Hence, the total number of TRIMs where $\Pi|\psi_{1\boldsymbol{\kappa}}\rangle = -|\psi_{1\boldsymbol{\kappa}}\rangle$ is even.

When there are several filled bands which do not touch each other, $\prod_{\boldsymbol{\kappa}} \eta_a(\boldsymbol{\kappa}) = 1$ for the a^{th} band separately, and $\prod_{\boldsymbol{\kappa}} \eta_{\boldsymbol{\kappa}} = 1$ follows. If bands do touch, another step is required to see that the product is still one, even though the product for a single band may be -1. Consider the curves determined by $s_a(\mathbf{k}) = \langle s|\psi_{a\mathbf{k}}\rangle = 0$ for all the occupied bands $1 \leq a \leq n$. Some of these curves may be open arcs; they may end at a Weyl point between band a and band $a \pm 1$ because $s_a(\mathbf{k})$ becomes discontinuous there. If that occurs, then there is always an arc leaving the Weyl point in the other band. Putting all the arcs from the occupied states together therefore produces a set of closed curves; these curves will be variegated if the arcs in each band are imagined to have different colors, but they are still closed. Hence we can still deduce that they pass through the TRIMs an even number of times total, *i.e.*,

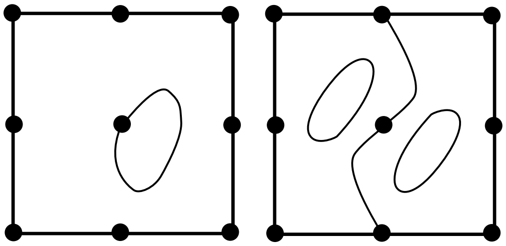

Figure 4.8: Inversion symmetric curves in the Brillouin zone.

Curves which are inversion symmetric must pass through an even number of TRIMs. On the left is an attempt at drawing a curve that passes through one TRIM fails to be inversion symmetric. On the right is an inversion symmetric figure; if there is just one curve passing through one of the TRIMs, it must go all the way around the Brillouin zone and pass through another TRIM on the way.

$\sum_{\boldsymbol{\kappa}} n_o(\boldsymbol{\kappa})$ is even.

4.3.3 Polarization and Hall conductivity

Next, we interpret the u indices, showing that $u_\alpha \equiv \tilde{\mathcal{G}}_{H\alpha}$ (mod 2) for each of the three directions $\alpha = x, y, z$, with $\tilde{\mathcal{G}}_{H\alpha} = \tilde{\mathcal{G}}_H \cdot \mathbf{R}_\alpha$. (Recall that $\tilde{\mathcal{G}}_H$ have integer coefficients and are related to the Hall conductivity by $\sigma_H = \frac{e^2}{h}\tilde{\mathcal{G}}_H$.) This result is equivalent to Eq. (4.6) and applies to 14 of the 16 insulating phases.

We will prove Eq. (4.6) momentarily, but it is logically necessary to derive the expression for the electrostatic polarization in one-dimension first. The polarization is not captured by the AB$_{31}$ crystal because it is not a *response* property. (With polarization taken into account, there are actually 8 × 16 different types of behavior that can occur in inversion symmetric phases.) Both polarization and the Hall coefficient can be expressed in terms of to the Berry connection, a vector function in momentum space. For a single band, the Berry connection is defined by

$$\mathbf{A}_a(\mathbf{k}) = i\langle u_{a\mathbf{k}}|\nabla_{\mathbf{k}}|u_{a\mathbf{k}}\rangle \tag{4.62}$$

and the total Berry connection $\mathcal{A}(\mathbf{k})$ is the sum of the Berry connections of the occupied bands. Here $u_{a\mathbf{k}}$ is the periodic part of the Bloch wavefunctions, *i.e*, $\psi_{a\mathbf{k}} = e^{i\mathbf{k}\cdot(\mathbf{r}-\mathbf{r}_0)}u_{a\mathbf{k}}(\mathbf{r})$. This expression includes an arbitrary origin $\mathbf{r}_0$ for the plane wave.

Consider a crystal in one-dimension. We will prove that the intrinsic polarization is given (modulo e times a lattice vector) by Eqs. (4.8), (4.9) starting from the formula in Ref. [167] for the intrinsic polarization of an arbitrary crystal, namely

$$P = P_e - \sum_i Z_i e(x_i - x_0)\,. \tag{4.63}$$

The first term is the polarization of the electrons relative to an origin, x_0, the second term is the polarization of the nuclei in the unit cell relative to x_0, Since the electrons are delocalized, calculating the former contribution is subtle. It is given by

$$P_e = \frac{e}{2\pi} \sum_a \oint dk \, A_a(k) \, . \tag{4.64}$$

This expression for the polarization is ambiguous up to multiples of e, as expected on account of surface charge. For example if the unit cell is redefined, some nuclei locations are shifted by one unit changing the second term of Eq. (4.63). Likewise if the Bloch wavefunctions are redefined by $u_{ak} \to e^{i\theta(k)} u_{ak}$, then the polarization shifts by $\frac{e}{2\pi}\big(\theta(2\pi) - \theta(0)\big)$, an integer multiple of e if $e^{i\theta(k)}$ winds around the unit circle.

To evaluate the polarization of an insulator with inversion symmetry, set $x_0 = 0$, the inversion center. First, consider a single band. The wavefunctions at k and $-k$ must be the same up to a phase, so $\psi_{-k} = e^{i\theta(k)}\psi_k$ for some phase $\theta(k)$. Therefore, $\mathcal{A}(k) + \mathcal{A}(-k) = \theta'(-k)$. Combining k and $-k$ together in Eq. (4.64) leads to

$$\tilde{P}_e = \frac{1}{2\pi} \int_0^{\pi} \theta'(-k) \, dk = \frac{1}{2\pi}\big(\theta(-\pi) - \theta(0)\big) \, . \tag{4.65}$$

Now $e^{i\theta(k)}$ is the parity of the wavefunction ±1 at TRIMs $k = 0, \pi$. Hence if the parities at the TRIMs are different, θ changes from 0 to π so $\tilde{P}_e \equiv \frac{1}{2} \pmod 1$. If there are many bands, we may sum the polarization over all of them and we find in general that

$$(-1)^{2\tilde{P}_e} = \eta_0 \eta_\pi \, . \tag{4.66}$$

The formula for the polarization in 3D can be deduced from this result – this is shown in detail below.

Now let us consider the Chern number for a 2D system, $H(k_x, k_y)$, and show that $(-1)^{\tilde{\mathcal{G}}_{Hz}} = \prod_{\boldsymbol{\kappa}} \eta_{\boldsymbol{\kappa}}$. This is the two-dimensional version of Eq. (4.6). The Hamiltonian leads to a 1D Hamiltonian H_{k_y} when k_y is fixed. As k_y changes, the polarization $P(k_y)$ of the one-dimensional system changes. This means current must flow from one end to the other. According to Thouless's pumping argument, the Hall conductivity $\tilde{\mathcal{G}}_{Hz}$ is equal to the total charge (divided by e) that flows in the 1D material when k_y changes by 2π [174]. (In real space, the one-dimensional system is just the two-dimensional system rolled into a tube along the y direction. Changing k_y corresponds to applying an electromotive force (emf) for a period of time around the y-direction. Hence the Hall effect implies that charge should flow.)

Thus $\tilde{\mathcal{G}}_{Hz} = -\frac{1}{e}\int_{-\pi}^{\pi} dP(k_y)$. (The polarization is not single-valued if $\tilde{\mathcal{G}}_{Hz} \neq 0$.) Now if $\prod_{\boldsymbol{\kappa}} \eta(\boldsymbol{\kappa}) = -1$ (as in either of the 2D xy-layers in Fig. 4.1b) then the polarization at $k_y = 0$ and $k_y = \pi$ differ by a half integer. Thus, $\int_0^{\pi} dP = (k + \frac{1}{2})e$. By inversion symmetry, $dP(k_y) = dP(-k_y)$ (P is an odd function so dP is even). Hence the full change in the polarization between 0 and 2π is $2(k + \frac{1}{2})e$ and the Hall coefficient is odd, $\tilde{\mathcal{G}}_{Hz} = -(2k+1)$.

This section concludes with the generalizations of these results to three-dimensions. The expression for the Hall coefficient in three-dimensions Eq. (4.6) is basically a restatement of the two-dimensional result. Each of the three components of $\tilde{\mathcal{G}}_H$ is equal to the two-dimensional Hall coefficient for any cross-section of the Brillouin zone:

$$\begin{aligned}\tilde{\mathcal{G}}_{Hz} &= \int \frac{dk_z}{2\pi}\,\tilde{\mathcal{G}}^{\mathrm{2D}}_{Hz}(k_z)\\ &= \tilde{\mathcal{G}}^{\mathrm{2D}}_{Hz}(k_z=0)\,. \end{aligned} \tag{4.67}$$

The Chern number for any cross-section k_z is the same, because varying k_z is like taking a 2D system and deforming it continuously. The Hall coefficient can be obtained modulo 2 by looking at an inversion symmetric plane, either $k_z = 0$ or $k_z = \pi$, giving Eq. (4.6). (Note that this gives another reason for the constraint $\prod_{\boldsymbol{\kappa}} \eta_{\boldsymbol{\kappa}} = 1$: the two planes have to agree about $\tilde{\mathcal{G}}_{Hz}$'s parity.)

The expression for the Hall coefficient can be understood also by studying the evolution of the Hamiltonian from a frozen one into one with the parities $\vec{m}_{xy}$ and studying the monopoles in the intervening semimetal phase, as in Fig. 4.7. When the monopoles move from $(\pi,\pi,0)$ through the Brillouin zone to (π,π,π) where they annihilate, they leave behind a magnetic flux, so the Chern number is 2π. In this process, the parities flip on the edge parallel to the flux; hence the product of η_κ on either of the perpendicular faces is -1.

Now consider the polarization in three-dimensions, which is given by

$$\mathbf{P}_e = e \iiint \frac{d^3\mathbf{k}}{(2\pi)^3}\,\mathcal{A}_a(\mathbf{k})\,. \tag{4.68}$$

For the polarization in 3D to be well-defined, σ_H must be 0, so that there are no surface modes. According to Eq. (4.8), the pattern of signs is then a plane wave; in this situation all the 1D polarizations at TRIMs, $P^x_{\mathrm{1D}}(\kappa_y,\kappa_z)$, are the same. This value in fact coincides with the three-dimensional polarization. For example, in Fig. 4.1d, each of the four horizontal lines through TRIMs looks like a 1D insulator with half-integer polarization, so the net polarization per unit cell of the 3D crystal is also $\frac{e}{2}\mathbf{R}_x$.

In more detail, the three-dimensional polarization is the integral over one-dimensional polarizations, $P^x = \iint \frac{dk_y dk_z}{(2\pi)^2} P^x_{\mathrm{1D}}(k_y,k_z)$, if $\mathcal{G}_{Hy} = \mathcal{G}_{Hz} = 0$. (This condition ensures that P^x is single-valued.) The integrand is not a constant, but by inversion symmetry $P^x_{\mathrm{1D}}(k_y,k_z) - P^x_{\mathrm{1D}}(0,0) = -\left[P^x_{\mathrm{1D}}(-k_y,-k_z) - P^x_{\mathrm{1D}}(0,0)\right]$. (Intuitively, one expects $P^x_{\mathrm{1D}}(k_y,k_z)$ to be an odd function, but only differences in polarization are inversion symmetric because of the ambiguity in the polarization.) Hence $P^x = P^x_{\mathrm{1D}}(0,0)$, proving Eqs. (4.8) and (4.9).

Note that if σ_H is nonzero, then part of the polarization is still well-defined. If σ_H is parallel to $\hat{\mathbf{x}}$ (or in a non-cubic lattice, $\mathbf{G}_1$) then the x-component of the polarization cannot leak through the surface modes. On a cylindrical sample of material whose axis is along the x-direction of the crystal, the chiral modes circle around the cylinder, so they do not provide a short circuit between the two ends which would have allowed the x polarization to leak out. This component of the polarization is still given by Eqs. (4.8) and (4.9).

The relationships we have proved so far give the physical interpretation of u_α and w_{xyz} modulo 2. They also have another meaning: they complete the problem of listing all the phases, by showing which combinations of the 11 integers $\tilde{\mathcal{G}}_H$ and $n_o(\boldsymbol{\kappa})$ occur in insulating materials. The 11 integers cannot be chosen independently (unlike the three Chern numbers in the non-symmetric classification); they must satisfy Eqs. (4.5) and (4.6).

4.3.4 Magnetoelectric response

Now we justify the relation $\frac{\theta}{\pi} = \frac{1}{2}\sum_{\boldsymbol{\kappa}} n_o(\boldsymbol{\kappa})$ [Eq. (4.7)], for insulators with $\sigma_H = 0$, by calculating θ for a special case, $\vec{n}_o = 2\vec{m}_{xyz}$. This is the only nontrivial point in the unit cell of the 8D classifying-crystal that is consistent with the conditions that the material is insulating and has no Hall conductivity, so any other case can be related to this one by deforming the insulator, and adding and subtracting frozen insulators to it. It is not possible to define θ for materials that have a Hall conductivity: for example, if θ is defined as $\frac{dP}{dB}$, the surface states interfere with defining P.

Now we need to show that $\theta = \pi$ for $2\vec{m}_{xyz}$. An insulator with the such parities can be deformed to one with time-reversal symmetry since the number of odd states at *each* TRIM is even (consistent with the Kramers degeneracy theorem).

However, the time-reversal symmetry is a red herring when studying the magnetoelectric response, and so we will give an alternative argument. To calculate θ for $\vec{n}_o = 2\vec{m}_{xyz}$, it is enough to consider systems with two filled bands and the appropriate parities. (Any insulator with any additional bands, which would have to be even at all the TRIMs, has the same value of θ because they can be obtained by adding frozen bands.) The expression for θ in terms of the Berry connection [60, 61, 175] can be evaluated directly for the insulator with two bands using symmetry, similar to how the polarization was obtained above. The evaluation of this integral follows closely Ref. [176]'s calculation for the TRS case. The first half of the argument for the time-reversal case applies to systems with inversion symmetry also, and leads to

$$\frac{\theta}{\pi} = \frac{1}{24\pi^2}\iiint d^3\mathbf{k}\,\epsilon^{\alpha\beta\gamma}\,\mathrm{Tr}\left[(B^\dagger\partial_\alpha B)(B^\dagger\partial_\beta B)(B^\dagger\partial_\gamma B)\right], \tag{4.69}$$

where $B_{ab}(\mathbf{k}) = \langle u_{a\,-\mathbf{k}}|\Pi|u_{a\mathbf{k}}\rangle$ is a matrix and $|u_{a\mathbf{k}}\rangle$ is a set of orthogonal wavefunctions spanning the occupied states (it might not be possible to take these as energy eigenfunctions, since $|u_{a\mathbf{k}}\rangle$ have to be continuous, and energy eigenfunctions are not continuous when the bands touch each other). The *spaces* of occupied states are symmetric under inversion symmetry. $B(\mathbf{k})$ is a unitary matrix measuring how far the wavefunctions chosen as a basis for them are from being inversion symmetric, just as $e^{i\theta(k)}$ measures the asymmetry for a single wavefunction in the calculation of the one-dimensional polarization. In a nontrivial phase, it is not possible to choose the basis functions in a continuous way without breaking the symmetry.

Now $B(\mathbf{k})$ gives a map from the 3D Brillouin zone to a unitary group. The expression above for $\frac{\theta}{\pi}$ is known to equal the degree of this map, *i.e.*, the pullback of the third cohomology classes $H^3(U) = \mathbb{Z} \to H^3(T^3) = \mathbb{Z}$. At the TRIMs, $B(\boldsymbol{\kappa})$ has eigenvalues ± 1 depending on $n_o(\boldsymbol{\kappa})$. In the case $\vec{n}_o = 2\vec{m}_{xyz}$ with two bands, *i.e.*, $B \in U(2)$, $B(\boldsymbol{\kappa}) = \mathbb{1}_2$ at each TRIM except for at $k_x = k_y = k_z = \pi$, where $B(\boldsymbol{\kappa}) = -\mathbb{1}_2$. An element of $U(2)$ may be decomposed as $e^{i\theta}U$, where $U \in SU(2)$. Note that this decomposition has a sign ambiguity, as both $\mathbb{1}_2$ and $-\mathbb{1}_2$ are in $SU(2)$, hence $\theta \mapsto \theta + \pi$, $U \mapsto -U$ gives an equally valid decomposition.

We first show that this decomposition is single-valued for the system of interest here. The pair $(\theta, U) \in U(1) \times SU(2)$ which is a double cover of $U(2)$, a single-valued decomposition is possible if and only if the map $B(\mathbf{k}) : T^3 \to U(2)$ can be lifted to the map $B'(\mathbf{k}) : T^3 \to U(1) \times SU(2)$. The covering $U(1) \times SU(2) \xrightarrow{p} U(2)$ induces a map $\pi_1\big(U(1) \times SU(2)\big) = \mathbb{Z} \xrightarrow{p_*} \pi_1\big(U(2)\big) = \mathbb{Z}$ which takes $n \mapsto 2n$. Being a cover, the only obstruction to a lift comes from π_1; as long as $B(\mathbf{k})$ can be lifted to $B'(\mathbf{k})$ along the 1-cells of the Brillouin zone T^3, the lift is possible everywhere in the BZ. This amounts to showing that the 'winding number' of $\operatorname{Det} B(\mathbf{k})$ along each of the three directions x, y, and z is even. One the line $k_y = k_z = 0$, the winding of the path $k_x \in [0, \pi]$ must be an integer, since $B(0,0,0) = B(\pi,0,0) = \mathbb{1}_2$. By inversion, $B(-\mathbf{k}) = B(\mathbf{k})^\dagger$, and the path $k_x \in [\pi, 2\pi]$ is the inversion image of the first half. Their phase winding must be the same integer,[14] and hence the combined winding is an even integer. This shows that in the x-direction, there are no obstruction to the lift from B to (θ, U). The same argument shows a similar result in the other two directions. Therefore, we can always decompose $B(\mathbf{k})$ as $e^{i\theta(\mathbf{k})}U(\mathbf{k})$, with $U \in SU(2)$. We resolve the two-fold ambiguity in the lift by letting $\theta(0,0,0) = 0$, such that $U(0,0,0) = \mathbb{1}_2$.

As a topological space, $SU(2)$ is homeomorphic to S^3, the degree of the map $T^3 \to S^3$ is the number of times the torus covers the 3-sphere. The degree of the map modulo 2 is the number of solutions to $B(\mathbf{k}) = -\mathbb{1}_2$ (or any fixed matrix, like $\mathbb{1}_2$). We may just count the TRIMs satisfying this condition, because all other solutions come in pairs at $\mathbf{k}$ and $-\mathbf{k}$, hence the number of TRIMs where B has this value is determined by $\vec{n}_o$. For the case $\vec{n}_o = \vec{m}_{xyz}$, exactly one TRIM has $B = -\mathbb{1}_2$ and hence that configuration has magnetoelectric coupling $\theta = \pi$.

4.4 Parities and the entanglement spectrum

We have found that only *some* combinations of the n_o parameters modulo 2 and 4 have physical interpretations. In this section, we will see that all the n_o-parameters do have interpretations in the entanglement spectrum. This will give another perspective on why only values of the n_o modulo 4 are important: the entanglement modes cannot be observed directly. However, numbers of entanglement modes modulo 2 are related to various observable properties.

The relations between the properties of the insulator and the parities can be derived geometrically using the entanglement spectrum of the insulator; there is a rule for counting the number of states in this spectrum based on the parities.

---

[14] $B \mapsto B^\dagger$ reverses the winding, but so does $\mathbf{k} \mapsto -\mathbf{k}$.

The entanglement spectrum measures quantum correlations in the ground state of a system (see *e.g.* Ref. [169]). It is defined using the Schmidt decomposition. The insulator is cut by an imaginary plane passing through a center of inversion symmetry. The many-body ground state wavefunction then decomposes,

$$|\Psi\rangle = \frac{1}{\sqrt{Z}} \sum_{\alpha} e^{-E^e_\alpha/2} |\alpha\rangle_L |\alpha\rangle_R \,. \tag{4.70}$$

where Z is a normalization constant and E^e_α controls the weight of a given term. It is called the "entanglement energy" because the probability of each term is given by the Boltzmann distribution. The states $|\alpha\rangle_L$ are called the entanglement states, and they are analogous to the surface states of the half of the system on the left side of the cut.

When the wavefunction of the entire system is a free system described by a Slater determinant, the entanglement states $|\alpha\rangle_L$ can also be written as Slater determinants [169]. They are formed just like the excited states of a system of free electrons, by selecting wavefunctions from a certain orthonormal family of single-particle wavefunctions $f^L_{i\mathbf{k}_\perp}(\mathbf{r})$. (These states may be labeled by the momentum along the surface, $\mathbf{k}_\perp$, by translational symmetry.) Each of these wavefunctions has an associated "energy" $\epsilon_{Li}(\mathbf{k}_\perp)$ as if they were eigenfunctions of a single-particle Hamiltonian. The "entanglement energy" E^e_α is the sum of all the "energies" of the occupied states.

The entanglement spectra, $\epsilon_{Li}(\mathbf{k}_\perp)$, can be used to determine "topological" properties of a system. When a material is insulating in the bulk, it may still have a gapless entanglement spectrum. This implies that electrons are delocalized across the cut, unlike the electrons in a frozen insulator. These delocalized states may be "topologically nontrivial." Physical topological surface states can be deduced from such entanglement spectrum states: the entanglement spectrum can be continuously deformed into the physical spectrum, so any topologically protected states are present in both [163, 164].

Determining basic properties of the entanglement spectrum is simple in the presence of inversion symmetry. In this case [164], the entanglement spectrum has a particle-hole symmetry Π_e that implies a rule for finding the number of entanglement states at each surface TRIM. The Π_e symmetry takes each mode to another mode whose momentum $\mathbf{k}_\perp$ and "energy" $\epsilon_{Li}(\mathbf{k}_\perp)$ have the opposite sign. Let us regard 0 as the "Fermi energy"; the state in the Schmidt decomposition with the smallest "energy" (*i.e.*, the largest weight) is obtained by filling up all states with $\epsilon_{Li} < 0$.

At surface TRIMs Π_e ensures that states appear in pairs with energies $\pm\epsilon$ when $\epsilon \neq 0$. There can be a single mode at zero. If present, this mode will stay exactly at zero no matter how the system is changed, because moving away would break the symmetry. More can be said about the zero-energy states: the "index" at each TRIM can be determined. The space of zero-"energy" states is invariant under Π_e so they can be classified by their parities. The index is the difference $\Delta N_e(\boldsymbol{\kappa}_\perp)$ between the number of modes of even and odd parity. This quantity is invariant because even and odd zero-energy states can 'cancel' one another and move to nonzero energies $\pm\epsilon$, while two states of the same parity cannot cancel. (If two states move away from zero energy, then they must turn into eigenstates f_1 and f_2 with energies of opposite sign. Thus, f_1 and f_2 are orthogonal states exchanged by Π_e. The corresponding parity eigenstates, $\frac{1}{\sqrt{2}}(f_1 \pm f_2)$, have *opposite* parities.) Thus, if $\Delta N_e(\boldsymbol{\kappa}_\perp)$ has some value, such as 2, then there must be at least 2 states at this TRIM.

The imbalance number can be found directly from the bulk band structure,

$$\Delta N_e(\boldsymbol{\kappa}_\perp) = \frac{1}{2}\big(\Delta N(\boldsymbol{\kappa}_1) + \Delta N(\boldsymbol{\kappa}_2)\big)\,, \tag{4.71}$$

where $\boldsymbol{\kappa}_1$ and $\boldsymbol{\kappa}_2$ are the two bulk inversion symmetric momenta that project to $\boldsymbol{\kappa}_\perp$ and $\Delta N(\boldsymbol{\kappa}_1)$ (*e.g.*) is related to $n_o(\boldsymbol{\kappa}_1)$: it is the difference between the number of even and odd occupied states at $\boldsymbol{\kappa}_1$, that is $n - 2n_o(\boldsymbol{\kappa}_1)$. This result applies in any dimension. In one-dimension, for example, there is only one ΔN_e (since there is only one surface momentum) to determine, and ΔN_e is equal to the number of even states at $\kappa = \pi$ minus the number of odd states at $\kappa = 0$. Note that the parities of the bulk states are to be calculated relative to an inversion center that is on the cutting plane.[15]

We will now explain how to define the particle-hole symmetry and how to derive the formula for ΔN_e. This derivation requires some results of Refs. [169, 178, 179]. As the building up of entanglement states from single-particle states suggests, the entanglement modes are actually eigenfunctions of a "Hamiltonian" H_L defined on the part of space to the left of the cutting plane. The eigenvalues of H_L are not equal to the entanglement energies ϵ_{Li}, but they are related to them,

$$H_L|f^L_{i\mathbf{k}_\perp}\rangle = \tfrac{1}{2}\tanh\left[\tfrac{1}{2}\epsilon_{Li}(\mathbf{k}_\perp)\right]|f^L_{i\mathbf{k}_\perp}\rangle\,. \tag{4.72}$$

The Hamiltonian H_L is just the result of confining the "flat-band Hamiltonian" H_{flat} in the whole space to the left half of space. H_{flat} is defined to have the same eigenfunctions as the true Hamiltonian but simpler eigenvalues, $-\frac{1}{2}$ for the occupied states and $+\frac{1}{2}$ for the empty ones. H_L has strange eigenstates – it has infinitely many surface bands, and for many cases, it has no states besides these. The reason is that the spectrum of H_L ranges from $-\frac{1}{2}$ to $\frac{1}{2}$. Each bulk state has an energy exactly equal to $\pm\frac{1}{2}$ (corresponding to $\epsilon_{Li} = \pm\infty$) so any state with a finite ϵ_{Li} is a surface state.

While H_L is obtained from H_{flat} by cutting off the right half of space, cutting away the left half of the space leads to a partner Hamiltonian H_R (whose eigenfunctions f_R generate the Schmidt states on the right). These three Hamiltonians have unusual interconnections that do not occur when a generic Hamiltonian is 'cleaved' by just confining it to half of space.

---

[15] The parities and the entanglement spectrum both depend on the inversion center, though the physical responses do not. Suppose in particular that we are working with a hopping model consisting of a chain of identical sites each with multiple orbitals. In order to avoid cutting an orbital in half, we have to make a cut on a *bond* midway between two sites. On the other hand, defining inversion parity relative to *sites* is the most natural choice. Defining the parities this way, $\Delta N_e = n_o(\pi) - n_o(0)$ since the parities of states at $\kappa = \pi$ are switched by the change in inversion center from a bond to a site. This is equivalent to the result obtained in Sec. IIIC of Ref. [177]. This article has an additional factor of 2 because it considers periodic boundary conditions, and cutting the chain creates two ends.

For example, many eigenstates of H_{flat} give eigenstates of H_L and H_R when the wavefunction is set to zero in the part of space that is being discarded. For a generic Hamiltonian, the wavefunction on the remaining half of the space would be depleted near the surface. The unusual relationships between the eigenfunctions of these three Hamiltonians follow because H_{flat} satisfies an identity $H_{\text{flat}}^2 = \frac{1}{4}$.

The connections between the eigenstates of the three Hamiltonians are as follows. The eigenfunctions of H_L and H_R are in one-to-one correspondence via a map $\mathcal{M}$. This map reverses the sign of the "energy." Furthermore, it is possible to build up a complete set of occupied states of H_{flat} from these pairs:

$$F_{i\mathbf{k}_\perp}(\mathbf{r}) = \sqrt{\frac{1}{2}\operatorname{sech}\frac{\epsilon_{Li}(\mathbf{k}_\perp)}{2}} \times \left[e^{-\frac{1}{4}\epsilon_{Li}(\mathbf{k}_\perp)} f^L_{i\mathbf{k}_\perp}(\mathbf{r}) + e^{\frac{1}{4}\epsilon_{Li}(\mathbf{k}_\perp)} \mathcal{M} f^L_{i\mathbf{k}_\perp}(\mathbf{r})\right]. \tag{4.73}$$

This is an occupied state since applying H_{flat} to it gives an eigenvalue of $-\frac{1}{2}$. As f_i^L varies over *all* eigenstates of H_L, the function F varies over a basis for the *occupied* states in the ground state. These states are strange eigenstates for a bulk Hamiltonian since they are localized; this is possible because wave packets do not move in H_{flat}: the group velocity is zero since the dispersion is flat. (Another curiosity of these partnered wavefunctions is that the weights in the superposition depend on the energy.)

When the system is inversion symmetric, $\mathcal{M}$ and Π can be combined together to give the symmetry Π_e; it is a transformation within the left half of the insulator, defined by $\Pi_e = \Pi\mathcal{M}$. Since Π is a symmetry of the wavefunction, it preserves ϵ while $\mathcal{M}$ reverses its sign. Therefore, Π_e acts as a particle-hole symmetry. Similarly, Π_e also reverses the sign of $\mathbf{k}_\perp$.

Now we can count the zero "entanglement energy" states at TRIMs. Let us call the parities of these states under Π_e as $\eta^e_{i\boldsymbol{\kappa}_\perp}$. A state $f^L_{i\boldsymbol{\kappa}_\perp}$ with this parity extends, by Eq. (4.73), to an occupied state

$$F_{i\boldsymbol{\kappa}_\perp} = \frac{1}{\sqrt{2}}\left[(f^L_{i\boldsymbol{\kappa}_\perp}(\mathbf{r}) + \eta^e_{i\boldsymbol{\kappa}_\perp} f^L_{i\boldsymbol{\kappa}_\perp}(-\mathbf{r})\right]. \tag{4.74}$$

where we have used $\Pi\mathcal{M}f^L_{i\boldsymbol{\kappa}_\perp} = \eta^e_{i\boldsymbol{\kappa}_\perp} f^L_{i\boldsymbol{\kappa}_\perp}$ to relate f^R to f^L. This state is invariant under ordinary inversion, and the parity is $\eta^e_{i\boldsymbol{\kappa}}$.

Let us determine the value of ΔN_e for a one-dimensional system. The result in higher dimensions follows since we can fix $\mathbf{k}_\perp = \boldsymbol{\kappa}$ to obtain a one-dimensional system. Consider a circular chain with an even number of cells, L. Now, count the number of even occupied states W_e minus the number of odd occupied states W_o, using two different bases. $W_e - W_o$ is equal to $\operatorname{tr}\Pi$ so it is the same in both bases; the equality will be Eq. (4.71).

One orthonormal basis will be obtained by cutting the system along a diameter. There will now be two cutting points 0 and $\frac{L}{2}$. Near each of these cuts are localized an orthonormal set of F states [Eq. (4.73)]. The two sets (plus bulk states if any exist) together form a full basis for the wavefunctions on the ring. The zero-"energy" states give parity eigenstates centered on each of the two cuts, according to Eq. (4.74). These contribute $2\Delta N_e$ to $W_e - W_o$. The remaining states do not contribute because they can be organized into inversion related pairs, $F_i(x)$ and $F_i(-x)$. These states states are all mutually orthonormal because their left and right halves correspond to different eigenvalues of H_L, H_R. The inversion matrix Π has only off-diagonal matrix elements between $F_i(x)$ and $F_i(-x)$.

On the other hand, instead of the localized wavefunctions, we can use the extended Bloch functions, $\psi_a(k_x)$. The wavefunctions at momentum $\pm k_x$ do not contribute to the trace of Π because they are exchanged, while the wavefunctions at the TRIMs contribute $(\Delta N(\pi)+\Delta N(0))$ to $W_e - W_o$. Setting the two expressions for $\operatorname{tr}\Pi$ equal to each other gives Eq. (4.71).

We can now count the entanglement states of a two-dimensional insulator to understand their *physical* surface properties. For example, applying the result to an insulator that has both time-reversal and inversion symmetry gives a simple derivation of the formulae from Ref. [43] for the indices of topological insulators. We will focus on the two-dimensional quantum spin Hall index, since the three dimensional indices are defined in terms of it. The quantum spin Hall index ν is the number (modulo 2) of physical edge modes between 0 and π. As we have just seen, finding states in the entanglement spectrum is easy because of the particle-hole symmetry (see Fig. 4.9). Once these are found in the entanglement spectrum, they remain when it is deformed into the physical spectrum, by the standard arguments.

Consider the entanglement spectrum created by dividing the system at $y = 0$. The spin Hall index is the parity of the number of curves in the dispersion $\epsilon(k_x)$ crossing $\epsilon = \text{const.}$ between $k_x = 0$ and π. Consider in particular the axis $\epsilon = 0$, strictly between 0 and π the axis crosses an even number of modes: the crossings come in pairs because the spectrum is symmetric under $\Theta\Pi_e$, which just flips the sign of ϵ. (Generically, these states will just mix and move off the axis.)

Therefore only the modes at the ends of the interval are important. We may assume that all the modes at either of these TRIMs have the same parity, because otherwise the states whose parity is in the minority may combine with the states in the majority and become gapped. Then by Eq. (4.71) the number of modes at, *e.g.*, $k_x = 0$ is

$$|\Delta N_e(0)| = |n - n_o(0,0) - n_o(0,\pi)| \,. \tag{4.75}$$

Since these modes are at the extremes of the interval from 0 to π, each one only qualifies as half a mode. To justify this guess, look at a line slightly above the axis. This line crosses half of the modes emanating from each TRIM, so the number of crossings, modulo 2, is $\nu \equiv \frac{1}{2}\sum_{k_x\in\{0,\pi\}} |n - n_o(k_x,0) - n_o(k_x,\pi)|$. This is congruent to $\frac{1}{2}\sum_{\boldsymbol{\kappa}} n_o(\boldsymbol{\kappa})$, summed over all four TRIMs, in agreement with the standard result.

When the flat band Hamiltonian is deformed into the true Hamiltonian, ν remains the same even though the surface states no longer have particle-hole symmetry. The energy curves form continuous loops or zigzags (see Fig. 4.9) because of the double-degeneracies are protected by the Kramers degeneracy theorem.

We can use a similar approach to understand the results in Sec. 4.3 for the polarization and Hall coefficient. These effects may be determined by sketching the arcs of the entanglement Fermi surface using the information about the number of zero energy states at the TRIMs.

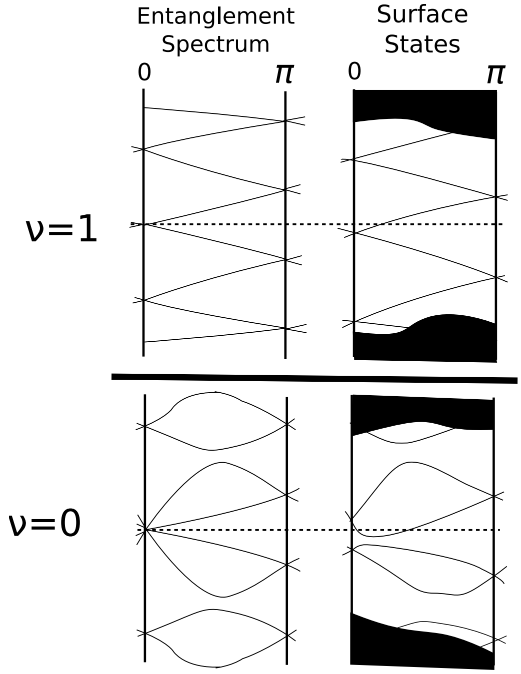

Figure 4.9: Determining the quantum spin Hall index using the entanglement spectrum.

The figure compares spectra of a nontrivial and a trivial system. The left spectrum for each system is the entanglement spectrum, and the right illustrates how the surface spectrum might look. In the entanglement spectrum, inversion symmetry protects degeneracies at zero energy at the TRIMs, allowing one to determine the index. But the two sets of spectra can be deformed into one another (the difference is probably more drastic than illustrated). Because time-reversal symmetry produces Kramers degeneracies at the TRIMs at all energies, the parity of the number of modes crossing the Fermi energy does not change.

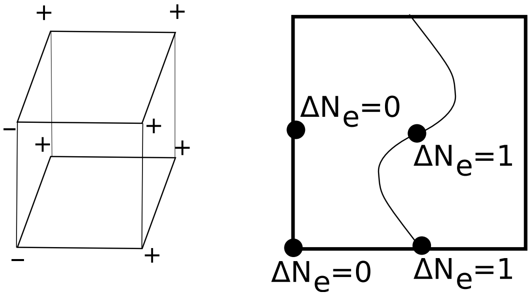

Figure 4.10: A model with the quantum Hall effect perpendicular to $\mathbf{R}_z$.

This model with a single filled band that has an odd quantum Hall effect parallel to $\mathbf{R}_z$. (Left) The parities at the TRIMs. (Right) The entanglement states on the xz-face of the Brillouin zone, determined using $\Delta N_e(\boldsymbol{\kappa}_\perp) = \frac{1}{2}\big(\Delta N(\boldsymbol{\kappa_1}) + \Delta N(\boldsymbol{\kappa}_2)\big)$.

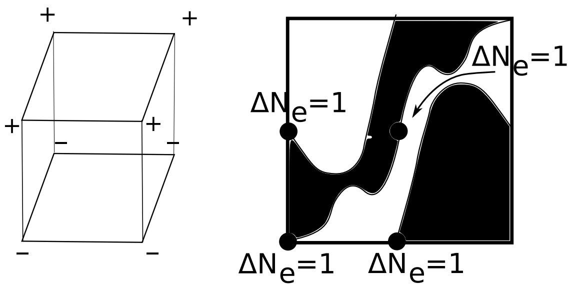

Figure 4.11: Determining the polarization from the entanglement spectrum.

(Left) Parities for an insulator with one filled band, with a half-filled Fermi sea in the entanglement spectrum. (Right) Possible entanglement Fermi arcs for a cut parallel to the xz plane. The arcs surround half the surface Brillouin zone. If there are no nuclei on $y = 0$, this crystal has a half-integer polarization in the y-direction.

While each zero energy state at a TRIM gives at least a Fermi point, not all of these points extend to Fermi arcs. Helpfully, the *parity* of the number of Fermi arcs *is* the same as ΔN_e's parity though.

Figure 4.10 shows how the modes might look for one set of parities. Consider the xz surface of this insulator. According to Eq. (4.71) there must be one arc (or an odd number) passing through $(\pi, 0)$ and (π, π), and an even number through the other two TRIMs. Minimally, there is only one Fermi arc, as illustrated in Fig. 4.10. Hence as one travels along k_x through the Brillouin zone, one crosses through the Fermi arc. Since the z-component of the Hall conductivity, $\tilde{\mathcal{G}}_{Hz}$ is the number of arcs (counted with a sign depending on the sign of the group velocity), $\tilde{\mathcal{G}}_{Hz} = \pm 1$. In more complicated cases, we can determine only that $\tilde{\mathcal{G}}_{Hz}$ is odd because there may be Fermi arcs that do not pass through TRIMs. These cannot be predicted from the $n_o(\boldsymbol{\kappa})$ parameters, but they come in pairs by inversion symmetry, so the parity of the Hall coefficient is uniquely determined.

Now consider the parities in Fig. 4.11. One possible choice of modes (with one passing through each TRIM point as required) is illustrated. If these modes are not chiral, then they separate the Brillouin zone into filled and empty states; exactly half the Brillouin zone is filled because of the symmetry. This will imply that $P^y = \frac{e}{2}$ if there are no nuclei on $y = 0$, and this will be seen to agree with the rule for the polarization.

The polarization is defined as the surface charge once the surface bands have been emptied. This definition may be applied also to the entanglement spectrum. Cut the system with a plane $y = 0$ through a point of inversion symmetry. If there are no nuclei on this plane (which would be indivisible), then the plane just divides the electronic part of the wavefunction in two parts.

Of all the terms in the Schmidt decomposition, consider the one with the largest coefficient, $|G\rangle_L |G\rangle_R$, where $|G\rangle_L$ and $|G\rangle_R$ are the ground states of H_L and H_R respectively, obtained by filling all the negative energy states. These states are mirror images of each other, so they both have the same surface charge Q_y, with net charge $2Q_y$. However, the

Schmidt state $|G\rangle_L|G\rangle_R$, obtained by collapsing the wavefunction by making a hypothetical measurement, has the same charge as the ground state. Each electron is pushed over to the side of the $y = 0$ plane where it is more likely to be, but no electrons appear or disappear. Thus, $2Q_y = 0$, *i.e.*, the ground state of H_L has no surface charge.

Now Fig. 4.11 shows that this ground state of H_L has a partially filled band. When this band (which covers half the Brillouin zone) is emptied, a charge of $-\frac{e}{2}$ per unit cell on the surface remains. Hence the polarization $P^y \equiv \frac{e}{2} \pmod e$.

To compare this result to Eq. (4.9), we need to calculate both contributions to this equation, from nuclei and electrons. Note that $P^y_e = 0$ for the given parities. Since there is one filled band of electrons, by neutrality, there must be a single charge $-e$ nucleus per unit cell, which contributes $P^y_n = \frac{e}{2}$. (The nuclei must be at $y \equiv -\frac{1}{2}$ because these are the only inversion symmetric points that are not on the cutting plane.)

We would also like to prove the rule for θ using the entanglement spectrum. The entanglement modes of such an insulator (see Fig. 4.2b) include a Dirac point. Such modes, if they were physical, would produce a half-integer Hall effect. However, this argument is incomplete since the entanglement modes are not physical.

4.5 Conclusions

This study shows that, beyond the Chern numbers that can be used to classify insulators without symmetry, the only protected quantities for insulators with inversion symmetry are the parities of the occupied states at the TRIMs.

For bulk materials, certain values of the parities imply non-vanishing electrical properties (the reverse of the usual use of parity symmetry, to prove the vanishing of certain quantities). In particular, if the number of odd occupied states is odd, the material is never a complete insulator.

The parities also provide a simple criterion for determining when a crystalline compound has a magnetoelectric response $\theta = \pi$, the generalization of the result on the strong topological index of an insulator with time-reversal symmetry as well as inversion symmetry. Hence, the magnetoelectric effect could occur in magnetic materials. There are two consequences: a magnetoelectric effect could be generated by the magnetic ordering, rather than spin-orbit coupling; thus there are more possible materials, besides ones containing elements with large atomic number Z so that the electrons are spin-orbit coupled. It would be interesting to search for such a material. Second, in a material with spontaneous magnetism and $\theta = \pi$, the magnetoelectric effect would be easier to observe than in a topological insulator, because the material does not have gapless surface states that would interfere with the observation.

Beyond these properties, the static polarization, and the Hall conductivities' parities, there are no independent response properties that are related to the inversion parities, since any two insulators which have these response properties in common can be deformed into one another, apart from some frozen electrons.

The properties of inversion symmetric insulators can be derived in a simple way with the help of the entanglement spectrum, illustrating how entanglement modes can be indirectly observed: a magnetoelectric response of $\theta = \pi$ corresponds to a material with an odd number of Dirac points in the entanglement spectrum (even when there are no surface states at all).

Understanding the stability of the parity invariants to interactions will be an interesting subject for future study. Ref. [180] shows in one-dimension that phases can merge when interactions are turned on. In non-interacting systems, more complicated point groups may also protect more interesting phases. Perhaps there are even *new* types of quantized responses in these phases.

Acknowledgments

This research was supported by NSF-DMR-0645691 and NSF-DMR-0804413. We thank Andrew M. Essin and Joel E. Moore for conversations about topological responses and Sergey Savrasov and Xiangang Wan for collaborating on a related project, thus helping to shape this article as well. Parallel work by Hughes *et al.* [177] considers many of the same issues about inversion symmetric insulators.

Chapter 5

Antiferromagnetic topological insulators

Topological insulators resulting from strong spin-orbit coupling were originally understood theoretically by classifying single-electron states of materials with time-reversal invariance. As long as TRS is preserved, these surface states are robust to (weak) perturbations and remain gapless. On the other hand, magnetic perturbations would destroy the topological distinction between thees materials and ordinary insulators.

Our goal in this chapter is to explain how three-dimensional antiferromagnetic insulators with *broken* TRS can nevertheless have nontrivial features similar to that of the topological insulators. Along some planar surfaces they have gapless surface modes, while along others the surface is gapped and there is a nonzero magnetoelectric coupling from the intrinsic material; an experimental signature in the latter case is the existence of 1D metallic states along step edges on the surface. We concentrate here on the conditions for an antiferromagnetic insulator to be in the topologically nontrivial class and on the measurable consequences at its surfaces.

The time-reversal invariant topological insulators are described by $\mathbb{Z}_2$ topological invariants (*i.e.*, there are only two possible values, "odd" and "even") that differ from the integer-valued topological invariants that underlie the integer quantum Hall effect (IQHE) in two-dimensional time-reversal-breaking systems. A simple picture of the state we discuss is obtained by starting from a nonmagnetic topological insulator on a bipartite Bravais lattice, then adding antiferromagnetic order that doubles the unit cell. One of the three-dimensional topological invariants survives in this process. Note that this differs in several ways from the two-dimensional model introduced by Haldane on the honeycomb lattice [42], which is classified by the standard IQHE integer-valued topological invariant (TKNN integer [14] or Chern number) and where the time-reversal breaking does not change the structural unit cell, which is on the hexagonal Bravais lattice. Another case previously considered is a system that breaks time-reversal Θ and spatial inversion Π but preserves the combination $\Theta\Pi$ (note that the Haldane model does not preserve this combination); here there are $\mathbb{Z}_2$ invariants in $d = 1, 2$ for spinless systems and no topological invariants for spin-1/2 systems [181].

The basic idea in this chapter is to classify crystals with broken time-reversal Θ but with an unbroken symmetry of the form $S = \Theta T_{1/2}$, where $T_{1/2}$ is a lattice translation symmetry of the 'primitive' (structural) lattice that is broken by the antiferromagnetic order. Because the topological invariant involves explicitly the lattice operation $T_{1/2}$, it is sensitive to how this lattice operation is modified by a surface, as mentioned above, and even the gapless surface state is not expected to be stable to disorder (in contrast to the conventional topological insulator). A macroscopic description is useful in order to understand the conditions for the topological antiferromagnet to be stable. The three-dimensional topological insulator can be characterized by the existence of a quantized magnetoelectric coupling in the electromagnetic Lagrangian [60, 61, 182] ($c = 1$):

$$\Delta\mathcal{L}_{\mathrm{EM}} = \frac{\theta e^2}{2\pi h}\mathbf{E}\cdot\mathbf{B}\,, \quad \theta = \pi\,. \tag{5.1}$$

The coupling θ is only defined modulo 2π, and ordinary insulators with time-reversal invariance have $\theta = 0$. The presence of either time-reversal symmetry or inversion symmetry is sufficient to guarantee that the other orbital magnetoelectric terms are absent [175, 183]. The product S is also enough to guarantee that the space-averaged θ is quantized to zero or π, since θ is odd under S.

The bulk value $\theta = \pi$ allows either metallic surfaces or gapped surfaces, but in the gapped case there must be a half-integer quantum Hall effect. In the conventional topological insulators, the surfaces are intrinsically metallic and observation of the magnetoelectric coupling seems to require adding a time-reversal-breaking perturbation. In the topological antiferromagnets, some surfaces have a gapped state just from the material's own time-reversal-breaking, which suggests that experimental confirmation that $\theta = \pi$, which has not yet occurred, may be easier in these materials, using the same techniques previously used to extract θ in $\mathrm{Cr_2O_3}$ [155]. Surface disorder would complicate that approach but would enable observation of special features at step edges as discussed below.

In the following section, we define the topological antiferromagnet in terms of band structure and verify the connection to the macroscopic description in terms of magnetoelectric response. Then the surface properties are discussed, which will likely be important for experimental detection. In closing we discuss the requirements for experiment and comment on the possibility that the antiferromagnetic Heusler alloy GdBiPt may realize this phase [184]; the possibility that such Heusler alloys may include several topological insulators has recently been a topic of interest [105, 106].

5.1 $\mathbb{Z}_2$ topological invariant

In this section, we construct the $\mathbb{Z}_2$ invariant which distinguishes between the trivial insulator and "antiferromagnetic topological insulator" (AFTI) phases. We consider a antiferromagnet breaking both the primitive lattice symmetry $T_{1/2}$ and time-reversal symmetry Θ, but preserving the combination $S = \Theta T_{1/2}$. The unit cell is effectively doubled as a result and $T_{1/2}^2$ is the new lattice translation (which accounts for the notation). In the following, lattice vectors are elements of this doubled lattice except where otherwise specified.

A free particle Hamiltonian takes the form $\mathcal{H} = \sum_{\mathbf{k}\in\mathrm{BZ}} \Psi_{\mathbf{k}}^\dagger H(k_1,k_2,k_3)\Psi_{\mathbf{k}}$ in reciprocal space, where $\Psi^\dagger$ and Ψ are fermion creation and annihilation operators; $k_1,k_2,k_3 \in [0,2\pi)$ are momentum coordinates defined by $k_i = \mathbf{k}\cdot\mathbf{a}_i$; and $\mathbf{a}_i$ are the lattice translation vectors. The eigenvectors $u_{\mathbf{k}}$ of the Hamiltonian $H(\mathbf{k})$ are related to the wavefunctions by Bloch's theorem $\psi_{\mathbf{k}} = e^{i\mathbf{k}\cdot\mathbf{r}}u_{\mathbf{k}}$. Consequently, the Hamiltonian is not periodic in $\mathbf{k}$, but rather satisfies $H(\mathbf{k}+\mathbf{G}) = e^{-i\mathbf{G}\cdot\mathbf{r}}H(\mathbf{k})e^{i\mathbf{G}\cdot\mathbf{r}}$, where $\mathbf{G}$ is a reciprocal lattice vector and $\mathbf{r}$ is the position operator in this context. Finally, we single out $\mathbf{a}_3$ such that $T_{1/2}^2$ gives a translation by $-\mathbf{a}_3$.

For spin-1/2 fermions, the time-reversal operator may be written as $\Theta = -i\sigma^y\mathcal{K}$ in a suitable basis, where $\mathcal{K}$ is the complex conjugation operator. In addition, Θ (and S) also flips the sign of the momentum: $\mathbf{k}\to-\mathbf{k}$. The translation operator $T_{1/2}(\mathbf{k})$ will move the lattice by half a unit cell, so that its representation in reciprocal space satisfies $T_{1/2}^2(\mathbf{k}) = e^{ik_3}$. Explicitly,

$$T_{1/2}(\mathbf{k}) = e^{\frac{i}{2}k_3}\begin{bmatrix} 0 & \mathbb{1} \\ \mathbb{1} & 0 \end{bmatrix}, \tag{5.2}$$

where $\mathbb{1}$ is the identity operator on half the unit cell. Note that the operators Θ and $T_{1/2}$ commute so that $\Theta T_{1/2}(\mathbf{k}) = T_{1/2}(-\mathbf{k})\Theta$.

The combination $S_{\mathbf{k}} = \Theta T_{1/2}(\mathbf{k})$ is antiunitary like Θ itself, but with an important difference: while $\Theta^2 = -1$ for spin-1/2 particles, $S^2 = S_{-\mathbf{k}}S_{\mathbf{k}} = -e^{ik_3}$. The Hamiltonian is invariant under the combination of time-reversal and translation:

$$S_{\mathbf{k}}H(\mathbf{k})S_{\mathbf{k}}^{-1} = H(-\mathbf{k}) \tag{5.3}$$

At the Brillouin zone (BZ) plane $k_3 = 0$ the Hamiltonian satisfies $SH(k_1,k_2,0)S^{-1} = H(-k_1,-k_2,0)$ with $(S|_{k_3=0})^2 = -1$. These properties lead to a $\mathbb{Z}_2$ topological classification of this two-dimensional system, by analogy to the $\mathbb{Z}_2$ invariant in the quantum spin Hall (QSH) effect [3] (the same invariant can be rederived in the Hamiltonian picture used here) [1]. At the plane $k_3 = \pi$, by contrast, $S^2 = +1$ and there are no topological invariants associated with this plane [77].

The $\mathbb{Z}_2$ invariant may be computed from the Berry connection and curvature [1, 19] on the $k_3 = 0$ plane, or in the presence of spatial inversion by looking at the four time-reversal momenta at $k_1, k_2 \in \{0,\pi\}$ [43].

Even though the topological invariant is calculated from a two-dimensional slice in the Brillouin zone for a particular choice of unit cell, it reflects the topology of the three-dimensional band structure. For example, S symmetry gives no invariants in 1D or 2D. In Sec. 5.1.3, we show that the 3D $\mathbb{Z}_2$ invariant is independent of unit cell choice. In the remainder of this section, we will give a more detailed picture of this topological phase.

5.1.1 Relation to the time-reversal invariant topological insulator

If we imagine the system described by a time-reversal breaking order parameter M (*e.g.*, a staggered magnetization), what happens when we restore time-reversal symmetry by letting M go to zero while maintaining the insulating phase (band gap)?

To understand what happens, it is useful to recall briefly the classification of three-dimensional time-reversal band insulators. In the Brillouin zone, there are six planes which satisfy time-reversal $\Theta H(\mathbf{k})\Theta^{-1} = H(-\mathbf{k})$, and each has a corresponding $\mathbb{Z}_2$ invariant: ν_1, μ_1, ν_2, μ_2, ν_3, μ_3 classify the planes $k_1 = 0, \pi$, $k_2 = 0, \pi$, and $k_3 = 0, \pi$ respectively. Here, we use the convention 0 (even) and 1 (odd) to denote the elements of $\mathbb{Z}_2$. The six values must satisfy the constraint $\nu_0 \equiv \nu_1 + \mu_1 = \nu_2 + \mu_2 = \nu_3 + \mu_3$, all modulo 2, so only four combinations of these quantities are independent: ν_0, ν_1, ν_2, ν_3. The value ν_0 is the strong topological invariant, and the other three $\mathbb{Z}_2$ are known as the weak invariants; together they classify the 3D system. A strong topological insulator (STI) is one in which ν_0 is nontrivial, that is, $\nu_0 = 1$.

Upon doubling the unit cell in the $\mathbf{a}_3$ direction, the Brillouin zone halves by folding in the k_3 direction. (In this subsection only, $\mathbf{a}_3$ is the lattice vector of the structural lattice, and $\mathbf{a}_3^d = 2\mathbf{a}_3$ is the lattice vector of the 'doubled' system which supports an antiferromagnetic coupling.) We can write the Hamiltonian of the doubled system $H^d_{\mathbf{k}}$ in terms of the undoubled Hamiltonian $H_{\mathbf{k}}$:

$$\begin{aligned} H^d\left(k_3^d\right) &= \mathcal{U}\begin{bmatrix} H(k_3^d/2) & 0 \\ 0 & H(k_3^d/2+\pi) \end{bmatrix}\mathcal{U}^\dagger \\ \mathcal{U} &= \frac{1}{\sqrt{2}}\begin{bmatrix} \mathbb{1} & e^{i\mathbf{G}_3^d\cdot\mathbf{r}} \\ \mathbb{1} & -e^{i\mathbf{G}_3^d\cdot\mathbf{r}} \end{bmatrix}. \end{aligned} \tag{5.4}$$

Here $\mathbf{G}_3^d$ is the reciprocal lattice vector dual to $\mathbf{a}_3^d$, $\mathbf{r}$ is the position operator, and the dependence on k_1 and k_2 are omitted for brevity. The unitary transformation $\mathcal{U}$ ensures that the eigenvectors of H^d satisfy Bloch's theorem.

Under the doubling process, the $k_3 = 0$ and $k_3 = \pi$ planes collapse onto the $k_3^d = 0$ plane. The new invariant ν_3^d is given as a sum $\nu_3 + \mu_3 = \nu_0$ since the unitary transformation $\mathcal{U}$ does not affect any these topological invariants. On the other hand, the planes $k_3 = \pm\pi/2$ map to the plane $k_3^d = \pi$. Since $\pm\pi/2$ are time-reversal conjugate and those planes (like all BZ planes, by assumption) have vanishing Chern numbers, it can be seen that μ_3^d is always zero.

Adding an antiferromagnetic (Θ-breaking) parameter M to a STI produces an AFTI. Alternatively, as we turn down the time-reversal breaking parameter M, the antiferromagnet reverts to the doubled system. The $\mathbb{Z}_2$ invariant describing our system is $\nu_3^d = \nu_0$ and we have a STI at $M = 0$ (provided the bulk gap does not close). This gives a natural way to construct a nontrivial topological antiferromagnet – by taking a STI and introducing a staggered magnetization which breaks time-reversal but preserves S.

5.1.2 Magnetoelectric effect and the Chern-Simons integral

The strong topological insulator exhibits a quantized magnetoelectric effect, which can be taken as its definition [60, 61, 182]. To review briefly, the magnetoelectric response tensor

$$\alpha^i_j = \frac{\partial P^i}{\partial B^j}\bigg|_{\mathbf{B}=0} \tag{5.5}$$

is odd under the action of time-reversal. In a Θ-invariant medium, this immediately restricts the off-diagonal elements of the tensor to vanish. However, the ambiguity in defining the bulk polarization [185, 186] allows the diagonal elements to take a nonzero value. In fundamental units, the strong topological insulator has

$$\alpha^i_j = \frac{1}{2}\frac{e^2}{h}\delta^i_j = \frac{\theta}{2\pi}\frac{e^2}{h}\delta^i_j \tag{5.6}$$

with $\theta = \pi$.

The antiferromagnetic topological insulator suggested here does not have time-reversal symmetry microscopically; the relevant symmetry operation is S. This distinction should not affect the macroscopic response of the system to uniform fields (*i.e.*, θ), although there could be short-wavelength components of α^i_j.

From the general theory of orbital magnetoelectric responses in band insulators, the nonzero contribution to α^i_j in cases of discrete symmetries such as time-reversal comes from the Chern-Simons integral,

$$\begin{aligned} \theta &= \frac{1}{4\pi}\int_{\mathrm{BZ}} cs_3\,, \\ cs_3 &= \operatorname{Tr} A \wedge F + \tfrac{i}{3} A \wedge A \wedge A\,, \end{aligned} \tag{5.7}$$

where $A^{\mu\nu} = \langle u^\mu_{\mathbf{k}} | id | u^\nu_{\mathbf{k}} \rangle$ is the Berry connection (a matrix-valued 1-form), and μ, ν label filled bands. The curvature 2-form is $F = dA - iA \wedge A$. Under a gauge transformation (a unitary transformation between the bands), the Chern-Simons integral will change by an integer multiple of 2π, hence only $\theta \bmod 2\pi$ is physical.

Under time-reversal $|u_{\mathbf{k}}\rangle \to \Theta|u_{\mathbf{k}}\rangle$, the quantities $\mathbf{k} \to -\mathbf{k}$ and $cs_3 \to -cs_3$, and θ changes sign. The translation operator $T_{1/2} = e^{\frac{i}{2}k_3}\left[\begin{smallmatrix} 0 & \mathbb{1} \\ \mathbb{1} & 0 \end{smallmatrix}\right]$ changes cs_3 by an exact form (total derivative) and does not affect θ. Together, S symmetry implies that $\theta = -\theta + 2\pi n$ for some integer n, which quantizes θ to 0 (topologically-trivial phase) or π (topological insulator phase).

The topological phase remains well-defined even when the single-particle invariant is not, in the case with electron-electron interactions. The macroscopic θ angle remains quantized (at 0 or π) as long as the bulk gap does not close, so the AFTI is stable to sufficiently weak interactions.

The presence of S symmetry forces the Chern numbers on all BZ planes to be zero. In a three-dimensional system, the three Chern numbers are the only obstruction to finding a set of continuous wavefunctions in the Brillouin zone (respecting Bloch boundary conditions). This guarantees the existence of a single-valued connection A for Eq. (5.7). Such A might not respect S symmetry, but this is no impediment to computing the Chern-Simons integral.

5.1.3 Invariance to choice of unit cell

The construction of the $\mathbb{Z}_2$ invariant in Sec. 5.1 required a certain choice of unit cell. In this section, we will demonstrate that different choices of the unit cell will yield the same result. In particular, we show that different ways to choose the doubled unit cell are equivalent given a choice of structural cell.

Begin with a Hamiltonian H defined for a set of primitive translation vectors $\mathbf{a}_i$, along with the operators $T_{1/2}$ such that $T_{1/2}^2$ translate by $-\mathbf{a}_3$. We can always divide the Hilbert space in to two subspaces: X and Y, such that the translation operator $T_{1/2}$ takes Y to X, and X to the Y in another unit cell. Physically X and Y represent the structural unit cell whose symmetry is broken by antiferromagnetism.

Construct a new unit cell by leaving X fixed but taking Y from a cell $\mathbf{R}$ relative to the original. In the new system the lattice vector $\tilde{\mathbf{a}}_3 = \mathbf{a}_3 + 2\mathbf{R}$ such that $\tilde{T}_{1/2}^2$ translates the system by $-\tilde{\mathbf{a}}_3$. We want to show that the $\mathbb{Z}_2$ invariant calculated for the new Hamiltonian ($\tilde{H}$ on the $\tilde{k}_3 = 0$ plane) is identical to that of the original one (H on the $\tilde{k}_3 = 0$ plane).

Here we review the method used in this section to compute the $\mathbb{Z}_2$ topological invariant [1, 19]. First we pick an "effective Brillouin zone" (EBZ) which is half of the Brillouin zone such that time-reversal will map it to the other half. The boundary of EBZ must be time-reversal image of itself. The element of $\mathbb{Z}_2$ is computed by the integrating the connection and curvature:

$$D = \frac{1}{2\pi}\left[\oint_{\partial\text{EBZ}} \mathcal{A} - \int_{\text{EBZ}} \mathcal{F}\right] \operatorname{mod} 2, \tag{5.8}$$

where the $[U(1)]$ connection $\mathcal{A} = \sum_{\text{occ.}} \langle u|id|u\rangle$ is summed over occupied bands and curvature $\mathcal{F} = d\mathcal{A}$ is its exterior derivative in momentum space. The curvature $\mathcal{F}$ is 'gauge invariant' (does not depend on the choice of basis functions for occupied states), but $\mathcal{A}$ depends on a particular choice of gauge for the wavefunctions. The boundary integral in the formula above requires that the wavefunctions at $\mathbf{k}$ and $-\mathbf{k}$ be S-conjugate pairs. Any choice of the EBZ will give the same $\mathbb{Z}_2$ invariant.

The effect of the coordinate transformation $k_1, k_2, k_3 \to \tilde{k}_1, \tilde{k}_2, \tilde{k}_3$ changes the EBZ on which we compute the topological invariant. Since the momentum variables are related by $\tilde{k}_3 = k_3 + 2\mathbf{R}\cdot\mathbf{k}$, we can always choose the EBZ for the new and old systems such that they share a common boundary, namely, the two lines satisfying $\mathbf{R}\cdot\mathbf{k} \in \{0, \pi\}$. This guarantees that the boundary integral terms ($\oint\mathcal{A}$) in Eq. (5.8) are identical in the two cases.

As for the term integrating curvature over the EBZ, we can try to deform the new EBZ to match the old EBZ. This deformation is allowed by the fact that $\mathcal{F} = d\mathcal{A}$ is a closed 2-form; any local deformation to the surface (*i.e.*, one that preserves $\mathcal{A}$ on the boundary) will preserve the integral $\int\mathcal{F}$. As Fig. 5.1c shows, we cannot always deform one EBZ to the other; however, we can always decompose the new EBZ into the old EBZ plus planes with no boundaries. These closed planes which are either contractible, or they span a torus in the Brillouin zone. S symmetry requires that the Chern number vanishes on all closed two-dimensional surfaces, and it follows that the integral Eq. (5.8) evaluates to the same

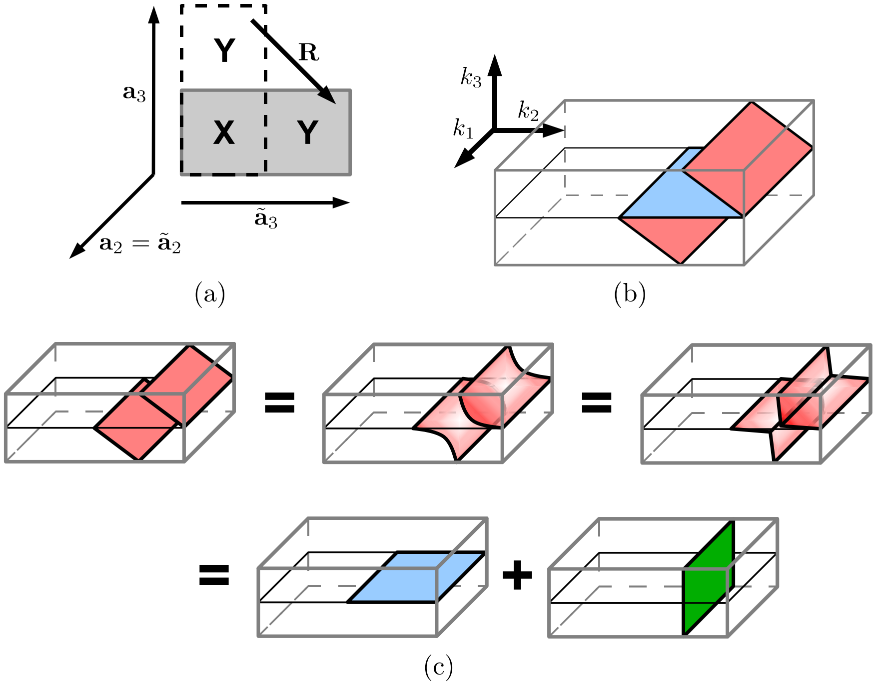

(a) (b) (c)

Figure 5.1: Example of changing the unit cell while computing the AFTI $\mathbb{Z}_2$ invariant.

(a) The original cell (rectangle with dashed border) is transformed to the new cell (shaded rectangle with solid border) by keeping the X portion fixed and changing Y, where $\mathbf{R} = -\mathbf{a}_2 - \mathbf{a}_3$ is the displacement vector. In this example, the original vectors $\mathbf{a}_2 = -\hat{\mathbf{x}} - \hat{\mathbf{y}}$, $\mathbf{a}_3 = 2\hat{\mathbf{y}}$, and $\mathbf{a}_1$ points out of the plane. The new vectors $\tilde{\mathbf{a}}_3 = \mathbf{a}_3 + 2\mathbf{R} = -2\mathbf{a}_2 - \mathbf{a}_3 = 2\hat{\mathbf{x}}$ and we choose $\tilde{\mathbf{a}}_1$ and $\tilde{\mathbf{a}}_2$ to remain fixed. (b) The Brillouin zone. The blue plane is the effective Brillouin zone (EBZ) for $k_3 = 0$, and the red plane is the EBZ for $\tilde{k}_3 = 0$. The $\mathbb{Z}_2$ invariant computed for these two planes are the same. (c) Deformation of the new EBZ (red), which decomposes into the old EBZ (blue) and a boundaryless plane (green).

value for new and old unit cell. In other words, the $\mathbb{Z}_2$ invariant does not depend on how we choose the unit cell.

We can also view the $\mathbb{Z}_2$ invariant as an obstruction to finding a continuous basis (along with the appropriate Bloch periodic boundary conditions) for the wavefunctions respecting S symmetry in the entire Brillouin zone [19]. The material is in a trivial phase if such a basis exists. This interpretation is much harder to 'compute' then the original definition, but is powerful in what it implies. For example, any (single-valued) unitary transformation or a change of coordinates will not affect the obstruction of finding such basis, and it is rather straightforward from the definition that the $\mathbb{Z}_2$ invariant is independent of unit cell choice.

5.2 Construction of effective Hamiltonian models

In this section, we present two explicit examples of Hamiltonians in the antiferromagnetic topological insulator class. Henceforth, we refer these as "model A" (Sec. 5.2.1) and "model B" (Sec. 5.2.2).

5.2.1 Construction from strong topological insulators

As noted in Sec. 5.1.1, we can create an antiferromagnetic topological insulator by adding a staggered time-reversal breaking term to a strong topological insulator. Here we present an explicit Hamiltonian constructed in such way.

We start with a four-band model on a cubic lattice by Hosur *et al.* [187] with four orbitals/spins per cubic site,

$$\begin{aligned} &H(k_x, k_y, k_z) \\ &\qquad = v\tau^x \otimes (\sin k_x \sigma^x + \sin k_y \sigma^y + \sin k_z \sigma^z) + \big[m + t(\cos k_x + \cos k_y + \cos k_z)\big]\tau^z, \end{aligned} \tag{5.9}$$

where $\boldsymbol{\sigma}$ and $\boldsymbol{\tau}$ are two sets of Pauli matrices. This Hamiltonian is in the strong topological phase when $|t| < |m| < 3|t|$ and $\lambda \neq 0$, with the time-reversal operator represented by $-i\sigma^y\mathcal{K}$.

To double the Hamiltonian in the z direction, first decompose $H(k_x, k_y, k_z)$ into a hopping Hamiltonian as follows:

$$H(k_x, k_y, k_z) = B^0 + \sum_{\mu} \left(B_\mu e^{-ik_\mu} + B_\mu^\dagger e^{ik_\mu} \right), \tag{5.10}$$

where $\mu = x, y, z$. The matrices B_μ describe hopping from adjacent cells from the $-\mu$ direction, $B_\mu^\dagger$ are hopping from $+\mu$ direction, and B^0 describes the 'self-interaction' of a cell. The new lattice vectors are:

$$\begin{bmatrix} \mathbf{a}_1 \\ \mathbf{a}_2 \\ \mathbf{a}_3 \end{bmatrix} = \begin{bmatrix} 1 & 0 & 1 \\ 0 & 1 & 1 \\ 0 & 0 & 2 \end{bmatrix} \begin{bmatrix} \mathbf{a}_x \\ \mathbf{a}_y \\ \mathbf{a}_z \end{bmatrix} \tag{5.11}$$

which defines a face-centered-cubic (FCC) lattice with the primitive unit cell whose volume is double that of the original cubic cell.

Doubling the unit cell gives the following eight-band Hamiltonian:

$$\begin{aligned} H^d(k_1, k_2, k_3) = &\begin{bmatrix} B^0 + M & B_z^\dagger e^{i\frac{k_3}{2}} \\ B_z e^{-i\frac{k_3}{2}} & B^0 - M \end{bmatrix} + \begin{bmatrix} 0 & B_z \\ 0 & 0 \end{bmatrix} e^{-i\frac{k_3}{2}} + \begin{bmatrix} 0 & 0 \\ B_z^\dagger & 0 \end{bmatrix} e^{i\frac{k_3}{2}} + \begin{bmatrix} 0 & B_x \\ B_x & 0 \end{bmatrix} e^{i(\frac{k_3}{2} - k_1)} \\ &+ \begin{bmatrix} 0 & B_x^\dagger \\ B_x^\dagger & 0 \end{bmatrix} e^{i(k_1 - \frac{k_3}{2})} + \begin{bmatrix} 0 & B_y \\ B_y & 0 \end{bmatrix} e^{i(\frac{k_3}{2} - k_2)} + \begin{bmatrix} 0 & B_y^\dagger \\ B_y^\dagger & 0 \end{bmatrix} e^{i(k_2 - \frac{k_3}{2})}, \end{aligned} \tag{5.12}$$

where M is a term odd under time-reversal (such as σ^z or τ^y) and represents the added antiferromagnetic coupling in this example. The time-reversal operator takes the form

$$\Theta = -i \begin{bmatrix} 1_\tau \otimes \sigma^y & 0 \\ 0 & 1_\tau \otimes \sigma^y \end{bmatrix} \mathcal{K}. \tag{5.13}$$

In the absence of M this system also has two parity (spatial inversion) centers, given by the operators:

$$\Pi_1 = e^{i\frac{k_3}{2}} \begin{bmatrix} 0 & \tau^z \\ \tau^z & 0 \end{bmatrix} \qquad \Pi_2 = \begin{bmatrix} \tau^z & 0 \\ 0 & \tau^z \end{bmatrix} \tag{5.14}$$

The inversion center for Π_1 is between the two cubic sublattices X and Y, such that it swaps X and Y. The inversion center for Π_2 is at X, such that it takes Y to the next unit cell. Their product results in a translation by half a unit cell: $\Pi_1\Pi_2 = T_{1/2}$.

5.2.2 Construction from magnetically induced spin-orbit coupling

Motivation

Consider four atoms placed in a rhombus geometry on the xy-plane as shown in Fig. 5.2, with X and Y on opposite corners of the rhombus. In the simplest model, the spin-orbit coupling term from X to Y is given by $i\lambda_{\mathrm{SO}} \sum \mathbf{d}_1 \times \mathbf{d}_2 \cdot \boldsymbol{\sigma}$, where the sum is over the two paths $X \to M_1 \to Y$, $X \to M_2 \to Y$, and $\mathbf{d}_1$, $\mathbf{d}_2$ are the vectors along the bonds $X \to M_*$ and $M_* \to Y$ that the electron travels through [2, 42]. In this geometry this coupling vanishes as the cross products $\mathbf{d}_1 \times \mathbf{d}_2$ from the two paths cancel.

Now let M_1 and M_2 be magnetized in the $+z$ direction. This creates a net magnetic field inside the rhombus breaking the symmetry between the two paths $X \to M_* \to Y$. We can estimate its orbital effect by attaching an Aharonov-Bohm phase $e^{\pm i\phi}$ to each of the two paths, to produce a flux 2ϕ. The coupling from X to Y now takes the form

$$H_{\mathrm{SO}} = i\lambda_{\mathrm{SO}} \left[e^{i\phi} \mathbf{r}_1 \times \mathbf{r}_2 + e^{-i\phi} \mathbf{r}_2 \times \mathbf{r}_1 \right] \cdot (c_Y^\dagger \boldsymbol{\sigma} c_X) \approx 2\phi\lambda_{\mathrm{SO}} |\mathbf{r}_2 \times \mathbf{r}_1| (c_Y^\dagger \sigma^z c_X), \tag{5.15}$$

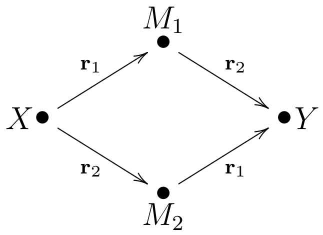

Figure 5.2: Four atoms placed in a rhombus configuration on the xy-plane.

The coupling between X and Y depends on the magnetization of M_1 and M_2, and the strength of the spin-orbit effect.

where we expect ϕ to be proportional to the z-magnetization of M_*. Hence the magnetization of intermediate sites M_1 and M_2 induces a spin-orbit interaction between the sites X and Y.

If spins on M_1 and M_2 are aligned oppositely in the $\pm z$ direction, by contrast, there is no net magnetization in the rhombus and the symmetry between the two paths $X \to M_* \to Y$ is restored. Rotating the system by π along the axis through points X and Y, taking M_1 to M_2 and vice versa, we see that there are no σ^z couplings between the two sites. Both cases are important in motivating the model to follow.

Effective Hamiltonian

We start with a rock-salt (FCC) structure with the conventional cubic unit cell of side length 1. In this setup there are four 'A' sites located at $(0,0,0)$ and permutations of $(\frac{1}{2},\frac{1}{2},0)$, while the '$B$' sites are located at $(\frac{1}{2},\frac{1}{2},\frac{1}{2})$ and permutations of $(0,0,\frac{1}{2})$. The B sites develop antiferromagnetic order along the (111) planes and magnetization in $\pm(1,1,1)$ direction. In the antiferromagnetic state, the unit cell consists of four layers: $A1$, $B\uparrow$, $A2$, and $B\downarrow$.

In this model there are spin up and spin down degrees of freedom at $A1$ and $A2$, but the electronic degrees of freedom at B are eliminated, giving four 'orbitals' per primitive cell. The electrons hop between A atoms by traveling through the magnetized B sites, and we can see that there are always two such paths $A \to B \to A$ between adjacent A's. From Fig. 5.3, it is apparent that spin-orbit coupling between two $A1$'s on the same layer vanishes by our argument earlier, as the intermediate sites have opposite magnetization. In contrast, the spin-orbit coupling between $A1$ and $A2$ does not vanish.

Now we describe our model with the following hopping terms: (1) spin-independent hoppings between $A1$ and $A2$ atoms with coefficient t, (2) spin-independent hoppings between A atoms on the same plane with coefficient t', and (3) spin-orbit term between $A1$ and $A2$ with effective coupling $\pm\lambda$. As mentioned earlier, we take the energy to reside on B sites as far above the energy scales λ, t, t', effectively eliminating those degrees of freedom in our model.

$$\begin{array}{ccccc}
A1\bullet & & A1\bullet & & A1\bullet \\
 & \uparrow & & B\uparrow & \\
A2\bullet & & A2\bullet & & A2\bullet \\
 & \downarrow & & B\downarrow & \\
\bullet & & \bullet & & A1\bullet
\end{array}$$

Figure 5.3: Cross section of model B at (100) plane.

The layers in a unit cell are $A1$, $B\uparrow$, $A2$, $B\downarrow$. Note that the magnetizations are not in-plane, but are only illustrated as such in this figure.

We choose the primitive lattice vectors

$$\begin{bmatrix}\mathbf{a}_1\\ \mathbf{a}_2\\ \mathbf{a}_3\end{bmatrix} = \begin{bmatrix}-\frac{1}{2} & 0 & \frac{1}{2}\\ 0 & -\frac{1}{2} & \frac{1}{2}\\ 1 & 1 & 0\end{bmatrix}\begin{bmatrix}\mathbf{a}_x\\ \mathbf{a}_y\\ \mathbf{a}_z\end{bmatrix} \tag{5.16}$$

in terms of the conventional cubic basis $\mathbf{a}_x$, $\mathbf{a}_y$, $\mathbf{a}_z$. The atoms $A1$ and $A2$ are placed at $-\frac{\mathbf{a}_3}{4}$ and $\frac{\mathbf{a}_3}{4}$ respectively within the unit cell. Written in the basis $|A_1^{\uparrow}\rangle, |A_1^{\downarrow}\rangle, |A_2^{\uparrow}\rangle, |A_2^{\downarrow}\rangle$, the Hamiltonian takes the form

$$H = \begin{bmatrix}T' & U^\dagger\\ U & T'\end{bmatrix}, \tag{5.17}$$

where,

$$\begin{aligned} T' &= 2t'\big[\cos(k_1) + \cos(k_2) + \cos(k_1 - k_2)\big]\mathbb{1}, && (5.18a)\\ U &= 2t\big[\cos(\tfrac{k_3}{2}) + \cos(k_1 + \tfrac{k_3}{2}) + \cos(k_2 + \tfrac{k_3}{2})\big]\\ &\quad - 2i\lambda\big[\sin(\tfrac{k_3}{2})\sigma^z + \sin(k_1 + \tfrac{k_3}{2})\sigma^x + \sin(k_2 + \tfrac{k_3}{2})\sigma^y\big], && (5.18b)\end{aligned}$$

which is gapped (in the bulk) when $|t'| < |t|, \frac{1}{\sqrt{3}}|\lambda|$. The time-reversal operator has the representation

$$\Theta = -i\begin{bmatrix}\sigma^y & 0\\ 0 & \sigma^y\end{bmatrix}\mathcal{K}. \tag{5.19}$$

We are interested in the regime where t' is much smaller than t and λ, as this leads to a gap in the surface spectrum also. Unfortunately, we cannot provide a good argument why t' (in-plane hopping) should be much less than t (interplane hopping) in a real material.

This model has spatial inversion symmetry, given by the operator

$$\Pi = \begin{bmatrix}0 & \mathbb{1}\\ \mathbb{1} & 0\end{bmatrix}, \tag{5.20}$$

which in effect swaps the layers $A1$ and $A2$. The filled bands at the momenta $(k_1, k_2, k_3) = (0,0,0), (0,\pi,0), (\pi,0,0), (\pi,\pi,0)$ have parity $-1, -1, -1, +1$ respectively, so the model is in the nontrivial topological phase.

In this model, λ is related to the parameter breaking time-reversal symmetry, at the same time protecting the bulk gap. If we turn the parameter λ down to zero, we will not get a STI at $\lambda = 0$, rather, the model becomes conducting.

5.3 Surface band structure

The bulk electronic band structure of an AFTI must be gapped to allow the topological distinction between the trivial phase and the nontrivial phase. At the boundary between domains of two topologically distinct phases we typically expect a gapless surface spectrum, as is the case at the edges of quantum Hall and quantum spin Hall systems, as well as at the surfaces of the STI (vacuum is in the trivial phase). However, it should be noted that this is not strictly necessary. For example, while time-reversal symmetry requires doubly degenerate states, leading to gapless boundary modes between topological phases, it is known that breaking time-reversal but preserving inversion can give a topological phase whose surface states are gapped [164].

We distinguish between two classes of surfaces, depending on the plane of the cut relative to the crystal structure. We call a surface **type F**(erromagnetic) if it breaks the S symmetry in the bulk, and **type A**(ntiferromagnetic) if it preserves the symmetry. Heuristically, the distinction can be visualized by imagining a ferromagnetic/antiferromagnetic moment with a Zeeman coupling to the electron's spin, as in model A above. Then a type F surface will have all its spins aligned, and a net magnetization on the surface. A type A surface will have antiferromagnetic order such that we can always choose the primitive lattice vector $\mathbf{a}_3$ parallel to the surface. As an example: In model A with staggered magnetization on a cubic lattice, $\{111\}$ planes are type F, while planes $\{110\}$ and $\{100\}$ are type A.

There are an odd number of Dirac cones on a clean type A surface, analogous to the STI. We can see why the surface (parallel to $\mathbf{a}_3$) is gapless by looking at the $k_3 = 0$ line on the surface spectrum, which is the boundary of the $k_3 = 0$ plane in the bulk BZ. Since the plane carries a nontrivial topological (QSH) phase, its boundary must be gapless.

The Dirac cone's stability may also be explained by looking at a constant energy curve γ in the surface spectrum. This curve must be its own time-reversal image because of the symmetry between $\mathbf{k}$ and $-\mathbf{k}$. The Berry phase of this curve $\phi = \oint_\gamma \operatorname{Tr} A$ is ambiguous by integer multiples of 2π, so S symmetry forces this to be 0 or π, for the same reason it forced $\theta = \pi$ in Sec. 5.1.2. As in the STI, a π phase implies that the Fermi surface encloses an odd number of Dirac cones. However, any defect or impurity will break the translational and S symmetry on the surface, thereby opening a gap. This is analogous to the effect of a magnetic defect on the surface of a STI.

For a type F surface, S symmetry is broken on the surface and the usual protection for Dirac cones or conducting surfaces no longer exists. If the bulk and surface spectrum are fully gapped (*i.e.*, not a semi-metal), then the surface will exhibit the half-integer quantum Hall effect, to be discussed in the next section.

In Fig. 5.4, we present the band structure of model A for slabs with type A and type F surfaces. Since this model is built from a STI, the band structures are similar [4].

For model B, the surface parallel to $\mathbf{a}_1$ and $\mathbf{a}_2$ is type F and its excitations are exactly solvable, with dispersion

$$E_s(k_1, k_2) = 2t' \big(\cos k_1 + \cos k_2 + \cos(k_1 - k_2) \big). \tag{5.21}$$

As the dispersion shows, a surface spectrum exists for all values of t' and nonzero values of t and λ. This model has the peculiar feature that the surface spectrum is completely disconnected from the bulk, that is, it forms a complete two-dimensional band structure.

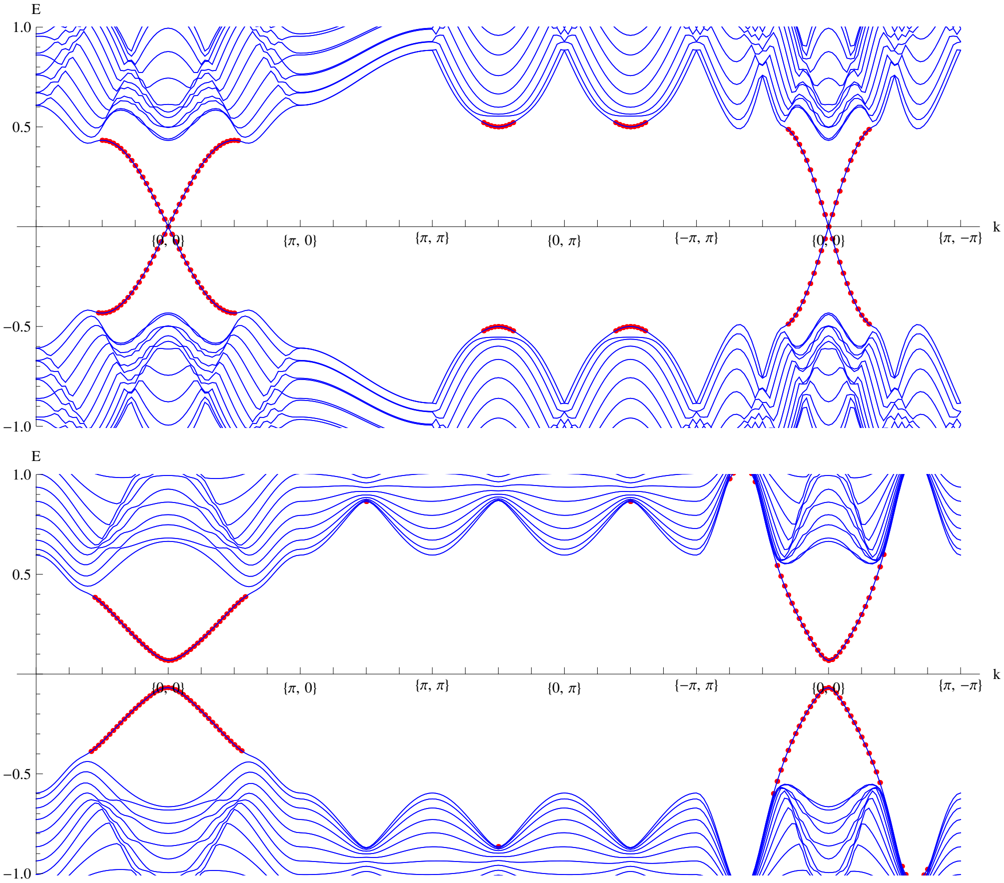

Figure 5.4: The bulk and surface band structure for model A.

The top and bottom band structures are plot along the (100) (type A, parallel to $\mathbf{a}_2, \mathbf{a}_3$) and $(\bar{1}\bar{1}1)$ plane (type F, parallel to $\mathbf{a}_1, \mathbf{a}_2$) respectively. The red dots indicate surface modes. The parameters used are: $v = 0.5, m = 2, t = 1, M = \sigma^z$ with 13 layers.

Figure 5.5 shows the bulk and surface band structure for two different cuts. In the (111) cut, a small t' is desired if we want to avoid band overlaps between the valence, conductance, and surface spectrum, giving us an insulator.

In the presence of a sufficient number of random defects, we expect that the surface electronic states are described by the unitary symmetry class because of the broken time-reversal symmetry. That symmetry class only has extended states at isolated values of the chemical potential; in general the surface state will have zero diagonal conductivity, with half-integer quantum Hall plateaus. The transitions between these plateaus appear when the chemical potential passes through an extended state. These transitions can be regarded as a realization of the two-dimensional quantum Hall effect in zero net field discussed by Haldane [42]. Note that since both top and bottom surfaces of a slab will have half-integer plateaus, the total quantum Hall effect when diagonal conductivity is zero is always integral,

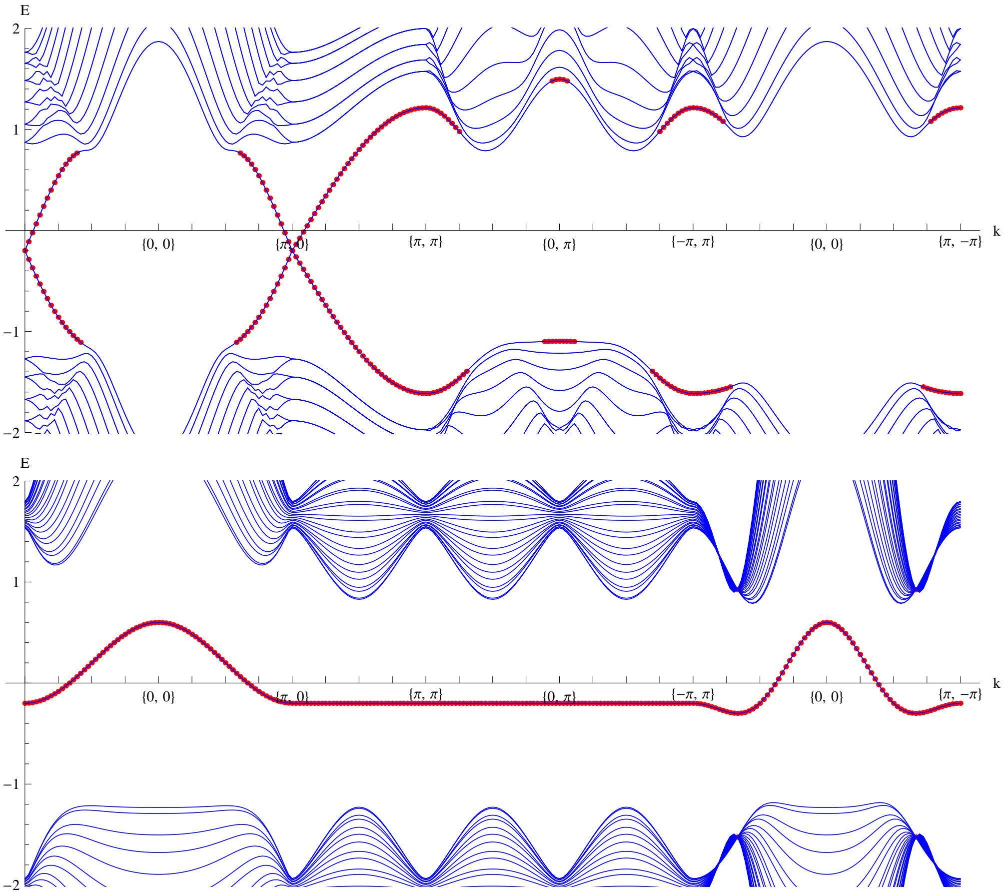

Figure 5.5: The bulk and surface band structure for model B.

The top and bottom band structures are plot along the $(1\bar{1}\bar{1})$ plane (type A, parallel to $\mathbf{a}_2, \mathbf{a}_3$) and (111) plane (type F, parallel to $\mathbf{a}_1, \mathbf{a}_2$) respectively. The red dots indicate surface modes.The parameters used are: $\lambda = 0.5, t = 1, t' = 0.1$ with 13 layers.

as required for a single-electron two-dimensional system.

5.4 Surfaces with half-integer quantum Hall effect

In this section we present two perspectives on the half quantum Hall effect on type F surfaces, along with numerical calculations to justify our claim.

If one views the antiferromagnet as a STI with time-reversal breaking term opening a surface gap, then the half QHE can be viewed as the root of the bulk magnetoelectric coupling $\theta = \pi$. This effect follows from the gapped Dirac dispersion of the surface states. The sign of the Hall conductance depends on the sign of the effective Dirac mass [42, 188, 189], which here is set by the direction of the Zeeman field at the surface.

An alternate perspective of the AFTI surface comes from a comparison to the quantum

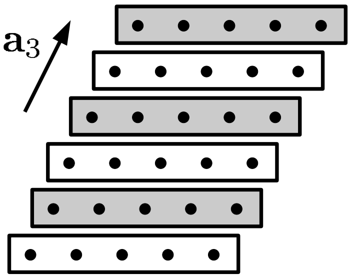

Figure 5.6: Construction of an AFTI by staggering quantum Hall layers.

The shaded and unshaded boxes represents Chern number of ±1. The left and right surfaces are type A and gapless, while the top and bottom surfaces are type F with half-quantum Hall effect.

spin Hall effect. As described in Sec. 5.1, the $\mathbb{Z}_2$ invariant is computed from the two-dimensional plane $k_3 = 0$ and the symmetry operator $S|_{k_3=0}$ in precisely the way that the quantum spin Hall (QSH) invariant is computed from the two-dimensional BZ and Θ. The QSH insulator may be constructed by combining two copies of a QH layer with opposite spin and Chern number $\pm n$. Time-reversal takes one layer to the other, making the combination of the two Θ-invariant. In reality spin is rarely conserved, allowing the two layers to mix, making the Chern number of each spin ill-defined. However, a residual $\mathbb{Z}_2$ topological invariant remains [2, 3], and we can consider the QSH as being adiabatically connected to the two-QH-layer model, but with the topological invariant n only preserved $\bmod 2$.

By analogy, we can construct an AFTI by stacking QH layers, with alternating Chern number of ±1 (Hall conductivity $\pm e^2/h$), as shown in Fig. 5.6. The 'up' (+1) layers are related to the 'down' (−1) layers by S symmetry, hence they are spatially offset from one another. Just like the QSH case, we can expect the layers to couple to one another, in a way that makes the Chern number ill-defined on a per-layer basis. Once again, it is appropriate to consider the AFTI to be adiabatically connected the staggered QH layer model. In the stacked QH model, the Hall conductance in the bulk averages to zero, as the conductance of any individual layer is canceled by neighboring layers of opposite type. In other words, any long-wavelength probe of the system will be unable to discern the individual QH layers However, the QH layers at either end of the stack are not completely canceled, there is a half QHE at both surface.

To confirm this picture, we can consider a slab with type F surfaces and compute the 2D Hall conductivity as a function of position (layer). In units of e^2/h, the (two-dimensional) conductivity in layer n can be computed from [61]

$$C(n) = \frac{i}{2\pi} \int \operatorname{tr} \left[\mathcal{P}(d\mathcal{P}) \wedge \tilde{\mathcal{P}}_n(d\mathcal{P}) \right] . \tag{5.22}$$

Here $\mathcal{P} = \sum_{\text{occ.}} |u_{\mathbf{k}}\rangle\langle u_{\mathbf{k}}|$ is the projector onto occupied wavefunctions at $\mathbf{k}$ and $\tilde{\mathcal{P}}_n$ is the projector onto basis states localized in layer n.

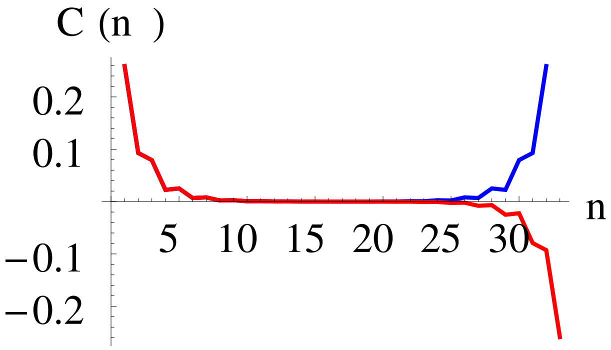

Figure 5.7: Spatially resolved Hall conductance for model B.

The plot is the Hall conductance spatially resolved for 32 (blue) and 33 (red) layers of model B. The Fermi level is set below zero to include only the bulk valence modes and no surface modes. The parameters used for this plot are: $\lambda = 0.5, t = 1, t' = 0.1$.

Figure 5.7 shows the results of such a computation on a slab cut from the rock-salt model B introduced in Eq. (5.18b) with type F surfaces. In this model, when the Zeeman field on opposite surfaces points in opposite directions (blue, upper curve) the total conductance of the slab is $C = 1$, with each surface having a net $C = 1/2$; adding a layer such that the two surfaces have the same Zeeman field switches the conductance on that surface from $+1/2$ to $-1/2$, so that the total slab conductance vanishes. Note that the total conductance of a slab is always an integer, as required [14, 29, 42].

Now, at the interface between two integer quantum Hall domains whose conductance C differs by 1, there will be a chiral boundary mode with conductance e^2/h, which can be thought of as 'half a quantum wire.' In the situation outlined above, putting the two slabs with different conductance together is equivalent to making a slab with a step edge on one surface, and the chiral mode will reside at this step edge. Such a mode should give an observable signature in a tunneling experiment (Fig. 5.8).

It is natural to ask, what if one rotates the antiferromagnetic moment by π, flipping all the spins and effectively 'peeling' off a layer of type F surface? Since the sign of the surface conductance C changes during this process, the surface (or bulk) gap must close at some magnetization orientation. This is analogous to applying a magnetic field $\mathbf{B}$ to an STI surface. For $\mathbf{B}$ parallel to the surface, the Dirac cone shifts in momentum space but no gap opens. Any infinitesimal component of $\mathbf{B}$ out of the plane will open a gap, hence going from $\mathbf{B}$ out of the surface to $\mathbf{B}$ into the surface must necessarily close the surface gap. (In model B, the bulk gap would close while rotating the magnetization.)

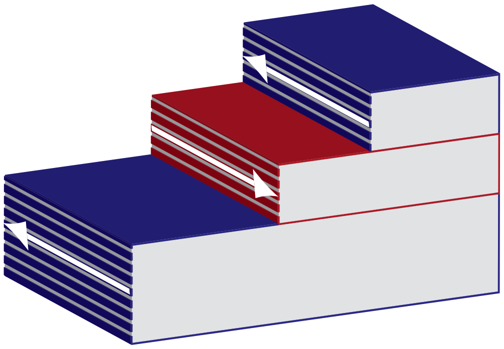

Figure 5.8: 1D quantum wire on type F surface step edge.

The red and blue regions represent ferromagnetic layers magnetized in opposite directions. There is a gapless chiral quantum wire at each step edge, with chirality indicated by the arrow at the edge.

5.5 Conclusions and possible physical realizations

In this chapter, we have looked at the topological classification of materials breaking both time-reversal Θ and translational symmetry $T_{1/2}$, but preserving the combination $S = \Theta T_{1/2}$, and found a $\mathbb{Z}_2$ classification within the S symmetry class that leads to the existence of an antiferromagnetic topological insulator (AFTI). In the most basic picture, an AFTI can be obtained from adding a staggered magnetization to a strong topological insulator. Macroscopically, S symmetry implies a quantized magnetoelectric response $\frac{\partial P}{\partial B}\Big|_{B=0} = \frac{\theta}{2\pi}\frac{e^2}{h}$ with $\theta = \pi$ for an AFTI. We have also demonstrated that the surface spectrum depends on the surface cut, classified as type A/F. Type A surfaces possess an antiferromagnetic order that preserves S symmetry, with associated gapless excitations that can be gapped by disorder. Type F surfaces break S symmetry and are typically gapped, analogously to the situation of a Zeeman field on the surface of a STI. The new AFTI state is topological in a weaker sense than the strong 3D topological insulator, because its surface state is dependent on the surface plane and not generally stable to disorder; in that respect it is similar to the weak topological insulator in 3D or the “Hopf insulator” [170]. (The number of Dirac cones in a STI also depends on the surface plane, but there is always an odd number of such cones.)

The magnetoelectric coupling $\theta = \pi$ requires the half quantum Hall effect at the surface, provided the surface spectrum is gapped. Our numerical calculations based on explicit band models agree with these results. Finally, we predict the existence of chiral 1D quantum wires at type F surface step boundaries, an experimental signature verifiable via scanning tunneling measurements.

The recent proposals that many Heusler compounds may be topological insulators [105, 106], together with the antiferromagnetic order in GdBiPt below 9 K [184], suggest a possible candidate for the state proposed here. Transport [184, 190] and ARPES [191] experiments indicate that GdBiPt is a semiconductor with a narrow gap. While the Gd sites form an

FCC lattice and hence their antiferromagnetic interaction is frustrated, the compound have been experimentally shown to possess [111] antiferromagnetic ordering compatible with S described here [192]. Unfortunately, *ab-initio* studies and ARPES of the material have been inclusive in determining if GdBiPt has band-inversion, to distinguish between a normal AF insulator and an AFTI [191]. Finally, we would also like to note that a physical realization of AFTIs could come from cold atomic gases [193].

We have provided a topological classification and experimental consequences for a particular combination of time-reversal symmetry and a lattice symmetry ($S = \Theta T_{1/2}$). Other such combinations of time-reversal and crystal symmetries could lead to new topological materials beyond those in the exhaustive classification of topological insulators stable to disorder [77, 78].

Acknowledgments

The authors gratefully acknowledge discussions with Shinsei Ryu, Oleg Yazyev, and David Vanderbilt. The work was supported by NSF under Grant No. DMR-0804413 (RM and JEM) and WIN (AE).

Part III

Edge Spectrum and the Bulk-Boundary Correspondence

Chapter 6

Computing the edge spectrum in Dirac Hamiltonians

Although a topological invariant is an abstract quantity defined for a fully periodic system, it is manifested physically as midgap surface states [194]. In IQH systems, the quantized Hall conductance can be formulated in terms of the the number of chiral edge states [20, 36]. Similarly, the 2D/3D $\mathbb{Z}_2$ invariant for TRS systems determines whether there are an odd or even number of helical modes/Dirac cones at a given edge or surface [19]. In the cases above, the edge states smoothly connect the bulk valence and conduction bands and the number of such modes is protected by the topological invariant: they cannot be deformed into a single bulk band unless the bulk gap closes. By contrast, edge modes in an ordinary system do not traverse the bulk gap and are thus susceptible to localization by disorder. For superconducting systems, the topological invariants determine the number of Majorana modes localized at the edge or in vortices [79, 89]. These states are at zero energy and are protected by particle-hole symmetry and the superconducting gap. Systems such as $p + ip$ superconductors in the "weak pairing phase" or SC-TI heterojunctions can support Majorana modes which obey non-abelian statistics [82, 84, 144].

The goal of this chapter is to derive a rigorous connection between the bulk invariants and the surface dispersion. A heuristic way to understand this bulk-boundary correspondence is as follows. Consider a domain wall between two bulk insulators with suitably defined topological invariants that take the values ν_L and $\nu_R \neq \nu_L$ in some regions. Since the value of the invariant cannot change for finite energy gap, this means the bulk gap closes at some interface. Midgap excitations can thus exist, but they are confined to the interface by the bulk gap in the other regions. This argument applies to domain walls between regions with different values of the invariant, of which an edge is a special case where one of the regions is the vacuum (trivial phase) [195, 196].

In light of recent interest in topological insulators and superconductors, it would be useful to formalize the relation between bulk topological quantities and properties of midgap edge states. This connection has been proved specifically for IQH states on a square lattice by deriving a winding number for the edge states [38, 39]. Another approach using twisted boundary conditions has the advantage of including interactions and disorder, but cannot prove that the states exist at an open boundary [37].

There has also been recent progress on analytic solutions of edge states in topological insulators [57, 197, 198] and topological superconductors [199]. These calculations are often based on models using a specific Dirac Hamiltonian. Dirac systems are ubiquitous in condensed matter and particle physics systems and give rise to many exotic states. For example, every single-particle topologically ordered system can be realized with a Dirac Hamiltonian. [78, 181] They are used to model a variety of systems including polyacetylene, quantum Hall insulators, graphene, topological insulators and superconductors, *etc.* [4, 42, 79, 89, 200–203].

Our work applies specifically to tight-binding Dirac Hamiltonians with nearest-layer hopping. For these systems we present a prescription for the edge states spectrum and prove the bulk-boundary correspondence. In addition, we derive a simple geometric method to calculate the energies and penetration depth of the edge states analytically.

The organization of the chapter is as follows. In Sec. 6.1, we introduce the bulk quantities of a lattice Hamiltonian that determine topological behavior. In Sec. 6.2, we state the first main result of the chapter, Theorem 1 relating the parameters of the bulk Hamiltonian to the surface spectrum in a geometric way. We provide two different way of proofs, given in Sec. 6.3 and Sec. 6.4. The second main result is given in Sec. 6.5, where Theorem 2 provides the bulk-boundary correspondence between chiral edge states and the Chern number. In Sec. 6.6, we demonstrate the range of applicability of our theorems and give examples of topologically ordered systems. We also show how the bulk $\mathbb{Z}_2$ invariant for a time-reversal symmetric insulator relates to the number of surface Dirac cones in Sec. 6.6.3. In Sec. 6.7, we extend the results from lattice Hamiltonians to continuum quadratic Hamiltonians (Theorem 3), with discussions on its implications. In closing, we discuss the possible extension of the work to other classes of topological superconductors beyond IQH and TRS systems.

6.1 Characterization of the nearest-layer Hamiltonian

To study a system with edges, consider a 2D/3D crystal that terminates on a line/surface. Translational symmetry is thus broken in the direction normal to the edges However, we assume it is unbroken parallel to the surface, and the corresponding momentum $\mathbf{k}_\parallel$ is a good quantum number. In this way, any higher dimensional system can be decoupled into a family of one-dimension (1D) problems parametrized by $\mathbf{k}_\parallel$.

The Dirac Hamiltonian in momentum space $H(\mathbf{k})$ can always be expressed as a linear combination of gamma matrices, $H(\mathbf{k}) = \mathbf{h}(\mathbf{k}) \cdot \mathbf{\Gamma}$. Here $\mathbf{\Gamma}$ is a vector of the hermitian gamma matrices (independent of $\mathbf{k}$) which satisfy the Clifford algebra $\Gamma^i\Gamma^j + \Gamma^j\Gamma^i = 2\delta^{ij}$. $\mathbf{h}$ is a real vector that maps the Brillouin zone to a closed curve in a g-component vector space, where there are g gamma matrices Γ^i. The Pauli matrices are examples of gamma matrices: any 2×2 traceless matrix can written as a $\mathbf{h} \cdot \boldsymbol{\sigma}$ where $\mathbf{h}$ is a 3-component vector and $\boldsymbol{\sigma} = (\sigma^x, \sigma^y, \sigma^z)$.

Squaring the Hamiltonian gives $H^2 = (\mathbf{h}\cdot\mathbf{\Gamma})^2 = |\mathbf{h}|^2$. The eigenvalues of H, given by $E(\mathbf{k}) = \pm|\mathbf{h}(\mathbf{k})|$, can be thought of as the distance of the vector $\mathbf{h}$ to the origin. If $H(\mathbf{k})$ describes a band insulator with a bulk gap, then the locus of points traced by $\mathbf{h}(\mathbf{k})$ never intersects the origin.

Let us consider Dirac Hamiltonians with coupling between neighboring layers:

$$\mathcal{H} = \sum_{n,\mathbf{k}_\parallel} \Psi^\dagger_{n,\mathbf{k}_\parallel} \mathbf{\Gamma} \cdot \left[\mathbf{b}\, \Psi_{n-1,\mathbf{k}_\parallel} + \mathbf{b}^0\, \Psi_{n,\mathbf{k}_\parallel} + \mathbf{b}^*\, \Psi_{n+1,\mathbf{k}_\parallel} \right], \tag{6.1}$$

where n labels the layers. Both $\mathbf{b}$ and $\mathbf{b}^0$ are dependent on $\mathbf{k}_\parallel$ but we will not write this dependence explicitly. $\Psi_{n,\mathbf{k}_\parallel}$ is a vector of quasiparticle annihilation operators at layer n that captures all the degrees of freedom (*i.e.*, spin, pseudospin) at every site. Fourier transforming ($n \to k_\perp$) in the direction away from the edge, the bulk Hamiltonian becomes

$$\mathcal{H} = \sum_{k_\perp,\mathbf{k}_\parallel} \Psi^\dagger_{\mathbf{k}} \left[\mathbf{h}(\mathbf{k}) \cdot \mathbf{\Gamma}\right] \Psi_{\mathbf{k}}\,, \tag{6.2}$$

with

$$\begin{aligned}\mathbf{h}(\mathbf{k}) &= \mathbf{b}e^{-ik_\perp} + \mathbf{b}^0 + \mathbf{b}^* e^{ik_\perp} \\ &= \mathbf{b}^0 + 2\mathbf{b}^r \cos k_\perp + 2\mathbf{b}^i \sin k_\perp\,,\end{aligned} \tag{6.3}$$

where $\mathbf{b}^r$ and $\mathbf{b}^i$ are the real and imaginary components of the vector $\mathbf{b}$ respectively. We point out that $\mathbf{b}$ and $\mathbf{b}^0$ are independent of $k_\perp$

The curve traced out by $\mathbf{h}(\mathbf{k})$ for fixed $\mathbf{k}_\parallel$ is an ellipse living in the plane spanned by $\mathbf{b}^r$ and $\mathbf{b}^i$. $\mathbf{b}^0$ can be decomposed into a component $\mathbf{b}^0_\perp$ that is normal to this plane, and $\mathbf{b}^0_\parallel$ that lies within it. $\mathbf{b}^0_\parallel$ shifts the ellipse within the plane, while $\mathbf{b}^0_\perp$ lifts it uniformly. It will be useful to define

$$\mathbf{h}_\parallel(\mathbf{k}) = \mathbf{b}^0_\parallel + 2\mathbf{b}^r \cos k_\perp + 2\mathbf{b}^i \sin k_\perp \tag{6.4}$$

as the projection of $\mathbf{h}(\mathbf{k})$ on to the 2D plane spanned by $\mathbf{b}^r$ and $\mathbf{b}^i$. Note that this plane contains the origin, while the plane containing $\mathbf{h}$ is offset from the origin by the vector $\mathbf{b}^0_\perp$. Since $\mathbf{h}_\parallel$ maps the Brillouin zone to closed curves, it can be divided into two classes: ellipses that enclose the origin, and ellipses that do not.

6.2 Edge state theorem

As we shall state precisely in a moment, the behavior of $\mathbf{h}(k_\perp)$ completely determines the topological nature of the system and holds the key to understanding the relation between existence of edge states and bulk topological invariants. This section contains one of the main result of the chapter, relating the spectrum of edge states to $\mathbf{h}$.

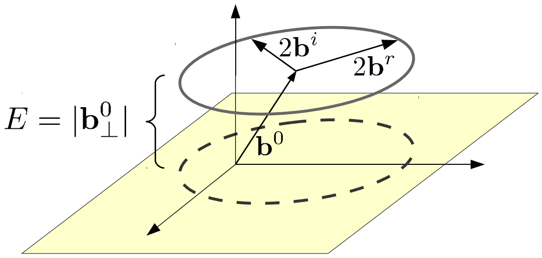

Figure 6.1: An illustration of Theorem 1.

The gray ellipse is traced out by $\mathbf{h}(k_\perp) = \mathbf{b}^0 + 2\mathbf{b}^r \cos k_\perp + 2\mathbf{b}^i \sin k_\perp$ for a fixed parallel momentum $\mathbf{k}_\parallel$ [Eq. (6.3)]. The dotted ellipse ($\mathbf{h}_\parallel$) is $\mathbf{h}$ projected on to the plane spanned by $\mathbf{b}^r$ and $\mathbf{b}^i$. The displacement of the ellipse $\mathbf{h}$ from the dotted ellipse $\mathbf{h}_\parallel$ is given by $\mathbf{b}^0_\perp$, the component of $\mathbf{b}^0$ perpendicular to this plane. Theorem 1 says that an edge state exists if and only if the dotted ellipse encloses the origin (which holds true for the diagram above), and its energy is determined by the displacement $|\mathbf{b}^0_\perp|$.

6.2.1 Edge state energy

Theorem 1.
a. The system has midgap edge states if and only if $\mathbf{h}_\parallel(k_\perp)$ encloses the origin.
b. The energies of the edge states are given by the distance from the origin to the plane containing $\mathbf{h}$, *i.e.* $E_s = \pm|\mathbf{b}^0_\perp|$. When the gamma matrices are the Pauli matrices, the energy of the left edge state (semi-infinite slab with $n > 0$) is given by:

$$E_s = \mathbf{b}^0 \cdot \frac{\mathbf{b}^r \times \mathbf{b}^i}{|\mathbf{b}^r \times \mathbf{b}^i|} \,. \tag{6.5}$$

Here we only sketch the main ideas behind two equivalent proofs of the theorem, deferring the full details to the next two sections. We present two approaches to this problem: a proof utilizing Green's functions [204] (*c.f.* Sec. 6.3) and a proof via transfer matrices [205] (*c.f.* Sec. 6.4). In this section, we consider one block of the decoupled system corresponding to fixed $\mathbf{k}_\parallel$.

We begin by writing the Green's function of the system without edges, where the full translational invariance makes a momentum space representation possible. A system with edges is then created from the fully periodic system by deleting the couplings between one pair of neighboring sites. The poles in the Green's function $G(E)$ at midgap energies E indicate the presence of edge states.

The bulk Green's function is given by

$$G_0\left(E; k_\perp\right) = \sum_i \frac{|\psi_i\rangle\langle\psi_i|}{E - E_i} \,, \tag{6.6}$$

where i sums over the energy eigenstates of $H(k_\perp)$. Since we are interested in a boundary localized in real space, it is necessary to Fourier transform the bulk Green's function. For a system of size L this results in a $L \times L$ block matrix $G_0(E; y_i, y_j)$, where each block corresponds to mixing between the lattice sites y_i and y_j.

Next we write an expression V for the terms in the Hamiltonian that create the boundary by subtracting the hopping terms between sites y_{left} and y_{right}. For models with nearest-neighbor interactions, the only nonzero matrix elements of V are those between y_{left} and y_{right}. The Dyson equation gives an exact expression for the open boundary Green's function G in terms of the bulk Green's function G_0 and the cuts V needed to take the system from one geometry to the other:

$$G(E) = \big(1 - G_0(E)V\big)^{-1} G_0(E) \,. \tag{6.7}$$

The poles of $G(E)$ occur when the edge state energy satisfies Det $\big[1 - G_0(E)V\big] = 0$. If an edge state exists with wavefunction u, it must satisfy $(I - G_0 V)u = 0$. We note that this is the same as the Schrödinger equation $(E - H_0 - V)u = 0$. The benefit of the Green's function formalism is that it reduces the problem to only edge degrees of freedom and enables an analytic solution. This implies the following two statements:

$$\int dk_\perp \frac{\mathbf{h}_\parallel}{|\mathbf{h}_\parallel|^2} = 0 \,, \tag{6.8a}$$

$$\int dk_\perp \, e^{ik_\perp} \frac{\mathbf{h}_\parallel \cdot \mathbf{b}^*}{|\mathbf{h}_\parallel|^2} = \pi \,. \tag{6.8b}$$

These conditions are satisfied if and only if $\mathbf{h}_\parallel$ encloses the origin, and the edge mode energy is given by $\pm|\mathbf{b}^0_\perp|$, where the sign is given by the orientation of $\mathbf{h}_\parallel$.

To prove Thm. 1 using transfer matrices, we consider a semi-infinite system with unit cells labeled by $n = 1, 2, 3,$ *etc.* We seek a solution ψ_n to the single-particle Schrödinger equation:

$$\mathbf{b} \cdot \mathbf{\Gamma} \psi_{n-1} + \mathbf{b}^0 \cdot \mathbf{\Gamma} \psi_n + \mathbf{b}^* \cdot \mathbf{\Gamma} \psi_{n+1} = E \psi_n \tag{6.9}$$

for $n > 1$. At the edge site $n = 1$, we have $\mathbf{b}^0 \cdot \mathbf{\Gamma}\psi_1 + \mathbf{b}^* \cdot \mathbf{\Gamma}\psi_2 = E\psi_1$. This condition is enforced by applying Eq. (6.9) for $n = 1$ but stipulating that $\psi_0 = 0$. The recursion relation (6.9) relates ψ_{n+1} to ψ_n and ψ_{n-1}. Hence given ψ_1 (and $\psi_0 = 0$), we can recursively calculate all of ψ_n and construct the wavefunction.

An edge state requires ψ_n to be exponentially decaying as n increases, hence the solution ψ takes the form:

$$\psi_n = u_a \lambda_a^n + u_b \lambda_b^n \,, \tag{6.10}$$

where $u_a = -u_b$, and λ_a, λ_b are complex with $|\lambda_a|, |\lambda_b| < 1$. Algebraically, this is equivalent to having $E = \pm|\mathbf{b}^0_\perp|$ and finding two roots within the unit circle of the functions $L(\lambda)$ or $\bar{L}(\lambda)$, defined as

$$\begin{aligned} L(\lambda) &= \mathbf{h}_\parallel(-i\ln\lambda) \cdot (\hat{\mathbf{v}}_1 + i\hat{\mathbf{v}}_2) \,, \\ \bar{L}(\lambda) &= \mathbf{h}_\parallel(-i\ln\lambda) \cdot (\hat{\mathbf{v}}_1 - i\hat{\mathbf{v}}_2) \,, \end{aligned} \tag{6.11}$$

where $\hat{\mathbf{v}}_1, \hat{\mathbf{v}}_2$ are two orthonormal vectors that live in the plane of $\mathbf{h}_{\|}$. When $\lambda = e^{ik_\perp}$ lies on the unit circle, $L(\lambda)$ and $\bar{L}(\lambda)$ trace out the ellipse $\mathbf{h}(k_\perp)$ in the complex plane clockwise and counterclockwise, respectively. Because of this property, the number of times $\mathbf{h}(k_\perp)$ wraps the origin determines the number of zeros of $L(\lambda)$ and whether the two solutions $\lambda_{a,b}$ in (6.10) exists. In Sec. 6.4, we provide the full details bridging these steps, and also compute the sign of the edge state energy as well as their penetration depth.

6.2.2 Discussion

Theorem 1 gives a simple way to compute the spectrum of edge states from properties of the bulk Hamiltonian. The existence of zero-energy edge states is determined by whether or not the ellipse traced by $\mathbf{h}_{\|}$ encloses the origin. Intuitively, the size of the ellipse is a measure of the coupling strength $\mathbf{b}$ between neighboring layers, while the in-plane displacement of the ellipse $\mathbf{b}_{\|}^0$ is a measure of coupling within the layers. From this perspective, Thm. 1a says that an edge state exists if the nearest-layer coupling is 'stronger' than the intralayer coupling. This is a straightforward extension of the edge states of polyacetylene, a 1D chain with alternating bond strengths $t \neq t'$, which supports an edge state if the chain terminates on the weaker bond [200].

The argument presented above can also be used to calculate the penetration depth ξ of the surface states:

$$\xi = \frac{a}{2\ln(1/|\lambda|)} \,. \tag{6.12}$$

a is the distance between layers, λ is the characteristic decay parameter such that the wavefunction decays as $\psi_n \sim \lambda^n$ in the bulk. $|\lambda|$ is the larger of $|\lambda_a|, |\lambda_b|$ [defined in Eq. (6.10)]. $|\lambda|$ is always less than one and is determined by the location of the origin inside the ellipse $\mathbf{h}_{\|}(k_\perp)$. When the origin touches the edge of the ellipse, λ has unit modulus and ξ tends to infinity, indicating a bulk propagating mode. At this point the surface spectrum ends and merges with the bulk bands. The decay parameter can be computed by

$$|\lambda| = \frac{l + \sqrt{l^2 - f^2}}{M + m} \,, \tag{6.13}$$

where M and m are the major and minor diameters of $\mathbf{h}_{\|}(k_\perp)$ respectively, $f = \sqrt{M^2 - m^2}$ is the distance between the foci of the ellipse, and l is the sum of the distances from the origin to the two foci. (See Fig. 6.2.)

6.3 Proof by Green's functions

It is difficult to study a system with edges because of the broken translational invariance. We begin by writing the Green's function for an easier problem: a periodic system with no boundary [204]. The full translational invariance allows us to work in momentum space,

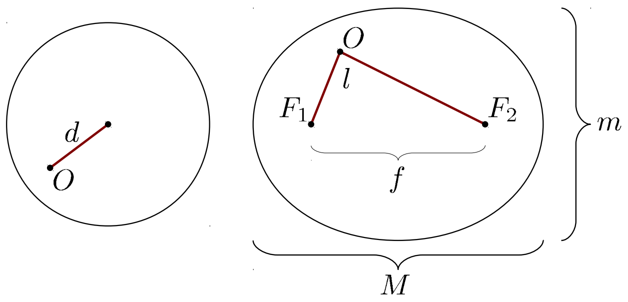

Figure 6.2: Determining the penetration depth from the ellipse $\mathbf{h}_\parallel$.

The distances from the foci of the ellipse $\mathbf{h}_\parallel(k_\perp)$ to the origin determine the characteristic decay parameter λ, which in turns gives the penetration depth $\xi = -a/2 \ln|\lambda|$. In the case where $\mathbf{h}_\parallel$ traces a circle, $|\lambda| = d/r$, where d is the distance of the origin to the center of the circle, and r is the radius of the circle. In the general case $\mathbf{h}_\parallel$ traces an ellipse, $|\lambda| = \frac{l+\sqrt{l^2-f^2}}{M+m}$, where M and m are the major and minor diameters, f is the distance between the foci $|F_1F_2|$, and l is the sum of distances $|OF_1| + |OF_2|$. (When the ellipse is a circle, we have $f = 0, M = m = 2r$ and the expression for λ reduces to that of the circular case.)

reducing the dimension of the Hamiltonian in momentum space. Next, the geometry of the system is changed from a periodic to an open system by subtracting all interactions between a particular pair of nearest-neighbors. We use the Dyson equation to calculate the Green's function for the open geometry and show that there are poles – and thus bound states – at midgap energies. The form of the potential required to cut the periodic system greatly reduces the degrees of freedom in the problem and enables an analytic solution.

We prove Theorem 1 for the case of 2×2 Dirac Hamiltonians, which can be decomposed in terms of the Pauli matrices σ^i. For higher dimensional Hamiltonians, it is always possible to find three gamma matrices Γ^i that whose sub-blocks are the Pauli matrices, *e.g.* $\tau^z\sigma^x$, $\tau^z\sigma^y$, and $\tau^z\sigma^z$. A suitable unitary transformation rotates the Hamiltonian so that it is a linear combination of these three gamma matrices, and the arguments of this section apply to each sub-block.

6.3.1 Bulk Green's function

We prove Theorem 1 for 2×2 Hamiltonians, which can be expressed in the following form:

$$H(k) = E_k \begin{bmatrix} \cos\theta & \sin\theta\, e^{-i\phi} \\ \sin\theta\, e^{i\phi} & -\cos\theta \end{bmatrix}. \tag{6.14}$$

Decomposing H into the Pauli matrices $(\sigma^x, \sigma^y, \sigma^z)$ gives $H = \mathbf{h}\cdot\boldsymbol{\sigma}$ for

$$\mathbf{h} = E_k(\sin\theta\cos\phi, \sin\theta\sin\phi, \cos\theta)\,. \tag{6.15}$$

The eigenstates are given by

$$|\psi_-\rangle = \begin{pmatrix} \sin\frac{\theta}{2} \\ -\cos\frac{\theta}{2}e^{i\phi} \end{pmatrix}, \qquad |\psi_+\rangle = \begin{pmatrix} \cos\frac{\theta}{2} \\ \sin\frac{\theta}{2}e^{i\phi} \end{pmatrix}. \tag{6.16}$$

To express $\mathbf{h}$ in terms of the parameters defined in Sec. 6.1, we assume $\mathbf{b}^r$ and $\mathbf{b}^i$ lie along $+\hat{\mathbf{x}}$ and $+\hat{\mathbf{y}}$ respectively, with $\mathbf{b}^0_\perp$ along $\hat{\mathbf{z}}$. The Hamiltonian takes the form

$$\begin{aligned} E_k \sin\theta\cos\phi\,\hat{\mathbf{x}} &= 2\mathbf{b}^r\cos k + (\mathbf{b}^0_\parallel\cdot\hat{\mathbf{x}})\,\hat{\mathbf{x}}\,, \\ E_k \sin\theta\sin\phi\,\hat{\mathbf{y}} &= 2\mathbf{b}^i\sin k + (\mathbf{b}^0_\parallel\cdot\hat{\mathbf{y}})\,\hat{\mathbf{y}}\,, \\ E_k\cos\theta\,\hat{\mathbf{z}} &= \mathbf{b}^0_\perp\,. \end{aligned} \tag{6.17}$$

Here $\mathbf{h}_\parallel$ lies in the xy-plane. For the remainder of this section, we will use the notation $b_r = |\mathbf{b}^r|$ and $b_i = |\mathbf{b}^i|$. Note that any Hamiltonian may be brought to this form by an appropriate gauge transformation.

The first step in calculating the edge mode energies is to write the Green's function for the fully periodic system. Utilizing the full translational invariance, we work for now in the momentum representation. The α-β matrix element of the bulk Green's function is given by

$$G_0^{\alpha\beta}(E;k) = \sum_i \frac{|\psi_i\rangle^\alpha \langle\psi_i|^\beta}{E - E_i}\,, \tag{6.18}$$

where i sums over the energy eigenstates of $H_{\mathbf{k}}$. The four matrix elements are given by

$$G_0^{11}(E;k) = \frac{E + E_k\cos\theta}{E^2 - E_k^2}\,, \tag{6.19a}$$

$$G_0^{22}(E;k) = \frac{E - E_k\cos\theta}{E^2 - E_k^2}\,, \tag{6.19b}$$

$$G_0^{12}(E;k) = E_k\frac{\sin\theta\cos\phi - i\sin\theta\sin\phi}{E^2 - E_k^2}\,, \tag{6.19c}$$

$$G_0^{21}(E;k) = E_k\frac{\sin\theta\cos\phi + i\sin\theta\sin\phi}{E^2 - E_k^2}\,. \tag{6.19d}$$

In order to include the effects of a boundary that is localized in real space, the bulk Green's function is written in real space via a Fourier transformation.

$$G_0(E;y) = \begin{bmatrix} B^0 & B^\dagger & \cdots & & & B \\ B & B^0 & B^\dagger & & & \\ \vdots & B & B^0 & B^\dagger & & \\ & & B & B^0 & & \\ & & & & \ddots & \\ & & & & & \\ B^\dagger & & & & & \end{bmatrix}, \tag{6.20}$$

for

$$B^0 = \int \frac{dk}{2\pi} G_0(E;k)\,, \quad B = \int \frac{dk}{2\pi} e^{ik} G_0(E;k)\,. \tag{6.21}$$

There are of course more nonzero matrix elements, corresponding to the mixing of matrix elements separated by more than one lattice constant. However, for systems with nearest-neighbor hopping, the matrix elements contained in B^0 and B are the only ones needed to prove the existence of zero energy states.

6.3.2 Green's function of the open system

Next we write an expression V that deletes the coupling terms to create a system with edges. In a system with nearest-layer interactions, the only nonzero matrix elements are those between a single pair of neighboring layers:

$$V = \begin{bmatrix} 0 & \cdots & & V_b \\ \vdots & 0 & & \\ & & \ddots & \\ V_b^\dagger & & & 0 \end{bmatrix}. \tag{6.22}$$

Here $V_b = -\mathbf{b}\cdot\boldsymbol{\sigma}$, and for the Hamiltonian described in Eq. (6.17) takes the form

$$V_b = \begin{bmatrix} 0 & -b_r - b_i \\ -b_r + b_i & 0 \end{bmatrix}. \tag{6.23}$$

We are now ready to compute the Green's function for the open system. The Dyson equation gives an exact expression for the open Green's function G in terms of the periodic Green's function G_0 and the cuts V needed to take the system from one geometry to the other:

$$G(E;y) = \big(I - G_0(E;y)V\big)^{-1} G_0(E;y)\,. \tag{6.24}$$

Substituting Eqs. (6.22) and (6.20) into Eq. (6.24) gives the following condition for an edge state wavevector u:

$$(1 - G_0 V)u = \begin{bmatrix} \mathbb{1}_2 - BV_b^\dagger & & & -B^0 V_b \\ & \mathbb{1}_2 & & \\ \vdots & & \ddots & \vdots \\ & & \mathbb{1}_2 & \\ -B^0 V_b^\dagger & & & \mathbb{1}_2 - B^\dagger V_b \end{bmatrix} u = 0\,. \tag{6.25}$$

The ellipses indicate the only nonzero sub-blocks: the first and last columns, and copies of the identity ($\mathbb{1}_2$) along the diagonal.

6.3.3 Existence and spectrum of edge modes

Since an edge state wavevector u has nonzero components in the sub-block corresponding to one of the edges, Eq. (6.25) can be satisfied in two ways. There is an edge mode on the left edge when the first two columns of Eq. (6.25) are linearly dependent, and on the right edge when the last two columns are linearly dependent. Recalling the expressions for the bulk Green's functions, Eq. (6.19), we introduce some notation for the open Green's function:

$$a_0 = \int \frac{dk}{2\pi} \frac{E}{E^2 - E_k^2}\,, \tag{6.26a}$$

$$a_x = \int \frac{dk}{2\pi} \frac{E_k \sin\theta \cos\phi}{E^2 - E_k^2}\,, \tag{6.26b}$$

$$a_y = \int \frac{dk}{2\pi} \frac{E_k \sin\theta \sin\phi}{E^2 - E_k^2}\,, \tag{6.26c}$$

$$a_z = \int \frac{dk}{2\pi} \frac{E_k \cos\theta}{E^2 - E_k^2}\,, \tag{6.26d}$$

$c_0 = \int \frac{dk}{2\pi} e^{ik} \frac{E}{E^2-E_k^2}$, and similar for c_x, c_y, and c_z. Let us first examine the conditions required for a left edge mode. Collapsing the matrix in Eq. (6.25) to the subspace corresponding to the lattice sites on each edge, the first two columns can be written as

$$X_1 = \begin{bmatrix} 1 + (b_r + b_i)(c_x - ic_y) \\ (b_r + b_i)(c_0 - c_z) \\ (b_r + b_i)(a_x - ia_y) \\ (b_r + b_i)(a_0 - a_z) \end{bmatrix}, \qquad X_2 = \begin{bmatrix} (b_r - b_i)(c_0 + c_z) \\ 1 + (b_r - b_i)(c_x + ic_y) \\ (b_r - b_i)(a_0 + a_z) \\ (b_r - b_i)(a_x + ia_y) \end{bmatrix}. \tag{6.27}$$

Now we examine the conditions required for the system to have a left edge state, *i.e.*, when the columns X_1 and X_2 are linearly dependent. This is done by writing X_1 and X_2 as a 4×2 matrix X and requiring that the determinant of any 2×2 sub-block vanish. This constraint takes on the following form for the sub-blocks of X created by the bottom two rows, the top two rows, and the second and fourth rows, respectively:

$$0 = (b_r^2 - b_i^2)(a_x^2 + a_y^2 - a_0^2 + a_z^2)\,, \tag{6.28a}$$

$$0 = 1 + 2(b_r c_x - i b_i c_y) + (b_r^2 - b_i^2)(c_x^2 + c_y^2 - c_0^2 + c_z^2)\,, \tag{6.28b}$$

$$0 = (b_r^2 - b_i^2)(c_0 - c_z)(a_x + ia_y) - (b_r^2 - b_i^2)(c_x + ic_y)(a_0 - a_z) - (b_r + b_i)(a_0 - a_z)\,. \tag{6.28c}$$

The conditions are equivalent to $B^0 V_b^\dagger u_L = 0$ and $(\mathbb{1}_2 - BV_b^\dagger)u_L = 0$, which together require $\operatorname{Det} B^0 = 0$. To see this, note that although the first condition is satisfied when either $\operatorname{Det} B^0 = 0$ or $V_b^\dagger u_L = 0$, the second case cannot satisfy $(\mathbb{1}_2 - BV_b^\dagger)u_L = 0$.

6.3.4 Constraints on $\mathbf{h}_\parallel$ and E^2

We begin by showing that

$$\operatorname{Det} B^0 = a_0^2 - a_x^2 - a_y^2 - a_z^2 \tag{6.29}$$

is zero *if and only if* $\mathbf{h}_{\|}$ encloses the origin and the edge state energy is given by $E = \pm|\mathbf{b}_{\perp}^{0}|$. For a geometric view of the variables a_0, a_x, *etc.*, note that $E_k(\sin\theta\cos\phi, \sin\theta\sin\phi)$ are the (x, y) coordinates of $\mathbf{h}_{\|}$, and $E_k\cos\theta = \mathbf{b}_{\perp}^{0}\cdot\hat{\mathbf{z}}$. E_k^2 is given by $|\mathbf{b}_{\perp}^{0}|^2 + |\mathbf{h}_{\|}|^2$, and $E^2 - E_k^2 < 0$ for a midgap state. We examine two cases, when $\mathbf{h}_{\|}$ encloses the origin and when it does not.

Suppose the ellipse does not enclose the origin. Let $\mathbf{h}_{\|}^{\min}$ be the point on the ellipse $\mathbf{h}_{\|}$ closest to the origin. Because the ellipse is convex and does not contain the origin, it must lie in the half of the plane (spanned by $\mathbf{b}^r, \mathbf{b}^i$) for which $\mathbf{r}\cdot\mathbf{h}_{\|}^{\min}$ is positive. In other words, $\mathbf{h}_{\|}(k)\cdot\mathbf{h}_{\|}^{\min}$ is positive definite. Moreover, $\mathbf{h}_{\|}(k)\cdot\mathbf{h}_{\|}^{\min} \geq |\mathbf{h}_{\|}^{\min}|^2$ from its definition. The Cauchy-Schwarz inequality says that

$$\left|(a_x\hat{\mathbf{x}} + a_y\hat{\mathbf{y}})\cdot\mathbf{h}_{\|}^{\min}\right| \leq |a_x\hat{\mathbf{x}} + a_y\hat{\mathbf{y}}|\left|\mathbf{h}_{\|}^{\min}\right|, \tag{6.30}$$

therefore

$$\begin{aligned} |a_x\hat{\mathbf{x}} + a_y\hat{\mathbf{y}}| &\geq \frac{1}{|\mathbf{h}_{\|}^{\min}|}\int\frac{dk}{2\pi}\,\frac{\mathbf{h}_{\|}\cdot\mathbf{h}_{\|}^{\min}}{E_k^2 - E^2} \\ &\geq \frac{1}{|\mathbf{h}_{\|}^{\min}|}\int\frac{dk}{2\pi}\,\frac{|\mathbf{h}_{\|}^{\min}|^2}{E_k^2 - E^2}\,. \end{aligned} \tag{6.31}$$

This sets an upper bound to $\operatorname{Det} B^0$:

$$a_0^2 - a_z^2 - a_x^2 - a_y^2 \leq \left(E^2 - |\mathbf{b}_{\perp}^{0}|^2\right)\mathcal{I}^2 - |\mathbf{h}_{\|}^{\min}|^2\mathcal{I}^2\,, \tag{6.32}$$

where $\mathcal{I} = \int\frac{dk}{2\pi}\frac{1}{E_k^2 - E^2}$. Since $|\mathbf{b}_{\perp}^{0}|^2 + |\mathbf{h}_{\|}^{\min}|^2 > E^2$, the expression is always negative and never zero. Hence no edge states can exist when the ellipse $\mathbf{h}_{\|}$ fails to enclose the origin.

Now we consider the case when the ellipse $\mathbf{h}_{\|}$ encloses the origin and show that an edge state exists only when $E^2 = |\mathbf{b}_{\perp}^{0}|^2$. First, when $E^2 = |\mathbf{b}_{\perp}^{0}|^2$, the integrals a_x and a_y are both zero. Because $E = |\mathbf{b}_{\perp}^{0}|$, $a_0^2 - a_z^2 = 0$ and the determinant is zero.

To see why $a_x = a_y = 0$ in this case, note that the denominator of $\mathcal{I}$ becomes $|\mathbf{h}_{\|}|^2$, and we can express the conditions geometrically. Here we use Gauss's law in 2D to show that $\int dk\frac{\mathbf{h}_{\|}}{|\mathbf{h}_{\|}|^2}$ is zero if and only if $\mathbf{h}_{\|}$ encloses the origin. We can visualize the expression from an electrostatics point of view: for a charged ellipse in 2D with a charge distribution $\int dk\,\delta^2(\mathbf{r} - \mathbf{h}_{\|})$, the electric field ($\propto \frac{1}{r}$ in 2D) at the origin is given by $\int dk\frac{\mathbf{h}_{\|}}{|\mathbf{h}_{\|}|^2}$. Analogous to a uniformly charged circle, the charges are distributed such that the electric field is vanishing in the interior but nonzero in the exterior:

$$a_x\hat{\mathbf{x}} + a_y\hat{\mathbf{y}} = -\int dk\frac{\mathbf{h}_{\|}}{|\mathbf{h}_{\|}|^2} = 0\,. \tag{6.33}$$

Now we show that $\operatorname{Det} B^0 = 0$ is not satisfied for any other value of E^2. If $E^2 < |\mathbf{b}_{\perp}^{0}|^2$ then $|E| < |\mathbf{b}_{\perp}^{0}| = |E_k\sin\theta\sin\phi|$. It follows that $a_0^2 - a_z^2 = (E^2 - |\mathbf{b}_{\perp}^{0}|^2)\mathcal{I}^2 < 0$, hence there are no edge states.

If $E^2 > |\mathbf{b}_\perp^0|^2$, we let $E^2 = \epsilon^2 + |\mathbf{b}_\perp^0|^2$, such that $E_k^2 - E^2 = |\mathbf{h}_\|| ^2 - \epsilon^2 > 0$. a_0 and a_z can be written as:

$$-a_0 = \int \frac{dk}{2\pi} \frac{E}{|\mathbf{h}_\||^2 - \epsilon^2}\,, \tag{6.34a}$$

$$-a_z = \int \frac{dk}{2\pi} \frac{|\mathbf{b}_\perp^0|}{|\mathbf{h}_\||^2 - \epsilon^2}\,, \tag{6.34b}$$

which combine to give:

$$a_0^2 - a_z^2 = (|E^2 - \mathbf{b}_\perp^0|^2)\mathcal{I}^2 = \epsilon^2 \mathcal{I}^2\,. \tag{6.34c}$$

For a_x and a_y, we use the manipulation

$$\frac{1}{|\mathbf{h}_\||^2 - \epsilon^2} - \frac{1}{|\mathbf{h}_\||^2} = \frac{\epsilon^2}{(|\mathbf{h}_\||^2 - \epsilon^2)|\mathbf{h}_\||^2}$$

to get:

$$-a_x\hat{\mathbf{x}} - a_y\hat{\mathbf{y}} = \epsilon \int \frac{dk}{2\pi} \frac{\mathbf{h}_\| \epsilon}{(|\mathbf{h}_\||^2 - \epsilon^2)|\mathbf{h}_\||^2}\,. \tag{6.34d}$$

By the triangle inequality: $\left|\int dk\, \mathbf{u}(k)\right| \le \int dk\, |\mathbf{u}(k)|$, we can put an upper bound

$$\begin{aligned} |a_x\hat{\mathbf{x}} + a_y\hat{\mathbf{y}}| &\le \epsilon \int \frac{dk}{2\pi} \frac{|\mathbf{h}_\||\epsilon}{(|\mathbf{h}_\||^2 - \epsilon^2)|\mathbf{h}_\||^2} \\ &= \epsilon \int \frac{dk}{2\pi} \frac{\epsilon}{(|\mathbf{h}_\||^2 - \epsilon^2)|\mathbf{h}_\||} \\ &< \epsilon \int \frac{dk}{2\pi} \frac{1}{(|\mathbf{h}_\||^2 - \epsilon^2)} \\ &= \epsilon \mathcal{I}\,. \end{aligned} \tag{6.35}$$

We have used the fact that $|\mathbf{h}_\|| > \epsilon$ to go from the second to third line. This implies $a_x^2 + a_y^2 < \epsilon^2\mathcal{I}^2$ and sets a lower bound to Eq. (6.29): $a_0^2 - a_z^2 - a_x^2 - a_y^2 > 0$ for $|E| > |\mathbf{b}_\perp^0|$.

Hence we have shown that $\mathrm{Det}\, B^0 = 0$ if and only if $E^2 = |\mathbf{b}_\perp^0|$ and the ellipse $\mathbf{h}_\|$ encloses the origin.

Turning now to the second constraint, Eq. (6.28b), we note that $E = \pm|\mathbf{b}_\perp^0|$ implies that $c_0^2 = c_z^2$. In the following, we use the fact that $c_x = -ic_y$. Substituting this into Eq. (6.28b) gives the constraint $1 + 2(b_r c_x - i b_i c_y) = 0$, which may be expressed as

$$1 - 2\int \frac{dk}{2\pi} e^{ik} \frac{\mathbf{h}_\| \cdot \mathbf{b}^*}{|\mathbf{h}_\||^2} = 0\,. \tag{6.36}$$

In order to satisfy Eq. (6.28a) and Eq. (6.28b) simultaneously, Eq. (6.36) must be true if and only if $\mathbf{h}_\|$ encloses the origin. This integral can be evaluated for an arbitrary ellipse centered at $\mathbf{b}_\|^0$ and with semimajor and semiminor axes given by $2\mathbf{b}^r$ and $2\mathbf{b}^i$ to give the desired result.

6.3.5 Sign of the energy

The final constraint, Eq. (6.28c), determines the sign of the edge state energy. Note that the first two terms vanish because $a_x = a_y = 0$ and $c_x = -ic_y$. Getting rid of the remaining term requires choosing a particular sign for the energy. The condition is satisfied with the choice $a_0 = a_z$.

The constraints for the left edge can be summarized as

1a. $E = +\mathbf{b}^0_\perp \cdot \hat{\mathbf{z}}$,

1b. $1 + 2(b_r c_x - ib_i c_y) = 0$.

A similar calculation for the right edge, using the last two columns of Eq. (6.25), gives the following conditions:

2a. $E = -\mathbf{b}^0_\perp \cdot \hat{\mathbf{z}}$,

2b. $1 + 2(b_r c_x + ib_i c_y) = 0$.

Condition 2b. can be expressed as $1 - 2\int \frac{dk}{2\pi}\, e^{-ik} \frac{\mathbf{h}_\| \cdot \mathbf{b}}{|\mathbf{h}_\||^2} = 0$. Hence it is also satisfied when $\mathbf{h}_\|$ encloses the origin, but with opposite orientation as for the left edge. The conditions for edge modes are now equivalent to two statements:

1. The function $\mathbf{h}_\|$ must enclose the origin,
2. The energy is given by $E = \pm\mathbf{b}^0_\perp \cdot \hat{\mathbf{z}}$, with the sign determined by the orientation of loop $\mathbf{h}_\|$.

We have succeeded in analytically deriving the condition for the $2L \times 2L$ matrix representing the Hamiltonian for an open system to have zero eigenvalues. The power of the method lies in the fact that V has nonzero matrix elements only in the 4×4 subspace of electron operators at the two edges. Thus the effect of the boundary can be seen by examining the 4×4 subspace, which can be handled analytically.

6.4 Proof by transfer matrices

In this section, we prove Theorem 1 for a hard-edge at a fixed $\mathbf{k}_\|$. We begin by defining a new function $\boldsymbol{\beta}$ (which is like a complex extension of $\mathbf{h}$), and the form of our edge states.

In the Hamiltonian (6.1), $\mathbf{b} \cdot \mathbf{\Gamma}$, $\mathbf{b}^0 \cdot \mathbf{\Gamma}$, $\mathbf{b}^* \cdot \mathbf{\Gamma}$ are the hopping matrices from the previous, same, and next layers respectively. We consider a semi-infinite system where the layers are labeled by positive integers with $n = 1$ denoting the layer at the surface. Hence we ignore the terms $\Psi_1^\dagger \Psi_0$ and $\Psi_0^\dagger \Psi_1$ in considering our semi-infinite system. Consequently, an excitation $\psi^\dagger = \sum_n \Psi_n^\dagger \psi_n$ of the Hamiltonian (6.1) satisfies the following properties:

$$\mathbf{b} \cdot \mathbf{\Gamma}\psi_{n-1} + \mathbf{b}^0 \cdot \mathbf{\Gamma}\psi_n + \mathbf{b}^* \cdot \mathbf{\Gamma}\psi_{n+1} = E\psi_n \qquad n \geq 1\,, \tag{6.37a}$$

$$\psi_0 = 0\,. \tag{6.37b}$$

An edge state ψ is one for which ψ_n is exponentially decreasing as a function of n. Due to the translational invariance in the bulk, we use the ansatz

$$\psi_n = \sum_\mu u_\mu \lambda_\mu^n \tag{6.38}$$

in our solutions [205].[1] An edge solution requires that $|\lambda_\mu| < 1$ for all μ and that $\sum_\mu u_\mu = 0$.

For each decaying mode (λ, u) we have:[2]

$$\lambda\left[\boldsymbol{\beta}(\lambda)\cdot\boldsymbol{\Gamma} - E\right] u = 0\,, \tag{6.39}$$

where we have defined

$$\boldsymbol{\beta}(\lambda) \equiv \lambda^{-1}\mathbf{b} + \mathbf{b}^0 + \lambda\mathbf{b}^*\,. \tag{6.40}$$

Notice that when λ has unit modulus, we recover the Bloch equation for the bulk (propagating) modes of the system:

$$\boldsymbol{\beta}\left(e^{ik_\perp}\right) = \mathbf{h}(k_\perp)\,. \tag{6.41}$$

Hence we need to find an energy E and a set of λ's all within the unit circle, such that their corresponding null vector u defined by (6.39) sum to zero [Eq. (6.37b)].

The outline of the proof is as follows. First, we derive the particle-hole relationship between left edge and right edge modes. Second, we establish the algebraic relations between the λ's and E of an edge state [Eq. (6.44)]. Third, we define complex functions $L, \bar{L}$ which represents the ellipse traced out by $\boldsymbol{\beta}(e^{ik})$. Next, we show (assuming an edge state exists) that the energy of an edge state is given by the displacement of the ellipse $|\mathbf{b}^0_\perp|$. We then proceed to prove Thm. 1a, the condition which governs the existence of an edge state (*i.e.*, when all $|\lambda_\mu| < 1$). Finally, we compute the edge states projectors [Eq. (6.51)] and determine the sign of the edge state energies, which completes the proof for Thm. 1b.

6.4.1 Relation between left-right boundaries

Lemma. For every left edge state with energy E, there is a corresponding right edge state with energy $-E$, and vice versa.

The recursion relation (6.37a) and boundary condition (6.37b) describe a semi-infinite system with a "left" edge. We can write a similar system for the "right" edge simply changing the condition in (6.37a) to $n \leq -1$ xor swapping $\mathbf{b}$ with $\mathbf{b}^*$ in the equation. The first transformation amounts to finding a set of λ's outside the unit circle, *i.e.*, $|\lambda_\mu| > 1$, such that the edge wavefunction ψ_n decays with decreasing n. The second transformation is

---

[1] A solution of the form $u_\mu n \lambda_\mu^{n-1}$ is also possible, when λ_μ is a double root of (6.42). In such situation, we can tackle the problem as a limiting case of two roots approaching each other: $\lambda'_\mu \to \lambda_\mu$.

[2] We cannot cross off λ on both sides because $\lambda = 0$ is a valid solution when $Bu_\mu = 0$.

equivalent to taking the complex conjugate of $\mathbf{b}$, and the two transformation are the same owing to the fact that $\boldsymbol{\beta}^*(\lambda) = \boldsymbol{\beta}(1/\lambda^*)$.

When the gamma matrices are the Pauli matrices, there is a charge conjugation operator $C = -i\sigma^y\mathcal{K}$ which takes $\mathbf{b}\cdot\boldsymbol{\sigma} \to -\mathbf{b}^*\cdot\boldsymbol{\sigma}$, where $\mathcal{K}$ is the complex conjugation operator. Since $C\boldsymbol{\beta}(\lambda)\cdot\boldsymbol{\sigma}C^{-1} = -\boldsymbol{\beta}^*(\lambda^*)\cdot\boldsymbol{\sigma}$, C turns a left edge state with energy E into a right edge state with energy $-E$ and vice versa.

When the Dirac matrices are larger then 2×2, such a C operator still exists, as it is always possible to find an antiunitary operator which flips the sign of three of the gamma matrices. This operator C will depend on what $\mathbf{b}$ and $\mathbf{b}^0$ are, meaning that C is a function of $\mathbf{k}_{\|}$, making it a non-local operator. However, the conclusion remains the same.

For the remainder of the proof, we will only be focused on left edge states.

6.4.2 Algebraic relation between λ_a, λ_b and E

For any E, there are (at most) four possible λ's satisfying (6.39), evident from squaring $\lambda\boldsymbol{\beta}(\lambda)\cdot\boldsymbol{\Gamma}$ to get the quartic equation

$$\lambda\boldsymbol{\beta}(\lambda)\cdot\lambda\boldsymbol{\beta}(\lambda) - E^2\lambda^2 = 0\,. \tag{6.42}$$

Note that if λ is a root to this equation, then so is $1/\lambda^*$. Hence there can be at most two solutions of for λ within the unit circle, which we call λ_a and λ_b.

The edge wavefunction takes the form $\psi_n = u_a\lambda_a^n + u_b\lambda_b^n$ with $u_a = -u_b$ to satisfy the hard-edge boundary condition (6.37b), where the coefficient u_a is a (right) null vector of the matrix $\lambda_a(\boldsymbol{\beta}(\lambda_a)\cdot\boldsymbol{\Gamma} - E)$ and similarly for u_b. It follows that the matrices $\lambda_a(\boldsymbol{\beta}(\lambda_a) - E)$ and $\lambda_b(\boldsymbol{\beta}(\lambda_b) - E)$ must share a nonzero null vector, or equivalently, any linear combinations of the two matrices must be non-invertible. In other words, an edge state at energy E exists only if the following conditions are satisfied:[3]

$$\operatorname{Det}\lambda_a(\boldsymbol{\beta}(\lambda_a)\cdot\boldsymbol{\Gamma} - E) = 0\,, \tag{6.43a}$$

$$\operatorname{Det}\lambda_b(\boldsymbol{\beta}(\lambda_b)\cdot\boldsymbol{\Gamma} - E) = 0\,, \tag{6.43b}$$

$$\operatorname{Det} c_a\lambda_a(\boldsymbol{\beta}(\lambda_a)\cdot\boldsymbol{\Gamma} - E) + c_b\lambda_b(\boldsymbol{\beta}(\lambda_b)\cdot\boldsymbol{\Gamma} - E) = 0\,, \tag{6.43c}$$

for arbitrary c_a, c_b and for $|\lambda_a|, |\lambda_b| < 1$. The converse statement is also true, as (6.43a) and (6.43b) implies that the ranks of the matrices $\lambda_{a,b}(\boldsymbol{\beta}(\lambda_{a,b})\cdot\boldsymbol{\Gamma} - E)$ are at most half their dimension (a property of gamma matrices). The last equation (6.43c) means that the two matrices must share a right null vector or a left null vector. In the former case we have a left edge state at energy E, and in the latter case we have a right edge state at energy E, which by our lemma implies a left edge state at energy $-E$.

---

[3] Equations (6.43a), (6.43b) are redundant, but useful to be written out explicitly.

We may rewrite the equations in a more useful form:

$$\lambda_a^2 E^2 = \lambda_a^2 \boldsymbol{\beta}(\lambda_a) \cdot \boldsymbol{\beta}(\lambda_a)\,, \tag{6.44a}$$

$$\lambda_b^2 E^2 = \lambda_b^2 \boldsymbol{\beta}(\lambda_b) \cdot \boldsymbol{\beta}(\lambda_b)\,, \tag{6.44b}$$

$$\lambda_a \lambda_b E^2 = \lambda_a \lambda_b \boldsymbol{\beta}(\lambda_a) \cdot \boldsymbol{\beta}(\lambda_b)\,. \tag{6.44c}$$

6.4.3 Introducing functions L, $\bar{L}$

Similar to $\mathbf{b}^0 = \mathbf{b}^0_\parallel + \mathbf{b}^0_\perp$ and $\mathbf{h} = \mathbf{h}_\parallel + \mathbf{b}^0_\perp$, we decompose $\boldsymbol{\beta}$ into components parallel and perpendicular to the 2D plane (1D if the ellipse is degenerate) spanned by $\{\mathbf{b}^r, \mathbf{b}^i\}$: $\boldsymbol{\beta}(\lambda) = \boldsymbol{\beta}_\parallel(\lambda) + \mathbf{b}^0_\perp$ Keep in mind that while $\mathbf{b}^0_\perp$ is a real vector, $\boldsymbol{\beta}_\parallel(\lambda) = \lambda^{-1}\mathbf{b} + \mathbf{b}^0_\parallel + \lambda \mathbf{b}^*$ is generally a complex vector, unless $\lambda = e^{ik}$ has unit modulus.

We want to find complex functions which trace out the same ellipse as $\boldsymbol{\beta}_\parallel(e^{ik})$ in the complex plane. We first choose two real orthogonal unit vectors $\hat{\mathbf{v}}_1, \hat{\mathbf{v}}_2$ as a coordinate basis of the 2D plane. Let

$$\begin{aligned} L(\lambda) &= \boldsymbol{\beta}_\parallel(\lambda) \cdot \hat{\mathbf{v}}_1 + i\boldsymbol{\beta}_\parallel(\lambda) \cdot \hat{\mathbf{v}}_2\,, \\ \bar{L}(\lambda) &= \boldsymbol{\beta}_\parallel(\lambda) \cdot \hat{\mathbf{v}}_1 - i\boldsymbol{\beta}_\parallel(\lambda) \cdot \hat{\mathbf{v}}_2\,. \end{aligned} \tag{6.45}$$

The loci $L(e^{ik})$ and $\bar{L}(e^{ik})$ both trace out the ellipse in the complex plane identical to $\boldsymbol{\beta}_\parallel(e^{ik})$, but with different orientations. In general, $L(\lambda)$ and $\bar{L}(\lambda)$ are not conjugate pairs unless λ lies on the unit circle. Expanding their definitions, we can see that both $\lambda L(\lambda)$ and $\lambda \bar{L}(\lambda)$ are quadratic polynomials in λ:

$$\begin{aligned} L(\lambda) &= q\lambda + w + p\lambda^{-1}\,, \\ \bar{L}(\lambda) &= p^*\lambda + w^* + q^*\lambda^{-1}\,. \end{aligned} \tag{6.46}$$

where $p = \mathbf{b} \cdot (\hat{\mathbf{v}}_1 + i\hat{\mathbf{v}}_2)$, $w = \mathbf{b}^0_\parallel \cdot (\hat{\mathbf{v}}_1 + i\hat{\mathbf{v}}_2)$ and $q = \mathbf{b}^* \cdot (\hat{\mathbf{v}}_1 + i\hat{\mathbf{v}}_2)$.

It is straightforward to show from (6.45) that $\boldsymbol{\beta}_\parallel(\lambda_a) \cdot \boldsymbol{\beta}_\parallel(\lambda_b) = \frac{1}{2}(L_a\bar{L}_b + \bar{L}_a L_b)$, where $L(\lambda_a)$ is abbreviated as L_a, *etc.* Equations (6.44) become

$$\lambda_a^2(E^2 - \Delta^2) = \lambda_a^2 L_a \bar{L}_a\,, \tag{6.47a}$$

$$\lambda_b^2(E^2 - \Delta^2) = \lambda_b^2 L_b \bar{L}_b\,, \tag{6.47b}$$

$$\lambda_a\lambda_b(E^2 - \Delta^2) = \tfrac{\lambda_a\lambda_b}{2}(L_a\bar{L}_b + L_b\bar{L}_a)\,, \tag{6.47c}$$

where $\Delta \equiv |\mathbf{b}^0_\perp|$.

6.4.4 Edge state energy

In this portion, we show that the existence of an edge state requires: $E = \pm\Delta$, $|\lambda_{a,b}| < 1$, and either $L_a = L_b = 0$ or $\bar{L}_a = \bar{L}_b = 0$. The converse statement is trivially true by inspecting Eq. (6.47). Hence if an edge state of the semi-infinite chain exists, we show here that it must have energy $E = \pm|\mathbf{b}_\perp^0|$. (First half of Thm. 1b.)

Assuming that neither λ_a or λ_b are zero, then

$$E^2 - \Delta^2 = L_a \bar{L}_a \,, \tag{6.48a}$$

$$E^2 - \Delta^2 = L_b \bar{L}_b \,, \tag{6.48b}$$

$$E^2 - \Delta^2 = \tfrac{1}{2}(L_a \bar{L}_b + L_b \bar{L}_a) \,. \tag{6.48c}$$

which we can combine to get

$$(L_a - L_b)(\bar{L}_a - \bar{L}_b) = 0 \,. \tag{6.49}$$

Equations (6.48) and (6.49) are simply reformulations of the recursion relation (6.37a) and boundary condition (6.37b). We now proceed to show that $E = \pm\Delta$.

Proof by contradiction Suppose that $E^2 - \Delta^2 \neq 0$. Then $L_a, L_b, \bar{L}_a, \bar{L}_b$ are all nonzero. Eq. (6.49) implies that $L_a = L_b$ or $\bar{L}_a = \bar{L}_b$. Eq. (6.48a) and (6.48b) together means that one equality implies the other, and hence $L_a = L_b$ and $\bar{L}_a = \bar{L}_b$ are both true. Here we have two polynomials with roots λ_a and λ_b:

$$q\lambda^2 + (w - L_a)\lambda + p = 0 \,,$$
$$p^*\lambda^2 + (w^* - \bar{L}_a)\lambda + q^* = 0 \,,$$

which means that $p/q = q^*/p^* = \lambda_a \lambda_b$. However, since $|\lambda_a \lambda_b| < 1$, we have a contradiction as $|p/q|$ cannot be less than one and greater than one at the same time. Hence we have shown, should an edge state exist, it must have energy $E = \pm\Delta$. Now (6.48a) tells us that either L_a or $\bar{L}_a$ is zero which combined with (6.49) leads to the desired result.

If one of λ_a, λ_b is zero, say $\lambda_b = 0$ (which happens when the ellipse is a circle), then the expressions simplify as $\lambda_b L_b = p$ and $\lambda_b \bar{L}_b = q^*$. From (6.47b), either $\lambda_b L_b$ or $\lambda_b \bar{L}_b$ is zero. From (6.47c) we have either $L_a = L_b = 0$ or $\bar{L}_a = \bar{L}_b = 0$, and in either case, (6.47a) implies that $E^2 - \Delta^2 = 0$.

If both λ_a and λ_b are zero (which happens when the circle is centered on the origin), then $\lambda = 0$ must be a double root to the polynomial (6.42). In this case, we have a flat band, and it is much easier to refer back to (6.37) and solve the system directly. One easily finds that the statement about edge states holds.

6.4.5 Existence of edge states

Finally, we use the fact that $|\lambda_a|, |\lambda_b| < 1$ to determine when an edge mode is present. Recall that there are four zeros (and two poles) to the equation $L(\lambda)\bar{L}(\lambda) = 0$, and that at most two of the roots have modulus less than one. An edge mode exists if either $L(\lambda)$ or $\bar{L}(\lambda)$ has both roots λ within the unit circle. (No edge mode exists if each function $L, \bar{L}$ has one root within the unit circle.)

We can compute the number of zeros (inside the unit circle) of the function L by the contour integral $\frac{1}{2\pi i}\oint \frac{L'(z)}{L(z)}dz$ along the unit circle, which computes the number of zeros minus number of poles within the unit circle. As $L(\lambda)$ has one pole (at $\lambda = 0$), $L(\lambda)$ has two zeros if and only if the ellipse $L(e^{ik})$ wraps around the origin counterclockwise, leading to an edge state. On the other hand, if L wraps around the origin clockwise, then $\bar{L}(e^{ik})$ wraps around the origin counterclockwise, and there are two zeros for $\bar{L}(\lambda)$ within the unit circle which also leads to an edge state. In the case where the ellipse $\boldsymbol{\beta}_{\parallel}$ does not wrap the origin, then neither L or $\bar{L}$ has two roots within the unit circle, and an exponentially decaying solution to the semi-infinite system does not exist.

This completes the proof for Theorem 1a, which relates the presence of edge states to the properties of the ellipse $\boldsymbol{\beta}(e^{ik}) = \mathbf{h}(k)$.

6.4.6 Sign of edge state energy

In this section, we determine whether the left edge state energy is $+\Delta$ or $-\Delta$, where $\Delta \equiv |\mathbf{b}^0_{\perp}| \geq 0$. This will complete the final statement of Theorem 1b.

Define $\hat{\mathbf{v}}_{\perp}$ as the unit vector parallel to $\mathbf{b}^0_{\perp}$ (assume $\Delta > 0$). Recall that $\hat{\mathbf{v}}_1, \hat{\mathbf{v}}_2$ are unit vectors used in the definitions of $L, \bar{L}$, and so the three unit vectors are mutually orthogonal. Define the corresponding gamma matrices $\Gamma^x = \hat{\mathbf{v}}_1 \cdot \boldsymbol{\Gamma}, \Gamma^y = \hat{\mathbf{v}}_2 \cdot \boldsymbol{\Gamma}, \Gamma^{\perp} = \hat{\mathbf{v}}_{\perp} \cdot \boldsymbol{\Gamma}$, which pairwise anticommute. As $\boldsymbol{\beta}_{\parallel} \cdot \hat{\mathbf{v}}_1 = \frac{1}{2}(L + \bar{L})$ and $\boldsymbol{\beta}_{\parallel} \cdot \hat{\mathbf{v}}_2 = \frac{1}{2i}(L - \bar{L})$,

$$\lambda(\boldsymbol{\beta}(\lambda) \cdot \boldsymbol{\Gamma} - E) = \lambda(\Delta\Gamma^{\perp} - E) + \frac{\lambda L(\lambda)}{2}(\Gamma^x - i\Gamma^y) + \frac{\lambda \bar{L}(\lambda)}{2}(\Gamma^x + i\Gamma^y)\,. \tag{6.50}$$

The first term annihilates the projector $\frac{1}{2}(1 + \frac{E}{\Delta}\Gamma^{\perp})$ while the second and third terms annihilate $\frac{1}{2}(1 + i\Gamma^x\Gamma^y)$ and $\frac{1}{2}(1 + i\Gamma^x\Gamma^y)$ respectively.

By inspection, the projector $P = \sum uu^{\dagger}$ on to the edge state depends on whether L or $\bar{L}$ has two zeros inside the unit circle, as well as the energy E:

$$P_{\pm} = \begin{cases} \frac{1}{4}(1 \pm \Gamma^{\perp})(1 - i\Gamma^x\Gamma^y) & L_a = L_b = 0 \\ \frac{1}{4}(1 \pm \Gamma^{\perp})(1 + i\Gamma^x\Gamma^y) & \bar{L}_a = \bar{L}_b = 0 \end{cases}, \tag{6.51}$$

where $P_{\pm}$ projects on to the edge states with energy $E = \pm\Delta$.

When the irreducible representations of $\boldsymbol{\Gamma}$ are 2×2, the product $i\Gamma^x\Gamma^y$ must equal either $\Gamma^{\perp}$ or $-\Gamma^{\perp}$, hence either P_+ or P_- must be zero. This implies that an edge state occurs only at Δ or $-\Delta$ but not both. For example, when $\Gamma^x\Gamma^y = i\Gamma^{\perp}$ and $L = 0$, then $P_+ = \frac{1}{2}(1 + \Gamma^{\perp}), P_- = 0$ and there is exactly one edge state at energy Δ. In general, we can determine E via the orientation of the ellipse $\mathbf{h}$:

$$E = \mathbf{b}^0 \cdot \frac{\mathbf{b}^r \times \mathbf{b}^i}{|\mathbf{b}^r \times \mathbf{b}^i|}\,, \tag{6.52}$$

where the cross product is defined from the commutation algebra $\mathbf{b}^r \times \mathbf{b}^i = -\frac{i}{4}\operatorname{Tr}\left\{\boldsymbol{\sigma}\left[\mathbf{b}^r \cdot \boldsymbol{\sigma}, \mathbf{b}^i \cdot \boldsymbol{\sigma}\right]\right\}$. This result gives us Theorem 1b.

When the irreducible representations of $\mathbf{\Gamma}$ are $2^m \times 2^m$ with $m \geq 2$, there are edge states at both Δ and $-\Delta$. As $P_+ + P_- = \frac{1}{2}(1 \mp i\Gamma^x\Gamma^y)$, there are a total of 2^{m-1} left edge states. Notice that the projectors P_+ and P_- are related by the similarity transformation $P_+ = \Gamma^w P_- \Gamma^w$, where Γ^w anticommutes with $\Gamma^{x,y,\perp}$, and so there must be 2^{m-2} edge states at each energy.

6.4.7 Effective surface Hamiltonian

We can use the edge state projector to construct the effective surface Hamiltonian. The operator

$$P_s = P_+ + P_- = \tfrac{1}{2}(1 - i\Gamma^x\Gamma^y) \tag{6.53}$$

projects on to the edge states (assuming $\hat{\mathbf{v}}_1$ and $\hat{\mathbf{v}}_2$ are chosen such that $L = 0$). Notice that it only depends on $\mathbf{b} \cdot \mathbf{\Gamma}$, the nearest-neighbor coupling and not the on-site potential:

$$\begin{aligned} \tfrac{1}{2}(1 - i\Gamma^x\Gamma^y) &= \frac{1}{2}\left(1 - i\frac{[\mathbf{b}^r \cdot \mathbf{\Gamma}, \mathbf{b}^i \cdot \mathbf{\Gamma}]}{2|\mathbf{b}^r \times \mathbf{b}^i|}\right) \\ &= \frac{1}{2}\left(1 + \frac{[\mathbf{b} \cdot \mathbf{\Gamma}, \mathbf{b}^* \cdot \mathbf{\Gamma}]}{\frac{4}{\pi}(\text{Area of ellipse})}\right). \end{aligned} \tag{6.54}$$

The effective surface Hamiltonian is

$$\begin{aligned} H_s &= EP_+ - EP_- + E_\infty(1 - P_s) \\ &= P_s(\mathbf{b}^0_\perp \cdot \mathbf{\Gamma}) + E_\infty(1 - P_s), \end{aligned} \tag{6.55}$$

where $E_\infty \to \infty$ such that the low energy theory describes the surface states.

6.5 Bulk Chern number and chiral edge correspondence

In this section we states and prove our second theorem, relating the bulk Chern number ν with the number of chiral edge modes for 2×2 Hamiltonians.

Theorem 2. A chiral edge mode exists for a 2D bulk insulator if the bulk has a nonzero Chern number, *i.e.*, $\mathbf{h}(\mathbf{k})$ wraps the origin. The number of chiral edge modes, counterclockwise minus clockwise, is given precisely by the Chern number.

When the irreducible representation of $\mathbf{\Gamma}$ are 4×4 or larger, it can be shown that the Chern number is always zero. The edge states of any surface always appear in pairs with energy $+E_s$ and $-E_s$ and so the number of clockwise and counterclockwise chiral modes are always equal. We are particularly interested in 2×2 Hamiltonians because they can have nonzero Chern numbers and support chiral modes.

Consider an insulator in two-dimensions whose Hamiltonian is written as a 2×2 traceless matrix: $H(k_x, k_y) = \mathbf{h}(k_x, k_y) \cdot \boldsymbol{\sigma}$. Because the bulk gap of an insulator is nonzero, $\mathbf{h}$ is nonzero at all points in the Brillouin zone. Hence $H(\mathbf{k})$ is a map from the Brillouin zone (torus) to a set of nonzero vectors with 3 components ($\mathbb{R}^3 - \{0\}$), and such maps can be characterized by a $\nu \in \mathbb{Z}$ topological invariant, known as the Chern number.[4] Hamiltonians with different Chern numbers ν cannot be deformed into one another without closing the bulk gap. In this context, the invariant ν determines the number of times the torus $\mathbf{h}(\mathbf{k})$ wraps around the origin.

To examine the edge states for an arbitrary edge, say one parallel to $\hat{\mathbf{y}}$, we analyze the spectrum as a function of $k_\parallel = k_y$. The torus $\mathbf{h}(\mathbf{k})$ can be divided into a family of loops $\mathbf{h}(k_x)|_{k_y}$, each at a fixed value of k_y and giving information of the edge state at that momentum.

Before proceeding to the technical proof, we present a geometric argument with the aid of Fig. 6.3, which shows an example of a bulk insulator with Chern number $\nu = 1$. The important loops of fixed k_y are highlighted in black. Since ν is nonzero and the torus wraps the origin, it is always possible to find two loops that are coplanar with the origin, one of which encloses the origin and one that does not. In this example, the latter case occurs at $k_y = 0$, indicating no midgap edge states at this k_y. As we scan through different values of k_y, the loop moves out of this plane. At some critical momentum k_c (given by $\frac{\pi}{3}$ in Fig. 6.3), the projection of the loop onto this plane intersects the origin and an edge state emerges from the bulk conduction bands. At $k_y = \pi$, the loop is coplanar with the origin and encloses the origin, indicating zero-energy edge states at this value of k_y. As the plane of the loop passes through the origin, the energy of the edge state changes sign. The presence of edge modes for this range of momentum is shown as orange shading in Fig. 6.3. Eventually at some critical momentum k_v (given here by $\frac{5\pi}{3}$), the loop moves away from the origin and the edge state disappears in to the bulk valence band. Since the edge state energies at k_v and k_c have opposite signs, the edge band connects the bulk valence and the bulk conduction bands.

Formally, we can describe each loop $\mathbf{h}(k_x)|_{k_y}$ by the Berry phase $\phi(k_y)$ living in a circle $[0, 2\pi]$ with $0 \sim 2\pi$ [32]. The Berry phase can be formulated in various ways:

$$\phi(k_y) = -\oint_0^{2\pi} dk_x \, A_x(k_x, k_y) \tag{6.56a}$$

$$= \int_0^{k_y} dk'_y \oint_0^{2\pi} dk_x \, F(k_x, k'_y) \tag{6.56b}$$

$$= \frac{1}{2}\Omega(\mathbf{h}) \, , \tag{6.56c}$$

---

[4] Technically the Chern number is not defined for the map $\mathbf{h} : T^2 \to \mathbb{R}^3 - \{0\}$. However, we can compose $\mathbf{h}$ with the deformation retract $r : \mathbb{R}^3 - \{0\} \to S^2 = \mathbb{CP}^1$ and the inclusion map $i : \mathbb{CP}^1 \to \mathbb{CP}^\infty$ to make the Chern number (first Chern class) well defined: $\varphi = i \circ r \circ \mathbf{h} : T^2 \to \mathbb{CP}^\infty$. What it boils down to is that we are calling the induced map between the cohomology classes $\mathbf{h}^* : H^2(\mathbb{R}^3 - \{0\}) \to H^2(T^2)$ the Chern number.

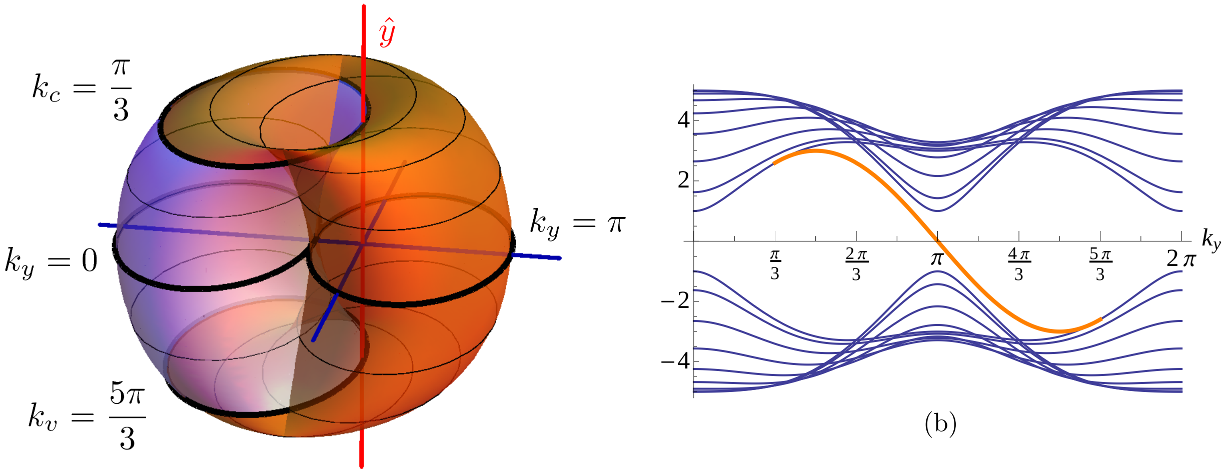

(a)

(b)

Figure 6.3: Illustration of bulk-boundary correspondence.

(a) The torus traced out by $\mathbf{h}(k_x, k_y)$ for a bulk insulator with Chern number $\nu = 1$. Each black loop maps out $\mathbf{h}(k_x)|_{k_y}$ for fixed values of k_y, the thick black lines guiding the eye to important loops. Setting $k_y = \pi$ gives the black loop on the right that encloses the origin, meaning there is a zero-energy edge mode at this value of k_y. At $k_y = 0$, the black loop on the left lies in the plane of the origin without containing it, indicating no edge mode at $k_y = 0$. The black loops on the top and bottom ($k_c = \frac{\pi}{3}, k_v = \frac{5\pi}{3}$) have projections which intersect the origin, indicating the values of k_y where the edge band merges with the bulk bands. (Note that in this model, each loop at fixed k_y lies in the xz-plane.)

(b) The band structure of the system with the edge mode drawn in orange. Notice that the edge band touches the conduction band at $k_y = \frac{\pi}{3}$, has zero energy at $k_y = \pi$, and merges with the valence band at $k_y = \frac{5\pi}{3}$.

The model presented here is a $p + ip$ superconductor described in Sec. 6.6.2 [see Eq. (6.60)] with parameters: $t = 1$, $\Delta_0 = 3$, $\mu = 1$.

where $A_j(\mathbf{k}) = i\langle\psi_\mathbf{k}|\partial_j\psi_\mathbf{k}\rangle$ is the Berry connection of the filled energy states of $H(\mathbf{k})$, $F = \partial_x A_y - \partial_y A_x$ is the Berry curvature. Geometrically, ϕ is half the oriented solid angle $\Omega(\mathbf{h})$ subtended by the loop $\mathbf{h}(k_x)$ as seen from the origin. The integral of $\frac{1}{2\pi}F$ over the entire Brillouin zone gives the Chern number: $\frac{1}{2\pi}\oint_{\text{BZ}} F = \nu$. Both ϕ and k_y live on a circle, and from Eq. (6.56b), $\phi(k_y)$ is a map $S^1 \to S^1$ with winding number ν.

At the values of $\phi(k_y) = 0$ or π, the origin is in the plane of the ellipse $\mathbf{h}(k_x)|_{k_y}$, and lies outside or inside the ellipse respectively. Hence there is a zero energy edge state when $\phi(k_y) = \pi$, and no edge state if $\phi(k_y) = 0$ (or 2π). The family of loops as k_y is varied connects these two special cases smoothly. For example, the upper critical momentum k_c has Berry phase $0 \leq \phi(k_c) < \pi$, while the lower critical momentum k_v has Berry phase $\pi < \phi(k_v) \leq 2\pi$. Thm. 1b says that if an edge state exists, $0 < \phi < \pi$ implies it has energy $E_s > 0$, and $\pi < \phi < 2\pi$ implies $E_s < 0$. Therefore in between $k_c < k_y < k_v$, a gapless (counterclockwise) chiral mode must exist connecting the bulk bands.

For an insulator with Chern number ν, the Berry phase $\phi(k_y)$ goes from 0 to $2\pi\nu$ as k_y is varied from 0 to 2π. Each time the phase $\phi(k_y)$ winds around the circle, $2\pi\alpha \to 2\pi(\alpha+1)$, a pair of critical momenta $(k_{c\alpha}, k_{v\alpha})$ defines a range in which a chiral mode connects the bulk valence and conduction band, $k_{c\alpha} < k_y < k_{v\alpha}$. This chiral mode is counterclockwise as the phase ϕ increases by 2π. Similarly, there is a clockwise chiral mode as ϕ decreases by 2π. Therefore, the total number of chiral edge modes (counterclockwise − clockwise) is given by the Chern number of the bulk Hamiltonian.

6.5.1 Discussion

The bulk-boundary correspondence described in Thm. 2 holds even in the presence of weak interactions. The number of edge states is a topological property of the bulk and is robust to small perturbations that do not close the bulk insulating gap. Such weak interactions have the effect of altering the edge state dispersion from the simple formula derived in Thm. 1. Nevertheless, we may still view the result of Thm. 1 as a starting point where the weak interactions are added perturbatively. With strong interactions, the electronic excitations may no longer behave as a Fermi liquid, leading to a break down of the bulk-boundary correspondence described here. For example, electron-electron interactions may drive the 1D edge states of QSH insulators to become Luttinger liquids, which have been shown to break the topological distinction between the insulating and helical edge states [45, 206].

6.6 Applications of Theorem 1

In this section, we illustrate how Theorem 1 may be used the edge state dispersion in various systems.

6.6.1 Example: graphene

As an illustration of how Thm. 1 can be used to calculate edge state energies, we examine the zigzag edge of graphene. Because the bulk energy bands are degenerate at two inequivalent points in the Brillouin zone, there is no well-defined topological invariant and Thm. 2 does not apply.

Consider the tight-binding model for graphene on a honeycomb lattice with primitive translational vectors $\mathbf{a}_1$ and $\mathbf{a}_2$ taken to be 120° apart. The zigzag boundary parallel to either $\mathbf{a}_1$ or $\mathbf{a}_2$ is known to support edge modes, while the armchair boundary parallel to

$\mathbf{a}_1 - \mathbf{a}_2$ has no edge modes. Using the reciprocal space coordinates $k_1 = \mathbf{k} \cdot \mathbf{a}_1, k_2 = \mathbf{k} \cdot \mathbf{a}_2$, the tight-binding Hamiltonian takes the form

$$H = t \begin{bmatrix} 0 & 1 + e^{ik_1} + e^{-ik_2} \\ 1 + e^{-ik_1} + e^{ik_2} & 0 \end{bmatrix}, \tag{6.57}$$

written in the (A, B) basis, where A and B are the inequivalent sublattices. The Hamiltonian can be written in terms of the Pauli matrices as $H = \mathbf{h} \cdot \boldsymbol{\sigma}$ with

$$\mathbf{h}(\mathbf{k}) = t(1 + \cos k_1 + \cos k_2, -\sin k_1 + \sin k_2, 0)\,. \tag{6.58}$$

For a zigzag edge parallel to $\mathbf{a}_1$, we examine the curves traced by $\mathbf{h}$ for fixed k_1.[5] The k_2-dependent terms in $\mathbf{h}$ are written as

$$\begin{aligned} 2\mathbf{b}^r \cos k_2 &= (t, 0, 0) \cos k_2\,, \\ 2\mathbf{b}^i \sin k_2 &= (0, t, 0) \sin k_2\,, \end{aligned}$$

while the remaining k_2-independent terms become

$$\mathbf{b}^0_{\parallel} = (t + t\cos k_1, -t \sin k_1, 0)\,, \qquad \mathbf{b}^0_{\perp} = 0\,.$$

$\mathbf{h}_{\parallel}$ lies in the plane spanned by $\mathbf{b}^r$ and $\mathbf{b}^i$, and for this system is a circle in the xy-plane. It encloses the origin only if the magnitude of $\mathbf{b}^0$ is less than t, *i.e.*, when $|1 + e^{ik_1}| < 1$ or equivalently when $2(1 + \cos k_1) < 1$. Thus for $\frac{2\pi}{3} < k_1 < \frac{4\pi}{3}$, $\mathbf{h}_{\parallel}$ encloses the origin and the system has midgap edge modes. According to Thm. 1b, the energies of these edge modes are given by $\pm|\mathbf{b}^0_{\perp}|$, which is zero. We have shown that the zigzag boundary supports zero energy edge states when $\frac{2\pi}{3} < k_1 < \frac{4\pi}{3}$, in agreement with previous work [202, 207].

To see why such edge modes do not exist at armchair boundaries, consider the edge parallel to $\mathbf{a}_1 - \mathbf{a}_2$. By rewriting the Hamiltonian in terms of $k_{\parallel} \equiv k_1 - k_2$ and $k_{\perp} = k_1$, we can again examine the behavior of $\mathbf{h}_{\parallel}$ at fixed $k_{\parallel}$. In this case, it is possible to show that $\mathbf{h}_{\parallel}$ never encloses the origin, and thus never satisfies the condition for midgap edge states.

6.6.2 Example: $p + ip$ superconductor (lattice model)

We study a $p + ip$ system, which in the weak-pairing phase is characterized by chiral Majorana modes at the edge [79]. We consider a model on a square lattice with p-wave pairing between nonrelativistic spinless electrons, shown in Fig. 6.3. The bulk Hamiltonian is given by

$$H(\mathbf{k}) = \begin{bmatrix} \xi_{\mathbf{k}} - \mu & \Delta_{\mathbf{k}} \\ \Delta^*_{\mathbf{k}} & -\xi_{\mathbf{k}} + \mu \end{bmatrix}, \tag{6.59}$$

---

[5] Despite our notation, the basis vector $\mathbf{a}$ corresponding to $k_{\perp}$ doesn't have to be perpendicular to the surface, it just has to be a displacement that takes one layer parallel to the surface to the next.

where H is written in the $(c_{\mathbf{k}}, c^{\dagger}_{-\mathbf{k}})^T$ basis. The kinetic energy is given by $\xi_{\mathbf{k}} = -2t(\cos k_x + \cos k_y)$ and the pair potential is given by $\Delta_{\mathbf{k}} = \Delta_0(\sin k_y + i \sin k_x)$, with Δ_0 real. Eq. (6.59) can be expressed as $H = \mathbf{h} \cdot \boldsymbol{\tau}$, where τ^i are the Pauli matrices in Bogoliubov-de Gennes (BdG) space:

$$\mathbf{h}(k_x, k_y) = (\Delta_0 \sin k_y, -\Delta_0 \sin k_x, -2t \cos k_x - 2t \cos k_y - \mu) . \tag{6.60}$$

For a system with edges parallel to $\hat{\mathbf{x}}$, we examine the ellipses traced by $\mathbf{h}(k_y)$ for fixed values of k_x. Following Eq. (6.3), the k_y-dependence of $\mathbf{h}$ is decomposed as

$$\begin{aligned} 2\mathbf{b}^r \cos k_y &= (0, 0, -2t) \cos k_y \, , \\ 2\mathbf{b}^i \sin k_y &= (\Delta_0, 0, 0) \sin k_y \, . \end{aligned}$$

The remaining k_y-independent term is decomposed as

$$\begin{aligned} \mathbf{b}^0_{\parallel} &= (0, 0, -2t \cos k_x - \mu) \, , \\ \mathbf{b}^0_{\perp} &= (0, -\Delta_0 \sin k_x, 0) \, . \end{aligned}$$

For this model $\mathbf{h}_{\parallel}(k_y)$, which lies the plane spanned by $\mathbf{b}^r$ and $\mathbf{b}^i$, is an ellipse in the xz-plane. The condition for the ellipse to enclose the origin is $|2t \cos k_x + \mu| < |2t|$, which is only possible for the range of chemical potential $|\mu| < 4|t|$. According to Thm. 1, when this condition is satisfied, the system has midgap states at the left edge with energy

$$\begin{aligned} E_s &= \mathbf{b}^0_{\perp} \cdot \frac{\mathbf{b}^r \times \mathbf{b}^i}{|\mathbf{b}^r \times \mathbf{b}^i|} = \mathbf{b}^0_{\perp} \cdot (-\hat{\mathbf{y}}) \\ &= \Delta_0 \sin k_x \, , \end{aligned}$$

assuming $t\Delta_0 > 0$. The right edge state energy is given by $-E_s = -\Delta_0 \sin k_x$. The two edge states can become degenerate at $E_s = 0$ at either $k_x = 0$ or π for an appropriate range of μ: the degeneracy occurs at $k_x = 0$ when $-4 < \mu/t < 0$, and at $k_x = \pi$ when $0 < \mu/t < 4$. The bulk gap closes and there is a transition at $\mu/t = 0$ or ± 4.

6.6.3 Example: 3D topological insulator

In this section we show that the surface states of a strong topological insulator have an odd number of Dirac cones, and derive an effective surface theory. As an example of a topological insulator, we use a model on a cubic lattice by Hosur *et al.* [187]:

$$H = v\tau^z \Big(\sum_{\mu} \sigma^{\mu} \sin k_{\mu} \Big) + \Big(M - t \sum_{\mu} \cos k_{\mu} \Big) \tau^x \tag{6.61}$$

for $\mu = x, y, z$. In the basis of Dirac matrices $\boldsymbol{\Gamma} = (\tau^z\sigma^x, \tau^z\sigma^y, \tau^z\sigma^z, \tau^x)$, we can write $H = \mathbf{h} \cdot \boldsymbol{\Gamma}$, with

$$\mathbf{h}(\mathbf{k}) = \big(v \sin k_x, v \sin k_y, v \sin k_z, m(\mathbf{k}) \big) \, , \tag{6.62}$$

where the "mass" is given by $m(\mathbf{k}) = M - t\sum \cos k_\mu$. (The 'fifth' Dirac matrix is τ^y, but it is never used in this model.) For the (001) surface parallel to $\hat{\mathbf{x}}$ and $\hat{\mathbf{y}}$, we solve for the edge states as a function of k_x, k_y:

$$\begin{aligned}\mathbf{h}(k_z)\big|_{k_x,k_y} &= (v\sin k_x, v\sin k_y, 0, M - t\cos k_x - t\cos k_y) \\ &\quad + (0,0,0,-t)\cos k_z + (0,0,v,0)\sin k_z\,,\end{aligned}$$

which lies on the *34*-plane (in $\mathbf{\Gamma}$ space) displaced by $v(\sin k_x, \sin k_y)$ from the origin. An edge state exists if and only if $|M - t\cos k_x - t\cos k_y| < |t|$ with Dirac cone spectrum $E_s = \pm v\sqrt{\sin^2 k_x + \sin^2 k_y}$.

At any of the surface TRIMs (k_x, k_y), the ellipse $\mathbf{h}_\parallel(k_z)|_{k_x,k_y}$ has one of its diameters stretching from $m(k_x, k_y, 0)$ to $m(k_x, k_y, \pi)$ along the Γ^4 axis. This ellipse encloses the origin if and only if the two endpoints straddles the origin; equivalently, a Dirac cone appears at the surface TRIM if the mass in the bulk Hamiltonian changes sign [208], *i.e.*,

$$m(k_x, k_y, 0)\, m(k_x, k_y, \pi) < 0\,. \tag{6.63}$$

In this basis the time-reversal operator has the form $\Theta = -i\sigma^y\mathcal{K}$, where $\mathcal{K}$ is the complex conjugation operator. The spatial inversion operator is $\Pi = \Gamma^4 = \tau^x$. At the eight bulk TRIMs, the Hamiltonian commutes with the inversion operator: $[H(\mathbf{k}_{\text{TRIM}}), \Pi] = 0$. In fact, H is a multiple of Π:

$$H(\mathbf{k}_{\text{TRIM}}) = m(\mathbf{k}_{\text{TRIM}})\Pi\,. \tag{6.64}$$

Hence, the sign of the mass determines the parity eigenvalue of the pair of filled states. The strong $\mathbb{Z}_2$ topological invariant is the product of the parity eigenvalues at these TRIMs [43], and hence

$$\nu_0 = \prod_{\text{TRIM }\mathbf{k}} \operatorname{sgn} m(\mathbf{k})\,. \tag{6.65}$$

It is clear that the bulk $\mathbb{Z}_2$ invariant dictates whether there are an even or odd number of Dirac cones on the surface [4, 208].

Generically, all TRS topological insulators written in 4×4 Dirac matrices take on a similar form to (6.61), and most importantly they satisfy (6.64) at the eight bulk TRIMs. Hence it is straightforward to establish the bulk-boundary correspondence for 3D TRS topological insulators.

We now proceed to examine the surface eigenstates following the derivation in Sec. 6.4.7. When $1 < m/t < 3$, the model is in the strong topological insulating phase with a single Dirac cone at $(k_x, k_y) = (0, 0)$. The surface Hamiltonian is of the form $H_s = (\mathbf{b}_\perp^0 \cdot \mathbf{\Gamma})P_s$ where P_s is the projector of the two surface states: $P_s = \frac{1}{2}(1 - i(-\Gamma^4)\Gamma^3) = \frac{1}{2}(1 + \tau^y\sigma^z)$. To examine the Hamiltonian in the reduced vector space, it is useful to apply a unitary transformation $\bar{H} = UHU^{-1}$ where $U = \exp(-i\frac{\pi}{4}\tau^x)$. The projector becomes diagonal in the new basis

$$\bar{P}_s = UP_sU^{-1} = \frac{1}{2}(1 + \tau^z\sigma^z)\,,$$

projecting onto the first and last row. The "edge energy" term $\mathbf{b}_\perp^0 \cdot \mathbf{\Gamma}$ transforms as

$$\begin{aligned} \bar{V}_\perp^0 = U(\mathbf{b}_\perp^0 \cdot \mathbf{\Gamma})U^{-1} &= -v\tau^y(\sigma^x \sin k_x + \sigma^y \sin k_y) \\ &\approx -v\tau^y(\sigma^x k_x + \sigma^y k_y)\,. \end{aligned}$$

Since $\bar{P}_s$ is diagonal with entries $(1,0,0,1)$, it suffices to examine only the four corners of $\bar{V}_\perp^0$. The effective surface Hamiltonian can be computed:[6]

$$\begin{aligned} \bar{H}_s = \bar{V}_\perp^0 \bar{P}_s &\approx v \begin{bmatrix} 0 & k_y + ik_x \\ k_y - ik_x & 0 \end{bmatrix} \\ &= v(\boldsymbol{\sigma} \times \mathbf{k}) \cdot \hat{\mathbf{z}}\,. \end{aligned} \tag{6.66}$$

The basis of the surface Hamiltonian $\bar{H}_s$ is, in terms of the basis of H, $(1,0,i,0)^T/\sqrt{2}$ and $(0,1,0,i)^T/\sqrt{2}$ (The first and last columns of $U^\dagger$). The spin degrees of freedom ($\boldsymbol{\sigma}$) and the orbital degree of freedom ($\boldsymbol{\tau}$) are entangled in the surface states.

6.7 Continuum Hamiltonians quadratic in momentum

The bulk-edge correspondence stated in Sec. 6.1 may also be extended to Hamiltonians in the continuum. Given a translationally invariant Dirac Hamiltonian quadratic in momentum $\mathbf{p} = -i\nabla$, of the form:

$$\begin{aligned} H(p; \mathbf{p}_\parallel) &= C^0(\mathbf{p}_\parallel) + C^1(\mathbf{p}_\parallel)p + C^2(\mathbf{p}_\parallel)p^2 \\ &= \left[\mathbf{c}^0(\mathbf{p}_\parallel) + \mathbf{c}^1(\mathbf{p}_\parallel)p + \mathbf{c}^2(\mathbf{p}_\parallel)p^2\right] \cdot \mathbf{\Gamma}\,, \end{aligned} \tag{6.67}$$

where $\mathbf{p}_\parallel$ and p are, respectively, the momentum parallel and perpendicular to the edge/surface. For a fixed momentum $\mathbf{p}_\parallel$, the vector

$$\mathbf{h}(p)\big|_{\mathbf{p}_\parallel} = \mathbf{c}^0 + \mathbf{c}^1 p + \mathbf{c}^2 p^2 \tag{6.68}$$

traces a parabola. This parabola lies on some 2D plane spanned by $\mathbf{c}^1$ and $\mathbf{c}^2$, and we can always decompose $\mathbf{c}^0$ and $\mathbf{h}$ into in-plane and out-of-plane components: $\mathbf{c}^0 = \mathbf{c}_\perp^0 + \mathbf{c}_\parallel^0$ and $\mathbf{h}(p) = \mathbf{c}_\perp^0 + \mathbf{h}_\parallel(p)$. In this section we state the main theorem:

Theorem 3.
a. An edge state (with zero Dirichlet or Neumann boundary condition) exists if and only if the origin is within the concave side of the parabola $\mathbf{h}_\parallel(p)$.
b. The energy of the edge state is given by the distance of the plane to the origin, *i.e.*, $E_s = \pm|\mathbf{c}_\perp^0|$. When the gamma matrices are the Pauli matrices, the left edge (semi-infinite slab with $x \geq 0$) energy is given by:

$$E_s = \mathbf{c}^0 \cdot \frac{\mathbf{c}^1 \times \mathbf{c}^2}{|\mathbf{c}^1 \times \mathbf{c}^2|}\,. \tag{6.69}$$

The proof of Theorem 3 is given later in Sec. 6.7.3.

---

[6] The Rashba coupling results from our choice of U. It is also possible with a different choice of U to arrive at the surface Hamiltonian of the form $\boldsymbol{\sigma} \cdot \mathbf{k}$.

6.7.1 Discussion

The proof of Thm. 3 uses the ansatz $\psi(x) = u_a e^{i\kappa_a x} + u_b e^{i\kappa_b x}$ and derives the condition when $\operatorname{Im}\kappa_{a,b} > 0$ for edge states. Physically, $\xi = (\operatorname{Im}\kappa)^{-1}$ gives the penetration depth of the edge modes. We may think of the continuum as a limiting case of the lattice as the lattice spacing a goes to zero. The ellipse $\mathbf{h}_\parallel$ becomes a parabola for vanishing a as the quantities $\mathbf{c}^0 = \mathbf{b}^0 + 2\mathbf{b}^r$, $\mathbf{c}^1 = 2\mathbf{b}^i a$, $\mathbf{c}^2 = -\mathbf{b}^r a^2$ are held constant. Theorem 2 also extends to the continuum case as the paraboloid $\mathbf{h}(k_x, k_y)$ determines the number of chiral edge states.

In addition to Dirichlet and Neumann boundary conditions, there is also a mixed type with $\psi'(0) = \eta\psi(0)$ for a positive number η. The origin of this boundary condition comes from requiring the wavefunction outside ($x < 0$) to satisfy $H_{\text{vac}} = W + \frac{p^2}{2m}$, where $W > E_s$ is the work function. Our analysis and result holds even for this boundary condition.

Notice that the quadratic term C^2p^2 is crucial for the existence of edge states. Without it, the polynomial (6.73) will be quadratic and there can only be one solution for κ in the upper half plane. The form of the solution $\psi = ue^{i\kappa x}$ makes it impossible to satisfy either type of boundary condition.

In the lattice model, we can compute the edge spectrum only for certain surfaces because of the nearest-layer requirement. For example, we can only compute the $\{100\}$, $\{110\}$ and $\{111\}$ surface dispersion of the TI model on a cubic lattice. In the continuum case with the Hamiltonian bilinear in momentum, any surface cut will still yield a Hamiltonian quadratic in $p_\perp$. Consequently, we can compute the surface excitation spectrum and wavefunctions of the system for all linear surfaces.

6.7.2 Example: $p + ip$ superconductor (continuum model)

We use the simplest model of a $p + ip$ superconductor [79]:

$$H(p_x, p_y) = \begin{bmatrix} \frac{p^2}{2m^*} - \mu & \Delta_0(p_x - ip_y) \\ \Delta_0(p_x + ip_y) & \mu - \frac{p^2}{2m^*} \end{bmatrix}. \tag{6.70}$$

Equivalently, with $H(\mathbf{p}) = \mathbf{h}(\mathbf{p}) \cdot \boldsymbol{\tau}$,

$$\mathbf{h}(\mathbf{p}) = \left(\Delta_0 p_x, \Delta_0 p_y, \frac{p^2}{2m^*} - \mu\right). \tag{6.71}$$

This model is isotropic, and without loss of generality, we take a semi-infinite plane $x \geq 0$ with $\hat{\mathbf{y}}$ parallel to the edge. At a fixed p_y, the $\mathbf{h}$ vector becomes:

$$\begin{aligned} \mathbf{h}(p_x) = &\left(0, \Delta_0 p_y, \tfrac{p_y^2}{2m^*} - \mu\right) \\ &+ (\Delta_0, 0, 0)p_x + \left(0, 0, \tfrac{1}{2m^*}\right) p_x^2 \end{aligned}$$

which lies in the xz-plane with $y = \Delta_0 p_y$. The parabola is concave towards the $+\hat{\mathbf{z}}$ direction, and hence an edge state exists if and only if $p_y^2/2m^* - \mu < 0$. Edge states can only exist when μ is positive, or in other words in the 'weak pairing phase' of $p + ip$ superconductors.

The edge state energy dispersion is given by Thm. 3b.

$$\begin{aligned} E_s &= \mathbf{c}^0 \cdot \frac{\mathbf{c}^1 \times \mathbf{c}^2}{|\mathbf{c}^1 \times \mathbf{c}^2|} = \Delta_0 p_y \hat{\mathbf{y}} \cdot (\hat{\mathbf{x}} \times \hat{\mathbf{z}}) \\ &= -\Delta_0 p_y \,. \end{aligned}$$

Referring to Eq. (6.53), the edge state wavefunction is given by the projector $P_s = \frac{1}{2}(1 - i\tau^x\tau^z) = \frac{1}{2}(1-\tau^y)$. Hence the edge states parallel to the y-axis are eigenstates of τ^y.

6.7.3 Proof for continuum Hamiltonians

The proof of Theorem 3 is very similar to the proof of Thm. 1 using transfer matrices, and so we present here a condensed version of the proof.

Consider a semi-infinite system with $x \geq 0$, and either $\psi(0) = 0$ (Dirichlet) or $\psi'(0) = 0$ (Neumann) boundary condition. The momentum parallel to the surface is a good quantum number, and so we fix $\mathbf{p}_\parallel$ to get an effective 1D problem. We seek a solution of the form[7] $\psi(x) = \sum_\mu e^{i\kappa_\mu x} u_\mu$, with $\operatorname{Im}\kappa_\mu > 0$. Each pair (κ, u) satisfies:

$$(C^0 + C^1\kappa + C^2\kappa^2 - E)u = (\mathbf{h}(\kappa)\cdot\mathbf{\Gamma} - E)u = 0\,. \tag{6.72}$$

Squaring $\mathbf{h}\cdot\mathbf{\Gamma}$ gives us the quartic equation

$$\mathbf{h}(\kappa)\cdot\mathbf{h}(\kappa) - E^2 = 0 \tag{6.73}$$

with real coefficients. Hence if κ is a root, then κ^* is also a root. Once again, we have at most two solutions for κ in the upper half of the complex plane, and so the wavefunction must take the form $\psi(x) = u_a e^{i\kappa_a x} + u_b e^{i\kappa_b x}$. With either Dirichlet ($u_a = -u_b$) or Neumann ($\kappa_a u_a = -\kappa_b u_b$) boundary condition, we have $u_a \propto u_b$ and so $\mathbf{h}(\kappa_a)\cdot\mathbf{\Gamma} - E$ and $\mathbf{h}(\kappa_b)\cdot\mathbf{\Gamma} - E$ share a null vector. By a similar argument to that in Sec. 6.4.2, the existence of an edge state is equivalent to

$$\operatorname{Det} c_a(\mathbf{h}(\kappa_a)\cdot\mathbf{\Gamma} - E) + c_b(\mathbf{h}(\kappa_b)\cdot\mathbf{\Gamma} - E) = 0\,, \tag{6.74}$$

for all c_a, c_b and $\operatorname{Im}\kappa_a, \operatorname{Im}\kappa_b > 0$. Equivalently, we have

$$E^2 = \mathbf{h}(\kappa_a)\cdot\mathbf{h}(\kappa_a) = \mathbf{h}(\kappa_b)\cdot\mathbf{h}(\kappa_b) = \mathbf{h}(\kappa_a)\cdot\mathbf{h}(\kappa_b)\,. \tag{6.75}$$

We introduce the functions $L(\kappa), \bar{L}(\kappa)$:

$$\begin{aligned} L(\kappa) &= \mathbf{h}_\parallel(\kappa)\cdot\hat{\mathbf{v}}_1 + i\mathbf{h}_\parallel(\kappa)\cdot\hat{\mathbf{v}}_2\,, \\ \bar{L}(\kappa) &= \mathbf{h}_\parallel(\kappa)\cdot\hat{\mathbf{v}}_1 - i\mathbf{h}_\parallel(\kappa)\cdot\hat{\mathbf{v}}_2\,, \end{aligned} \tag{6.76}$$

---

[7] A summand of the form $\kappa e^{i\kappa}$ is also permissible, provided κ is a double root of the polynomial (6.73).

where $\hat{\mathbf{v}}_1, \hat{\mathbf{v}}_2$ form an orthonormal coordinate basis in the plane spanned by $\mathbf{c}^1$ and $\mathbf{c}^2$. $L(\kappa), \bar{L}(\kappa)$ are quadratic polynomials in κ:

$$\begin{aligned} L(\kappa) &= (c_x^0 + ic_y^0) + (c_x^1 + ic_y^1)\kappa + (c_x^2 + ic_y^2)\kappa^2 \,, \\ \bar{L}(\kappa) &= (c_x^0 - ic_y^0) + (c_x^1 - ic_y^1)\kappa + (c_x^2 - ic_y^2)\kappa^2 \,. \end{aligned} \tag{6.77}$$

When $\kappa = p$ is real, $L(p)$ and $\bar{L}(p)$ trace out the parabola $\mathbf{h}_{\|}(p)$ in the complex plane with opposite orientations. Using the relation $\mathbf{h}_{\|}(\kappa_a) \cdot \mathbf{h}_{\|}(\kappa_b) = \frac{1}{2}(L_a\bar{L}_b + \bar{L}_a L_b)$, where $\bar{L}(\kappa_a)$ is abbreviated as $\bar{L}_a$, *etc.*, Eq. (6.75) become

$$E^2 - \Delta^2 = L_a\bar{L}_a \,, \tag{6.78a}$$

$$E^2 - \Delta^2 = L_b\bar{L}_b \,, \tag{6.78b}$$

$$E^2 - \Delta^2 = \tfrac{1}{2}(L_a\bar{L}_b + L_b\bar{L}_a) \,, \tag{6.78c}$$

where $\Delta \equiv |\mathbf{c}_\perp^0|$. The equations combine to get

$$(L_a - L_b)(\bar{L}_a - \bar{L}_b) = 0 \,, \tag{6.79}$$

Equations (6.78a), (6.78b) and (6.79) together with $\operatorname{Im}\kappa_{a,b} > 0$ are true if and only if an edge state exists at energy $\pm E$.

We construct a proof by contradiction showing that $E = \pm\Delta^2$. Suppose $E^2 \neq \Delta^2$, then all of $L_a, L_b, \bar{L}_a, \bar{L}_b$ are nonzero. Equating (6.78a) and (6.78b) gives $L_a/L_b = \bar{L}_a/\bar{L}_b$, and combining with (6.79) implies $L_a = L_b$ and $\bar{L}_a = \bar{L}_b$. Hence the polynomials $L(\kappa) - L_a$ and $\bar{L}(\kappa) - \bar{L}_a$ have identical roots (κ_a and κ_b). The sum of the roots $\kappa_a + \kappa_b$ must lie in the upper half plane, and it is equal to $(c_x^1 + ic_y^1)/(c_x^2 + ic_y^2)$ and $(c_x^1 - ic_y^1)/(c_x^2 - ic_y^2)$ from (6.77). This leads to a contradiction as the expressions are complex conjugate pairs. Therefore, an edge state requires $E = \pm\Delta$ and either $L_a = L_b = 0$ or $\bar{L}_a = \bar{L}_b = 0$.

Finally we impose the condition that $\operatorname{Im}\kappa_a, \operatorname{Im}\kappa_b > 0$. There are no poles in the function $L(\kappa)$, and so the number of zeros in the upper half plane is given by $\frac{1}{2\pi i}\oint \frac{L'(z)}{L(z)}dz$, integrated along the real line from $-R$ to R and closed on the upper half plane $Re^{i\theta}$ for $0 \leq \theta \leq \pi$, where R is taken to infinity. Assuming that $\mathbf{c}^2$ is nonzero and so L is a quadratic function of z, the contour of $L(z)$ for $z = Re^{i\theta}$ always wraps the origin by 2π radians counterclockwise.

Hence $L(\kappa)$ has two roots in the upper half plane if and only if the parabola $L(p)$ wounds around the origin counterclockwise. Similarly, $L(\kappa)$ has zero roots (so $\bar{L}(\kappa)$ has two roots) in the upper half plane if the parabola wounds around the origin clockwise. An edge state exists in both these cases, which occur when the origin lies in the concave side of $\mathbf{h}_{\|}(p)$. If the origin is not in the concave side of the parabola $\mathbf{h}_{\|}(p)$, then $L(\kappa)$ and $\bar{L}(\kappa)$ only have one root in the upper half plane and the system has no edge states. This completes the proof for Theorem 3a.

To determine the sign of the edge states, we construct the projectors for $E = \pm\Delta$. The projectors in the continuum case is identical to that of the lattice case (6.51), hence by the same argument used for Thm. 1b, we can prove Theorem 3b.

$$E = \mathbf{c}^0 \cdot \frac{\mathbf{c}^1 \times \mathbf{c}^2}{|\mathbf{c}^1 \times \mathbf{c}^2|} \,. \tag{6.80}$$

In addition, one may also derive the effective surface Hamiltonian:

$$\begin{aligned} H_s &= EP_+ - EP_- + E_\infty(1 - P_s) \\ &= P_s(\mathbf{c}_\perp^0 \cdot \mathbf{\Gamma}) + E_\infty(1 - P_s)\,. \end{aligned} \tag{6.81}$$

6.8 Outlook

In this chapter, we provided two main results. Theorem 1 gives a general prescription for finding edge states of Dirac Hamiltonians (with nearest-layer coupling) on a lattice (and the corresponding Theorem 3 in the continuum). Its range of applicability includes 'accidental edge states' which may not be topologically protected, such as in boron nitride. Theorem 2 relates the bulk Chern number of a 2D insulator to the number of chiral edge modes. This establishes the bulk-boundary correspondence for a class of quantum Hall insulators.

For 3D time-reversal invariant insulators, we demonstrated in Sec. 6.6.3 how the $\mathbb{Z}_2$ strong topological invariant determines whether there is an odd or even number of Dirac cones in the surface spectrum. Although we have used a specific TI model in the example, the argument is easily generalizable for all TRS Dirac Hamiltonians.

This work can be extended beyond quantum Hall insulators (class A) and TRS topological insulators (class AII) to other insulators within the Altland and Zirnbauer classification [76, 209]. The periodic table of topological insulators and superconductors provide an exhaustive topological classification of non-interacting electronic systems [77, 78, 194]. As there are model Dirac Hamiltonians [4, 42, 181, 187] in each class, our work provides the machinery to relate the bulk topological invariants [78] to the surface properties [77, 194] of these systems.

Acknowledgments

The authors thank Dung-Hai Lee for suggesting the approach using Green's functions. We gratefully acknowledge discussions with Andrew M. Essin and Pouyan Ghaemi, and useful comments and feedback on the manuscript from Jens H. Bárðarson, Jérôme Cayssol, Joel E. Moore, and Michael Zaletel.

This work is supported by NSF DMR-0804413 (VS) and the Center for Functional Engineered Nanoarchitectures (RM).

Chapter 7

Majorana fermions at the ends of superconductor vortices in doped topological insulators

Majorana fermions have been pursued by neutrino physicists for several decades, but have remained elusive so far. They are intriguing because they are, by definition, their own antiparticles, in contrast to conventional Dirac fermions such as electrons. Of late, the search for Majorana fermions has shifted towards condensed matter systems [79, 89, 210]. Naively, the energy scales involved here are usually too small to talk about true antiparticles and hence, Majorana fermions. The situation, however, is rescued by superconductors (SCs), which have an inherent charge-conjugation or 'particle-hole' symmetry which ensures all states appear in pairs with equal and opposite energies. Then, a single state at zero energy is its own particle-hole conjugate and hence, a Majorana state or a *Majorana zero mode* (MZM). As the particle-hole symmetry in a SC cannot be broken by a local disturbance, these states are immune to local noise and hence, considered strong candidates for storing quantum information and performing fault tolerant quantum computation [86]. Moreover, they are expected to show non-abelian rather than Bose or Fermi statistics due to them being effectively fractionalized electrons, which is a truly extraordinary phenomenon [82].

In this section, we describe a simple way of obtaining a MZM, namely, by creating a vortex in an appropriate conventional SC. Here, a MZM is trapped at each end of the vortex line. We assume inversion and time-reversal symmetry in the absence of the vortex, since it leads to technical simplifications and captures many real materials. For weak pairing, what the appropriate SC is is found to depend on properties of the bands of the normal phase metal. For instance, if the metal is obtained by doping a strong topological insulator (TI), then the corresponding SC vortex will carry MZMs if the Fermi level is below a critical value μ_c. As the Fermi level is tuned past μ_c, the vortex, undergoes a phase transition in which its topological state changes from one that has end MZMs to one that does not. If verified, this vortex phase transition (VPT) may be the first instance of a phase transition inside a topological defect. For more general band structures, we find that the occurrence of the VPT is related to the Berry phase around a loop on the Fermi surface (FS), normal to the vortex. Clearly, μ_c will depend on the vortex orientation. Note that systems with time-reversal and inversion symmetry have doubly degenerate bands, so the Berry phase will be an $SU(2)$ matrix and thus non-abelian in general [211]. Using this criterion and available band structures we find that c-axis vortices in Cu doped Bi_2Se_3 [125] are near the VPT, but those in p-doped Bi_2Te_3 which become superconducting under pressure [212], have vortex end MZMs.

A recent proposal for obtaining MZMs involved proximity inducing conventional s-wave superconductivity on the surface of a strong TI, which has gapless surface states. The vortex core of this surface SC was shown to trap a MZM [144]. Later, several TIs were found to exhibit bulk superconductivity on doping, which raised the natural question: will a vortex in this bulk SC host surface MZMs? A heuristic rule often applied to answer this question is to examine whether the normal state bulk FS is well separated from surface states in the Brillouin zone. If it is, MZMs are assumed to persist in the bulk SC. While this may indicate the presence of low energy states, it is not a topological criterion since it depends on non-universal details of surface band structure, and cannot signal the presence of true MZMs. For MZMs to disappear, a gapless channel must open that allows pairs to approach each other and annihilate. Perturbations that only modify surface state properties should not affect MZMs as long as the gap remains open. We therefore search for and offer a bulk rather than surface criterion.

7.1 A vortex in superconducting topological insulators

Consider a 3D insulating band structure H, which we dope by changing the chemical potential μ away from the middle of the band gap. In addition, consider adding conventional 's-wave' even parity pairing Δ_0 (in contrast to the odd parity topological SCs of Ref. [93]).

Introduce a single vortex line into the pairing function $\Delta_{\mathbf{r}}$, stretching between the top and bottom surfaces. We neglect the effect of the magnetic field used to generate the vortices, assuming extreme type II limit. When H is a strong TI, and μ is in the band gap, the pair potential primarily induces superconductivity on the surface states. In this limit it is known [144] that MZMs appear on the surface, inside the vortex core.[1] Now consider tuning the chemical potential deep into the bulk bands. By modifying states well below the Fermi level, one could tune the band structure to one with uninverted bands. One now expects 'normal' behavior, and the absence of Majorana zero modes. Therefore, a quantum phase transition must occur between these limits.

The vortex phase transition (VPT) may be viewed as a change in the topology of the electronic structure of the vortex line. The relevant energy scale is of the order of the minigap $\delta \ll \Delta_0$, with excitations localized within the 1D vortex core. The vortex admits particle-hole symmetry $\mathcal{C}$ but breaks time-reversal Θ and hence, belongs to class D of the

---

[1] It is convenient to discuss pairing over the entire range of μ, using the mean field Hamiltonian (7.1), although in reality superconductivity only appears once bulk carriers are induced.

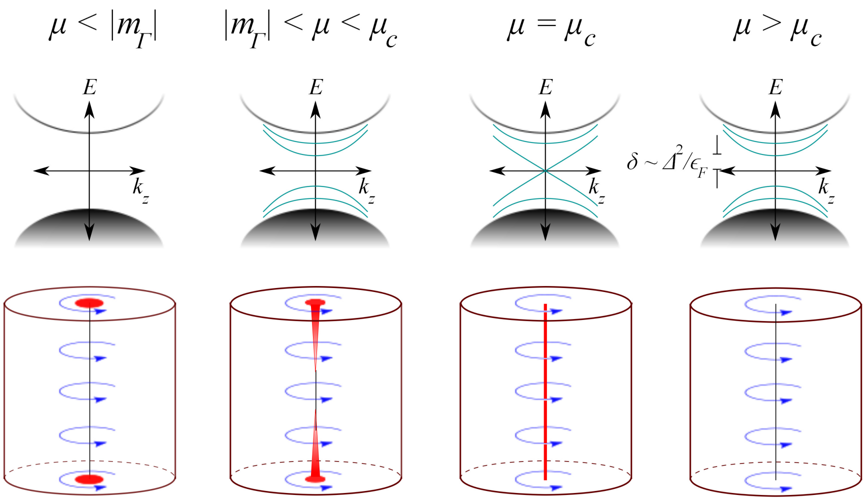

Figure 7.1: The vortex phase transition.

Evolution of the dispersion within the vortex (top row) and of the surface MZMs (middle row) as the chemical potential μ is varied. At $\mu = 0$, the normal phase is a strong TI and a superconducting vortex traps a MZM at its ends. As μ is increased, it first touches the bottom of the conduction band and midgap states appear inside the vortex. For $\mu < \mu_c$, the vortex stays gapped, but with a minigap δ smaller than the bulk gap, meanwhile the MZMs remain trapped near the surface. At μ_c, the gap vanishes signaling a phase transition. Beyond μ_c, the vortex is gapped again, but there are no surface MZMs.

Altland-Zirnbauer classification [76]. Thus, the problem reduces to classifying gapped phases in 1D within the symmetry class D, which are known to be distinguished by a $\mathbb{Z}_2$ topological invariant [89]. The two kinds of phases differ in whether they support MZMs at their ends; the topologically nontrivial phase has such zero modes. We identify the surface MZMs with these edge modes and hence the $\mu < \mu_c$ phase of the vortex line with the topologically nontrivial phase. On raising the chemical potential, the vortex line transitions into the trivial phase, via a quantum critical point at which it is gapless along its length. This is reminiscent of recent proposals to generate Majorana fermions at the ends of superconducting quantum wires [91, 92, 213, 214]. Note, since there is no 'local' gap in the vortex core, the powerful defect topology classification of [196] cannot be applied.

The mean field Hamiltonian is $\mathcal{H} = \frac{1}{2}\sum_{\mathbf{k}} \Psi^\dagger_{\mathbf{k}} H^{\mathrm{BdG}}_{\mathbf{k}} \Psi_{\mathbf{k}}$ where $\Psi^\dagger_{\mathbf{k}} = (\mathbf{c}^\dagger_{\mathbf{k}\uparrow}, \mathbf{c}^\dagger_{\mathbf{k}\downarrow}, \mathbf{c}_{-\mathbf{k}\downarrow}, -\mathbf{c}_{-\mathbf{k}\uparrow})$

and $\mathbf{c}^\dagger_{\mathbf{k}\sigma}$ is assumed to have $a = 1 \dots N$ orbital components $c^\dagger_{\mathbf{k}\sigma a}$ and

$$H^{\mathrm{BdG}}_{\mathbf{k}} = \begin{bmatrix} H_{\mathbf{k}} - \mu & \Delta \\ \Delta^* & \mu - H_{\mathbf{k}} \end{bmatrix}. \tag{7.1}$$

where scalars like the chemical potential μ and singlet pairing Δ multiply the identity matrix $\mathbb{1}_{2N}$. The band Hamiltonian, $H_{\mathbf{k}}$, is a $2N \times 2N$ matrix with Θ symmetry: $\sigma^y H^*_{-\mathbf{k}} \sigma^y = H_{\mathbf{k}}$, where σ^y acts on the spin, which yields the Hamiltonian structure above. When inversion symmetry (Π) is also present, the normal state band Hamiltonian $H_{\mathbf{k}}$ will be doubly degenerate, since the combined operation leads to a Kramers pair at every momentum. The Bogoliubov-de Gennes (BdG) Hamiltonian has particle-hole symmetry implemented by the transformation $\mathcal{C} = \upsilon^y \sigma^y \mathcal{K}$, where υ matrices act on Nambu particle-hole indices, and $\mathcal{K}$ is complex conjugation. A vortex breaks Θ but preserves $\mathcal{C}$ via complex phases in the pairing term $\Delta(\mathbf{r})$. (For example, along the z direction, $\Delta(\mathbf{r}) = |\Delta(r)| e^{-i\theta}$, where $re^{i\theta} = x + iy$.)

Consider a straight vortex along the z direction. Labeling states by k_z, the momentum along the vortex line, leads to a gapped dispersion as in Fig. 7.2 with minigap δ. A topological phase transition requires closing of the minigap which then reopens with inverted sign. However, the $\mathbb{Z}_2$ topological index is only changed by an odd number of such band crossings. The only relevant momenta to investigate such gap closing is $k_z = 0, \pi$. Band touchings at other k_z points occur in pairs at $\pm k_z$ which do not alter the $\mathbb{Z}_2$ index [89]. In the weak pairing limit, one expects the critical point μ_c to be determined by a FS property, which will be outlined in detail below. Here we simply observe that the relevant FSs to consider lie in the $k_z = 0, \pi$ planes, the planes determined by the vortex orientation. This implies that the topological phase of the vortex, and hence μ_c depend in general on its orientation.

7.2 Vortex phase transition in models and numerical results

Before discussing the general criterion for a VPT, we present numerical and analytical evidence in a specific lattice model from Ref. [187]. While the numerics explicitly demonstrate the phase transition, the analytical treatment of the continuum limit allows us to conjecture a Berry phase condition for the transition, which is later proved.

7.2.1 Lattice model

The model is on a simple cubic lattice with two orbitals per site: The Hamiltonian is

$$H_{\mathbf{k}} = \tau^x \mathbf{d}_{\mathbf{k}} \cdot \boldsymbol{\sigma} + m_{\mathbf{k}} \tau^z - \mu, \tag{7.2}$$

where τ^i and σ^i are Pauli matrices in the orbital and spin basis respectively. The components of $\mathbf{d}_{\mathbf{k}}$ are $d^i_{\mathbf{k}} = 2t \sin k_i$, the 'mass' is given by $m_{\mathbf{k}} = (M + m_0 \sum_i \cos k_i)$, where $i = x, y, z$ labels the components of the vectors. t, m_0 and M are parameters of the model and μ is

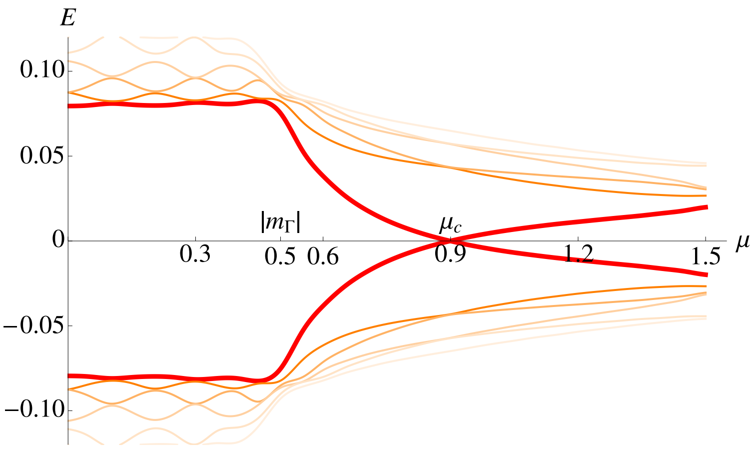

Figure 7.2: Band crossing in a vortex phase transition.

Evolution of the lowest bulk/vortex states at $k_z = 0$ of the dispersion within the vortex. as μ is varied when the normal phase has a band inversion at Γ. At $\mu = 0$, the normal phase is a strong TI and a superconducting vortex traps a MZM at its ends. As μ is increased, it first enters the conduction band at $\mu = |m_\Gamma| = 0.5$ and midgap states appear inside the vortex. For $|m_\Gamma| < \mu < \mu_c$, the vortex stays gapped, but with a minigap δ smaller than the bulk gap. In this region a bulk Fermi surface exists but the MZMs remain trapped near the surface. At $\mu_c = 0.9$, the gap vanishes at the vortex phase transition. Above μ_c, the vortex becomes gapped again, but there are no surface MZMs. We used the lattice Hamiltonian with the parameters $t = 0.5$, $M = 2.5$ and $m_0 = -1.0$. The pairing strength is $\Delta_0 = 0.1$ far away from the vortex and drops sharply to zero at the core. Other gap profiles give similar results.

the chemical potential. The model is in the strong TI phase if $-3 < M/m_0 < -1$. We add a mean field s-wave pairing to this Hamiltonian, insert a unit winding into the pairing function and diagonalize the Hamiltonian numerically. We focus on $k_z = 0$.

Figure 7.2 illustrates the evolution of the bulk vortex bound states, the dispersion within the vortex and the surface MZMs as a function of μ, when the normal state has a band inversion only at the $\Gamma = (0, 0, 0)$-point, *i.e.*, $m_\Gamma < 0$. In its normal phase, the system's gap is simply $|m_\Gamma|$. At $\mu = 0$, the bulk is gapped and must have a pair of MZMs on opposite surfaces in a slab geometry. As μ is raised, these MZMs leak deeper into the bulk, but survive even after μ crosses $|m_\Gamma|$ despite the bulk now having a FS in the normal phase, gapped by superconductivity. A VPT eventually occurs at $\mu_c = 0.9$, at which the vortex is gapless and the surface MZMs merge into vortex line. Beyond μ_c, there are no longer any protected MZMs on the surface.

7.2.2 Continuum model

In the continuum limit of the lattice model with cubic symmetry, we can analytically calculate μ_c. For $k_z = 0$ and small $k_{x,y}$ around Γ, the lattice model reduces to the isotropic form

$$H_{\mathbf{k}} = \tau^x \boldsymbol{\sigma} \cdot \mathbf{k} + (m - \epsilon k^2)\tau^z - \mu\,. \tag{7.3}$$

In this form, a band inversion exists if $m\epsilon > 0$. Thus, $m\epsilon > 0$ (< 0) characterizes an STI (trivial insulator). At $k = \sqrt{m/\epsilon}$, $m_{\mathbf{k}} = m - \epsilon k^2$ vanishes and $H_{\mathbf{k}}$ resembles two copies of a pure Dirac Hamiltonian. In particular, the Berry phase around each $\tau^x = \pm 1$ FS is π. We will show later that this leads to a pair of vortex zero modes, signaling the VPT at $\mu_c = \sqrt{m/\epsilon}$.

We solve analytically for the two bulk zero modes at μ to first order in Δ_0 by assuming a superconducting gap profile $|\Delta(\mathbf{r})| = \Delta_0 \Theta_H(r - R)$, where Θ_H is the step function and R is a large radius such that $R(\Delta_0/\hbar) \gg 1$. In this approximation, the zero energy solutions can be calculated separately for $r \leq R$ and $r \geq R$. Matching these solutions at the boundary $r = R$ gives a pair of zero modes, only when $\mu = \sqrt{m/\epsilon}$, for all vortex orientations, precisely where the momentum dependent 'mass' term changes sign. Using the model parameters and the linearized approximation gives an estimate of $\mu_c \approx 1$, in agreement with the lattice model numerics.

In the basis $\big(\psi(\mathbf{r}), i\sigma^y\psi^\dagger(\mathbf{r})\big)$ where $\psi(\mathbf{r})$ is a four-component spinor of electron annihilation operators indexed by spin and orbital indices, the Bogoliubov-de Gennes Hamiltonian in real space for a unit vortex is

$$H^{\mathrm{BdG}} = \begin{bmatrix} H_{\mathbf{r}} & \Delta_0\Theta_H(r-R)e^{i\theta} \\ \Delta_0\Theta_H(r-R)e^{-i\theta} & -H_{\mathbf{r}} \end{bmatrix}, \tag{7.4}$$

where $H_{\mathbf{r}} = -i\tau^x\boldsymbol{\sigma}\cdot\nabla + \tau^z(m + \epsilon\nabla^2) - \mu$. The θ-dependence of H^{BdG} can be removed by observing that it commutes with the generalized angular momentum operator

$$L_z = -i\partial_\theta + \frac{\sigma^z + \upsilon^z}{2}\,. \tag{7.5}$$

Since $\{L_z, \mathcal{C}\} = 0$, a single MZM, such as the one on the surface, must have an eigenvalue of L_z, equal to zero. Now, the bulk zero modes can be thought of as the avenues through which the surface MZMs penetrate the bulk. Thus, they must have $n = 0$ as well. The vortex preserves a mirror symmetry about the xy-plane described by $\mathcal{M} = \tau^z\sigma^z$. Thus, H^{BdG} can be block-diagonalized into sectors with opposite $\mathcal{M}$ eigenvalues. The two blocks are particle-hole conjugates since $\{\mathcal{M}, \mathcal{C}\} = 0$ and each must contribute a single bulk MZM at μ_c. The radial Hamiltonian for the $\mathcal{M} = +1$ sector is

$$\begin{aligned} H_{\mathrm{rad}} = {} & -i\upsilon^z\nu^y\left(\partial_r + \frac{1}{2r}\right) + \frac{\nu^x}{2r} + \upsilon^z\nu^z\left[m + \epsilon\left(\partial_r^2 + \frac{1}{r}\partial_r - \frac{1}{2r^2}\right)\right] - \frac{\epsilon}{2r^2} \\ & - \upsilon^z\mu + \upsilon^x\Delta_0\Theta_H(r-R)\,, \end{aligned} \tag{7.6}$$

where ν^i are Pauli matrices in a combined orbital (τ^i) and spin (σ^i) space. For $r < R$, H_{rad} has four zero energy solutions

$$\begin{pmatrix} -k_\pm J_1(k_\pm r) \\ (\mu - m_{\boldsymbol{k}_\pm}) J_0(k_\pm r) \\ 0 \\ 0 \end{pmatrix}, \begin{pmatrix} 0 \\ 0 \\ -k_\pm J_0(k_\pm r) \\ (\mu - m_{\boldsymbol{k}_\pm}) J_1(k_\pm r) \end{pmatrix}, \tag{7.7}$$

where $k_\pm$ are roots of $g(k) = \epsilon^2 k^4 + (1 - 2m\epsilon)k^2 + (m^2 - \mu^2)$ and $J_\nu(x)$ are Bessel functions of the first kind of order ν. For $r > R$, we drop all terms that contain r in the denominator. The zero modes of the remaining Hamiltonian are of the form $e^{i\lambda_\pm r}\chi_\pm$, where $\lambda_\pm$ is a root of $\epsilon^2\lambda^4 + (1 - 2m\epsilon)\lambda^2 + (m^2 - (\mu \pm i\Delta_0)^2) = 0$ with positive imaginary part and

$$\chi_\pm = \begin{pmatrix} -i\lambda_\pm \\ \mu \mp i\Delta_0 - m + \epsilon\lambda_\pm^2 \\ \pm\lambda_\pm \\ \pm i(\mu \mp i\Delta_0 - m + \epsilon\lambda_\pm^2) \end{pmatrix}. \tag{7.8}$$

Matching the solutions and their derivatives at $r = R$ to first order in Δ_0, using the asymptotic forms of the Bessel functions, is only possible at $\mu_c = \sqrt{m/\epsilon}$. This gives an analytic solution to the critical chemical potential μ_c.

7.3 General Fermi surface Berry phase condition

For weak pairing, the VPT is expected to be governed by properties of the bulk FS. Specifically, we have argued that only $k_z = 0$ and $k_z = \pi$ planes will cause a VPT. In this section, we argue that the VPT occurs when an appropriately defined Berry phase for these FSs is π.

7.3.1 Summary of the argument and results

Here we give a short summary of the main ideas and results of this section. A convenient model for the vortex is $\Delta(\mathbf{r}) = \frac{\Delta_0}{\xi}(x - iy)$. The linear profile here simplifies calculations, but does not affect location of the zero mode. The choice of ξ as the length scale gives the right minigap scale for the low energy excitations. Working in momentum space we substitute $\mathbf{r}$ by $i\partial_{\mathbf{k}}$, which gives

$$H^{\text{BdG}}_{\mathbf{k}} = \begin{bmatrix} H_{\mathbf{k}} - \mu & i\frac{\Delta_0}{\xi}(\partial_{k_x} - i\partial_{k_y}) \\ i\frac{\Delta_0}{\xi}(\partial_{k_x} + i\partial_{k_y}) & \mu - H_{\mathbf{k}} \end{bmatrix}, \tag{7.9}$$

transforming now to the band basis $|\varphi^\nu_{\mathbf{k}}\rangle$, which are eigenstates of the band Hamiltonian $H_{\mathbf{k}}|\varphi_{\mathbf{k}}\rangle = E|\varphi_{\mathbf{k}}\rangle$. Since we are only interested in very low energy phenomena, we project onto the degenerate bands near the Fermi energy. We assume for the moment that there are two such bands at $k_z = 0$ plane (and none for $k_z = \pi$ plane). The projected Hamiltonian then is:

$$\tilde{H}^{\text{BdG}}_{\mathbf{k}} = \begin{bmatrix} E_{\mathbf{k}} - \mu & i\frac{\Delta_0}{\xi}(D_{k_x} - iD_{k_y}) \\ i\frac{\Delta_0}{\xi}(D_{k_x} + iD_{k_y}) & -E_{\mathbf{k}} + \mu \end{bmatrix}. \tag{7.10}$$

where $D_{k_\alpha} = \partial_{k_\alpha} - i\mathbf{A}_\alpha(\mathbf{k})$ and $\mathbf{A}_\alpha(\mathbf{k})$, the $SU(2)$ connections, are 2×2 matrices:

$$[\mathbf{A}]^{\mu\nu}_\alpha(\mathbf{k}) = i\langle\varphi^\mu_{\mathbf{k}}|\partial_{k_\alpha}|\varphi^\nu_{\mathbf{k}}\rangle. \tag{7.11}$$

Let us first consider the case when an additional quantum number (such as spin up and down) can be used to label the degenerate FSs. Then, $[\mathbf{A}]^{\mu\nu}_\alpha$ must be diagonal, and reduces to a pair of $U(1)$ connections for the two FSs. In this situation, Eq. (7.10) is identical to the effective Hamiltonian for a $p_x + ip_y$ superconductor, if we interpret momenta as position and ignore the gauge potential. The diagonal terms represent a transition from weak to strong pairing phase on crossing the FS when $E_{\mathbf{k}} = \mu$ [79]. Thus midgap are expected, composed of states near the Fermi energy. Due to the finite size of the FS, these states have an energy spacing of $\mathcal{O}\big(\frac{\Delta_0}{k_F\xi}\big)$, the minigap energy scale. However, a zero energy state appears if the FS encloses a π-flux [79]. This can be implemented via the gauge potential if $\oint_{\text{FS}} \mathbf{A}\cdot d\mathbf{l} = \pi$ leading to a pair of zero modes, since the other FS has the same Berry phase by time-reversal.

In the absence of any quantum number distinguishing the bands, one integrates the vector potential $\mathbf{A}(\mathbf{k})$ around the FS in the $k_z = 0$ plane, to give the non-abelian Berry phase [211]: $U_B = \mathcal{P}\exp\big[i\oint_{\text{FS}} \mathbf{A}\cdot d\mathbf{l}\big] \in SU(2)$, where $\mathcal{P}$ denotes path ordering. (There is no $U(1)$ phase by Θ symmetry.) Although U_B itself depends on the choice of basis, its eigenvalues $e^{\pm i\phi_B}$ are gauge invariant. A semiclassical analysis gives the Bohr-Sommerfield type quantization condition for the low energy levels:

$$E_n = \frac{\Delta_0}{l_F\xi}(2\pi n + \pi \pm \phi_B) \tag{7.12}$$

where n is an integer and l_F is the FS perimeter. A pair of zero modes appears when $\phi_B = \pi$, *i.e.*, when $U_B = -\mathbb{1}$.

We have considered a single closed FS in the $k_z = 0$ plane. Such a FS necessarily encloses a time-reversal invariant momentum (TRIM), (*e.g.* Γ), given the symmetries. When there are multiple FSs, the condition above is applied individually to each FS, since tunneling between them is neglected in the semiclassical approximation. Note that closed FSs that do not enclose a TRIM, or pairs of open FSs, cannot change the vortex topology.

7.3.2 Bogoliubov-de Gennes Hamiltonian

We consider a 3D system with s-wave pairing, where the bulk is pierced by a quantum flux $h/2e$. Assuming that the metallic Hamiltonian $H_{\mathbf{k}}$ (the system without superconductivity/quantum flux) has time-reversal symmetry, we will derive the condition which governs the existence of zero vortex modes to the properties of the FS, namely the Berry phase.

The mean field BdG Hamiltonian with s-wave pairing is of the form:

$$\mathcal{H} = \frac{1}{2}\sum_{\mathbf{k}\mathbf{k}'} \Psi^\dagger_{\mathbf{k}} H^{\mathrm{BdG}}(\mathbf{k},\mathbf{k}')\Psi_{\mathbf{k}'}\,, \tag{7.13}$$

where $\Psi^\dagger_{\mathbf{k}} = \left(\mathbf{c}^\dagger_{\mathbf{k}}, \mathbf{c}^T_{-\mathbf{k}}(i\sigma^y)\right)$ is written in the Nambu basis, capturing all orbital and spin degrees of freedom. The single-particle Hamiltonian is

$$H^{\mathrm{BdG}}(\mathbf{k},\mathbf{k}') = \begin{bmatrix} (H_{\mathbf{k}}-\mu)\delta_{\mathbf{k}\mathbf{k}'} & \Delta(\mathbf{r}) \\ \Delta^*(\mathbf{r}) & (\mu - \sigma^y H^*_{-\mathbf{k}}\sigma^y)\delta_{\mathbf{k}\mathbf{k}'} \end{bmatrix}, \tag{7.14}$$

where the pairing potential, given by $\Delta^*(\mathbf{r}) = \left\langle \Psi^\dagger_\uparrow(\mathbf{r})\Psi^\dagger_\downarrow(\mathbf{r})\right\rangle$, is position dependent due to the vortex.

The quasiparticle operators $\Psi^\dagger, \Psi$ are defined in such as a way that leads to spin singlet pairing. Since the metallic Hamiltonian $H_{\mathbf{k}}$ has time-reversal symmetry, $\sigma^y H^*_{-\mathbf{k}}\sigma^y = H_{\mathbf{k}}$ and the BdG Hamiltonian may be written as

$$H^{\mathrm{BdG}} = \begin{bmatrix} H_{\mathbf{k}}-\mu & \Delta(\mathbf{r}) \\ \Delta^*(\mathbf{r}) & \mu - H_{\mathbf{k}} \end{bmatrix}. \tag{7.15}$$

(We drop the $\mathbf{k},\mathbf{k}'$ dependence, treating H^{BdG} as an operator.)

We take the vortex to lie in the $\hat{\mathbf{z}}$ direction, hence the pairing term takes the form $\Delta^*(\mathbf{r}) = \Delta(r_\perp)e^{i\theta}$, independent of z, where $r_\perp e^{i\theta} = x + iy$. The pairing amplitude becomes constant for large $r_\perp$: $\Delta(r_\perp) \to \Delta_0$. Although the vortex breaks translational symmetry in the xy-plane, it is preserved in the z direction and hence, k_z remains a good quantum number. The 3D system thus decouples into many 2D Hamiltonians enumerated by k_z. Henceforth, we refer to $r_\perp$ as simply r, and $\mathbf{k}$ as the 2D momentum coordinate (k_x, k_y).

The time-reversal operator is $\Theta = -i\sigma^y\mathcal{K}$, taking $k_z \to -k_z$, $\mathbf{k} \to -\mathbf{k}$, which is broken by the imaginary part of Δ. In addition, the system must have particle-hole (charge conjugation) symmetry given by the operator $\mathcal{C} = \upsilon^y\sigma^y\mathcal{K}$, where υ^i are the Pauli matrices acting on particle-hole space. Note that $\mathcal{C}$ also takes $k_z \to -k_z$, $\mathbf{k} \to -\mathbf{k}$, hence particle-hole is a symmetry of the 2D system only when $k_z \sim -k_z$ (*i.e.*, at 0 or π).

In the remainder of this section, we do not assume anything about the value of k_z, nor the symmetries of the 2D Hamiltonian $H_{\mathbf{k}}|_{k_z}$ at a fixed k_z. Our results remain valid applied to any 2D slice (with a smooth FS) of the 3D Brillouin zone, as long as the 3D Hamiltonian has time-reversal symmetry.

7.3.3 Pairing potential

In this section, we compute the pairing potential of a vortex in k-space via a Fourier transform. We confine our system to be on a disk with radius ξ, the superconducting

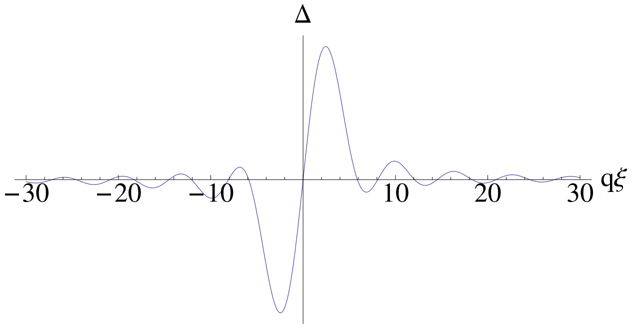

Figure 7.3: The pairing potential.

The pairing potential $\Delta_{\mathbf{k}'\mathbf{k}}$ as a function of $q\xi$ where $q = |\mathbf{k} - \mathbf{k}'|$ and ξ is the system radius. The wavefunction $\psi(\mathbf{k})$ is smooth on the scale of ξ^{-1}, and hence the pairing potential may be modeled as $-\delta'(q)$.

correlation length. The matrix element $\Delta_{\mathbf{k}'\mathbf{k}}$ is

$$\begin{aligned}\Delta_{\mathbf{k}'\mathbf{k}} &= \langle \mathbf{k}'|\Delta(\mathbf{r})|\mathbf{k}\rangle \\ &= \frac{1}{\pi\xi^2}\int d^2r\, e^{i(\mathbf{k}-\mathbf{k}')\cdot\mathbf{r}}\Delta(\mathbf{r}) \\ &= \frac{1}{\pi\xi^2}\int_0^{\xi} r\,dr\,\Delta(r)\int_0^{2\pi} d\theta\, e^{iqr\cos(\theta-\theta_q)}e^{-i\theta}\,, \end{aligned} \tag{7.16}$$

where $\mathbf{q} = \mathbf{k} - \mathbf{k}' = q(\cos\theta_q \hat{\mathbf{x}} + \sin\theta_q \hat{\mathbf{y}})$. The θ integral evaluates to a Bessel function (of the first kind): $2\pi i e^{-i\theta_q} J_1(qr)$. The matrix element becomes

$$\Delta_{\mathbf{k}'\mathbf{k}} = \frac{2\pi i e^{-i\theta_q}}{\pi\xi^2}\int_0^{\xi} r\,dr\,\Delta(r) J_1(qr)\,. \tag{7.17}$$

- At large q ($q\xi \gg 1$), $J_1(qr) \approx \sin qr/\sqrt{qr}$, and $\Delta(r) \to \Delta_0$ becomes constant. The integral scales as $\frac{\Delta_0}{q^2}(q\xi)^{1/2}\cos q\xi$ and the matrix element $\Delta_{\mathbf{k}'\mathbf{k}} \approx i\Delta_0 e^{-i\theta_q}(q\xi)^{-3/2}\cos q\xi \to 0$.
- At small q ($q\xi < 1$), $J_1(qr) \approx qr/2$ and the integral evaluates to $q\Delta_0\xi^3/6$. The matrix element scales as $\frac{i}{3}\Delta_0 e^{-i\theta_q} q\xi$ and is linear in q.

We can model the pairing matrix element as a derivative of the delta function: $\Delta_{\mathbf{k}'\mathbf{k}} \propto ie^{-i\theta_q}(-\delta'(q))$, this approximation is valid in the regime where the wavefunction $\psi(\mathbf{k})$ is smooth on the length scale of ξ^{-1}. In Cartesian coordinates, the pairing term becomes $i\Delta_e(\partial_{k_x} - i\partial_{k_y})$, where Δ_e is the effective $p + ip$ pairing strength, with units energy × length^{-1}. From a simple analysis, we expect that $\Delta_e \approx \Delta_0/\xi$.

The Hamiltonian in k-space is of the form:

$$H^{\mathrm{BdG}} = \begin{bmatrix} H_{\mathbf{k}} - \mu & i\Delta_e(\partial_{k_x} - i\partial_{k_y}) \\ i\Delta_e(\partial_{k_x} + i\partial_{k_y}) & \mu - H_{\mathbf{k}} \end{bmatrix}. \tag{7.18}$$

The eigenstates are of the form

$$|\psi\rangle = \sum_{\mathbf{k},\nu} \psi_\nu(\mathbf{k})|\varphi^\nu_{\mathbf{k}}\rangle\,, \tag{7.19}$$

where $|\varphi^\nu_{\mathbf{k}}\rangle$ is an eigenstate of $H_{\mathbf{k}}$ and ν labels the band index.

7.3.4 Projecting to the low energy states

Solutions to the Hamiltonian (7.18) will consists of mostly states near the FS, where $E_{\mathbf{k}} \sim \mu$. Hence we can simplify the system by projecting to the band eigenstates $|\varphi^\mu_{\mathbf{k}}\rangle$ with energy near the chemical potential, where μ, ν is the band index:

$$\tilde{H} = \langle\varphi^\mu_{\mathbf{k}}|H|\varphi^\nu_{\mathbf{k}}\rangle\,. \tag{7.20}$$

If inversion symmetry is present, each band will be doubly degenerate.

The projection of the metallic Hamiltonian $H_{\mathbf{k}}$ gives a diagonal matrix $E^{\mu\nu}_{\mathbf{k}} = \langle\varphi^\mu_{\mathbf{k}}|H_{\mathbf{k}}|\varphi^\nu_{\mathbf{k}}\rangle$ with its entries being the energies. The projection of the derivative operator gives the Berry connection: $\langle\varphi^\mu_{\mathbf{k}}|i\nabla_{\mathbf{k}}|\varphi^\nu_{\mathbf{k}}\rangle = i\nabla_{\mathbf{k}} + \mathbf{A}^{\mu\nu}$, where the non-abelian Berry connection is defined as:

$$\mathbf{A}^{\mu\nu} = i\langle\varphi^\mu_{\mathbf{k}}|\nabla_{\mathbf{k}}|\varphi^\nu_{\mathbf{k}}\rangle\,. \tag{7.21}$$

Explicitly:

$$\tilde{H} = \begin{bmatrix} E^{\mu\nu}_{\mathbf{k}} - \mu & \Delta_e \begin{pmatrix} i(\partial_{k_x} - i\partial_{k_y}) \\ +A^{\mu\nu}_x - iA^{\mu\nu}_y \end{pmatrix} \\ \Delta_e \begin{pmatrix} i(\partial_{k_x} + i\partial_{k_y}) \\ A^{\mu\nu}_x + iA^{\mu\nu}_y \end{pmatrix} & -E^{\mu\nu}_{\mathbf{k}} + \mu \end{bmatrix}. \tag{7.22}$$

The connections A_x, A_y are hermitian matrices which depends on the choice of Bloch states $|\varphi^\nu_{\mathbf{k}}\rangle$.

Dropping the band indices and writing $E_{\mathbf{k}}$ as $E(\mathbf{k})$, the Hamiltonian is:

$$\tilde{H} = \begin{bmatrix} E(\mathbf{k}) - \mu & \Delta_e \begin{pmatrix} i(\partial_{k_x} - i\partial_{k_y}) \\ +A_x - iA_y \end{pmatrix} \\ \Delta_e \begin{pmatrix} i(\partial_{k_x} + i\partial_{k_y}) \\ +A_x + iA_y \end{pmatrix} & -E(\mathbf{k}) + \mu \end{bmatrix}, \tag{7.23}$$

If we interpret momenta ($\mathbf{k}$) as position, then we can treat $A_{x,y}$ as a gauge potential and the Berry curvature $F = \partial_{k_x}A_y - \partial_{k_y}A_x - i[A_x, A_y]$ as an effective magnetic field in the model. This system was studied by Read, Green, Ludwig, Bocquet and Zirnbauer in context of a Dirac Hamiltonian with random mass as well as $p+ip$ superconducting systems [79, 215, 216].

While superficially similar to a $p + ip$ superconductor, there is an important distinction – our system may not have particle-hole symmetry (unless $k_z = 0$ or π), and hence does not belong to the D class (particle-hole symmetry). To illustrate how $\mathcal{C}$ is broken, suppose that there is only one FS and hence A_i are simply 1×1 (abelian) matrices. The system resembles a superconductor with $p + ip$ pairing, but with the Berry curvature $\nabla_{\mathbf{k}} \times \mathbf{A}(\mathbf{k})$ being the effective magnetic field. Unlike a superconductor, the effective field does not have to be localized nor quantized within the FS.

Consequently, the spectrum of vortex states in our 2D system does not have any symmetry, and the zero modes are not topologically protected. We can only show that these modes are stable within the weak pairing limit under perturbation theory. We can restore particle-hole symmetry by combining the 2D systems at k_z with that at $-k_z$, at the cost of doubling the number of zero energy states.

In the remainder of the section, we will explicitly show the following: when (an eigenvalue of) the Berry phase of the FS ϕ_F is π, there is an effective half quantum flux $\frac{h}{2e}$ in the system which supports a Majorana mode.

7.3.5 Explicit solution with rotational symmetry

This section is not necessary to the solution, but is instructive and aids in the understanding of what the terms in the more general solutions mean. For simplicity, we only consider a single FS at wavevector k_F. We also assume an abelian Berry connection, so A_x, A_y are simply real numbers.

With rotational symmetry, we can simplify the expressions in polar coordinates: $k_x + ik_y = ke^{i\theta}$: $E(\mathbf{k}) = E(k)$, $\partial_{k_x} - i\partial_{k_y} = e^{-i\theta}(\partial_k - \frac{i}{k}\partial_\theta)$, $A_x - iA_y = e^{-i\theta}(A_k - \frac{i}{k}A_\theta)$. In addition, it is possible to find a gauge for which $A_k = 0$, and A_θ is a function of k, but independent of θ. Explicitly, the Berry connection is

$$2\pi A_\theta(k) = 2\pi \int_0^k k' dk' \, F(k') \,, \tag{7.24}$$

where $F(\mathbf{k}) = \nabla_{\mathbf{k}} \times \mathbf{A}$ is the Berry curvature. The left side of (7.24) is the Berry phase along a circle of radius k, while the right side is the integrated Berry curvature.

Our Hamiltonian simplifies to

$$\tilde{H} = \begin{bmatrix} E(k) - \mu & i\Delta_e e^{-i\theta}\left(\partial_k - \frac{i\partial_\theta + A_\theta}{k}\right) \\ i\Delta_e e^{i\theta}\left(\partial_k + \frac{i\partial_\theta + A_\theta}{k}\right) & -E(k) + \mu \end{bmatrix}. \tag{7.25}$$

The Hamiltonian commutes with $J_z = -i\partial_\theta + \upsilon^z$, that is to say that the solutions are of the form

$$\psi(k, \theta) = \frac{1}{\sqrt{k}} \begin{pmatrix} u(k) e^{i(n-1)\theta} \\ -iv(k) e^{in\theta} \end{pmatrix} , \tag{7.26}$$

for integers n (required by the wavefunction being single-valued). Via the transformation

$$W_{\text{ph}} = k^{\frac{1}{2}} \begin{bmatrix} e^{-i(n-1)\theta} & \\ & i\, e^{-in\theta} \end{bmatrix}, \tag{7.27}$$

the effective Hamiltonian for (u, v) is

$$\begin{aligned}\tilde{H}_n &= W_{\text{ph}}\,\tilde{H}\,W_{\text{ph}}^{-1} \\ &= \begin{bmatrix} E(k)-\mu & \Delta_e\left(\partial_k + \frac{n-\frac{1}{2}-A_\theta}{k}\right) \\ \Delta_e\left(\frac{n-\frac{1}{2}-A_\theta}{k} - \partial_k\right) & -E(k)+\mu \end{bmatrix}.\end{aligned} \tag{7.28}$$

Notice that the Hamiltonian is symmetric except for the terms proportional to ∂_k, due to our choice of W_{ph}.

Our assumption is to replace k by the Fermi wavevector k_F, A_θ by $A_\theta^F = A_\theta(k_F)$ and $\frac{1}{k}$ by $\frac{1}{k_F}$. This is justified as the amplitude of the wavefunction $|u(k)|, |v(k)|$ is largest at the FS $k = k_F$ and exponentially decays away from the FS. The resulting Hamiltonian is equivalent to the Jackiw-Rebbi model [195]:

$$\tilde{H}_n = \frac{\Delta_e}{k_F}\left(n - A_\theta^F - \tfrac{1}{2}\right)v^x + i\Delta_e\partial_k v^y + \big(E(k)-\mu\big)v^z\,. \tag{7.29}$$

A midgap state exists whenever $E(k) - \mu$ changes sign, with energy

$$\mathcal{E}_n = \frac{\Delta_e}{k_F}\left(n - \frac{\phi_F}{2\pi} - \frac{1}{2}\right), \tag{7.30}$$

where $\phi_F = 2\pi A_\theta^F$ is the Berry phase of the FS. Hence, a zero energy solution exists when ϕ_F is an odd multiple of π.

Explicitly, the eigenstates are of the form [79, 195]

$$u(k) = \exp\int^k \beta(k')\,dk'\,, \tag{7.31}$$

where $\beta(k)$ must a be a decreasing function of k for $u(k)$ to be normalizable. Assuming that $E(k)$ is an increasing function of k, then

$$\beta(k) = \frac{\mu - E(k)}{\Delta_e}\,, \tag{7.32a}$$

$$v(k) = u(k)\,. \tag{7.32b}$$

By inspection, this satisfies Schrödinger's equation for the Hamiltonian (7.29):

$$\tilde{H}_n\begin{pmatrix}u\\v\end{pmatrix} = \begin{bmatrix}-\Delta_e\beta & \mathcal{E}_n + \Delta_e\beta \\ \mathcal{E}_n - \Delta_e\beta & \Delta_e\beta\end{bmatrix}\begin{pmatrix}1\\1\end{pmatrix} = \begin{pmatrix}\mathcal{E}_n\\ \mathcal{E}_n\end{pmatrix}. \tag{7.33}$$

For a Fermi velocity v_F, $E(k) - \mu \approx \hbar v_F(k - k_F)$. We can see that $u(k)$ is a Gaussian with width $\sqrt{\Delta_e/\hbar v_F} \approx \sqrt{\Delta_0/\hbar v_F \xi}$, which justifies the substitution $k \to k_F$ earlier.

We would like to point the reader to one last detail before moving on to the general solution. Putting our solution back in to the wavefunction (7.26) gives

$$\psi(k,\theta) = \frac{u(k)e^{in\theta}}{\sqrt{k}} \begin{pmatrix} e^{-i\theta} \\ -i \end{pmatrix}. \tag{7.34}$$

The pseudo-spinor (in the Nambu basis) is an eigenstate of $\mathbf{t}\cdot\boldsymbol{v}$, where $\mathbf{t}$ is a vector tangent to the FS at (k_F,θ). The pseudo-spin locking to the the momentum gives rise to the π phase around the FS in the Hamiltonian (7.28) and Eq. (7.30).

7.3.6 General solution without rotational symmetry

The solution is similar in spirit to the case with circular symmetry. Now, we label the momentum by energy contours (E,η) instead of (r,θ) and demand constant E contours to be orthogonal to constant η contours. Similar to θ, η is periodic with periodicity of 2π.

The idea of the derivation is as follows. We rewrite the Hamiltonian in a Jackiw-Rebbi form as a function E, perpendicular to the FS. Let Γ^1, Γ^2, Γ^3 be matrices which anticommute with each other, and square to the identity matrix. Then the differential equation

$$\Gamma^1(i\Delta_e\partial_E) + i\Gamma^2(E-\mu) + \Gamma^3 f(\eta) \tag{7.35}$$

has a bound state when $E-\mu$ changes sign, the bound state is an eigenvector of Γ^3 and has energy $f(\eta)$ [195]. The remaining η degree of freedom governs the existence of zero energy states, by requiring the wavefunction $\psi(E,\eta)$ to be single valued.

Define the vectors tangent and normal to the energy contours $\mathbf{t} = \frac{\partial\mathbf{k}}{\partial\eta}$, $\mathbf{n} = \frac{\partial\mathbf{k}}{\partial E}$. Clearly, $\mathbf{t}\perp\mathbf{n}$ (see Fig. 7.4). The derivatives and connections in (E,η) coordinates are related to those in the Cartesian coordinates:

$$\begin{pmatrix} \partial_E \\ \partial_\eta \end{pmatrix} = \begin{bmatrix} n^x & n^y \\ t^x & t^y \end{bmatrix} \begin{pmatrix} \partial_{k_x} \\ \partial_{k_y} \end{pmatrix}, \tag{7.36}$$

and we define the 2×2 matrix to be J^{-1}.

$$\begin{pmatrix} \partial_{k_x} \\ \partial_{k_y} \end{pmatrix} = J \begin{pmatrix} \partial_E \\ \partial_\eta \end{pmatrix}, \qquad \begin{pmatrix} A_x \\ A_y \end{pmatrix} = J \begin{pmatrix} A_E \\ A_\eta \end{pmatrix}, \tag{7.37}$$

where J is the Jacobian matrix:

$$J = \frac{\partial(E,\eta)}{\partial(k_x,k_y)} = \begin{bmatrix} J_x^E & J_x^\eta \\ J_y^E & J_y^\eta \end{bmatrix}. \tag{7.38}$$

From $J^{-1}J = \mathbb{1}$, we can see that $\mathbf{J}^E\cdot\mathbf{t} = 0$, $\mathbf{J}^\eta\cdot\mathbf{n} = 0$, hence $\mathbf{J}^E \parallel \mathbf{n}$ and $\mathbf{J}^\eta \parallel \mathbf{t}$.

First we rewrite the pairing term in terms of E and η. We have

$$i(\partial_{k_x} - i\partial_{k_y}) + A_x - iA_y = d_E + d_\eta\,, \tag{7.39}$$

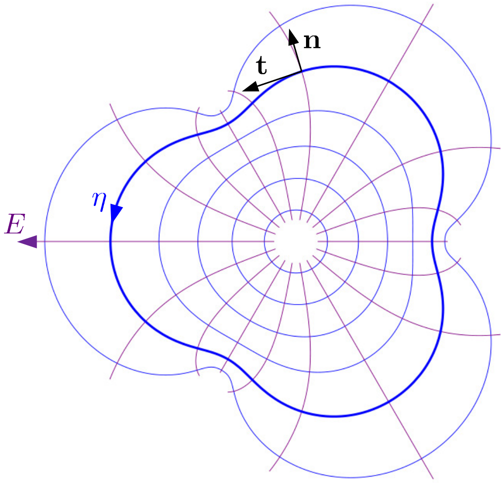

Figure 7.4: Parametrization of the reciprocal space with orthogonal coordinates (E, η). The (blue) closed contours are plotted for constant energies E, with the bold contour being the FS at the chemical potential μ. The (purple) open contours are at constant η, running from 0 to 2π. At each point, $\mathbf{t}(E,\eta) = \frac{\partial \mathbf{k}}{\partial \eta}$ and $\mathbf{n}(E,\eta) = \frac{\partial \mathbf{k}}{\partial E}$ are vectors tangent and normal, respectively, to the energy contours. Notice that, for a closed FS, the direction of the vectors $\mathbf{t}$ and $\mathbf{n}$ rotate once counterclockwise as η is varied around the surface.

where

$$d_E = i(J_x^E - iJ_y^E)(\partial_E - iA_E)\,, \tag{7.40a}$$

$$d_\eta = i(J_x^\eta - iJ_y^\eta)(\partial_\eta - iA_\eta)\,. \tag{7.40b}$$

It is always possible to find a gauge transformation which eliminates A_E near the FS. The transformation is of the form $U_A^\dagger = \mathcal{P}\exp\left[i\int_0^E A_E(E')dE'\right]$, where $\mathcal{P}$ is the path-ordering operator. Since $\partial_E U_A^\dagger = iA_E U_A^\dagger$,

$$U_A(\partial_E - iA_E)U_A^\dagger = \partial_E\,. \tag{7.41}$$

This transformation will alter A_η, since the derivative ∂_η acts on $U_A^\dagger$. In general, it impossible to make both A_E and A_η disappear.

We make the substitution $J_x^E - iJ_y^E = |\mathbf{J}^E|e^{-i\theta_\mathbf{n}}$, where $\theta_\mathbf{n}$ gives the direction of the normal vector $\mathbf{n}$. As $\mathbf{t}$ is perpendicular to $\mathbf{n}$, $J_x^\eta - iJ_y^\eta = -i|\mathbf{J}^\eta|e^{-i\theta_\mathbf{n}}$, Eq. (7.40) becomes

$$d_E = ie^{-i\theta_\mathbf{n}}|\mathbf{J}^E|\partial_E, \tag{7.42a}$$

$$d_\eta = e^{-i\theta_\mathbf{n}}|\mathbf{J}^\eta|(\partial_\eta - iA_\eta). \tag{7.42b}$$

At the moment, our Hamiltonian (7.23) is of the form:

$$\tilde{H} = \begin{bmatrix} E-\mu & \Delta_e e^{-i\theta_\mathbf{n}}\left(i|\mathbf{J}^E|\partial_E + |\mathbf{J}^\eta|(\partial_\eta - iA_\eta)\right) \\ \Delta_e e^{i\theta_\mathbf{n}}\left(i|\mathbf{J}^E|\partial_E - |\mathbf{J}^\eta|(\partial_\eta - iA_\eta)\right) & -E+\mu \end{bmatrix}. \tag{7.43}$$

The angle $\theta_{\mathbf{n}}$ rotates by $+2\pi$ around a closed FS as η varies from 0 to 2π. The $e^{i\theta_{\mathbf{n}}}$ phase in the off diagonal terms of the Hamiltonian give rise to a π phase in the eigenstates. We transform this phase away via the unitary transformation:

$$U_{\text{ph}} = \begin{bmatrix} e^{i\theta_{\mathbf{n}}} & \\ & \mathbb{1} \end{bmatrix}, \tag{7.44}$$

such that

$$U_{\text{ph}}\,\tilde{H}\,U_{\text{ph}}^{\dagger} = \begin{bmatrix} E-\mu & \Delta_e D^- \\ \Delta_e D^+ & \mu - E \end{bmatrix}. \tag{7.45}$$

where

$$D^- = i|\mathbf{J}^E|\partial_E - i|\mathbf{J}^\eta|(i\partial_\eta + A_\eta)\,, \tag{7.46a}$$

$$D^+ = i|\mathbf{J}^E|\partial_E + i|\mathbf{J}^\eta|(i\partial_\eta + A_\eta) + i|\mathbf{J}^\eta|\frac{\partial\theta_{\mathbf{n}}}{\partial\eta}\,. \tag{7.46b}$$

We have ignored the term $\partial_E\theta_{\mathbf{n}}$ from the assumption that the FS is smooth (no cusps). The term $\partial_\eta\theta_{\mathbf{n}}$ is extremely important as it will give us the π Berry phase shift.

At any fixed value of η, we write the Hamiltonian in the form of Eq. (7.35):

$$U_{\text{ph}}\tilde{H}U_{\text{ph}}^{\dagger} = (E-\mu)\tau^z + \Delta_e D^x\tau^x + \Delta_e D^y\tau^y, \tag{7.47}$$

where D^x and D^y are the symmetric and the antisymmetric parts of off the diagonal elements $D^\pm$.

$$D^x = \frac{D^+ + D^-}{2} = i|\mathbf{J}^E|\partial_E + i\frac{|\mathbf{J}^\eta|}{2}\frac{\partial\theta_{\mathbf{n}}}{\partial\eta}\,, \tag{7.48a}$$

$$D^y = \frac{D^+ - D^-}{2i} = |\mathbf{J}^\eta|\left(i\partial_\eta + A_\eta + \frac{1}{2}\frac{\partial\theta_{\mathbf{n}}}{\partial\eta}\right). \tag{7.48b}$$

In the first expression (7.48a), there is an extra term $\frac{i|\mathbf{J}^\eta|}{2}\frac{\partial\theta_{\mathbf{n}}}{\partial\eta}$, which we can absorb in to the energy derivative via the transformation

$$\exp\left[\int g_\eta\,dE\right]\,\partial_E\,\exp\left[-\int g_\eta\,dE\right] = \partial_E - g_\eta \tag{7.49}$$

where $g_\eta(E) = \frac{|\mathbf{J}^\eta|}{2|\mathbf{J}^E|}\frac{\partial\theta_{\mathbf{n}}}{\partial\eta}$. This introduces a term $\partial_\eta g_\eta$ in D^y, but is irrelevant as g_η is single-valued. (In the case with rotational symmetry, the term $\exp\int g_\eta$ is $k^{1/2}$ in (7.27).)

The (E dependent portion of the) solution to Jackiw-Rebbi Hamiltonian (7.47) is:

$$\psi(E,\eta) \sim u(\eta)\,\exp\left[-\int\frac{E-\mu}{\Delta_e|\mathbf{J}^E|}\,dE\right]\begin{pmatrix}1\\-i\end{pmatrix}, \tag{7.50}$$

by treating D^y as a constant (independent of E) on the energy scale of $\sqrt{\Delta_e|\mathbf{J}^E|}$. The effective Hamiltonian is $H_\eta = -\Delta_e D^y$.

Finally, we solve for $D^y(\eta)u(\eta) = 0$ for a Majorana vortex bound state, subject to the constraint that $u(\eta)$ is single-valued. We can solve for $u(\eta)$ explicitly:

$$u(\eta) = \mathcal{P}\exp\left[i\int_0^\eta d\eta'\left(A_\eta(\eta') + \frac{1}{2}\frac{\partial\theta_{\mathbf{n}}}{\partial\eta}\right)\right]u(0)\,. \tag{7.51}$$

Since $\theta_{\mathbf{n}}$ winds by 2π around a *closed* FS, $\oint\frac{1}{2}\partial_\eta\theta_{\mathbf{n}} = \pi$ gives an overall phase of -1. We have $u(2\pi) = -U_B u(0)$, where the Berry phase of the FS is

$$U_B = \mathcal{P}\exp\left[i\oint_0^{2\pi} A_\eta\,d\eta\right]. \tag{7.52}$$

Hence a solution exists for every -1 eigenvalue of U_B.

7.3.7 Vortex bound states

We can solve for the spectrum Caroli-de Gennes-Matricon bound states [217]. For an arbitrary energy $\mathcal{E}$, the 'angular' portion of the wavefunction satisfies $-\Delta_e D^y u(\eta) = \mathcal{E}u(\eta)$, equivalent to:

$$-i\partial_\eta u(\eta) = \left(\frac{\mathcal{E}}{\Delta_e|\mathbf{J}^\eta|} + A_\eta + \frac{1}{2}\frac{\partial\theta_{\mathbf{n}}}{\partial\eta}\right)_{E=\mu}u(\eta)\,. \tag{7.53}$$

Note that $|\mathbf{J}^\eta|^{-1} = |\mathbf{t}|$. The solution for $u(\eta)$ is a path-ordered exponential

$$u(\eta) = \mathcal{P}\exp\left[i\int_0^\eta\left(\frac{\mathcal{E}|\mathbf{t}|}{\Delta_e} + A_\eta + \frac{1}{2}\frac{\partial\theta_{\mathbf{n}}}{\partial\eta}\right)_{E=\mu}d\eta'\right]u(0)\,. \tag{7.54}$$

The full solution to the Hamiltonian (7.43) is:

$$\psi(E,\eta)\;\propto\;u(\eta)\exp\left[-\int^E\left(\frac{E'-\mu}{\Delta_e|\mathbf{J}^E(E')|} + g_\eta(E')\right)dE'\right]\begin{pmatrix}e^{-i\theta_{\mathbf{n}}}\\ -i\end{pmatrix}. \tag{7.55}$$

While A_η is a hermitian matrix, $\mathcal{E}|\mathbf{t}|/\Delta_e$ and $\partial_\eta\theta_{\mathbf{n}}$ are simply numbers, hence the integral may be evaluated separately for each term. The integral $\oint_0^{2\pi}|\mathbf{t}|d\eta$ is simply the perimeter of the FS l_F. The integral $\frac{1}{2}\oint_0^{2\pi}\partial_\eta\theta_{\mathbf{n}}d\eta$ is π for a closed FS, and 0 for an open FS (modulo 2π). The single-valued requirement $u(2\pi) = u(0)$ (for a closed FS) becomes:

$$u(0) = -\exp\left(i\frac{l_F}{\Delta_e}\mathcal{E}\right)U_B u(0)\,. \tag{7.56}$$

From this, we can calculate the allowed energies for an arbitrary Berry phase:

$$\mathcal{E}_n = \frac{\Delta_e}{l_F}(2\pi n + \pi - \phi)\,, \tag{7.57}$$

for integers n, where $e^{i\phi}$ are the eigenvalues of U_B. Note that the eigenvalues always come in pairs $\pm\phi$ due to the particle-hole symmetry of the system (considering both k_z and $-k_z$ slices of the BZ).

7.4 Candidate materials

We now apply the Berry phase criterion to some candidate materials to see which of them can have protected MZMs at the ends of vortices. Note our results assumes an s-wave superconducting pairing for these materials.

In all these case, we note that the VPT could potentially be probed via thermal transport along the vortex line. A hurdle to accessing this physics is the small minigap scale ($\Delta_0/k_F\xi \sim \Delta_0^2/E_F$), and long confinement length of surface MZMs along the vortex line, which may be ameliorated by considering strong coupling superconductors or materials such as heavy fermions where E_F is effectively reduced.

7.4.1 $\mathrm{Cu}_x\mathrm{Bi}_2\mathrm{Se}_3$ with s-wave pairing

The insulating phase of $\mathrm{Bi}_2\mathrm{Se}_3$ is a strong TI with a single band inversion occurring at the Γ point. On Cu doping, $\mathrm{Bi}_2\mathrm{Se}_3$ becomes n-type with an electron pocket at Γ and is reported to superconduct below $T_c = 3.8\,\mathrm{K}$ [125, 218]. Photoemission measurements show $\mu \approx 0.25\,\mathrm{eV}$ above the conduction band minimum at optimal doping ($x = 0.12$) [219]. We calculate the Berry phase eigenvalues for a FS around the Γ point numerically as a function of μ, which evaluates to $\pm\pi$ at $\mu_c \approx 0.24\,\mathrm{eV}$ above the conduction band minimum for a vortex along the c-axis of the crystal. $\mu \gtrsim \mu_c$ indicates c-axis vortices are near the topological transition, and more accurate band structures may be needed for a definitive conclusion.

Numerical calculation of the Berry phase for $\mathrm{Bi}_2\mathrm{Se}_3$

The insulating phase of $\mathrm{Bi}_2\mathrm{Se}_3$ is a strong TI, with a band inversion occurring at the Γ point in its rhombohedral Brillouin zone. $\mathrm{Cu}_x\mathrm{Bi}_2\mathrm{Se}_3$ is reported to superconduct below $T_c = 3.8\,\mathrm{K}$ [125, 218]. Before the superconducting transition, the carrier (electron) density is approximately $2 \times 10^{20}\,\mathrm{cm}^{-3}$ from Hall measurements [125]. Using the effective eight-band model from Ref. [203], we estimate μ theoretically in this material from the carrier density to be $\approx 0.4\,\mathrm{eV}$ relative to the conduction band bottom. However, photoemission measurements show $\mu \approx 0.25\,\mathrm{eV}$ above the bottom of the conduction band at the optimal doping ($x = 0.12$) [219].

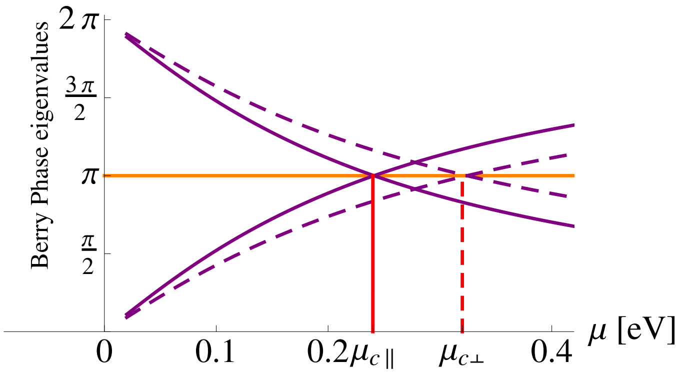

Figure 7.5: Berry phase eigenvalues ϕ_B for Bi_2Se_3 as a function of μ.

The chemical potential μ is measured relative to the bottom of the conduction band for a Fermi surface. The Berry phases are computed for the Fermi surfaces relevant to a vortex along the c-axis (solid curves) and perpendicular to the c-axis at an angle of $\pi/6$ to the binary axis (dashed curves) of Bi_2Se_3. The eigenvalues appear in $\pm$ pairs and are only defined modulo 2π. The phases ϕ_B are zero (modulo 2π) at both the conduction band minimum and at energies far above the conduction band. Clearly, the $\phi_B = \pi$ at $\mu_{c\|} = 0.24\,\mathrm{eV}$ and $\mu_{c\perp} = 0.24\,\mathrm{eV}$, signaling a VPT. Photoemission measurements show $\mu \approx 0.25\,\mathrm{eV} \sim \mu_c$ above the conduction band minimum at optimal doping [219], and hence Cu doped Bi_2Se_3 is predicted to be near the vortex phase transition for a c-axis vortex, and to have end MZMs for vortices sufficiently tilted off the c-axis.

The conduction band minimum is at the Γ-point. For small carrier densities, we expect the FS to be centered around Γ. Using the same model from Ref. [203], we determine μ_c for this material by calculating the Berry phase eigenvalues for a FS around the Γ point numerically as a function of μ for various vortex orientations. In Fig. 7.5, we show the results for a vortex parallel to the c-axis (solid line) and for a vortex perpendicular it making an angle of $\pi/6$ with the binary axis (dashed line).

This calculation is done by discretizing the FS contour and making the pair of Bloch functions continuous and the Berry connection vanish at all but one points on this contour. More precisely, we parametrize the FS via $\eta \in [0, 2\pi]$ and compute the eigenstates $|\varphi^\nu(\eta)\rangle$ for $\nu = 1, 2$. The phase is chosen such that $A_\eta^{\mu\nu} = i\langle\varphi^\mu(\eta)|\partial_\eta|\varphi^\nu(\eta)\rangle = 0$ for $0 < \eta < 2\pi$ along the FS.

In general, the Bloch functions will not be single-valued, *i.e.*, $|\varphi^\nu(2\pi)\rangle \neq |\varphi^\nu(0)\rangle$. The unitary transformation required to rectify the discontinuity at this one point is precisely the non-abelian phase: $|\varphi^\mu(0)\rangle = [U_B]^{\mu\nu}|\varphi^\nu(2\pi)\rangle$. Because of time-reversal symmetry in the normal phase of Bi_2Se_3, the Berry phase $U_B \in SU(2)$ has eigenvalues $e^{\pm i\phi}$ which come in complex conjugate pairs. Figure 7.5 shows the variation of the Berry phase eigenvalues ϕ as a function of μ for two different FSs of Bi_2Se_3 in the $k_z = 0$ plane, where the z-axis is along the vortex. Here, μ is measured relative to the bottom of the conduction band at the Γ point, which is where the band inversion occurs. When the vortex is along the c-axis, $\mu_c \approx 0.24\,\mathrm{eV}$, which happens to be close to the chemical potential for these doped materials according to ARPES [219]. Thus, we expect these vortices to be close to the phase transition. On the other hand, $\mu_c \approx 0.30\,\text{eV}$ for a vortex perpendicular to the c-axis – such a vortex should have end MZMs. Note that the model does not taken into account the modification of the Bi_2Se_3 bands due Cu doping.

Current status of $Cu_xBi_2Te_3$

We note that, since the publication of this work, there have been evidence that $Cu_xBi_2Te_3$ has odd-parity pairing, and may be a topological superconductor [93–96, 220]. If this is indeed the case, then the analysis above and the result of this work will not be applicable to the material.

7.4.2 p-doped $TlBiTe_2$, p-doped Bi_2Te_3 and $Pd_xBi_2Te_3$

The bands of $TlBiTe_2$ and Bi_2Te_3 are topologically nontrivial because of a band inversion at the Γ point [9, 57, 98–100, 102]. The topological character of Bi_2Te_3 is believed to be preserved under a pressure of up to 6.3 GPa, at which it undergoes a structural phase transition. On p-doping to a density of $6 \times 10^{20}\,\text{cm}^{-3}$ (3-6 $\times 10^{18}\,\text{cm}^{-3}$), $TlBiTe_2$ (Bi_2Te_3 under 3.1 GPa) becomes a SC below $T_c = 0.14\,\text{K}$ ($\sim 3\,\text{K}$) [212, 221], making it a natural system to search for the possibility of MZMs. Similarly, n-doping Bi_2Te_3 to a concentration of $9 \times 10^{18}\,\text{cm}^{-3}$ by adding Pd reportedly results in $T_c = 5.5\,\text{K}$ [125] in a small sample fraction. The superconductivity in Bi_2Te_3 under pressure, and in $TlBiTe_2$ ($Pd_xBi_2Te_3$) is believed to arise from six symmetry related hole (electron) pockets around the Γ-T line. This is an even number so vortex lines in superconducting $TlBiTe_2$ and both p- and n-type Bi_2Te_3 should have MZMs at their ends in all orientations.

7.4.3 Majorana zero modes from trivial insulators

The bulk criterion derived does not require a 'parent' topological band structure. As a thought example, say we have four TRIMs with Hamiltonians like Eq. (7.3) in their vicinity. Such band inversions at four TRIMs in a plane leads to a trivial insulator [43]. However, if their critical chemical potentials μ_c differ, then it could be possible to find a range of μ where there are an *odd* number of VPTs below and above μ, leading to topologically nontrivial vortices. Interestingly PbTe and SnTe are both trivial insulators with band inversions relative to each other at the four equivalent L points.[2] They both exhibit superconductivity on doping below $T_c = 1.5\,\text{K}$ [223] and $0.2\,\text{K}$ [224] respectively. A combination of strain (to break the equivalence of the four L points) and doping could potentially create the scenario described above in one of these systems. GeTe is similar to SnTe with $T_c \sim 0.3\,\text{K}$ [225] but undergoes

---

[2] Hsieh *et al.* [222] has shown that SnTe has four band inversions, while PbTe does not under normal circumstances. However, pressure ($\sim 3\,\text{GPa}$) may induce band inversions in PbTe.

a spontaneous rhombohedral distortion resulting in the desired symmetry. This general idea merits further investigation, since it could admit many more candidate materials.

Acknowledgment

We acknowledge insightful discussions with Ari M. Turner, Jens H. Bárðarson, L. Andrew Wray and Charles L. Kane, and funding from NSF-DMR 0645691. In parallel work, L. Fu, J. C. Y. Teo and C. L. Kane have arrived at similar conclusions.

Part IV

Surface Transport

Chapter 8

Quantum transport on the surface of weak topological insulators

Recall, that in 3D, topological insulators are classified as either strong (STI) or weak topological insulators (WTI). The surfaces of STIs have an odd number of 2D Dirac fermions and have garnered much of the attention, as TRS disorder cannot localize the surface states unless it is strong enough to move states across the bulk energy gap. In contrast, the WTIs have an even number of Dirac fermions and are *believed* to be unstable to disorder [21, 25, 26].

This belief stems partially from comparisons with graphene. Superficially, WTIs and graphene are similar in that their low energy electronic properties are described by an even number of Dirac fermions [226, 227]. While both systems have TRS implemented by an antiunitary time-reversal operator Θ, they differ fundamentally in that $\Theta^2 = +1$ for graphene from $SU(2)$ spin symmetry,[1] while for a WTI $\Theta^2 = -1$ due to the presence of strong spin-orbit coupling. This places graphene in the orthogonal (AI) symmetry class, while WTIs belong to the symplectic (AII) class in the Altland-Zirnbauer classification [76]. The consequences of the minus sign are profound. The first quantum correction to the Drude conductivity is determined by interference of time-reversal-symmetric paths. In the orthogonal class, this interference is constructive (weak localization) and eventually leads to localization of all single-particle states. In contrast, in the symplectic class, the interference is destructive (weak antilocalization) giving rise to an enhancement of the conductivity and a stable *symplectic metal* phase [70, 71]. Hence, the metallic phase of graphene is unstable to disorder coupling the Dirac fermions [228] but is stable in WTIs.

An STI is also in the symplectic class. With an odd number of Dirac fermions on its surface, it always flows into the symplectic metal [50, 51], reflecting the presence of a topological term in the effective field theory (nonlinear sigma model) describing diffusion [49, 229]. This topological term is absent in the same description of a WTI, suggesting that localization should occur. In conventional semiconductors with spin-orbit coupling, this

---

[1] An unbroken $SU(2)$ spin symmetry (*e.g.* in graphene) means that Θ can be taken just to be complex conjugation, effectively treating the fermions as spinless with $\Theta^2 = +1$.

leads to a metal-insulator transition at a critical conductivity $\sigma_c \approx 1.42\, e^2/h$ [230].

It is the purpose of this work to explore the precise conditions under which a WTI undergoes localization. One reason that this is an interesting question is the following argument [64]. If one considers obtaining a WTI by stacking 2D layers in the QSH phase, a surface parallel to the stacking direction would consist of pairs of 1D counterpropagating helical modes. The number of such modes taking part in transport can be even or odd depending on the number of layers. However, an odd number of 1D modes in the symplectic class necessarily leads to the presence of a perfectly transmitted mode and thus a minimum conductance of e^2/h [44, 231]. While this argument is one-dimensional in nature as the sample thickness is constant, it suggests that a WTI can under certain conditions avoid localization. In the extended two-dimensional surface, the meaning of this parity effect is unclear, raising the question: What is the scaling behavior of the conductivity in disordered WTIs?

In this chapter, we demonstrate, by numerical simulations, that the scaling flow depends on the presence or absence of a specific TRS mass, to be defined below. In the presence of this mass, a gap opens up in the spectrum which can lead to localization. Disorder can still drive the system into a metallic phase, realizing a metal-insulator transition at a critical value of conductivity consistent with what is observed in conventional semiconductors. In contrast, in the absence of this mass the system always flows into the symplectic metal. We demonstrate that this flow follows one-parameter scaling with a positive beta function, just as in the case of an STI [50, 51]. The phase diagram emerging from these observations (*cf.* Fig. 8.1) suggests that one-parameter scaling is not realized throughout, as one might expect from the minimal nonlinear sigma model description. Instead, we present data supporting two-parameter scaling, the effective field theory of which remains unknown.

8.1 Hamiltonian and disorder structure

In the following, we specialize to the case of a WTI with two Dirac cones, for which the low energy electronic properties are described by the Hamiltonian[2]

$$H = \hbar v_D \tau^0 (\sigma^x k_x + \sigma^y k_y) + V(\mathbf{r})\,, \tag{8.1}$$

where $\tau^0 = \sigma^0 = \mathbb{1}$ is the identity, $\tau^{x,y,z}$ and $\sigma^{x,y,z}$ are the Pauli matrices in valley and spin space, respectively. H is invariant under the time-reversal $\Theta = i\sigma^y \mathcal{K}$, where $\mathcal{K}$ is the complex conjugation operator. The momentum is shifted such that the Dirac cones are centered at $\mathbf{k} = 0$, The Dirac velocity v_D (taken isotropic for simplicity) and $\hbar$ are set to 1 henceforth. Time-reversal flips the spin in each valley, and is represented by the operator $\Theta = -i\sigma^y \mathcal{K}$,

---

[2] We choose to work with a Hamiltonian where the two Dirac fermions have the same chirality. All the results presented here also hold in the case when they have the opposite chirality, due to a similarity transformation between the two cases (*cf.* Sec. 8.1.1).

Disorder structure	Disorder type	Notation
$V_{x0} \cdot \tau^x$	scalar potential (2×AII)	
$V_{yx} \cdot \tau^y \sigma^x$	gauge potential (2×AIII)	
$V_{yy} \cdot \tau^y \sigma^y$	gauge potential (2×AIII)	
$V_{yz} \cdot \tau^y \sigma^z$	mass (2×D)	$m = \langle V_{yz} \rangle$
$V_{z0} \cdot \tau^z$	scalar potential (2×AII)	
$V_{00} \cdot \mathbb{1}$	scalar potential (2×AII)	$\mu = -\langle V_{00} \rangle$

Table 8.1: List of TRS disorder terms on the surface of a WTI with two Dirac cones. If only one of the disorder structures is present in the system, the type indicates the disorder class of the system and the effect of the disorder. For example, with *only* $V_{yz}(\mathbf{r})\tau^y\sigma^z$, the system breaks up into two systems, each identical to a Dirac cone with random mass in class D. Hence, multiple disorder structures are required for the system to be class AII.

where $\mathcal{K}$ is the complex conjugation operator. The disorder potential is written

$$V(\mathbf{r}) = \sum_{\alpha\beta} V_{\alpha\beta}(\mathbf{r})\, \tau^\alpha \otimes \sigma^\beta \tag{8.2}$$

with $V_{\alpha\beta}(\mathbf{r})$ a scalar potential and $\alpha, \beta \in \{0, x, y, z\}$. The six terms respecting time-reversal, listed in Tab. 8.1, are independently distributed with correlation

$$\big\langle \delta V_{\alpha\beta}(\mathbf{r})\, \delta V_{\alpha\beta}(\mathbf{r}') \big\rangle = g_{\alpha\beta} K(\mathbf{r} - \mathbf{r}') \tag{8.3}$$

where $\int d^2\mathbf{r}\, K(\mathbf{r}) = 1$. The two-terminal conductivity σ of a system of size L is obtained numerically by adapting the transfer matrix method of Ref. [50] to the current problem. (The width W is taken large enough that the conductivity is independent of the ratio W/L.) Each disorder term is Gaussian correlated with $K(\mathbf{r}) = \exp(-r^2/2\xi^2)/(2\pi\xi^2)$. We also take the averages $\langle V_{\alpha\beta}(\mathbf{r}) \rangle = 0$, except for V_{yz} and V_{00} as explained below.

It is useful to first analyze the system in the clean case, where $V_{\alpha\beta}$ are constants. $\langle V_{00} \rangle$ acts as the chemical potential μ which shifts the energy spectrum trivially. $\tau^y\sigma^z$ anticommutes with all the other potentials (except $\mathbb{1}$) as well as the kinetic term $\boldsymbol{\sigma} \cdot \mathbf{k}$; the presence of this term always gaps the system, and hence we refer to $m = \langle V_{yz} \rangle$ as the "mass." The energy spectrum of the system is given by

$$\begin{aligned}\big(E(\mathbf{k}) - \mu\big)^2 = k^2 &+ V_{x0}^2 + V_{yx}^2 + V_{yy}^2 + V_{z0}^2 \\ &\pm 2\sqrt{(V_{x0}^2 + V_{z0}^2)k^2 + (V_{yx}k_x + V_{yy}k_y)^2 + m^2}\,,\end{aligned} \tag{8.4}$$

with minima at $k^2 = V_{x0}^2 + V_{yx}^2 + V_{yy}^2 + V_{z0}^2$ and $k_x/k_y = V_{yx}/V_{yy}$, in which case we have $(E - \mu)^2 = m^2$. Therefore, the energy gap is $2|m|$ and the system is insulating when $|m| > |\mu|$. The cases $m > |\mu|$ and $m < -|\mu|$ correspond to the two topological sectors in the 2D AII class, *i.e.*, the trivial and QSH insulator.[3] The intermediate metallic region $-|\mu| < m < |\mu|$ separates the two phases.

8.1.1 Chirality of the Dirac cones

We digress briefly in this section we show that our results are independent of the Dirac cone chiralities. In the previous section we used a model in which the two Dirac cones have the same chirality:

$$H_0 = \hbar v_D \begin{bmatrix} \sigma^x k_x + \sigma^y k_y & \\ & \sigma^x k_x + \sigma^y k_y \end{bmatrix} . \tag{8.5}$$

Here H_0 refers to the kinetic portion of the Hamiltonian. As the momentum $\mathbf{k}$ rotates by 2π, the spin also rotates by 2π in the same direction, hence both Dirac cones have chirality of $+1$.

We can apply the unitary transformation U which flips only one of the Dirac cone's chirality.

$$U = \begin{bmatrix} \mathbb{1} & \\ & i\sigma^x \end{bmatrix} \qquad \Longrightarrow \qquad H_0' = U H_0 U^\dagger = \hbar v_D \begin{bmatrix} \sigma^x k_x + \sigma^y k_y & \\ & \sigma^x k_x - \sigma^y k_y \end{bmatrix} . \tag{8.6}$$

It is important to note that the transformation does not alter the form of time-reversal, *i.e.*, $U\Theta U^\dagger = \Theta = i\sigma^y \mathcal{K}$, and that it shuffles the disorder potentials:

$$(V_{x0}, V_{yx}, V_{yy}, V_{yz}, V_{z0}, V_{00}) \mapsto (V_{yx}, -V_{x0}, -V_{yz}, V_{yy}, V_{z0}, V_{00}) . \tag{8.7}$$

The mass for the new system is defined to be $m = \langle V_{yy} \rangle$ as $\tau^y \sigma^y$ anticommutes with H_0'. This shows that our results are independent of the chirality of the Dirac cones.

8.1.2 Constructing the mass for an arbitrary even number of Dirac cones

For the case of two Dirac cones, we have defined the mass $m = \langle V_{yz} \rangle$ with the following properties:

1. In absence of other potentials and disorder, the system gap is simply $2|m|$, and
2. the limits $m \to \infty$ and $m \to -\infty$ correspond to the system being in the trivial and QSH insulating phases, respectively.

---

[3] We avoid stating which state $\pm m$ is the trivial insulator and which is the topological (QSH) insulator, as this depends on the band structure away from the Dirac point. In a certain sense, we can think of them as $\pm\frac{1}{2}$QSH insulators [232].

Here we explicitly construct m for a system with four Dirac cones and give the procedure for finding m in the general case.

With four Dirac cones, the Hamiltonian is

$$H^{(4)} = \upsilon^0 \tau^0 \boldsymbol{\sigma} \cdot \mathbf{k} + V(\mathbf{r}) \,. \tag{8.8}$$

We use the Pauli matrices $\tau^{x,y,z}$ and $\upsilon^{x,y,z}$ acting in valley space to span all the possible intervalley couplings. ($\tau^0 = \upsilon^0 = \mathbb{1}$.) The disorder potential decomposes

$$V(\mathbf{r}) = \sum_{\alpha\beta\gamma} V_{\alpha\beta\gamma}(\mathbf{r}) \upsilon^\alpha \tau^\beta \sigma^\gamma \,, \quad \text{with } \alpha, \beta, \gamma \in \{0, x, y, z\} \,. \tag{8.9}$$

Of the twenty-eight disorder structures $\upsilon^\alpha \tau^\beta \sigma^\gamma$ compatible with time-reversal $\Theta = i\sigma^y \mathcal{K}$, only six anticommutes with the kinetic Hamiltonian $\boldsymbol{\sigma} \cdot \mathbf{k}$. These six are given by $(\alpha, \beta, \gamma) = (0, y, z), (y, x, z), (y, z, z), (y, 0, z), (x, y, z), (z, y, z)$. The first three anticommute with each other as do the last three, while all of the first three commute with any of the last three. The mass is thus given by:

$$m^{(4)} = \sqrt{\langle V_{0yz} \rangle^2 + \langle V_{yxz} \rangle^2 + \langle V_{yzz} \rangle^2} - \sqrt{\langle V_{y0z} \rangle^2 + \langle V_{xyz} \rangle^2 + \langle V_{zyz} \rangle^2} \,. \tag{8.10}$$

It can be shown that this definition satisfies both conditions 1. and 2. above.

In the general case with $2n$ Dirac cones, there will be $n(2n-1)$ linear independent disorder structures which opens a gap in the system, of the form $V \otimes \sigma^z$, where V is an $2n \times 2n$ matrix acting in valley space. V must be an antisymmetric pure-imaginary matrix, *i.e.*, an element of the Lie algebra $\mathfrak{so}(2n)$ (in the canonical representation). Seeing that $V \otimes \sigma^z$ anticommutes with $\boldsymbol{\sigma} \cdot \mathbf{k}$, the spectrum at $\mathbf{k} = 0$ is the set of eigenvalues of V. The mass is defined as follows: $|m|$ is the smallest non-negative eigenvalue of V while the sign of m is that of $\mathrm{Pf}(iV)$.

For the remainder of the text, we'll assume exactly two Dirac cones, although we expect the qualitative results to be identical for any even number $2n > 0$ number of Dirac cones.

8.2 Quantum spin Hall-metal-insulator transition

We return to the problem of analyzing the Hamiltonian (8.1). In the presence of disorder, a similar description applies just as in the clean case. – by varying m, one can take the system between the two insulating phases. As conjugation by τ^x flips the sign of m, a conducting state should be realized at $m = 0$. Because to the stability of the symplectic metal, one does not expect generically a direct transition between the insulating phases [233–235]. The resulting phase diagram is shown in Fig. 8.1. At a finite chemical potential, there is a range of mass values $|m| \lesssim |\mu|$ where the system undergoes two transitions with increasing disorder strength (dashed line in Fig. 8.1). The phase diagram holds generally for WTI surfaces even with more than 2 Dirac cones.

The shape of the phase diagram around the clean Dirac point $g = m = \mu = 0$ should also be consistent with the renormalization group flow of the coupling parameters $g_{\alpha\beta}$, m, and μ

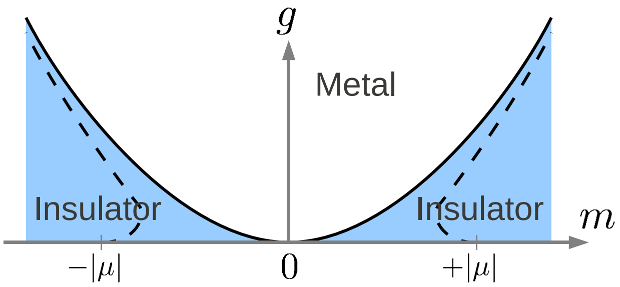

Figure 8.1: The phase diagram of the Hamiltonian (8.1).

The axes are mass $m = \langle V_{yz} \rangle$ and disorder strength $g_{\alpha\beta} = g$. The solid line marks the metal-insulator transition at $\mu = 0$, whereas the dashed line marks the transition at finite μ. At the clean Dirac point ($g = \mu = 0$), there is a topological phase transition between the two types of insulators. With increasing disorder or chemical potential μ, a metallic phase appears separating the two topological sectors.

away from that point. Disorder average, either using the replica trick or a supersymmetric representation, gives arise to an interacting field theory with coupling constants given by the amplitudes $g_{\alpha\beta}$ of the disorder correlator, as well as single-particle potentials with amplitudes μ and m [236, 237]. The clean Dirac point $g_{\alpha\beta} = m = \mu = 0$ is a fixed point of this theory. Under renormalization the coupling constants flow away from the clean Dirac point according to the equations:

$$\begin{aligned}
\pi \frac{dg_{00}}{d\ln L} &= g_{00}(g_{00} + g_{x0} + g_{yx} + g_{yy} + g_{yz} + g_{z0}) + g_{yz}(g_{yx} + g_{yy})\,,\\
\pi \frac{dg_{x0}}{d\ln L} &= g_{x0}(g_{00} + g_{x0} - g_{yx} - g_{yy} - g_{yz} - g_{z0}) + g_{z0}(g_{yx} + g_{yy})\,,\\
\pi \frac{dg_{yx}}{d\ln L} &= g_{x0}g_{z0} + g_{yz}g_{00} = \pi \frac{dg_{yy}}{d\ln L}\,,\\
\pi \frac{dg_{yz}}{d\ln L} &= g_{yz}(-g_{00} + g_{x0} + g_{yx} + g_{yy} - g_{yz} + g_{z0}) + g_{00}(g_{yx} + g_{yy})\,,\\
\pi \frac{dg_{z0}}{d\ln L} &= g_{z0}(g_{00} - g_{x0} - g_{yx} - g_{yy} - g_{yz} + g_{z0}) + g_{x0}(g_{yx} + g_{yy})\,,\\
\frac{d\mu}{d\ln L} &= \mu + \frac{\mu}{2\pi}(g_{00} + g_{x0} + g_{yx} + g_{yy} + g_{yz} + g_{z0})\,,\\
\frac{dm}{d\ln L} &= m + \frac{m}{2\pi}(-g_{00} + g_{x0} + g_{yx} + g_{yy} - g_{yz} + g_{z0})\,.
\end{aligned} \tag{8.11}$$

These equations have been obtained in one loop following the standard procedure used for Dirac fermions [238–241].

Since m initially flows away faster than the disorder couplings, this suggest the shape of the phase diagram around the clean point is as in Fig. 8.1. Apart from that observation and that the clean fixed point is unstable, the renormalization group equations (8.11) yield no

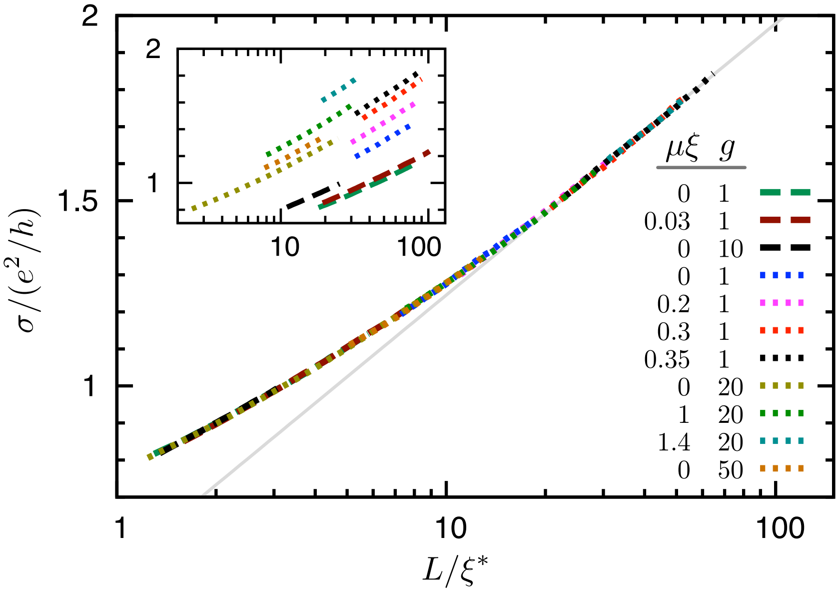

Figure 8.2: Demonstration of one-parameter scaling at $m = 0$.

Conductivity as a function of system size for various parameters all collapsed (by shifting the raw data horizontally) onto one scaling curve. At large σ, the slope $d\sigma/d\ln L$ approaches $1/\pi$ (gray line) consistent with weak antilocalization. Here $g_{00} = g$ for dotted lines and $g_{00} = 0$ for dashed lines. For all other $\alpha\beta$, $g_{\alpha\beta} = g$. (Inset) Raw data σ vs. L/ξ.

more information on the metal-insulator transition. Therefore the numerical simulations are crucial in order to answer such questions.

8.2.1 Numerical data

The numerical data supporting the phase diagram in Fig. 8.1 are shown in Fig. 8.2 and Fig. 8.3. At $m = 0$ the conductivity always flows to the symplectic metal, regardless of the strength of the disorder (see Fig. 8.2). By rescaling the length ($L/\xi \to L/\xi^*$), we can collapse all the data on a single curve demonstrating one-parameter scaling along the $m = 0$ line. At large conductivity, the beta function $\beta(\sigma) = d(\ln\sigma)/d(\ln L)$ approaches $1/\pi\sigma$ as predicted for weak antilocalization [70].

By varying m, it is possible to drive the system to an insulator, as shown in Fig. 8.3a. At small m, the system remains a symplectic metal. At some critical m, a metal-insulator transition occurs and it ceases to conduct. For a fixed nonzero m such that the clean system is insulating, disorder drives the system into a metallic phase at some critical disorder strength g_c that depends on m, as demonstrated in Fig. 8.3b. In both these cases, at large conductivity the slope $d\sigma/d\ln L$ approaches $1/\pi$, indicative of weak antilocalization.

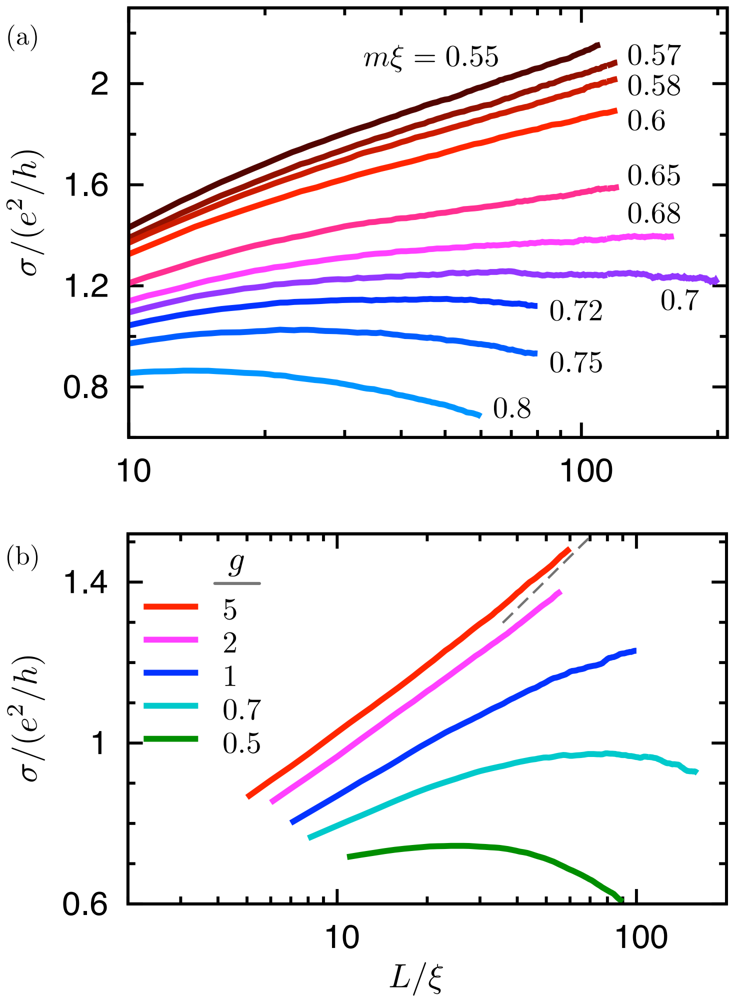

Figure 8.3: Metal-insulator transition as m, g are varied.

(a) Metal-insulator transition as m is varied. Conductivity is plotted vs. system size for fixed $\mu\xi = 1$ and $g_{x0} = g_{yz} = 2$. For large m the system flows to an insulating state, while for small m the system is conducting. Among the conducting curves, the slope $d\sigma/d\ln L$ approaches $1/\pi$ at large σ. The data shown here, in addition to the conductance distribution in Fig. 8.4, indicates an Anderson transition at $\sim 1.4\,e^2/h$, consistent with [230].
(b) Metal-insulator transition as disorder strength $g_{\alpha\beta} = g$ is varied. The plot is σ vs. L/ξ for fixed $m\xi = 0.05$ and $\mu = 0$. Increasing disorder increases the conductivity, inducing a transition from an insulating phase to a metallic one at some critical g. The dashed line indicates a slope of $1/\pi$. These figures are consistent with the phase diagram in Fig. 8.1.

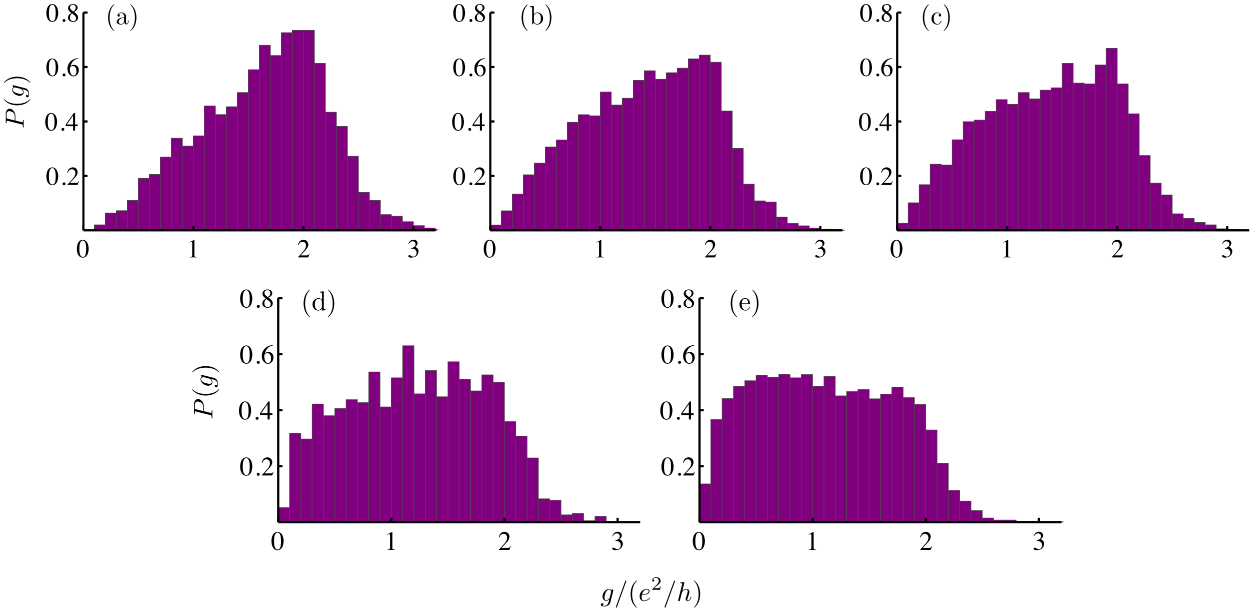

(f)

histogram	$m\xi$	L/ξ	samples
(a)	0.65	160	3456
(b)	0.67	80	9600
(c)	0.68	160	3456
(d)	0.7	160	1920
(e)	0.72	80	9600

$\mu\xi = 1$, $g_{x0} = g_{yz} = 2$.

Figure 8.4: Conductance distribution near the Anderson transition.

(a)-(e) The conductance distribution P as a function of the conductance g for a square geometry ($W = L$). The parameters used are those of Fig. 8.3a with varying m, given in the table (f). Comparing with the critical conductance distribution in Ref. [242] computed for network models, we see that the metal-insulator transition occurs between (b) and (c) ($0.67 < m\xi < 0.68$). This confirms that the 2D Anderson transition in the symplectic class is universal among both network models and continuous models with smooth disorder.

8.2.2 Conditions for localization

Since a WTI is always conducting in the absence of mass, it is pertinent to discuss under what circumstances one expects a nonzero mass. The potential $V_{yz}(\mathbf{r})$ couples valleys centered at different momenta and thus requires short-range scatters. Furthermore a nonzero mass can arise only when the surface potential is commensurate with an even number of unit cells, such as in the case of cleaving the surface at a crystal plane [64], or when the WTI is grown on a lattice-matching substrate. As such, a nonzero mass would be marked by an enlargement of the unit cell and would appear in a crystal diffraction experiment as a peak of order $\mathbf{G}_\nu/2$, where $\mathbf{G}_\nu$ is a reciprocal lattice vector characterizing the weak topological invariants of the WTI [4]. On the other hand, a period-doubling perturbation could indicate a valley-mixing term other than m (the other possible terms being $\langle V_{x0}\rangle$, $\langle V_{yx}\rangle$ or $\langle V_{yy}\rangle$). It may also be possible to measure m via spin- and angle-resolved photoemission spectroscopy (spin-resolved ARPES), by comparing the spin up and spin down intensities at wavevector $\mathbf{G}_\nu/2$. This proposal is motivated by the form of the potential $\tau^y\sigma^z$, which differentiates the up and down spins. Localization may also occur due to lattice effects or higher order terms in the Hamiltonian [233, 243, 244].

In the case where the WTI consists of an odd number of QSH layers, we argue that the mass must be identically zero. Consider stacking n QSH layers, with each layer in the $\mathbf{a}_1, \mathbf{a}_2$ plane, and the layers $\mathbf{a}_3$ offset from one another. For simplicity, we impose a periodic boundary condition in the $\mathbf{a}_3$ direction. The surface spectrum of a plane parallel to $\mathbf{a}_3$ will have two Dirac cones, centered on different time-reversal invariant momenta $\mathbf{k}_a$ and $\mathbf{k}_b$, such that $(\mathbf{k}_b - \mathbf{k}_a)\cdot\mathbf{a}_3 = (\mathbf{G}_\nu/2)\cdot\mathbf{a}_3 = \pi$. The second quantized kinetic Hamiltonian will be of the form $\Psi_a^\dagger(\mathbf{k}-\mathbf{k}_a)\cdot\boldsymbol{\sigma}\Psi_a + \Psi_b^\dagger(\mathbf{k}-\mathbf{k}_b)\cdot\boldsymbol{\sigma}\Psi_b$. $\Psi^\dagger$ and Ψ are the creation and annihilation operators satisfying the boundary condition $\Psi(\mathbf{r}+n\mathbf{a}_3) = \Psi(\mathbf{r})$. To cast this into the form of the effective Hamiltonian (8.1), we perform the gauge transformation $\Psi_\mu \to \Psi_\mu e^{i\mathbf{k}_\mu\cdot\mathbf{r}}$ for each of the fermion species. The gauge transformation will, in general, change the boundary condition for the operators Ψ_a and Ψ_b. Notice that $\exp[i(\mathbf{k}_a - \mathbf{k}_b)\cdot(n\mathbf{a}_3)] = (-1)^n$, and hence for odd n the transformed operators will have differing boundary conditions: *i.e.*, one periodic and one antiperiodic. The mass term coupling the fermion species together in the effective Hamiltonian must have antiperiodic boundary conditions and, hence, averages to zero. Therefore, for an odd number of stacked QSH layers, m is zero and the surface (parallel to the stacking direction) always flows to a metallic phase. These results settle the question of which of the two possible flow diagrams consistent with the quasi-1D numerics in Ref. [64] is actually realized.

8.3 Two-parameter scaling

The existence of one-parameter scaling along the line $m = 0$ suggests that there might be a two-parameter scaling collapse for the entire range of parameters when the mass is nonzero, analogous to the quantum Hall transition (in the A class) [245–247]. Figure 8.5

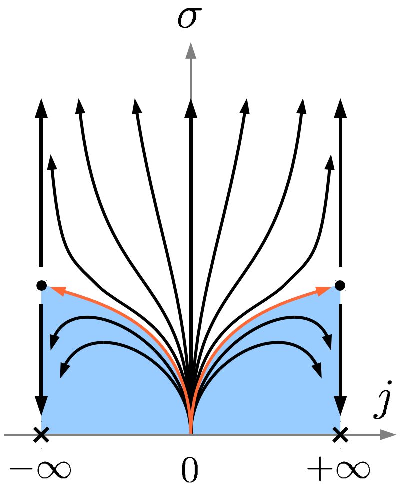

Figure 8.5: Two-parameter flow diagram in the symplectic class.

Two-parameter flow which captures the QSH-metal-insulator transition in the AII class. The scaling variables are σ and j, the latter of which separates the normal or QSH insulator phases.

shows a possible flow for conductivity σ and the (unknown) second scaling parameter j. The horizontal scale j distinguishes between the two topological phases, much in the same way as the Hall conductivity in the quantum Hall case.

Even without a precise definition of j as an experimental quantity, we may still infer a number of properties of the flow diagram.

1. For large conductivity σ, $\beta(\sigma)$ is positive and σ flows upward towards infinity.
2. There are two insulating stable fixed points (crosses) at $(\sigma, j) = (0, \pm\infty)$ and regions which flows toward them (shaded regions).
3. Consequently, there must be unstable fixed points (dots) at $j = \pm\infty$ which mark a metal-insulator transition.
4. Near $j = 0$, the system must flow to a metallic phase, as there should not be a direct phase transition between the two insulating phases.

Figure 8.5 gives the simplest flow diagram consistent with these requirements.

The two-parameter scaling of (σ, j) implies that $\sigma(L/\xi)$ cannot be collapsed onto a single scaling curve (as in Fig. 8.2), but onto a family of curves parametrized by a single variable x. The scaling form is

$$\sigma = f(L/\xi^*; x)\,, \tag{8.12}$$

where all the microscopic parameters m, μ, $g_{\alpha\beta}$, ξ, *etc.*, determine the conductivity only via the two functions x and ξ^*.

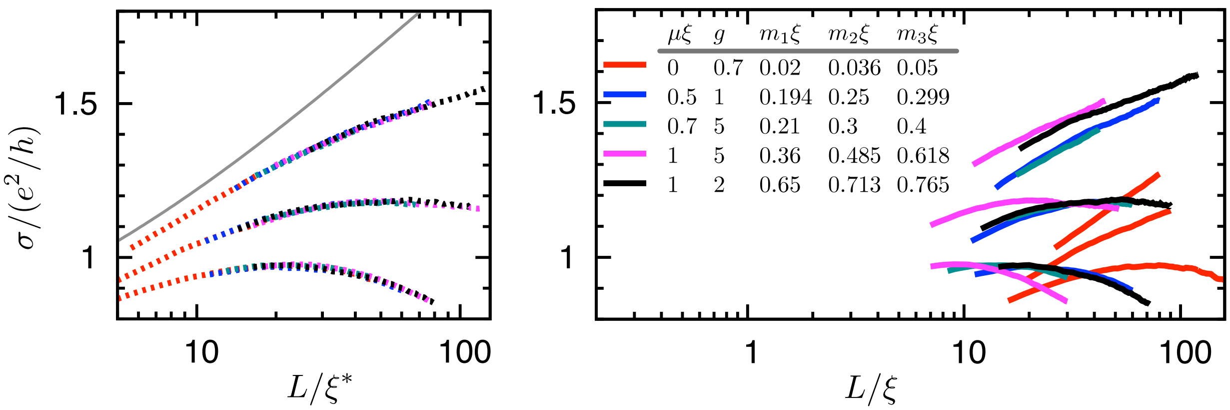

Figure 8.6: Two-parameter scaling data.

(Left) Numerical data $\sigma(L/\xi^*)$, demonstrating that the conductivity curves may be collapsed on to each other. The gray line is the data at $m = 0$ from Fig. 8.2 of the main text. (Right) Raw data $\sigma(L/\xi)$. For each data set (denoted by color), the parameters ξ, μ, $g_{\alpha\beta}$ are fixed. The black data set has $g_{x0} = g_{yz} = g$, while for other colors, $g_{\alpha\beta} = g$ for all $\alpha\beta$. Within each data set, m is varied until $\sigma(L/\xi^*)$ fit on top of one another. The numerical values are given as m_1, m_2, m_3. (Increasing m decreases the conductivity, hence the top curve of a data set has the smallest m.)

In Fig. 8.6, we present the accompanied data for our two-parameter scaling hypothesis, by collapsing σ vs. L/ξ^* onto a family of curves. For each curve, the parameters μ and $g_{\alpha\beta}$ were fixed while m is varied until $\sigma(L)$ overlaps with the existing set of curves. The data show reasonable agreement with the scaling form (8.12).

8.3.1 Possible realizations

Quantum transport at the surface of a weak topological insulator thus shows a scaling structure similar to that of the quantum Hall plateau transitions. It should be possible to interpret experiments on weak topological insulators in terms of the above Dirac model and possibly to control the parameter m by choosing a substrate whose lattice potential generates the massive perturbation.

In addition, the electronic structure of thin films of STIs can be mapped to the two Dirac cone system studied here, with the tunneling between the surfaces taking the role of the mass. The low-energy Hamiltonian for the thin film (with inversion symmetry) [137, 139] is

$$H_{\mathrm{STI}} = \begin{bmatrix} \hbar v_D \boldsymbol{\sigma} \times \mathbf{k} & \Delta \\ \Delta & -\hbar v_D \boldsymbol{\sigma} \times \mathbf{k} \end{bmatrix} + V(\mathbf{r})\,, \tag{8.13}$$

where $\boldsymbol{\sigma} \times \mathbf{k} = \sigma^x p_y - \sigma^y p_x$, and Δ is the tunneling amplitude between the two surfaces. The Hamiltonian is written in the basis $(\mathrm{t}\!\uparrow, \mathrm{t}\!\downarrow, \mathrm{b}\!\uparrow, \mathrm{b}\!\downarrow)$, where t and b represents the excitations for the top and bottom surfaces respectively.

The model for WTI may be mapped to H_{STI} via the transformation

$$H_{\mathrm{STI}} = UHU^{\dagger}\,, \qquad\qquad \text{where } U = \exp\left[i\tfrac{\pi}{4}\tau^{z}\sigma^{z}\right]. \tag{8.14}$$

(Again note that $U\Theta U^{\dagger} = \Theta = i\sigma^{y}\mathcal{K}$.) The mass corresponding to this system is $m = \langle V_{x0}\rangle = \Delta/\hbar v_{D}$, which is a measure of the tunneling amplitude between the surfaces. Consequently, the physics described in the main text may also be realized experimentally by a thin film of strong topological insulator, where the film's thickness can be used to tune m. (The mass m may oscillate between being positive and negative as the thickness is varied, as shown in Refs. [136, 137].)

The results here should motivate the search for WTI candidate materials, of which there are few, as well as further transport experiments in STI thin films. Finally, it remains to be seen if the two-parameter flow is generic to all non-interacting disordered systems in the symplectic class.

Acknowledgment

We gratefully acknowledge insightful discussions with Christopher Mudry, Shinsei Ryu, and Ashvin Vishwanath. This work is supported by FENA (RM), DOE BES (JHB), and NSF DMR-0804413 (JEM).

Bibliography

[1] Joel E. Moore and Leon Balents, “Topological invariants of time-reversal-invariant band structures,” Phys. Rev. B **75**, 121306(R) (2007).

[2] Charles L. Kane and Eugene J. Mele, “Quantum Spin Hall Effect in Graphene,” Phys. Rev. Lett. **95**, 226801 (2005).

[3] Charles L. Kane and Eugene J. Mele, “$\mathbb{Z}_2$ Topological Order and the Quantum Spin Hall Effect,” Phys. Rev. Lett. **95**, 146802 (2005).

[4] Liang Fu, Charles L. Kane, and Eugene J. Mele, “Topological Insulators in Three Dimensions,” Phys. Rev. Lett. **98**, 106803 (2007).

[5] Rahul Roy, “Topological phases and the quantum spin Hall effect in three dimensions,” Phys. Rev. B **79**, 195322 (2009).

[6] Markus König, Steffen Wiedmann, Christoph Brüne, Andreas Roth, Hartmut Buhmann, Laurens W. Molenkamp, Xiao-Liang Qi, and Shou-Cheng Zhang, “Quantum Spin Hall Insulator State in HgTe Quantum Wells,” Science **318**, 766–770 (2007).

[7] D. Hsieh, D. Qian, L. Wray, Y. Xia, Y. S. Hor, R. J. Cava, and M. Z. Hasan, “A topological Dirac insulator in a quantum spin Hall phase,” Nature **452**, 970–974 (2008).

[8] Y. Xia, D. Qian, D. Hsieh, L. Wray, A. Pal, H. Lin, A. Bansil, D. Grauer, Y. S. Hor, R. J. Cava, and M. Z. Hasan, “Observation of a large-gap topological-insulator class with a single Dirac cone on the surface,” Nature Physics **5**, 398–402 (2009).

[9] Y. L. Chen, J. G. Analytis, J. H. Chu, Z. K. Liu, S. K. Mo, X. L. Qi, H. J. Zhang, D. H. Lu, X. Dai, Z. Fang, S.-C. Zhang, I. R. Fisher, Z. Hussain, and Z.-X. Shen, “Experimental Realization of a Three-Dimensional Topological Insulator, Bi_2Te_3,” Science **325**, 178–181 (2009).

[10] Philip W. Anderson, “Absence of Diffusion in Certain Random Lattices,” Phys. Rev. **109**, 1492–1505 (1958).

[11] E. Abrahams, P. W. Anderson, D. C. Licciardello, and T. V. Ramakrishnan, “Scaling theory of localization: Absence of quantum diffusion in two dimensions,” Phys. Rev. Lett. **42**, 673–676 (1979).

[12] Patrick A. Lee and T. V. Ramakrishnan, “Disordered electronic systems,” Rev. Mod. Phys. **57**, 287–337 (1985).

[13] Klaus von Klitzing, G. Dorda, and M. Pepper, “New Method for High-Accuracy Determination of the Fine-Structure Constant Based on Quantized Hall Resistance,” Phys. Rev. Lett. **45**, 494–497 (1980).

[14] D. J. Thouless, M. Kohmoto, M. P. Nightingale, and M. den Nijs, “Quantized Hall Conductance in a Two-Dimensional Periodic Potential,” Phys. Rev. Lett. **49**, 405–408 (1982).

[15] Barry Simon, “Holonomy, the Quantum Adiabatic Theorem, and Berry’s Phase,” Phys. Rev. Lett. **51**, 2167–2170 (1983).

[16] Xiao-Gang Wen, “Topological orders and edge excitations in fractional quantum Hall states,” Adv. Phys. **44**, 405–473 (1995).

[17] L. D. Landau, “On The Theory of Phase Transitions I,” Phys. Z. Sowj. Un. **11**, 26–47 (1937).

[18] L. D. Landau, “On The Theory of Phase Transitions II,” Phys. Z. Sowj. Un. **11**, 545–555 (1937).

[19] Liang Fu and Charles L. Kane, “Time reversal polarization and a $\mathbb{Z}_2$ adiabatic spin pump,” Phys. Rev. B **74**, 195312 (2006).

[20] B. I. Halperin, “Quantized Hall conductance, current-carrying edge states, and the existence of extended states in a two-dimensional disordered potential,” Phys. Rev. B **25**, 2185–2190 (1982).

[21] M. Zahid Hasan and Charles L. Kane, “Colloquium: Topological insulators,” Rev. Mod. Phys. **82**, 3045–3067 (2010).

[22] Joel E. Moore, “Topological insulators: The next generation,” Nature Physics **5**, 378–380 (2009).

[23] Joel E. Moore, “The birth of topological insulators,” Nature **464**, 194–198 (2010).

[24] Xiao-Liang Qi and Shou-Cheng Zhang, “The quantum spin Hall effect and topological insulators,” Physics Today **63**, 33–38 (2010).

[25] Xiao-Liang Qi and Shou-Cheng Zhang, “Topological insulators and superconductors,” Rev. Mod. Phys. **83**, 1057–1110 (2011).

[26] M. Zahid Hasan and Joel E. Moore, “Three-Dimensional Topological Insulators,” Ann. Rev. Cond. Mat. Phys. **2**, 55–78 (2011).

[27] Charles Kittel, *Introduction to Solid State Physics*, 8th ed. (Wiley, John & Sons, Incorporated, 2004).

[28] Klaus von Klitzing, “Developments in the quantum Hall effect,” Phil. Trans. R. Soc. A **363**, 2203–2219 (2005).

[29] J. E. Avron, R. Seiler, and B. Simon, “Homotopy and Quantization in Condensed Matter Physics,” Phys. Rev. Lett. **51**, 51–53 (1983).

[30] Felix Bloch, “Über die Quantenmechanik der Elektronen in Kristallgittern,” Z. Physik **52**, 555–600 (1929).

[31] Shivaramakrishnan Pancharatnam, “Generalized theory of interference, and its applications. Part I. Coherent pencils,” Proc. Ind. Acad. Sci. A **44**, 247–262 (1956), reprinted in *Collected works of S. Pancharatnam* (Oxford University Press, 1975).

[32] Michael V. Berry, “Quantal phase-factors accompanying adiabatic changes,” Proc. Roy. Soc. Lond. A **392**, 45–57 (1984).

[33] Ganesh Sundaram and Qian Niu, “Wave-packet dynamics in slowly perturbed crystals: Gradient corrections and Berry-phase effects,” Phys. Rev. B **59**, 14915–14925 (1999).

[34] Paul A. M. Dirac, “Quantised Singularities in the Electromagnetic Field,” Proc. Roy. Soc. Lond. A **133**, 60–72 (1931).

[35] Qian Niu, D. J. Thouless, and Yong-Shi Wu, “Quantized Hall conductance as a topological invariant,” Phys. Rev. B **31**, 3372–3377 (1985).

[36] R. B. Laughlin, “Quantized Hall conductivity in two dimensions,” Phys. Rev. B **23**, 5632–5633 (1981).

[37] Xiao-Liang Qi, Yong-Shi Wu, and Shou-Cheng Zhang, “General theorem relating the bulk topological number to edge states in two-dimensional insulators,” Phys. Rev. B **74**, 045125 (2006).

[38] Yasuhiro Hatsugai, “Edge states in the integer quantum Hall effect and the Riemann surface of the Bloch function,” Phys. Rev. B **48**, 11851–11862 (1993).

[39] Yasuhiro Hatsugai, “Chern number and edge states in the integer quantum Hall effect,” Phys. Rev. Lett. **71**, 3697–3700 (1993).

[40] Roger S. K. Mong and Vasudha Shivamoggi, “Edge states and the bulk-boundary correspondence in Dirac Hamiltonians,” Phys. Rev. B **83**, 125109 (2011).

[41] Lukasz Fidkowski, T. S. Jackson, and Israel Klich, "Model Characterization of Gapless Edge Modes of Topological Insulators Using Intermediate Brillouin-Zone Functions," Phys. Rev. Lett. **107**, 036601 (2011).

[42] F. Duncan M. Haldane, "Model for a Quantum Hall Effect without Landau Levels: Condensed-Matter Realization of the "Parity Anomaly"," Phys. Rev. Lett. **61**, 2015–2018 (1988).

[43] Liang Fu and Charles L. Kane, "Topological insulators with inversion symmetry," Phys. Rev. B **76**, 045302 (2007).

[44] Tsuneya Ando and Hidekatsu Suzuura, "Presence of Perfectly Conducting Channel in Metallic Carbon Nanotubes," J. Phys. Soc. Japan **71**, 2753–2760 (2002).

[45] Cenke Xu and Joel E. Moore, "Stability of the quantum spin Hall effect: Effects of interactions, disorder, and $\mathbb{Z}_2$ topology," Phys. Rev. B **73**, 045322 (2006).

[46] Jens H. Bardarson, "A proof of the Kramers degeneracy of transmission eigenvalues from antisymmetry of the scattering matrix," J. Phys. A: Math. Theor. **41**, 405203 (2008).

[47] B. Andrei Bernevig, Taylor L. Hughes, and Shou-Cheng Zhang, "Quantum Spin Hall Effect and Topological Phase Transition in HgTe Quantum Wells," Science **314**, 1757–1761 (2006).

[48] Markus König, Hartmut Buhmann, Laurens W. Molenkamp, Taylor Hughes, Chao-Xing Liu, Xiao-Liang Qi, and Shou-Cheng Zhang, "The Quantum Spin Hall Effect: Theory and Experiment," J. Phys. Soc. Japan **77**, 031007 (2008).

[49] Shinsei Ryu, Christopher Mudry, Hideaki Obuse, and Akira Furusaki, "$\mathbb{Z}_2$ Topological Term, the Global Anomaly, and the Two-Dimensional Symplectic Symmetry Class of Anderson Localization," Phys. Rev. Lett. **99**, 116601 (2007).

[50] J. H. Bardarson, J. Tworzydło, P. W. Brouwer, and C. W. J. Beenakker, "One-Parameter Scaling at the Dirac Point in Graphene," Phys. Rev. Lett. **99**, 106801 (2007).

[51] Kentaro Nomura, Mikito Koshino, and Shinsei Ryu, "Topological Delocalization of Two-Dimensional Massless Dirac Fermions," Phys. Rev. Lett. **99**, 146806 (2007).

[52] Pedram Roushan, Jungpil Seo, Colin V. Parker, Y. S. Hor, D. Hsieh, Dong Qian, Anthony Richardella, M. Z. Hasan, R. J. Cava, and Ali Yazdani, "Topological surface states protected from backscattering by chiral spin texture," Nature **460**, 1106–1109 (2009).

[53] S. R. Park, W. S. Jung, Chul Kim, D. J. Song, C. Kim, S. Kimura, K. D. Lee, and N. Hur, "Quasiparticle scattering and the protected nature of the topological states in a parent topological insulator Bi_2Se_3," Phys. Rev. B **81**, 041405(R) (2010).

[54] D. Hsieh, Y. Xia, L. Wray, D. Qian, A. Pal, J. H. Dil, J. Osterwalder, F. Meier, G. Bihlmayer, C. L. Kane, Y. S. Hor, R. J. Cava, and M. Z. Hasan, "Observation of Unconventional Quantum Spin Textures in Topological Insulators," Science **323**, 919–922 (2009).

[55] D. Hsieh, Y. Xia, D. Qian, L. Wray, J. H. Dil, F. Meier, J. Osterwalder, L. Patthey, J. G. Checkelsky, N. P. Ong, A. V. Fedorov, H. Lin, A. Bansil, D. Grauer, Y. S. Hor, R. J. Cava, and M. Z. Hasan, "A tunable topological insulator in the spin helical Dirac transport regime," Nature **460**, 1101–1105 (2009).

[56] Su-Yang Xu, L. A. Wray, Y. Xia, R. Shankar, S. Jia, A. Fedorov, J. H. Dil, F. Meier, B. Slomski, J. Osterwalder, R. J. Cava, and M. Z. Hasan, "Observation of Topological Order in the $TlBiSe_2$ class : Probing the "spin" and "phase" on topological insulator surfaces," (2010), unpublished, arXiv:1008.3557 .

[57] Haijun Zhang, Chao-Xing Liu, Xiao-Liang Qi, Xi Dai, Zhong Fang, and Shou-Cheng Zhang, "Topological insulators in Bi_2Se_3, Bi_2Te_3 and Sb_2Te_3 with a single Dirac cone on the surface," Nature Physics **5**, 438–442 (2009).

[58] D. Hsieh, Y. Xia, D. Qian, L. Wray, F. Meier, J. H. Dil, J. Osterwalder, L. Patthey, A. V. Fedorov, H. Lin, A. Bansil, D. Grauer, Y. S. Hor, R. J. Cava, and M. Z. Hasan, "Observation of Time-Reversal-Protected Single-Dirac-Cone Topological-Insulator States in Bi_2Te_3 and Sb_2Te_3," Phys. Rev. Lett. **103**, 146401 (2009).

[59] S. Urazhdin, D. Bilc, S. D. Mahanti, S. H. Tessmer, Theodora Kyratsi, and M. G. Kanatzidis, "Surface effects in layered semiconductors Bi_2Se_3 and Bi_2Te_3," Phys. Rev. B **69**, 085313 (2004).

[60] Xiao-Liang Qi, Taylor L. Hughes, and Shou-Cheng Zhang, "Topological field theory of time-reversal invariant insulators," Phys. Rev. B **78**, 195424 (2008).

[61] Andrew M. Essin, Joel E. Moore, and David Vanderbilt, "Magnetoelectric Polarizability and Axion Electrodynamics in Crystalline Insulators," Phys. Rev. Lett. **102**, 146805 (2009), [erratum at Phys. Rev. Lett. **103**, 259902(E)].

[62] Ying Ran, Yi Zhang, and Ashvin Vishwanath, "One-dimensional topologically protected modes in topological insulators with lattice dislocations," Nature Physics **5**, 298–303 (2009).

[63] Ken-Ichiro Imura, Yositake Takane, and Akihiro Tanaka, "Weak topological insulator with protected gapless helical states," Phys. Rev. B **84**, 035443 (2011).

[64] Zohar Ringel, Yaacov E. Kraus, and Ady Stern, “The strong side of weak topological insulators,” (2011), unpublished, arXiv:1105.4351 .

[65] Roger S. K. Mong, Jens H. Bardarson, and Joel E. Moore, “Quantum Transport and Two-Parameter Scaling at the Surface of a Weak Topological Insulator,” Phys. Rev. Lett. **108**, 076804 (2012).

[66] Atsuo Shitade, Hosho Katsura, Jan Kuneš, Xiao-Liang Qi, Shou-Cheng Zhang, and Naoto Nagaosa, “Quantum Spin Hall Effect in a Transition Metal Oxide Na_2IrO_3,” Phys. Rev. Lett. **102**, 256403 (2009).

[67] Yogesh Singh and P. Gegenwart, “Antiferromagnetic Mott insulating state in single crystals of the hexagonal lattice material Na_2IrO_3,” (2010), unpublished, arXiv:1006.0437 .

[68] S. K. Choi, R. Coldea, A. N. Kolmogorov, T. Lancaster, I. I. Mazin, S. J. Blundell, P. G. Radaelli, Yogesh Singh, P. Gegenwart, K. R. Choi, S.-W. Cheong, P. J. Baker, C. Stock, and J. Taylor, “Spin Waves and Revised Crystal Structure of Honeycomb Iridate Na_2IrO_3,” Phys. Rev. Lett. **108**, 127204 (2012).

[69] H. A. Kramers, “Théorie générale de la rotation paramagnétique dans les cristaux,” Proc. Amst. Acad. **33**, 959–972 (1930), available online.

[70] Shinobu Hikami, Anatoly I. Larkin, and Yosuke Nagaoka, “Spin-Orbit Interaction and Magnetoresistance in the Two Dimensional Random System,” Prog. Theor. Phys. **63**, 707–710 (1980).

[71] Gerd Bergman, “Influence of Spin-Orbit Coupling on Weak Localization,” Phys. Rev. Lett. **48**, 1046–1049 (1982).

[72] L. P. Gor’kov, A. I. Larkin, and D. E. Khmel’nitskiĭ, “Particle conductivity in a two-dimensional random potential,” Pis’ma v Zh. Eksp. Teor. Fiz. **30**, 248–252 (1970), [Eng. transl. JETP Lett., **30**, 228–232 (1979)].

[73] P. W. Anderson, E. Abrahams, and T. V. Ramakrishnan, “Possible Explanation of Nonlinear Conductivity in Thin-Film Metal Wires,” Phys. Rev. Lett. **43**, 718–720 (1979).

[74] J. R. Schrieffer, *Theory of Superconductivity*, 1st ed. (W. A. Benjamin, Inc., New York, 1964).

[75] Pierre-Gilles de Gennes, *Superconductivity of metals and alloys* (Addison-Wesley, 1989).

[76] Alexander Altland and Martin R. Zirnbauer, “Nonstandard symmetry classes in mesoscopic normal-superconducting hybrid structures,” Phys. Rev. B **55**, 1142–1161 (1997).

[77] Andreas P. Schnyder, Shinsei Ryu, Akira Furusaki, and Andreas W. W. Ludwig, "Classification of topological insulators and superconductors in three spatial dimensions," Phys. Rev. B **78**, 195125 (2008).

[78] Alexei Kitaev, "Periodic table for topological insulators and superconductors," AIP Conference Proceedings **1134**, 22–30 (2009).

[79] N. Read and Dmitry Green, "Paired states of fermions in two dimensions with breaking of parity and time-reversal symmetries and the fractional quantum Hall effect," Phys. Rev. B **61**, 10267–10297 (2000).

[80] Ettore Majorana, "Teoria simmetrica dell'elettrone e del positrone," Nuovo Cimento **14**, 171–184 (1937), [Eng. transl. Soryushiron Kenkyu **63**(3), 149 (1981)].

[81] Frank Wilczek, "Majorana returns," Nature Physics **5**, 614–618 (2009).

[82] Gregory Moore and Nicholas Read, "Nonabelions in the fractional quantum Hall effect," Nucl. Phys. B **360**, 362–396 (1991).

[83] Chetan Nayak and Frank Wilczek, "$2n$-quasihole states realize 2^{n-1}-dimensional spinor braiding statistics in paired quantum Hall states," Nucl. Phys. B **479**, 529–553 (1996).

[84] Dmitri A. Ivanov, "Non-Abelian Statistics of Half-Quantum Vortices in p-Wave Superconductors," Phys. Rev. Lett. **86**, 268–271 (2001).

[85] Alexei Yu Kitaev, "Fault-tolerant quantum computation by anyons," Ann. Phys. (NY) **303**, 2–30 (2003).

[86] Chetan Nayak, Steven H. Simon, Ady Stern, Michael Freedman, and Sankar Das Sarma, "Non-Abelian anyons and topological quantum computation," Rev. Mod. Phys. **80**, 1083–1159 (2008).

[87] Andrew Peter Mackenzie and Yoshiteru Maeno, "The superconductivity of Sr_2RuO_4 and the physics of spin-triplet pairing," Rev. Mod. Phys. **75**, 657–712 (2003).

[88] V. Mourik, K. Zuo, S. M. Frolov, S. R. Plissard, E. P. A. M. Bakkers, and L. P. Kouwenhoven, "Signatures of Majorana Fermions in Hybrid Superconductor-Semiconductor Nanowire Devices," Science **Express** (2012), 10.1126/science.1222360.

[89] Alexei Yu Kitaev, "Unpaired Majorana fermions in quantum wires," Sov. Phys.–Uspeki **44**, 131 (2001).

[90] Jason Alicea, "Majorana fermions in a tunable semiconductor device," Phys. Rev. B **81**, 125318 (2010).

[91] Roman M. Lutchyn, Jay D. Sau, and S. Das Sarma, "Majorana Fermions and a Topological Phase Transition in Semiconductor-Superconductor Heterostructures," Phys. Rev. Lett. **105**, 077001 (2010).

[92] Yuval Oreg, Gil Refael, and Felix von Oppen, "Helical Liquids and Majorana Bound States in Quantum Wires," Phys. Rev. Lett. **105**, 177002 (2010).

[93] Liang Fu and Erez Berg, "Odd-Parity Topological Superconductors: Theory and Application to $\mathrm{Cu}_x\mathrm{Bi}_2\mathrm{Se}_3$," Phys. Rev. Lett. **105**, 097001 (2010).

[94] L. Andrew Wray, Su-Yang Xu, Yuqi Xia, Yew San Hor, Dong Qian, Alexei V. Fedorov, Hsin Lin, Arun Bansil, Robert J. Cava, and M. Zahid Hasan, "Observation of topological order in a superconducting doped topological insulator," Nature Physics **6**, 855–859 (2010).

[95] Pradip Das, Yusuke Suzuki, Masashi Tachiki, and Kazuo Kadowaki, "Spin-triplet vortex state in the topological superconductor $\mathrm{Cu}_x\mathrm{Bi}_2\mathrm{Se}_3$," Phys. Rev. B **83**, 220513(R) (2011).

[96] Satoshi Sasaki, M. Kriener, Kouji Segawa, Keiji Yada, Yukio Tanaka, Masatoshi Sato, and Yoichi Ando, "Topological Superconductivity in $\mathrm{Cu}_x\mathrm{Bi}_2\mathrm{Se}_3$," Phys. Rev. Lett. **107**, 217001 (2011).

[97] Grigory E. Volovik, *The Universe in a Helium Droplet* (Oxford University Press, 2003).

[98] Binghai Yan, Chao-Xing Liu, Hai-Jun Zhang, Chi-Yung Yam, Xiao-Liang Qi, Thomas Frauenheim, and Shou-Cheng Zhang, "Theoretical prediction of topological insulators in thallium-based III-V-VI_2 ternary chalcogenides," Europhys. Lett. **90**, 37002 (2010).

[99] Hsin Lin, R. S. Markiewicz, L. A. Wray, L. Fu, M. Z. Hasan, and A. Bansil, "Single-Dirac-Cone Topological Surface States in the TlBiSe_2 Class of Topological Semiconductors," Phys. Rev. Lett. **105**, 036404 (2010).

[100] S. Eremeev, Yu. Koroteev, and E. Chulkov, "Ternary thallium-based semimetal chalcogenides Tl-V-VI_2 as a new class of three-dimensional topological insulators," JETP Lett. **91**, 594–598 (2010).

[101] Takafumi Sato, Kouji Segawa, Hua Guo, Katsuaki Sugawara, Seigo Souma, Takashi Takahashi, and Yoichi Ando, "Direct Evidence for the Dirac-Cone Topological Surface States in the Ternary Chalcogenide TlBiSe_2," Phys. Rev. Lett. **105**, 136802 (2010).

[102] Yu Lin Chen, Zhong Kai Liu, James G. Analytis, Jiun-Haw Chu, Hai Jun Zhang, Bing Hai Yan, Sung-Kwan Mo, Robert G. Moore, Dong Hui Lu, Ian R. Fisher, Shou-Cheng Zhang, Zahid Hussain, and Z.-X. Shen, "Single Dirac Cone Topological Surface State and Unusual Thermoelectric Property of Compounds from a New Topological Insulator Family," Phys. Rev. Lett. **105**, 266401 (2010).

[103] Hsin Lin, R. S. Markiewicz, L. A. Wray, L. Fu, M. Z. Hasan, and A. Bansil, "Single-Dirac-Cone Topological Surface States in the $TlBiSe_2$ Class of Topological Semiconductors," Phys. Rev. Lett. **105**, 036404 (2010).

[104] K. Kuroda, M. Ye, A. Kimura, S. V. Eremeev, E. E. Krasovskii, E. V. Chulkov, Y. Ueda, K. Miyamoto, T. Okuda, K. Shimada, H. Namatame, and M. Taniguchi, "Experimental Realization of a Three-Dimensional Topological Insulator Phase in Ternary Chalcogenide $TlBiSe_2$," Phys. Rev. Lett. **105**, 146801 (2010).

[105] Stanislav Chadov, Xiao-Liang Qi, Jürgen Kübler, Gerhald H. Fecher, Claudia Felser, and Shou-Cheng Zhang, "Tunable Multifunctional Topological Insulators in Ternary Heusler Compounds," Nature Materials **9**, 541–545 (2010).

[106] Hsin Lin, L. Andrew Wray, Yuqi Xia, Suyang Xu, Shuang Jia, Robert J. Cava, Arun Bansil, and M. Zahid Hasan, "Half-Heusler ternary compounds as new multifunctional experimental platforms for topological quantum phenomena," Nature Materials **9**, 546–549 (2010).

[107] Di Xiao, Yugui Yao, Wanxiang Feng, Jun Wen, Wenguang Zhu, Xing-Qiu Chen, G. Malcolm Stocks, and Zhenyu Zhang, "Half-Heusler Compounds as a New Class of Three-Dimensional Topological Insulators," Phys. Rev. Lett. **105**, 096404 (2010).

[108] W. Al-Sawai, Hsin Lin, R. S. Markiewicz, L. A. Wray, Y. Xia, S.-Y. Xu, M. Z. Hasan, and A. Bansil, "Topological electronic structure in half-heusler topological insulators," Phys. Rev. B **82**, 125208 (2010).

[109] H. Lin, L. A. Wray, Y. Xia, S.-Y. Xu, S. Jia, R. J. Cava, A. Bansil, and M. Z. Hasan, "Single-Dirac-cone $\mathbb{Z}_2$ topological insulator phases in distorted Li_2AgSb-class and related quantum critical Li-based spin-orbit compounds," (2010), unpublished, arXiv:1004.0999 .

[110] Mattias Klintenberg, "The search for strong topological insulators," (2010), unpublished, arXiv:1007.4838 .

[111] Su-Yang Xu, L. A. Wray, Y. Xia, R. Shankar, A. Petersen, A. Fedorov, H. Lin, A. Bansil, Y. S. Hor, D. Grauer, R. J. Cava, and M. Z. Hasan, "Discovery of several large families of Topological Insulator classes with backscattering-suppressed spin-polarized single-Dirac-cone on the surface," (2010), unpublished, arXiv:1007.5111 .

[112] Binghai Yan, Hai-Jun Zhang, Chao-Xing Liu, Xiao-Liang Qi, Thomas Frauenheim, and Shou-Cheng Zhang, "Theoretical prediction of topological insulator in ternary rare earth chalcogenides," Phys. Rev. B **82**, 161108(R) (2010).

[113] Zhi Ren, A. A. Taskin, Satoshi Sasaki, Kouji Segawa, and Yoichi Ando, "Large bulk resistivity and surface quantum oscillations in the topological insulator Bi_2Te_2Se," Phys. Rev. B **82**, 241306(R) (2010).

[114] Lin-Lin Wang and Duane D. Johnson, "Ternary tetradymite compounds as topological insulators," Phys. Rev. B **83**, 241309 (2011).

[115] Tong Zhang, Peng Cheng, Xi Chen, Jin-Feng Jia, Xucun Ma, Ke He, Lili Wang, Haijun Zhang, Xi Dai, Zhong Fang, Xincheng Xie, and Qi-Kun Xue, "Experimental Demonstration of Topological Surface States Protected by Time-Reversal Symmetry," Phys. Rev. Lett. **103**, 266803 (2009).

[116] T. Hanaguri, K. Igarashi, M. Kawamura, H. Takagi, and T. Sasagawa, "Momentum-resolved Landau-level spectroscopy of Dirac surface state in Bi_2Se_3," Phys. Rev. B **82**, 081305(R) (2010).

[117] Peng Cheng, Canli Song, Tong Zhang, Yanyi Zhang, Yilin Wang, Jin-Feng Jia, Jing Wang, Yayu Wang, Bang-Fen Zhu, Xi Chen, Xucun Ma, Ke He, Lili Wang, Xi Dai, Zhong Fang, Xincheng Xie, Xiao-Liang Qi, Chao-Xing Liu, Shou-Cheng Zhang, and Qi-Kun Xue, "Landau Quantization of Topological Surface States in Bi_2Se_3," Phys. Rev. Lett. **105**, 076801 (2010).

[118] Hailin Peng, Keji Lai, Desheng Kong, Stefan Meister, Yulin Chen, Xiao-Liang Qi, Shou-Cheng Zhang, Zhi-Xun Shen, and Yi Cui, "Aharonov-Bohm interference in topological insulator nanoribbons," Nature Materials **9**, 225–229 (2010).

[119] A. A. Taskin and Yoichi Ando, "Quantum oscillations in a topological insulator $Bi_{1-x}Sb_x$," Phys. Rev. B **80**, 085303 (2009).

[120] James G. Analytis, Jiun-Haw Chu, Yulin Chen, Felipe Corredor, Ross D. McDonald, Z. X. Shen, and Ian R. Fisher, "Bulk Fermi surface coexistence with Dirac surface state in Bi_2Se_3: A comparison of photoemission and Shubnikov–de Haas measurements," Phys. Rev. B **81**, 205407 (2010).

[121] James G. Analytis, Ross D. McDonald, Scott C. Riggs, Jiun-Haw Chu, G. S. Boebinger, and Ian R. Fisher, "Two-dimensional surface state in the quantum limit of a topological insulator," Nature Physics **6**, 960–964 (2010).

[122] Dong-Xia Qu, Y. S. Hor, Jun Xiong, R. J. Cava, and N. P. Ong, "Quantum Oscillations and Hall Anomaly of Surface States in the Topological Insulator Bi_2Te_3," Science **329**, 821–824 (2010).

[123] Benjamin Sacépé, Jeroen B. Oostinga, Jian Li, Alberto Ubaldini, Nuno J.G. Couto, Enrico Giannini, and Alberto F. Morpurgo, "Gate-tuned normal and superconducting transport at the surface of a topological insulator," Nat. Commun. **2**, 575 (2011).

[124] Y. S. Hor, A. Richardella, P. Roushan, Y. Xia, J. G. Checkelsky, A. Yazdani, M. Z. Hasan, N. P. Ong, and R. J. Cava, "p-type Bi_2Se_3 for topological insulator and low-temperature thermoelectric applications," Phys. Rev. B **79**, 195208 (2009).

[125] Y. S. Hor, J. G. Checkelsky, N. P. Ong D. Qu, and R. J. Cava, "Superconductivity and non-metallicity induced by doping the topological insulators Bi_2Se_3 and Bi_2Te_3," (2010), unpublished, arXiv:1006.0317 .

[126] Dimitrie Culcer, "Transport in three-dimensional topological insulators: Theory and experiment," Physica E **44**, 860–864 (2012).

[127] Desheng Kong, Jason C. Randel, Hailin Peng, Judy J. Cha, Stefan Meister, Keji Lai, Yulin Chen, Zhi-Xun Shen, Hari C. Manoharan, and Yi Cui, "Topological Insulator Nanowires and Nanoribbons," Nano Lett. **10**, 329–333 (2010).

[128] Judy J. Cha, James R. Williams, Desheng Kong, Stefan Meister, Hailin Peng, Andrew J. Bestwick, Patrick Gallagher, David Goldhaber-Gordon, and Yi Cui, "Magnetic Doping and Kondo Effect in Bi_2Se_3 Nanoribbons," Nano Lett. **10**, 1076–1081 (2010).

[129] Guanhua Zhang, Huajun Qin, Jing Teng, Jiandong Guo, Qinlin Guo, Xi Dai, Zhong Fang, and Kehui Wu, "Quintuple-layer epitaxy of thin films of topological insulator Bi_2Se_3," Appl. Phys. Lett. **95**, 053114 (2009).

[130] Yi Zhang, Ke He, Cui-Zu Chang, Can-Li Song, Li-Li Wang, Xi Chen, Jin-Feng Jia, Zhong Fang, Xi Dai, Wen-Yu Shan, Shun-Qing Shen, Qian Niu, Xiao-Liang Qi, Shou-Cheng Zhang, Xu-Cun Ma, and Qi-Kun Xue, "Crossover of the three-dimensional topological insulator Bi_2Se_3 to the two-dimensional limit," Nature Physics **6**, 584–588 (2010).

[131] Yao-Yi Li, Guang Wang, Xie-Gang Zhu, Min-Hao Liu, Cun Ye, Xi Chen, Ya-Yu Wang, Ke He, Li-Li Wang, Xu-Cun Ma, Hai-Jun Zhang, Xi Dai, Zhong Fang, Xin-Cheng Xie, Ying Liu, Xiao-Liang Qi, Jin-Feng Jia, Shou-Cheng Zhang, and Qi-Kun Xue, "Intrinsic Topological Insulator Bi_2Te_3 Thin Films on Si and Their Thickness Limit," Adv. Mater. **22**, 4002–4007 (2010).

[132] J. Chen, H. J. Qin, F. Yang, J. Liu, T. Guan, F. M. Qu, G. H. Zhang, J. R. Shi, X. C. Xie, C. L. Yang, K. H. Wu, Y. Q. Li, and L. Lu, "Gate-Voltage Control of Chemical Potential and Weak Antilocalization in Bi_2Se_3," Phys. Rev. Lett. **105**, 176602 (2010).

[133] Minhao Liu, Cui-Zu Chang, Zuocheng Zhang, Yi Zhang, Wei Ruan, Ke He, Li-li Wang, Xi Chen, Jin-Feng Jia, Shou-Cheng Zhang, Qi-Kun Xue, Xucun Ma, and Yayu Wang, "Electron interaction-driven insulating ground state in Bi_2Se_3 topological insulators in the two-dimensional limit," Phys. Rev. B **83**, 165440 (2011).

[134] Jian Wang, Ashley M. DaSilva, Cui-Zu Chang, Ke He, J. K. Jain, Nitin Samarth, Xu-Cun Ma, Qi-Kun Xue, and Moses H. W. Chan, "Evidence for electron-electron interaction in topological insulator thin films," Phys. Rev. B **83**, 245438 (2011).

[135] Jacob Linder, Takehito Yokoyama, and Asle Sudbø, “Anomalous finite size effects on surface states in the topological insulator Bi_2Se_3,” Phys. Rev. B **80**, 205401 (2009).

[136] Hai-Zhou Lu, Wen-Yu Shan, Wang Yao, Qian Niu, and Shun-Qing Shen, “Massive Dirac fermions and spin physics in an ultrathin film of topological insulator,” Phys. Rev. B **81**, 115407 (2010).

[137] Chao-Xing Liu, HaiJun Zhang, Binghai Yan, Xiao-Liang Qi, Thomas Frauenheim, Xi Dai, Zhong Fang, and Shou-Cheng Zhang, “Oscillatory crossover from two-dimensional to three-dimensional topological insulators,” Phys. Rev. B **81**, 041307(R) (2010).

[138] Ryuji Takahashi and Shuichi Murakami, “Thermoelectric transport in perfectly conducting channels in quantum spin Hall systems,” Phys. Rev. B **81**, 161302(R) (2010).

[139] Pouyan Ghaemi, Roger S. K. Mong, and Joel E. Moore, “In-Plane Transport and Enhanced Thermoelectric Performance in Thin Films of the Topological Insulators Bi_2Te_3 and Bi_2Se_3,” Phys. Rev. Lett. **105**, 166603 (2010).

[140] O. A. Tretiakov, Ar. Abanov, Shuichi Murakami, and Jairo Sinova, “Large thermoelectric figure of merit for three-dimensional topological Anderson insulators via line dislocation engineering,” Appl. Phys. Lett. **97**, 073108 (2010).

[141] Vivek Goyal, Desalegne Teweldebrhan, and Alexander A. Balandin, “Mechanically-exfoliated stacks of thin films of Bi_2Te_3 topological insulators with enhanced thermoelectric performance,” Appl. Phys. Lett. **97**, 133117 (2010).

[142] Ferdows Zahid and Roger Lake, “Thermoelectric properties of Bi_2Te_3 atomic quintuple thin films,” Appl. Phys. Lett. **97**, 212102 (2010).

[143] O. A. Tretiakov, Ar. Abanov, and Jairo Sinova, “Holey topological thermoelectrics,” Appl. Phys. Lett. **99**, 113110 (2011).

[144] Liang Fu and Charles L. Kane, “Superconducting Proximity Effect and Majorana Fermions at the Surface of a Topological Insulator,” Phys. Rev. Lett. **100**, 096407 (2008).

[145] Liang Fu and C. L. Kane, “Josephson current and noise at a superconductor/quantum-spin-Hall-insulator/superconductor junction,” Phys. Rev. B **79**, 161408(R) (2009).

[146] Johan Nilsson, A. R. Akhmerov, and C. W. J. Beenakker, “Splitting of a Cooper Pair by a Pair of Majorana Bound States,” Phys. Rev. Lett. **101**, 120403 (2008).

[147] A. Cook and M. Franz, “Majorana fermions in a topological-insulator nanowire proximity-coupled to an s-wave superconductor,” Phys. Rev. B **84**, 201105(R) (2011).

[148] C. W. J. Beenakker, "Search for Majorana fermions in superconductors," (2011), unpublished, arXiv:1112.1950 .

[149] Jason Alicea, "New directions in the pursuit of Majorana fermions in solid state systems," (2011), unpublished, arXiv:1202.1293 .

[150] Ari M. Turner, Yi Zhang, Roger S. K. Mong, and Ashvin Vishwanath, "Quantized response and topology of magnetic insulators with inversion symmetry," Phys. Rev. B **85**, 165120 (2012).

[151] Roger S. K. Mong, Andrew M. Essin, and Joel E. Moore, "Antiferromagnetic topological insulators," Phys. Rev. B **81**, 245209 (2010).

[152] Pavan Hosur, Pouyan Ghaemi, Roger S. K. Mong, and Ashvin Vishwanath, "Majorana Modes at the Ends of Superconductor Vortices in Doped Topological Insulators," Phys. Rev. Lett. **107**, 097001 (2011).

[153] L. Pontryagin, "A classification of mappings of the three-dimensional complex into the two-dimensional sphere," Rec. Math. [Mat. Sbornik] N. S. **9(51)**, 331–363 (1941).

[154] Martin R. Zirnbauer, "Riemannian symmetric superspaces and their origin in random-matrix theory," J. Math. Phys. **37**, 4986–5018 (1996).

[155] Friedrich W. Hehl, Yuri N. Obukhov, Jean-Pierre Rivera, and Hans Schmid, "Relativistic analysis of magnetoelectric crystals: Extracting a new 4-dimensional P odd and T odd pseudoscalar from Cr_2O_3 data," Phys. Lett. A **372**, 1141–1146 (2008).

[156] Joseph Maciejko, Xiao-Liang Qi, H. Dennis Drew, and Shou-Cheng Zhang, "Topological Quantization in Units of the Fine Structure Constant," Phys. Rev. Lett. **105**, 166803 (2010).

[157] A. A. Abrikosov and S. D. Beneslavskii, "Possible Existence of Substances Intermediate Between Metals and Dielectrics," Zh. Eksp. Teor. Fiz. **59**, 1280–1298 (1970), [Eng. transl. JETP, **32**, 699–708 (1971)].

[158] G. E. Volovik, "Chiral anomaly and the law of conservation of momentum in ^{3}He-A," Pis'ma v Zh. Eksp. Teor. Fiz. **43**, 428–431 (1986), [Eng. transl. JETP Lett., **43**, 551–554 (1986)].

[159] Xiangang Wan, Ari M. Turner, Ashvin Vishwanath, and Sergey Y. Savrasov, "Topological semimetal and Fermi-arc surface states in the electronic structure of pyrochlore iridates," Phys. Rev. B **83**, 205101 (2011).

[160] Iván D. Rodríguez and Germán Sierra, "Entanglement entropy of integer quantum Hall states," Phys. Rev. B **80**, 153303 (2009).

[161] F. D. M. Haldane, "Entanglement Spectrum of Topological Insulators," (APS March Meeting, 2009) Session T13.00013.

[162] Noah Bray-Ali, Letian Ding, and Stephan Haas, "Topological order in paired states of fermions in two dimensions with breaking of parity and time-reversal symmetries," Phys. Rev. B **80**, 180504(R) (2009).

[163] Lukasz Fidkowski, "Entanglement Spectrum of Topological Insulators and Superconductors," Phys. Rev. Lett. **104**, 130502 (2010).

[164] Ari M. Turner, Yi Zhang, and Ashvin Vishwanath, "Entanglement and inversion symmetry in topological insulators," Phys. Rev. B **82**, 241102(R) (2010), a longer version of the paper is available at arXiv:0909.3119.

[165] Mehdi Kargarian and Gregory A. Fiete, "Topological phases and phase transitions on the square-octagon lattice," Phys. Rev. B **82**, 085106 (2010).

[166] Shuichi Murakami, "Phase transition between the quantum spin Hall and insulator phases in 3D: emergence of a topological gapless phase," New J. Phys. **9**, 356 (2007).

[167] Raffaele Resta and David Vanderbilt, "Physics of Ferroelectrics: A Modern Perspective," (Springer-Verlag, Berlin, 2007) Chap. "Theory of Polarization: A Modern Approach", pp. 31–68, available at the author's webpage.

[168] David Vanderbilt and R. D. King-Smith, "Electric polarization as a bulk quantity and its relation to surface charge," Phys. Rev. B **48**, 4442–4455 (1993).

[169] Ingo Peschel, "Calculation of reduced density matrices from correlation functions," J. Phys. A: Math. Gen. **36**, L205–L208 (2003).

[170] Joel E. Moore, Ying Ran, and Xiao-Gang Wen, "Topological Surface States in Three-Dimensional Magnetic Insulators," Phys. Rev. Lett. **101**, 186805 (2008).

[171] Allen Hatcher, *Algebraic Topology* (Cambridge University Press, 2002) available at the author's webpage.

[172] Volovik G. E., "Topological singularities on the surface of an ordered system," Pis'ma v Zh. Eksp. Teor. Fiz. **29**, 65–68 (1978), [Eng. transl. JETP Lett., **28**, 59–62 (1978)].

[173] V. P. Mineyev and G. E. Volovik, "Planar and linear solitons in superfluid ^{3}He," Phys. Rev. B **18**, 3197–3203 (1978).

[174] D. J. Thouless, "Quantization of particle transport," Phys. Rev. B **27**, 6083–6087 (1983).

[175] Andrew M. Essin, Ari M. Turner, Joel E. Moore, and David Vanderbilt, "Orbital magnetoelectric coupling in band insulators," Phys. Rev. B **81**, 205104 (2010).

[176] Zhong Wang, Xiao-Liang Qi, and Shou-Cheng Zhang, "Equivalent topological invariants of topological insulators," New J. Phys. **12**, 065007 (2010).

[177] Taylor L. Hughes, Emil Prodan, and B. Andrei Bernevig, "Inversion-symmetric topological insulators," Phys. Rev. B **83**, 245132 (2011).

[178] Alonso Botero and Benni Reznik, "BCS-like modewise entanglement of fermion Gaussian states," Phys. Lett. A **331**, 39–44 (2004).

[179] Israel Klich, "Lower entropy bounds and particle number fluctuations in a Fermi sea," J. Phys. A: Math. Gen. **39**, L85–L91 (2006).

[180] Lukasz Fidkowski and Alexei Kitaev, "Effects of interactions on the topological classification of free fermion systems," Phys. Rev. B **81**, 134509 (2010).

[181] Shinsei Ryu, Andreas Schnyder, Akira Furusaki, and Andreas W. W. Ludwig, "Topological insulators and superconductors: ten-fold way and dimensional hierarchy," New J. Phys. **12**, 065010 (2010).

[182] Frank Wilczek, "Two applications of axion electrodynamics," Phys. Rev. Lett. **58**, 1799–1802 (1987).

[183] Andrei Malashevich, Ivo Souza, Sinisa Coh, and David Vanderbilt, "Theory of orbital magnetoelectric response," New J. Phys. **12**, 053032 (2010).

[184] P. C. Canfield, J. D. Thompson, W. P. Beyermann, A. Lacerda, M. F. Hundley, E. Peterson, Z. Fisk, and H. R. Ott, "Magnetism and heavy fermion-like behavior in the RBiPt series," J. Appl. Phys. **70**, 5800 (1991).

[185] R. D. King-Smith and David Vanderbilt, "Theory of polarization of crystalline solids," Phys. Rev. B **47**, 1651–1654 (1993).

[186] Gerardo Ortiz and Richard M. Martin, "Macroscopic polarization as a geometric quantum phase: Many-body formulation," Phys. Rev. B **49**, 14202–14210 (1994).

[187] Pavan Hosur, Shinsei Ryu, and Ashwin Vishwanath, "Chiral topological insulators, superconductors, and other competing orders in three dimensions," Phys. Rev. B **81**, 045120 (2010).

[188] Roman Jackiw, "Fractional charge and zero modes for planar systems in a magnetic field," Phys. Rev. D **29**, 2375–2377 (1984).

[189] K. Ishikawa, "Chiral Anomaly and Quantized Hall Effect," Phys. Rev. Lett. **53**, 1615–1618 (1984).

[190] K. Matsubara, H. Anno, H. Kaneko, and Y. Imai, "Electrical properties of half-metallic PtMnSb-based Heusler alloys," (Eighteenth International Conference on Thermoelectrics, 1999) pp. 60–63, doi: 10.1109/ICT.1999.843334.

[191] Chang Liu, Yongbin Lee, Takeshi Kondo, Eun Deok Mun, Malinda Caudle, B. N. Harmon, Sergey L. Bud'ko, Paul C. Canfield, and Adam Kaminski, "Metallic surface electronic state in half-Heusler compounds RPtBi (R = Lu, Dy, Gd)," Phys. Rev. B **83**, 205133 (2011).

[192] A. Kreyssig, M. G. Kim, J. W. Kim, D. K. Pratt, S. M. Sauerbrei, S. D. March, G. R. Tesdall, S. L. Bud'ko, P. C. Canfield, R. J. McQueeney, and A. I. Goldman, "Magnetic order in GdBiPt studied by x-ray resonant magnetic scattering," Phys. Rev. B **84**, 220408(R) (2011).

[193] Andrew M. Essin and Victor Gurarie, "Antiferromagnetic topological insulators in cold atomic gases," (2011), unpublished, arXiv:1112.6013 .

[194] Andreas P. Schnyder, Shinsei Ryu, Akira Furusaki, and Andreas W. W. Ludwig, "Classification of Topological Insulators and Superconductors," AIP Conference Proceedings **1134**, 10–21 (2009).

[195] Roman Jackiw and C. Rebbi, "Solitons with fermion number 1/2," Phys. Rev. D **13**, 3398–3409 (1976).

[196] Jeffrey C. Y. Teo and C. L. Kane, "Topological defects and gapless modes in insulators and superconductors," Phys. Rev. B **82**, 115120 (2010).

[197] Shijun Mao, Yoshio Kuramoto, Ken-Ichiro Imura, and Ai Yamakage, "Analytic Theory of Edge Modes in Topological Insulators," J. Phys. Soc. Japan **79**, 124709 (2010).

[198] Shun-Qing Shen, Wen-Yu Shan, and Hai-Zhou Lu, "Topological insulator and the Dirac equation," SPIN **1**, 33–44 (2011).

[199] Andreas P. Schnyder, P. M. R. Brydon, Dirk Manske, and Carsten Timm, "Andreev spectroscopy and surface density of states for a three-dimensional time-reversal-invariant topological superconductor," Phys. Rev. B **82**, 184508 (2010).

[200] W. P. Su, J. R. Schrieffer, and A. J. Heeger, "Solitons in Polyacetylene," Phys. Rev. Lett. **42**, 1698–1701 (1979).

[201] David B. Kaplan, "A method for simulating chiral fermions on the lattice," Phys. Lett. B **288**, 342–347 (1992).

[202] Mitsutaka Fujita, Katsunori Wakabayashi, Kyoko Nakada, and Koichi Kusakabe, "Peculiar Localized State at Zigzag Graphite Edge," J. Phys. Soc. Japan **65**, 1920–1923 (1996).

[203] Chao-Xing Liu, Xiao-Liang Qi, Hai-Jun Zhang, Xi Dai, Zhong Fang, and Shou-Cheng Zhang, “Model Hamiltonian for topological insulators,” Phys. Rev. B **82**, 045122 (2010).

[204] H. Büttner and E. Gerlach, “On the extension of shockley surface states in metals,” Surface Science **32**, 687 – 693 (1972).

[205] D. H. Lee and J. D. Joannopoulos, “Simple scheme for surface-band calculations. I,” Phys. Rev. B **23**, 4988–4996 (1981).

[206] Congjun Wu, B. Andrei Bernevig, and Shou-Cheng Zhang, “Helical Liquid and the Edge of Quantum Spin Hall Systems,” Phys. Rev. Lett. **96**, 106401 (2006).

[207] A. R. Akhmerov and C. W. J. Beenakker, “Boundary conditions for Dirac fermions on a terminated honeycomb lattice,” Phys. Rev. B **77**, 085423 (2008).

[208] Jeffrey C. Y. Teo, Liang Fu, and C. L. Kane, “Surface states and topological invariants in three-dimensional topological insulators: Application to $\mathrm{Bi}_{1-x}\mathrm{Sb}_x$,” Phys. Rev. B **78**, 045426 (2008).

[209] P. Heinzner, A. Huckleberry, and M. R. Zirnbauer, “Symmetry Classes of Disordered Fermions,” Comm. Math. Phys. **257**, 725–771 (2005).

[210] Sankar Das Sarma, Chetan Nayak, and Sumanta Tewari, “Proposal to stabilize and detect half-quantum vortices in strontium ruthenate thin films: Non-Abelian braiding statistics of vortices in a $p_x + ip_y$ superconductor,” Phys. Rev. B **73**, 220502 (2006).

[211] Frank Wilczek and A. Zee, “Appearance of Gauge Structure in Simple Dynamical Systems,” Phys. Rev. Lett. **52**, 2111–2114 (1984).

[212] J. L. Zhang, S. J. Zhang, H. M. Weng, W. Zhang, L. X. Yang, Q. Q. Liu, S. M. Feng, X. C. Wang, R. C. Yu, L. Z. Cao, L. Wang, W. G. Yang, H. Z. Liu, W. Y. Zhao, S. C. Zhang, X. Dai, Z. Fang, and C. Q. Jin, “Pressure-induced superconductivity in topological parent compound $\mathrm{Bi_2Te_3}$,” Proc. Nat. Acad. Sci. USA **108**, 24–28 (2011).

[213] M. Wimmer, A. R. Akhmerov, M. V. Medvedyeva, J. Tworzydło, and C. W. J. Beenakker, “Majorana Bound States without Vortices in Topological Superconductors with Electrostatic Defects,” Phys. Rev. Lett. **105**, 046803 (2010).

[214] Andrew C. Potter and Patrick A. Lee, “Multichannel Generalization of Kitaev’s Majorana End States and a Practical Route to Realize Them in Thin Films,” Phys. Rev. Lett. **105**, 227003 (2010).

[215] N. Read and Andreas W. W. Ludwig, “Absence of a metallic phase in random-bond Ising models in two dimensions: Applications to disordered superconductors and paired quantum Hall states,” Phys. Rev. B **63**, 024404 (2000).

[216] M. Bocquet, D. Serban, and M. R. Zirnbauer, "Disordered 2d quasiparticles in class D: Dirac fermions with random mass, and dirty superconductors," Nucl. Phys. B **578**, 628–680 (2000).

[217] C. Caroli, P. G. de Gennes, and J. Matricon, "Bound Fermion states on a vortex line in a type II superconductor," Phys. Lett. **9**, 307–309 (1964).

[218] Y. S. Hor, A. J. Williams, J. G. Checkelsky, P. Roushan, J. Seo, Q. Xu, H. W. Zandbergen, A. Yazdani, N. P. Ong, and R. J. Cava, "Superconductivity in $Cu_xBi_2Se_3$ and its Implications for Pairing in the Undoped Topological Insulator," Phys. Rev. Lett. **104**, 057001 (2010).

[219] L. Andrew Wray, Su-Yang Xu, Yuqi Xia, Yew San Hor, Dong Qian, Alexei V. Fedorov, Hsin Lin, Arun Bansil, Robert J. Cava, and M. Zahid Hasan, "Observation of topological order in a superconducting doped topological insulator," Nature Physics **6**, 855–859 (2010).

[220] T. Kirzhner, E. Lahoud, K. B. Chaska, Z. Salman, and A. Kanigel, "Unconventional superconductivity in $Cu_{0.2}Bi_2Se_3$," (2011), unpublished, arXiv:1111.5805 .

[221] R. A. Hein and E. M. Swiggard, "Superconductivity in $TlBiTe_2$: A Low Carrier Density (III-V)VI_2 Compound," Phys. Rev. Lett. **24**, 53–55 (1970).

[222] Timothy H. Hsieh, Hsin Lin, Junwei Liu, Wenhui Duan, Arun Bansil, and Liang Fu, "Topological Crystalline Insulators in the SnTe Material Class," (2012), unpublished, arXiv:1202.1003 .

[223] Y. Matsushita, P. A. Wianecki, A. T. Sommer, T. H. Geballe, and I. R. Fisher, "Type II superconducting parameters of Tl-doped PbTe determined from heat capacity and electronic transport measurements," Phys. Rev. B **74**, 134512 (2006).

[224] R. A. Hein, "Critical magnetic fields of superconducting SnTe," Phys. Lett. **23**, 435–436 (1966).

[225] R. A. Hein, J. W. Gibson, R. Mazelsky, R. C. Miller, and J. K. Hulm, "Superconductivity in Germanium Telluride," Phys. Rev. Lett. **12**, 320–322 (1964).

[226] A. H. Castro Neto, F. Guinea, N. M. R. Peres, K. S. Novoselov, and A. K. Geim, "The electronic properties of graphene," Rev. Mod. Phys. **81**, 109–162 (2009).

[227] S. Das Sarma, Shaffique Adam, E. H. Hwang, and Enrico Rossi, "Electronic transport in two-dimensional graphene," Rev. Mod. Phys. **83**, 407–470 (2011).

[228] I. L. Aleiner and K. B. Efetov, "Effect of Disorder on Transport in Graphene," Phys. Rev. Lett. **97**, 236801 (2006).

[229] P. M. Ostrovsky, I. V. Gornyi, and A. D. Mirlin, "Quantum Criticality and Minimal Conductivity in Graphene with Long-Range Disorder," Phys. Rev. Lett. **98**, 256801 (2007).

[230] P. Markoš and L. Schweitzer, "Critical regime of two-dimensional Ando model: relation between critical conductance and fractal dimension of electronic eigenstates," J. Phys. A: Math. Gen. **39**, 3221 (2006).

[231] Ferdinand Evers and Alexander D. Mirlin, "Anderson transitions," Rev. Mod. Phys. **80**, 1355–1417 (2008).

[232] Chao-Xing Liu, Xiao-Liang Qi, and Shou-Cheng Zhang, "Half quantum spin Hall effect on the surface of weak topological insulators," Physica E **44**, 906–911 (2012).

[233] Hideaki Obuse, Akira Furusaki, Shinsei Ryu, and Christopher Mudry, "Two-dimensional spin-filtered chiral network model for the Z_2 quantum spin-Hall effect," Phys. Rev. B **76**, 075301 (2007).

[234] Andrew M. Essin and J. E. Moore, "Topological insulators beyond the Brillouin zone via Chern parity," Phys. Rev. B **76**, 165307 (2007).

[235] Ryuichi Shindou and Shuichi Murakami, "Effects of disorder in three-dimensional $\mathbb{Z}_2$ quantum spin Hall systems," Phys. Rev. B **79**, 045321 (2009).

[236] Konstantin Efetov, *Supersymmetry in Disorder and Chaos* (Cambridge University Press, 1997).

[237] Alexander Altland and Ben Simons, *Condensed Matter Field Theory*, 2^{nd} ed. (Cambridge University Press, 2010).

[238] John Cardy, *Scaling and Renormalization in Statistical Physics* (Cambridge University Press, 1996).

[239] Alexander Altland, B. D. Simons, and M. R. Zirnbauer, "Theories of low-energy quasi-particle states in disordered d-wave superconductors," Phys. Rep. **359**, 283–354 (2002).

[240] P. M. Ostrovsky, I. V. Gornyi, and A. D. Mirlin, "Electron transport in disordered graphene," Phys. Rev. B **74**, 235443 (2006).

[241] A. Schuessler, P. M. Ostrovsky, I. V. Gornyi, and A. D. Mirlin, "Analytic theory of ballistic transport in disordered graphene," Phys. Rev. B **79**, 075405 (2009).

[242] Tomi Ohtsuki, Keith Slevin, and Bernhard Kramer, "Conductance distribution at two-dimensional anderson transitions," Physica E **22**, 248–251 (2004).

[243] Ai Yamakage, Kentaro Nomura, Ken-Ichiro Imura, and Yoshio Kuramoto, "Disorder-Induced Multiple Transition Involving $\mathbb{Z}_2$ Topological Insulator," J. Phys. Soc. Japan **80**, 053703 (2011).

[244] S. Ryu, C. Mudry, A. W. W. Ludwig, and A. Furusaki, "High-gradient operators in perturbed Wess-Zumino-Witten field theories in two dimensions," Nucl. Phys. B **839**, 341–376 (2010).

[245] D. E. Khmel'nitskiĭ, "Quantization of Hall conductivity," Pis'ma v Zh. Eksp. Teor. Fiz. **38**, 454–458 (1983), [Eng. transl. JETP Lett., **38**, 552–556 (1983)].

[246] Adrianus M. M. Pruisken, "On localization in the theory of the quantized hall effect: A two-dimensional realization of the θ-vacuum," Nucl. Phys. B **235**, 277–298 (1984).

[247] Adrianus M. M. Pruisken, "Dilute instanton gas as the precursor to the integral quantum hall effect," Phys. Rev. B **32**, 2636–2639 (1985).